Royal Holloway University of London

Doctoral Thesis

Rifted margin architecture and the interplay between mantle, crustal and surface processes from geodynamic numerical experiments

Miguel Andrés-Martínez

Supervised by
Prof. Marta Pérez-Gussinyé
Prof. Jason P. Morgan
Prof. Lars Rüpke

A thesis submitted in fulfilment of the requirements
for the degree of Doctor of Philosophy

May 2016

Department of Earth Sciences
Royal Holloway University of London
Egham, United Kingdom

Declaration of Authorship

I, Miguel Andrés-Martínez hereby declare that this thesis and the work presented in it is entirely my own. Where I have consulted the work of others, this is always clearly stated.

Signed: _____

Date: _____

Abstract

Divergent margin development is a fundamental aspect of plate tectonics, yet it remains poorly understood. Key issues like the formation of tectonic asymmetry between conjugate margins, the detailed history of vertical movements, and the influence of sedimentation on margin architecture remain unresolved. In this PhD I developed accurate numerical tools essential to understand margins and their sedimentary response.

I placed particular emphasis in simulating uplift and subsidence for which I have developed a free-surface algorithm. Stress-free surfaces typically suffer from instabilities when the time step is bigger than the viscous relaxation time. The new free-surface algorithm improves performance of the models avoiding instability, so that the code yields stable and accurate dynamic topographies.

Subsequently, I explored the factors influencing the polarity of the asymmetry between conjugate margin pairs. Along the magma-poor stretch of the South Atlantic margins the polarity correlates with the distance of the rift to nearby cratons. Numerical experiments of extension show that the presence of a thick cratonic lithosphere inhibits asthenospheric flow from underneath the craton towards the fold belt, while flow from underneath the fold belt towards the craton is favoured thereby enhancing craton-ward faulting. These faults become dominant, resulting in a wide faulted margin in the fold belt, and a narrow conjugate margin in the craton side, as observed in nature.

Finally, I implemented surface processes into the models to study the feedbacks between tectonics and sedimentation. Models show that different rates in erosion/deposition have an important impact on margin subsidence and architecture. This influence is modulated by lower crust rheology. Furthermore, models showcase varying-in-time break-up unconformities along the margins, which are explained as a result of rift migration.

Although numerical models do not represent nature in its full complexity, they are an excellent testing tool for studying interplays between geological processes. Future work will include further addition of complexity into the codes to understand a variety of problems including oceanization and feedbacks between climate and tectonics.

Acknowledgements

This thesis would have not been possible without the help of many people who lend a hand in many different ways.

The first person to acknowledge is of course Marta Pérez-Gussinyé. I am very grateful to her for many reasons starting by the fact that she chose me for this PhD. She has nicely supervised the project with regular meetings, very stimulating scientific discussions, she has greatly helped to the development of my presenting and writing skills, and she has provided meticulous revisions of the thesis chapters. Furthermore, she gave me absolute freedom to choose what I wanted to do during my research. At a personal level she has been always a close person not only interested in the science, but with whom I can have a random conversation (for example, about how bad are the Spanish politicians, for what we always conclude that they are really really bad).

I would also like to acknowledge Jason P. Morgan. I have never found a mathematical or continuum-mechanics question stupid enough for him to loose his patience: he always gave me extended answers and recommend me very useful bibliography. The same applies to the reviews of my chapters, where he had to read over and over again the same prepositions in the wrong place and the weirdest acronyms I could have invented. I would also like to thank him for all the interesting talks about what to do next and how can we make better science. His input in this thesis has been crucial for the developing of the codes.

Lars Rüepke also helped me a lot introducing me into the former code and into the finite element method. I would also like to thank him for his rigorous review of the free surface manuscript and his valuable feedback for the peer-review.

John Armitage has been a very great person to work with. His daily need of a coffee outside of the department had lead to very interesting conversations about numerical modelling and life in general. It has been great to discuss about the sediments, their implementation and to have his feedback for the surface processes chapter.

I would like to also thank Christian Heine, Graeme Eagles, Lucía Pérez, Lloyd White and Philip Ball for their assistance with GMT, by providing data for some maps presented on this thesis and for their useful feedback.

If I were a pine tree in a bonsai pot my '*nebari*' would be my family and friends at Córdoba and Spain.

The gratitude to my whole family is unmeasurable, specially to my parents. I have always had their support and their incredibly valuable advice. They have always managed to make me feel at home anywhere I was. They have all my admiration and love.

And of course Pablo, that genius that happens to be my brother. Thanks a lot for all the times, good, bad, thanks for being there to talk about relationships, philosophy, music, games, science, '*porros folares*', etc.

I am also grateful to my uncle Jose Ramon, who is always happy to give valuable career advice and from whom I learnt how painful can be to fish a '*liberna*'.

To Juani also for being an example of self-improvement and a wonderful person.

MaRaLas, which basically stands for Manolo, Rafa and Laura, to you because you are always my friends, no matter for how long I disappear, it is always like I have never left. To David because we finally learnt English (more or less) and because we are the Londoners. And to Leti, because it never matters how different we are. And to Ana, Miguel Ángel, Mar, Esperanza, Alejandra, Francisco and Estefanía, because growing up with you has been a wonderful adventure!

Thanks also to Miriam and Pocababa, for incredibly funny and enjoyable times.

However, I am not a pine tree in a pot and my roots have grown all over the world. I knew I would meet many people but I didn't know I would keep in touch with them so often.

Thanks to Jesus because you are the only person I know that fully understands how important are the garlics.

Thanks to Francesco, Jorge and Jaron for amazing times in UCSB, Chile and Peru.

And Egham, that little town where nothing seems to happen but in fact there is always something going on. Very special thanks to Oris, Jorge1, Elena, Ivan, Arnaud, Giovanni and Seb. You have been my family here, without you, Egham would have been a very sad and boring place. Also thanks to Denise, the traveller. And to many many many more friends: Gerd, Viola M., Jorge2.0, Albert, Micio, Damiano, Giulia, Marianne, Lorenzo, Francisco, Maxim, Rebecca, Basim, Serena, Laura, Ed, Guy, Camilla, John P. and John B., Amanda, Chris, Sila, Eldert, Raquel, Viola W., Tim, Juliane, Ega, Oriol, Christof, Lidia, Mersiye, Ben and Azad.

And the last but no the least, a very special thanks to Cristina, for being always there, unconditionally.

An inspiration is what you are to me
inspiration, look, see...

'Thank you' by Led Zeppeling

Contents

List of Figures

List of Tables

To my family and friends

Chapter 1

Introduction

1.1 Rifting and breakup of a continent

The Earth is a extremely heterogeneous system where a great variety of processes interact at very different spatial and time scales. In order to explain these processes and their outcomes, geologists make use of a wide variety of techniques such as field studies, geophysical exploration, geochemical experiments, petrological analysis, radiometric dating, numerical modelling, etc. However, the heterogeneous character of the Earth, the lack of direct observations from its inside and the giant time and spatial scales of some of its processes have obscured our understanding of global dynamics. Only in the late 60s were all these techniques developed enough to overcome the scale limitations and set the paradigm of plate tectonics. Plate tectonics establishes that the Earth's outer most shell is divided in rigid plates which move relative to each other over a viscous layer (Wilson, 1963, 1965, 1966; McKenzie and Parker, 1967; Morgan, 1968; Le Pichon, 1968). As plates are considered rigid, relative displacements occur at their boundaries. Three types of plate boundaries can be defined based on the type of motion: 1) divergent where two plates separate leading to generation of new oceanic crust at oceanic ridges, 2) convergent where one plate subducts below another, and 3) transform where two plates move parallel to their boundary in opposite horizontal directions without creation or destruction of crust. Plate boundaries are not static features, they may become inactive and new boundaries can appear in the middle of a plate.

The process by which a continental crust horizontally stretches and vertically thins is known as **rifting** and, if the extension does not stop, results into a new divergent boundary where oceanic crust is generated (Baker et al., 1972; McConnell, 1972; Fairhead, 1976). Extension is accommodated by normal faults (upper crust) and viscous flow (lower crust

and mantle) which, more or less gradually, thin the lithosphere. **Passive margins** refer to the span of the continental crust thinned by this extension. Passive margins are of great interest from different perspectives: 1) scientifically because they represent the process of oceanization and because they are an expression of the inner-Earth dynamics, and 2) economically because the submarine environment of the deepest basins, which together with their infilling by sediments from the continent, allows for the formation of economic oil and gas deposits.

Rifting has been typically classified as volcanic or non-volcanic, also known as magma-rich and -poor, respectively. Although a decade ago, it was generally accepted that volcanic margins were associated to hot mantle temperatures and fast extension rates (Keen and Boutilier, 2000; Nielsen and Hopper, 2004), while non-volcanic occur at slow extension rates and cold lithospheres (Sibuet et al., 2007), more recent studies show that there are other important factors that condition rifting type, such as the rifting history or mantle composition (Müntener and Manatschal, 2006; Pérez-Gussinyé et al., 2006; Voss et al., 2009; Armitage et al., 2010).

1.2 Non-volcanic rifted margins

Initially, magma-poor or non-volcanic rifting was thought to be an uncommon byproduct of continental extension. However, it has been shown that non-volcanic extension may represent a more common than previously thought type of rifting. Margins considered non-volcanic are the West Iberia-Newfoundland conjugates, the Cretaceous Northeast Atlantic margins, the central sector of the South Atlantic conjugates and the margins of the Southern Sea (Fig. 1.1) (Sibuet, 1992; Manatschal and Bernoulli, 1999; Boillot and Froitzheim, 2001; Pérez-Gussinyé et al., 2001; Pérez-Gussinyé et al., 2001; Reston et al., 2001; Whitmarsh et al., 2001; Lundin and Doré, 2011).

Non-volcanic rifted margins are characterized by very little magmatism during extension and a wide continent-ocean transition, which is often interpreted as an expanse of exhumed and serpentinized mantle (Boillot and Froitzheim, 2001; Whitmarsh et al., 2001). The lack of magmatism in these margins may be related to very slow extension velocities (Minshull et al., 2001; Pérez-Gussinyé et al., 2006), a depleted composition of the mantle (Müntener and Manatschal, 2006; Pérez-Gussinyé et al., 2006) or to a mantle that is colder than sub-oceanic ridge mantle (Reston and Morgan, 2004). It has been shown that magma-poor margins all extend very slowly (Minshull et al., 2001; Pérez-Gussinyé et al., 2006; Heine et al., 2013). Slow extension velocities lead to cooling by conduction during extension. This results in the inhibition of melting during decompression and also

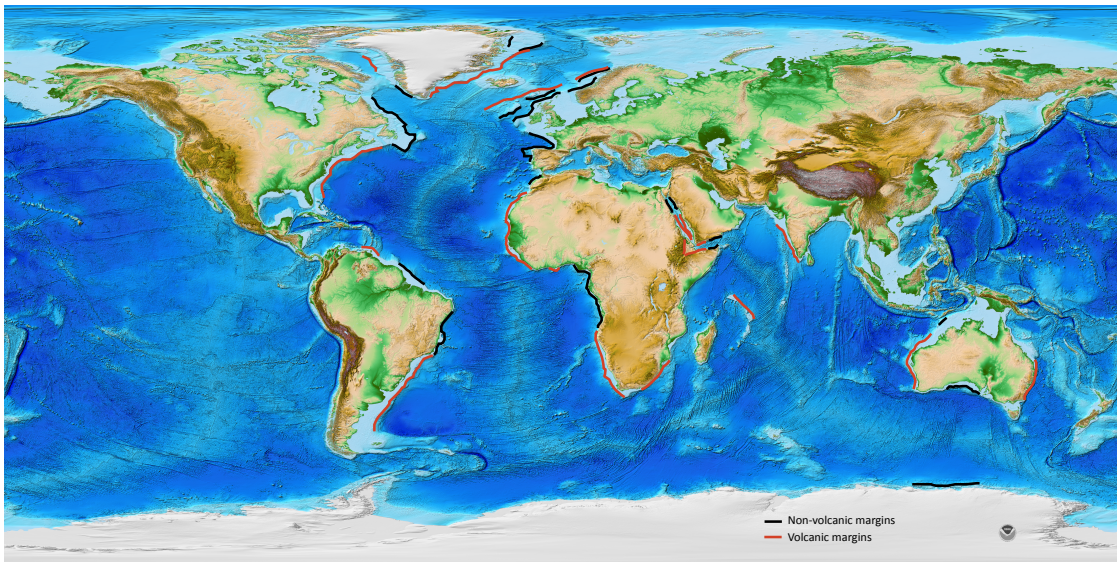

FIGURE 1.1: Volcanic and non-volcanic passive margins. Colors represent topography. Topographic map from ETOPO1 (Amante and Eakins, 2009). Margin type data from Sibuet, 1992; Manatschal and Bernoulli, 1999; Boillot and Froitzheim, 2001; Pérez-Gussinyé et al., 2001; Pérez-Gussinyé et al., 2001; Reston et al., 2001; Whitmarsh et al., 2001; Lundin and Doré, 2011; Minshull, 2009; Tugend et al., 2014; Hopper et al., 2003; Subrahmanya, 2001; Blaich et al., 2011; Menzies et al., 1997; Kelemen and Holbrook, 1995; Frey et al., 1998.

a change in rheology of the lower crustal rocks from ductile to brittle towards the end of the extension. Embrittlement of the crust allows faults to reach the mantle, and to bring enough water to serpentinize it. Crustal scale faults lead to crustal breakup and the exhumation of the mantle before enough melt has been generated to create a steady-state oceanic ridge. This results in a wide continent-ocean transition consisting of exhumed and serpentinised mantle before oceanic accretion starts (Pérez-Gussinyé et al., 2001; Peréz-Gussinyé and Reston, 2001).

It is not clear, however, whether all magma-poor margins exhibit a wide continent-ocean transition consisting of exhumed and serpentinised mantle or some have an abrupt transition to oceanic crust. In addition, magma-poor margins show a great architectural variability. Some present numerous faults that thin the crust smoothly such as the West Iberian Margin, while others show less faulting with larger offsets that thin the crust abruptly such as the Great Australian Bight (Fig. 1.2). Asymmetry of conjugate margins is also variable, for example conjugates of West Iberia and Newfondland, and some sectors of the South Atlantic (Camamu/Gabon conjugates) exhibit a large degree of asymmetry while other sectors of the South Altantic (Campos/Kwanza conjugates) showcase symmetry (see Chapter 4, Fig. 1). Factors that control the degree of asymmetry and the final architecture of the margins are poorly constrained. Therefore, one of the aims of this

thesis has been to investigate how factors such as pre-existing lithospheric structure and amount of sedimentation control margin architecture and degree of asymmetry.

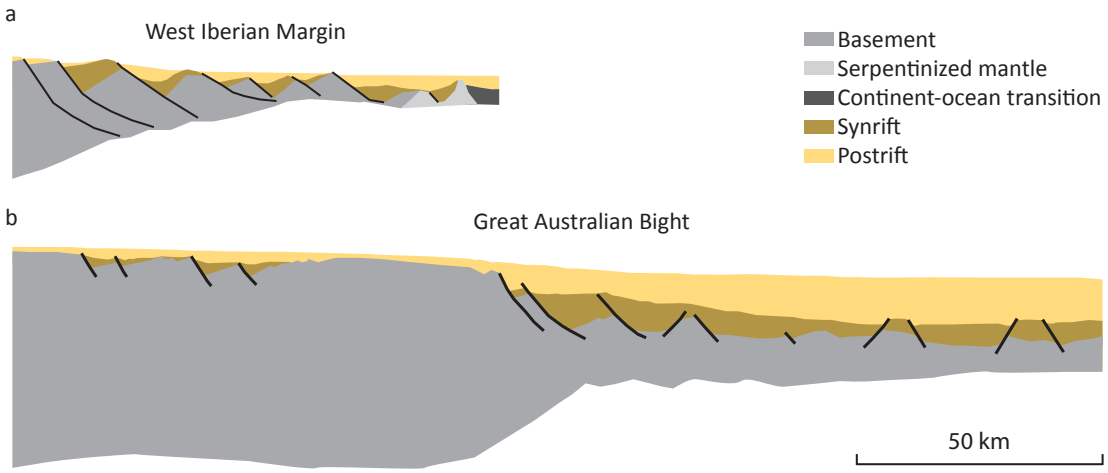

FIGURE 1.2: Non-volcanic margin architectures of a) West Iberian Margin (Ranero and Pérez-Gussinyé, 2010; Pérez-Gussinyé, 2013) and b) Great Australian Bight (Totterdell et al., 2000; Talwani et al., 1979; Falvey and Mutter, 1981; Pérez-Gussinyé et al., in prep.).

1.3 Motivation

Passive margins have been intensively studied since the beginning of the 20th century due to their economical interest. Nowadays, there is a great availability of passive-margin data such as boreholes and reflection and refraction seismics both in 2D and 3D. Furthermore, acquisition techniques for seismic imaging and signal processing are in constant revision which allows for a constant improvement of seismic image resolution. Particularly exciting new images on margin architecture are those of the pre-salt at the South Atlantic which, although similar in some aspects to the West Iberia/Newfoundland ones, are very different in terms of the width of the conjugate margins and perhaps also the transition to oceanic spreading. The next generation of 3D geophysical data and future IODP drillings, together with a scientific community better connected than ever, promise great findings on margin development in the next decades.

However, nowadays datasets still lack of the resolution needed to link the mineral-scale chemical and mechanical processes to the tectonic-scale events. Furthermore, every region of the highly heterogeneous Earth is unique, and it is the product of a unique combination of process interactions. Earth is also finite, in the sense that not all the possible combinations of process interplays are represented. Therefore, finite and heterogeneous

characteristics of the Earth limit and will limit our knowledge of the processes taking part in tectonics even if better datasets will be available in the near future.

In terms of rifting, all these limitations result into a wide variety of classifications and models of modes of extension built from observation. This models and interpretations are constantly tested, debated, modified and/or discarded. However, the limitations previously explained also make difficult for this models to converge into a generalised theory of extension. Also, models built from observations still fail to explain some aspects of the rifting processes, leaving many opened questions.

Most of these questions are of regional character and are typically related to the structure of the margins. Factors that influence conjugate margin asymmetry are starting to be better constrained (Brune et al., 2014). However, there is little knowledge on what controls the polarity of the asymmetry. There are also large number of evidences that prove surface processes such as erosion and sedimentation, have an impact on crustal deformation (Weissel and Karner, 1989; Buiter et al., 2008; Bialas and Buck, 2009; Kaus, 2010; Redfield and Osmundsen, 2012; Clift et al., 2015), but there are still uncertainties on what are the implications of surface processes in rifting evolution and final margin geometry and asymmetry. Regional sediment unconformities are typically observed at passive margins. Originally, they were interpreted to form at breakup time, when local subsidence by faulting is replaced by regional thermal subsidence (Falvey, 1974; McKenzie, 1978). However, nowadays it is widely accepted that faulting does not occur simultaneously along the whole span of the margins and that rift jump and rift migration are common during extension (i.e. Pérez-Gussinyé, 2013; Gillard et al., 2015). This has important implications for the tectonic meaning of regional unconformities, since they might not be necessarily related to breakup but to a change in the locus of the deformation followed by thermal subsidence. Further research is needed in this direction in order to obtain a catalogue of types of unconformities with their characteristics and associated modes of extension.

In a larger scale, questions that remain unsolved are related to the mechanisms driving rifting: Are far field stresses responsible for rifting? Are subduction zones responsible of these stresses? What is the role played by mantle convection in the rifting? What is the role of mantle plumes?. In order to address these questions it is important to integrate conclusions drawn from studies of different stages at the Wilson cycle. Furthermore, a better understanding of the development of passive margins could also help to better understand subduction initiation and the composition, water content, thermal state, etc. of the materials that are subducted or take part of the accretionary wedge. Therefore, it is essential to address the regional questions related to rifting in order to better understand Global Tectonics.

In this thesis I approach the regional questions presented above. As previously mentioned, the different scales of the processes involved in rifting and their interactions make regional studies complex. Here, I use numerical experiments together with systematic parameter exploration to better understand rift evolution and margin architecture. The main advantage of numerical modelling is that it is able to simultaneously integrate a wide variety of processes occurring in nature at different scales and allows for the study of their trade-offs and impacts on evolution and final geometry of passive margins. Then results can be contrasted with examples in nature.

In the last two decades numerical modelling has been successfully used to study rifting and continental breakup. Numerical codes have been applied to rifting to understand which thermo-mechanical conditions favour the different modes of extension observed in nature (Buck, 1991; Hopper and Buck, 1996; Buck and Lavier, 2001; Lavier and Buck, 2002; Huismans et al., 2005; Huismans and Beaumont, 2011; Buiter et al., 2008), which factors favour margin asymmetry (Brune et al., 2014), the importance of oblique rifting (Brune et al., 2012), the impact of precursor structures and lithosphere heterogeneities (Tommasi et al., 2009; Dunbar and Sawyer, 1989), and melt generation and serpentinization (Pérez-Gussinyé et al., 2006; Armitage et al., 2008, 2009, 2015). State-of-the-art 2D numerical codes typically account for multi-layered non-linear visco-elasto-plasticity, while 3D numerical models are typically multi-layered with non-linear viscosity.

Although these models are becoming very sophisticated, most of them still neglect surface processes or approach them in a very simplistic way. Additionally, when asymmetry occurs at these models the location of the narrow and the wide margins is random (random polarity of the asymmetry).

The aim of this thesis is to address questions related to: 1) which processes shape margin architecture, 2) which factors define the polarity of the conjugate asymmetry, 3) how do surface processes influence margin development and architecture, and 4) what is the tectonic meaning of the so called 'breakup' unconformities.

1.4 Thesis outline

This thesis is divided in seven chapters. Chapter 2 describes the numerical methodology used in the modelling. The core of this thesis is composed by three thematic blocks in the shape of journal publications or as manuscript drafts aimed for publication in the near future.

A large amount of the PhD time was spent on developing an algorithm to stabilize the topography modelled by the code. This algorithm allows the code to accurately and efficiently track topographies and recover subsidence and uplift, which were of great interest for later addressing surface processes. Chapter 3 is a methodology chapter resulting from the design and calibration of this topographic stabilization algorithm that was published on the journal Physics of the Earth and Planetary Interiors.

Chapter 4 addresses conjugate margin architecture, asymmetry and polarity when rifting occurs in the vicinity of a craton. This chapter is in the form of a manuscript draft for later publication.

Chapter 5 examines the influence of surface processes on margin architecture, asymmetry and modes of extension. Furthermore, the tectonic meaning of major unconformities observed in the sediments is addressed. This chapter is in the form of a manuscript draft for later publication.

Chapter 6 critically evaluates the results and methods used in this thesis and Chapter 7 summarizes the conclusions of this thesis.

Chapter 2

Methodology: Numerical modelling of crust and mantle dynamics

2.1 Introduction

The geology that we observe in the field results from the interaction of physico-chemical processes over a very broad range of spatial and temporal scales. A challenge in geology is to design experiments that help us to understand the processes that shape this geology. Analogue models can only represent these processes at much smaller spatial and temporal scales than those occurring in nature, so that the interpolation from the small scales of the lab to the large temporal scales observed in nature is uncertain. Moreover, typical analogue models cannot reproduce the feedbacks between rheology and temperature which take place in real deforming systems, as in most of the analogue experiments temperature and pressure do not meaningfully vary within the experimental box.

Numerical modelling of geodynamic processes helps us understand the physico-chemical interactions that shape the observed geology by solving for the basic physical laws that govern deformation in the crust and mantle, which are the conservation laws for mass, energy and momentum. These are solved assuming rheologies for mantle and crustal rocks obtained from experimental analysis in the laboratory. These rheologies also need to be extrapolated over orders of magnitude in time and space before they are used in numerical codes. As in analogue experiments, these extrapolations may be uncertain, but at least this allows us to explore the non-linear feedbacks between stress, strain and temperature, which is not possible with 'sand box' modelling. This is why numerical experiments have

become in the last two decades a very popular tool to investigate the geological structures observed in nature.

The combination of the laws for the conservation of mass, energy and momentum results in two differential equations, the Stokes equation of motion, which solves for the flow velocity of a viscous fluid in a gravity field, and the heat conservation equation, which solves for the temperature in the deforming crust and mantle. A large part of my PhD has consisted in developing a modified version of the finite element code MILAMIN (Dabrowski et al., 2008) which solves for these equations. The MILAMIN code first uses the Stokes equation to solve for the mechanical problem (i.e. the velocity of the rocks in the deforming Earth) and then the heat advection-diffusion equation to solve for the temperature of these rocks (the so-called thermal problem).

This thesis focuses on the numerical modelling of rifting. Although rifting is generally a strongly three-dimensional process, 3D modelling is nowadays computationally very expensive and the development of such a code is highly time-consuming. Instead, I choose to approach rifting by simulating a 2D cross section of the lithosphere, parallel to the extension velocity, so that the implementation of numerous processes involved in rifting could be accomplished during the PhD, and a larger number of experiments can be run with multiple combination of parameters and initial conditions. This section of virtual rock is then discretized into a finite element grid (see Sec. 2.4), where boundary conditions of constant velocities are applied at the edges of the box. The grid used here is composed of triangular (Fig. 2.1) Lagrangian elements (elements move with the material). The box is then divided into four layers: Upper Crust (UC), Lower Crust (LC), Dry-Olivine Mantle (DOM) or mantle lithosphere, and Wet-Olivine Mantle (WOM) or asthenosphere. These layers have distinct properties such as rheologies, densities, and thermal parameters. Finally, the mechanical and thermal problems are solved within this grid. In order to simulate rifting in a more realistic way I worked on the implementation of visco-elasto-plasticity, top free surface with a free-surface stabilization algorithm (see Chapter 3) in order to allow the model to generate stable dynamic topography, strain softening to simulate faulting and shear zones, and surface processes (i.e. erosion and sedimentation).

This chapter provides the formulation behind the mechanical and the thermal solvers, a brief description of the Finite Element Method (FEM), an explanation of the MILAMIN code and the modifications and implementations carried out during the project.

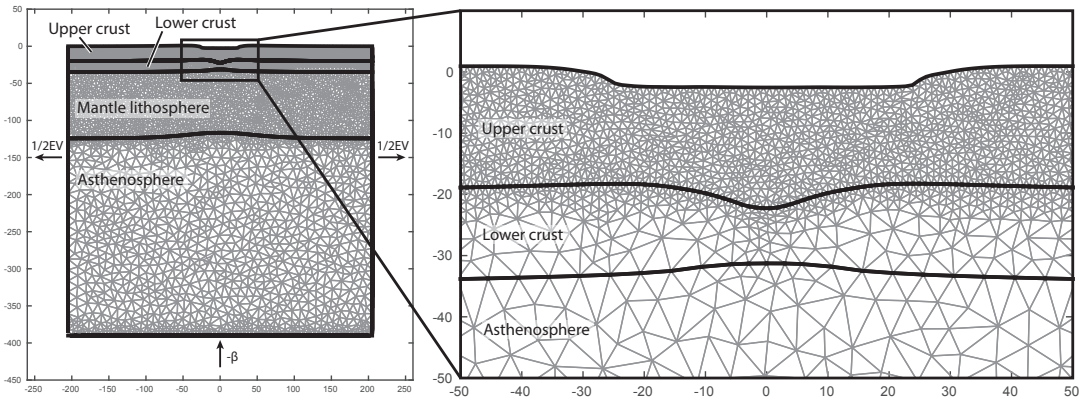

FIGURE 2.1: Finite element triangular grid. Different resolutions can be defined for the different layers and interfaces. Constant half extension velocities (1/2EV) are applied at the lateral edges of the grid as boundary conditions, while the bottom boundary condition corresponds to an upwelling of the same magnitude as the extension rate ($-\beta$).

2.2 The mechanical problem

The mechanical sub-problem consists of the procedure of solving the velocities and pressures inside a continuum under certain boundary conditions. Our model approaches rock dynamics assuming rocks behave as a highly viscous non-Newtonian (stress-strain rate non-linear relation) flow. Relevant concepts and definitions are given in the subsections 2.2.1, 2.2.2, 2.2.3 and 2.2.4, while subsection 2.2.5 details the actual formulation used in the code for solving the mechanical problem. Further documentation on stress, strain and momentum equation is provided in the appendix A sections A.0.1, A.0.2 and A.0.3 respectively.

2.2.1 Stress, strain rate and strain second invariants

Stress, strain rate and strain are tensors which respectively represent the internal distribution of forces, deformation rate and deformation states within a continuum (Malvern, 1969) (see appendix A.0.1 and A.0.2). However, it is convenient to express these tensors as total scalar magnitudes which are independent of the coordinate system. For this purpose we use the definition of square root of the second invariant.

The total magnitude of the deviatoric stress tensor expressed as a scalar is defined by the **square root of the second invariant of the deviatoric stress** τ_{II}:

$$\tau_{II} = \sqrt{(\tau_{11}^2 + \tau_{22}^2 + \tau_{33}^2)/2 + \sigma_{12}^2 + \sigma_{13}^2 + \sigma_{23}^2}, \tag{2.1}$$

The **square root of the second invariant of the deviatoric strain** ε_{II} and the **square root of the second invariant of the deviatoric strain rate** $\dot{\varepsilon}_{II}$ are scalars which account for the total magnitude of the deviatoric strain and the strain rate tensors respectively and they are defined as:

$$\varepsilon'_{II} = \sqrt{({\varepsilon'_{11}}^2 + {\varepsilon'_{22}}^2 + {\varepsilon'_{33}}^2)/2 + \varepsilon^2_{12} + \varepsilon^2_{13} + \varepsilon^2_{23}}, \tag{2.2}$$

$$\dot{\varepsilon}'_{II} = \sqrt{({\dot{\varepsilon}'_{11}}^2 + {\dot{\varepsilon}'_{22}}^2 + {\dot{\varepsilon}'_{33}}^2)/2 + \dot{\varepsilon}^2_{12} + \dot{\varepsilon}^2_{13} + \dot{\varepsilon}^2_{23}}. \tag{2.3}$$

2.2.2 Accumulated strain and deformation gradients

The square root of the second invariant of the accumulated strain, referred here as **historic strain scalar** ε_{II_h}, is the controlling parameter of our strain softening algorithm (section 2.6). As a root of the second invariant, ε_{II_h} is a scalar and, therefore, it represents an expression of the total strain in all directions. Previous deformations can be recovered in some particular directions or rotated through the time. Consequently, tracking the historic strain as a scalar is an inaccurate approach. Instead, we track the **historic change of deformation gradient** F_h (Malvern, 1969), which is a tensor that accounts for both rotation and strain:

$$F_{h(n)} = F_{h(n-1)} + \delta t \dot{F}, \tag{2.4}$$

where n refers to the current time step and $\dot{F}$ is the rate of change of the deformation gradient, defined by:

$$\dot{F} = L \cdot F_{h(n-1)}, \tag{2.5}$$

where $F_{h(1)}$ is the identity matrix I, and L is the **spatial gradient of the velocity** (Malvern, 1969), defined as the change of the velocities v_i along the different directions x_j:

$$L_{ij} = \frac{\partial v_i}{\partial x_j}. \tag{2.6}$$

Note that the components of the strain rate can be defined as $(L_{ij} + L_{ji})/2$. Strain ε can be defined in terms of change of deformation gradient F (Malvern, 1969):

$$\varepsilon = \frac{1}{2}(F^T \cdot F - I). \tag{2.7}$$

Then, it is possible to calculate a historic strain ε_h for each time step with the historic change of deformation gradient $F_{h(n)}$:

$$\varepsilon_h = \frac{1}{2}(F^T_{h(n)} \cdot F_{h(n)} - I), \tag{2.8}$$

and calculate the second invariant ε_{II_h} in the same way as for Eq. 2.2.

2.2.3 Viscosity

In fluid dynamics, the **viscosity** is as a measure of the resistance of a fluid to flow (Ranalli, 1994) and it is generally defined as the relationship between stress and strain rate. Its units on the SI system are the Pascal-second (Pa s). Viscosity varies among different materials and mechanisms of deformation. **Newtonian** (linear) fluids present a linear relation between stress and strain rate, while **non-Newtonian** (non-linear) fluids have a non-linear relation (Ranalli, 1994). For an isotropic medium the Newtonian fluid law is defined as:

$$\sigma_{ij} = -P_T\delta_{ij} + \lambda'\dot{\varepsilon}_{kk}\delta_{ij} + 2\eta\dot{\varepsilon}_{ij}, \tag{2.9}$$

where λ' and η are material parameters, and P_T is thermodynamic pressure, not necessarily equal to the mean pressure P since it depends on the temperature and density of the medium (Ranalli, 1994). Introducing deviatoric stress τ_{ij} and strain rate $\dot{\varepsilon}'_{ij}$ (appendix Eqs. A.8 and A.17):

$$\tau_{ij} = (P - P_T)\delta_{ij} + \kappa\dot{\varepsilon}_{kk}\delta_{ij} + 2\eta\dot{\varepsilon}'_{ij}, \tag{2.10}$$

where $\kappa = \lambda' + (2/3)\eta$ is the volumetric viscosity analogous to the bulk modulus in linear elasticity, and η is the dynamic shear viscosity, commonly referred as viscosity (Ranalli, 1994). If the medium is incompressible then $P = P_T$, $\dot{\varepsilon}_{kk} = 0$ or $\kappa = 0$, and $\dot{\varepsilon}'_{ij} = \dot{\varepsilon}_{ij}$, so:

$$\tau_{ij} = 2\eta\dot{\varepsilon}'_{ij}, \tag{2.11}$$

or

$$\tau_{ij} = 2\eta\dot{\varepsilon}_{ij}. \tag{2.12}$$

Then, we can calculate the root of the second invariant of the deviatoric stress using Eq. 2.1:

$$\tau_{II} = \sqrt{\frac{(2\eta\dot{\varepsilon}_{11})^2 + (2\eta\dot{\varepsilon}_{22})^2 + (2\eta\dot{\varepsilon}_{33})^2}{2} + (2\eta\dot{\varepsilon}_{12})^2 + (2\eta\dot{\varepsilon}_{13})^2 + (2\eta\dot{\varepsilon}_{23})^2}, \tag{2.13}$$

$$\tau_{II} = 2\eta\sqrt{1/2(\dot{\varepsilon}_{11}^2 + \dot{\varepsilon}_{22}^2 + \dot{\varepsilon}_{33}^2) + \dot{\varepsilon}_{12}^2 + \dot{\varepsilon}_{13}^2 + \dot{\varepsilon}_{23}^2}. \tag{2.14}$$

Substituting the root of the second invariant of the strain rate (Eq. 2.3) we can define the effective viscosity η as:

$$\eta = \frac{\tau_{II}}{2\dot{\varepsilon}_{II}}. \tag{2.15}$$

Consequently, it is possible to define the effective **dynamic viscosity** η as the ratio between the deviatoric stress τ_{ij} and twice the strain rate $\dot{\varepsilon}_{ij}$, as well as the ratio between the total amount of deviatoric stress τ_{II} and the total amount of strain rate $\dot{\varepsilon}_{II}$ (Gerya, 2010). See section 2.5 for a description on how the dynamic effective viscosity is calculated.

2.2.4 Stokes equation of a viscous flow

In order to solve the mechanical problem, lets consider the momentum equation for a continuum in the Lagrangian form (see appendix A.0.3):

$$\frac{\partial \sigma_{ij}}{\partial x_j} + \rho g_i = \rho \frac{\partial v_i}{\partial t}. \tag{2.16}$$

Lets also consider the definition of deviatoric stress (see appendix A.8):

$$\sigma_{ij} = \tau_{ij} - P\delta_{ij}. \tag{2.17}$$

Substituting Eq. 2.17 into 2.16 allows to introduce the pressure in the momentum equation. The resultant is known as the **Stokes equation** of motion:

$$\frac{\partial \tau_{ij}}{\partial x_j} - \frac{\partial P}{\partial x_i} + \rho g_i = \rho \frac{\partial v_i}{\partial t}. \tag{2.18}$$

The motion inside the mantle and the crust is approached as a highly viscous flow. Consequently, the flow is very slow and the inertial forces $\rho\frac{\partial v_i}{\partial t}$ are negligible (the infinite Prandtl-number approximation):

$$\frac{\partial \tau_{ij}}{\partial x_j} - \frac{\partial P}{\partial x_i} + \rho g_i = 0. \tag{2.19}$$

2.2.5 Solving the mechanical problem

Our model works under extension applied to the side boundaries of a 2D vertical section of the crust and upper mantle. As boundary conditions constant velocities are applied at the side boundaries of the grid. The velocities at the remaining grid nodes are the unknowns of the mechanical problem. The following formulation is expanded only in the 1 and 2 directions, since our problem is two-dimensional.

By substituting Eq. 2.11 into Eq. 2.19, and considering the definition of deviatoric strain rate (Eq. A.17):

$$\frac{\partial}{\partial x_j}[2\eta(\dot{\varepsilon}_{ij} - \frac{1}{3}\dot{\varepsilon}_{kk}\delta_{ij})] - \frac{\partial P}{\partial x_i} + \rho g_i = 0. \tag{2.20}$$

For plain strain $\left(\frac{\partial v_i}{\partial x_3} = 0\right)$, Eq. 2.20 turns into:

$$\frac{\partial}{\partial x_1}[2\eta(\dot{\varepsilon}_{11} - \frac{1}{3}\dot{\varepsilon}_{kk})] + \frac{\partial}{\partial x_2}(2\eta\dot{\varepsilon}_{12}) - \frac{\partial P}{\partial x_1} + \rho g_1 = 0, \tag{2.21}$$

for the x_1 axis and,

$$\frac{\partial}{\partial x_1}(2\eta\dot{\varepsilon}_{21}) + \frac{\partial}{\partial x_2}[2\eta(\dot{\varepsilon}_{22} - \frac{1}{3}\dot{\varepsilon}_{kk})] - \frac{\partial P}{\partial x_2} + \rho g_2 = 0, \tag{2.22}$$

for the x_2 axis. Writting $\dot{\varepsilon}$ in terms of velocity changes respect the axes (Eq. A.15) and reordering, the Eq. 2.21 for the x_1 axis is:

$$\frac{\partial}{\partial x_1}\left[2\eta\left(\frac{\partial v_1}{\partial x_1} - \frac{1}{3}\frac{\partial v_1}{\partial x_1} - \frac{1}{3}\frac{\partial v_2}{\partial x_2}\right)\right] + \frac{\partial}{\partial x_2}\left[\eta\left(\frac{\partial v_1}{\partial x_2} + \frac{\partial v_2}{\partial x_1}\right)\right] - \frac{\partial P}{\partial x_1} + \rho g_1 = 0, \tag{2.23}$$

and proceeding the same way with Eq. 2.22, the equation for the x_2 axis is:

$$\frac{\partial}{\partial x_1}\left[\eta\left(\frac{\partial v_1}{\partial x_2} + \frac{\partial v_2}{\partial x_1}\right)\right] + \frac{\partial}{\partial x_2}\left[2\eta\left(\frac{\partial v_2}{\partial x_2} - \frac{1}{3}\frac{\partial v_1}{\partial x_1} - \frac{1}{3}\frac{\partial v_2}{\partial x_2}\right)\right] - \frac{\partial P}{\partial x_2} + \rho g_2 = 0, \tag{2.24}$$

or, for the x_1 axis:

$$\frac{\partial}{\partial x_1}\left[\eta\left(\frac{4}{3}\frac{\partial v_1}{\partial x_1} - \frac{2}{3}\frac{\partial v_2}{\partial x_2}\right)\right] + \frac{\partial}{\partial x_2}\left[\eta\left(\frac{\partial v_1}{\partial x_2} + \frac{\partial v_2}{\partial x_1}\right)\right] - \frac{\partial P}{\partial x_1} = -\rho g_1, \tag{2.25}$$

and for the x_2 axis:

$$\frac{\partial}{\partial x_2}\left[\eta\left(\frac{4}{3}\frac{\partial v_2}{\partial x_2} - \frac{2}{3}\frac{\partial v_1}{\partial x_1}\right)\right] + \frac{\partial}{\partial x_1}\left[\eta\left(\frac{\partial v_1}{\partial x_2} + \frac{\partial v_2}{\partial x_1}\right)\right] - \frac{\partial P}{\partial x_2} = -\rho g_2, \tag{2.26}$$

where η is assumed to be the effective viscosity η_{eff} (see section 2.5.4, Eqs. 2.110 and 2.118). Note that the right-hand side of the equations are the body force vector fields. Pressure P is the other unknown of the mechanical problem, so another equation is needed. Taking the diagonal terms in the Eq. 2.10:

$$\tau_{ii} = 3(P - P_T) + 3\kappa\dot{\varepsilon}_{kk} + 2\eta\dot{\varepsilon}'_{ii}. \tag{2.27}$$

By assuming incompressibility so $\tau_{ii} = 0$ and $\dot{\varepsilon}'_{ii} = 0$:

$$P - P_T + \kappa\dot{\varepsilon}_{kk} = 0. \tag{2.28}$$

By considering neligible pressure changes due to thermal and chemical reaction dependency, $P_T \approx 0$, we obtain the barometric equation of the state:

$$P + \kappa\dot{\varepsilon}_{kk} = 0, \tag{2.29}$$

or

$$P + \kappa \bigtriangledown \cdot v = 0. \tag{2.30}$$

So it is possible to define the divergence of the velocity $\bigtriangledown \cdot v$ as:

$$\bigtriangledown \cdot v = -\frac{P}{\kappa}. \tag{2.31}$$

Eq. 2.30 could be written as:

$$\frac{\partial v_1}{\partial x_1} + \frac{\partial v_2}{\partial x_2} + \frac{P}{\kappa} = 0. \tag{2.32}$$

For incompressible conditions $\frac{\partial v_1}{\partial x_1} + \frac{\partial v_2}{\partial x_2} = 0$. Therefore, $P\kappa^{-1} = 0$, so κ must be a very big number to satisfy the incompressible condition. This formulation is known as the penalty-factor pressure formulation for incompressibility (Hughes, 2000). The mechanical solver of MILAMIN is based on Eqs. 2.25, 2.26 and 2.32 (Dabrowski et al., 2008).

2.3 The thermal problem

Stokes equation is strongly dependent on the viscosity, which is also dependent on the temperature (see section 2.5.1, Eqs. 2.82). Therefore, variations in temperature must be taken into account to solve for deformation. Advective and conductive heat transport are the main factors responsible of the temperature change in our model. The **heat conservation equation** relates temperature with both advective and conductive heat transport in addition to internal heat generation:

$$\rho C_p \frac{DT}{Dt} = -\frac{\partial q_i}{\partial x_i} + H, \tag{2.33}$$

where ρ is the density, C_p the heat capacity of the medium, q_i is the heat flux in the i axes direction 1, 2 and 3, H is the volumetric heat production, and $\frac{DT}{Dt} = \frac{\partial T}{\partial t} + v \cdot \nabla T$, where $v \cdot \nabla T$ is the advection term. The conductive heat flux q_i is defined as:

$$q_i = -k \frac{\partial T}{\partial x_i}. \tag{2.34}$$

where k is the thermal conductivity and $\frac{\partial T}{\partial x_i}$ is the temperature gradient. By using Eq. 2.34 into Eq. 2.33:

$$\frac{\partial}{\partial x_i}\left(k \frac{\partial T}{\partial x_i}\right) + H = \rho C_p \left(\frac{\partial T}{\partial t} + v \cdot \nabla T\right). \tag{2.35}$$

As the code uses a Lagrangian solver the advection term $v \cdot \nabla T$ is included in the intrinsic motion of the mesh. Consequently Eq. 2.35 can be written as:

$$\frac{\partial}{\partial x_i}\left(k\frac{\partial T}{\partial x_i}\right) + H = \rho C_p \frac{\partial T}{\partial t}. \tag{2.36}$$

In 2D Eq. 2.36 can be written as:

$$\frac{\partial}{\partial x_1}\left(k\frac{\partial T}{\partial x_1}\right) + \frac{\partial}{\partial x_2}\left(k\frac{\partial T}{\partial x_2}\right) = \rho C_p \frac{\partial T}{\partial t} - H. \tag{2.37}$$

By discretizing in the time domain $\frac{\partial T}{\partial t} \simeq \frac{T_n - T_{n-1}}{\delta t}$, Eq. 2.37 turns into:

$$\frac{\partial}{\partial x_1}\left(k\frac{\partial T}{\partial x_1}\right)\delta t + \frac{\partial}{\partial x_2}\left(k\frac{\partial T}{\partial x_2}\right)\delta t - \rho C_p T_n = -\rho C_p T_{n-1} - \delta t H, \tag{2.38}$$

where T_n is the unknown temperature at the current time step n, and T_{n-1} is the temperature at the previous time step $n-1$. The thermal solver subroutine of MILAMIN is based on Eq. 2.38.

2.4 The finite element method

The Finite Element Method (FEM) provides numerical solutions to differential equations with the strong form:

$$\frac{\partial^2 u}{\partial x^2} + f(x) = 0, \tag{2.39}$$

with boundary conditions $u(1) = g$ and $\frac{\partial u}{\partial x}(0) = -h$ (Hughes, 2000). A first step is to transform this strong formulation into its weak form. For this, lets assume a collection of square-integrable trial solutions for u which satisfy the boundary condition $u(1) = g$. Then, a second collection of functions is required such that $w(1) = 0$. This last set of functions are called weighting functions and represent the homogeneous counterpart of the boundary condition g (Hughes, 2000). By multiplying Eq. 2.39 by w and integrating through the interval [0, 1]:

$$\int_0^1 w\frac{\partial^2 u}{\partial x^2}dx + \int_0^1 w f(x)dx = 0. \tag{2.40}$$

The inclusion of w allows us for integration by parts of the first term of Eq. 2.40, so that:

$$\int_0^1 \frac{\partial w}{\partial x}\frac{\partial u}{\partial x}dx = \int_0^1 w f(x)dx + w\frac{\partial u}{\partial x}\Big|_0^1, \tag{2.41}$$

or

$$\int_0^1 \frac{\partial w}{\partial x}\frac{\partial u}{\partial x}dx = \int_0^1 wf(x)dx + w(1)\frac{\partial u}{\partial x}(1) - w(0)\frac{\partial u}{\partial x}(0). \tag{2.42}$$

By considering boundary conditions $\frac{\partial u}{\partial x} = -h$ and $w(1) = 0$, then we obtain the weak form for os Eq. 2.39:

$$\int_0^1 \frac{\partial w}{\partial x}\frac{\partial u}{\partial x}dx = \int_0^1 wf(x)dx + w(0)h. \tag{2.43}$$

The FEM consists of dividing a continuum into a finite number of elements to then solve the weak form of this type of equation for the discrete elements. Each element is characterised by nodes, integration points and shape functions N_i which variation is assumed to describe the variation of u in the element domain:

$$u(x_1, x_2) \simeq \sum_{i=1}^{nnod} N_i(x_1, x_2)u_i, \tag{2.44}$$

where *nnod* is the number of nodes in the discretized domain and u_i the values u for the i nodes. The shape functions are defined for the element domain. Their values at the boundaries of the element domain is 0. The derivatives of the shape functions are also known. Then the second derivative of u can be defined in terms of the shape function as:

$$\frac{\partial^2 u}{\partial x^2}_{ip} \simeq \sum_{i=1}^{nnod} \frac{\partial^2 N_i}{\partial x^2}u_{ij}, \tag{2.45}$$

where ip is the index for the integration points. By introducing a weight function w as in Eq. 2.40 and following the same scheme as the one to obtain Eq. 2.43 we can write Eq. 2.39 in its weak form where spatial variation of u is described by the shape function N_i. Note that the shape functions satisfy the conditions for weight functions and therefore we can use $w = N_j$. Then we can write:

$$\sum_{k=1}^{ip}\sum_{i=1}^{nnod}\sum_{j=1}^{nnod}\left(\frac{\partial N_i}{\partial x}\frac{\partial N_j}{\partial x}\right)u_{ij} = \sum_{k=1}^{ip}\sum_{j=1}^{nnod} N_j f(x) + N_j(0)h. \tag{2.46}$$

The solution of u is achieved by solving the linear system defined by Eq. 2.46. The term with the form of summation of the product of shape function derivatives is known as the **stiffness matrix**. The code builds this matrix K_e and integrates $N_j f(x)$ for each element, and assembles them into the global stiffness matrix K and the global right-hand-side vector (Rhs) respectively.

The code uses Crouzeix-Raviart triangular elements with quadratic velocity shape functions enhanced by a cubic bubble function and discontinuous linear interpolation pressure (Crouzeix and Raviart, 1973).

In the case of the **thermal solver** each element contains seven nodes, three at the vertices, three at the middle-point edges, and one in the center, and six integration points (Fig. 2.2). By using Eq. 2.45 into Eq. 2.38 and integrating over the element domain, the element stiffness matrix K_T^e for the thermal problem can be defined as:

$$K_T^e = \sum_{k=1}^{ip} \sum_{i=1}^{nnod} \sum_{j=1}^{nnod} k_e \delta t \left(\frac{\partial N_i}{\partial x_1} \frac{\partial N_j}{\partial x_1} + \frac{\partial N_i}{\partial x_2} \frac{\partial N_j}{\partial x_2} \right) - \rho C_p N_i N_j, \tag{2.47}$$

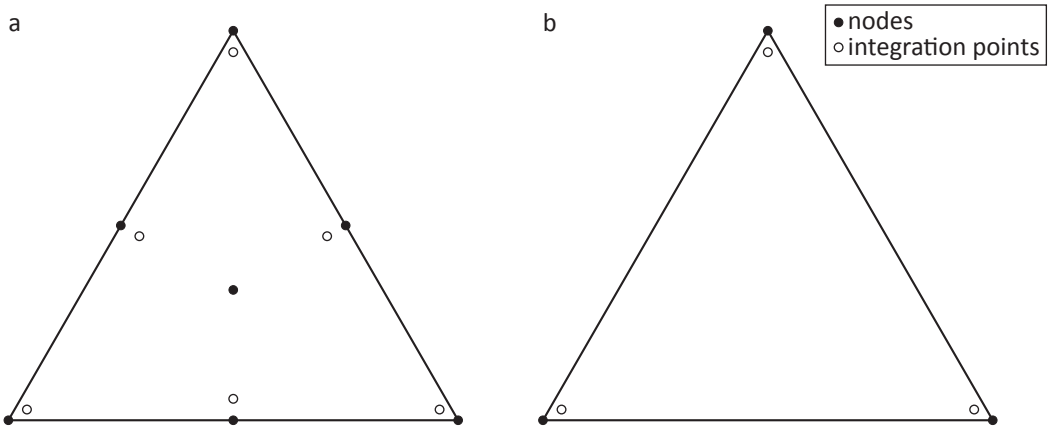

FIGURE 2.2: Triangular elements, a) for the velocities and temperatures, and b) for the pressures.

where k_e is the element thermal conductivity, i and j are node indexes from 1 to 7, and k are integration point indexes from 1 to 6. Consequently, the heat conservation equation (2.38) can be written in the FEM form:

$$K_T T = Rhs_T, \tag{2.48}$$

where the right-hand-side vector Rhs_T is defined as:

$$Rhs_T = -\rho C_p T_{n-1} - \delta t H. \tag{2.49}$$

The **mechanical solver** needs two kinds of shape functions: quadratic shape functions enhanced by a cubic bubble function for the velocity (N) and linear shape functions for the pressure (Π). For the velocities, the code uses the same triangular elements as the

ones of the thermal solver (Fig. 2.2), while only the three vertex nodes are used to define the linear pressure variation. The element stiffness matrix K_m^e for the mechanical problem is defined as:

$$K_m^e = \begin{pmatrix} A & Q^T \\ Q & M \end{pmatrix} \tag{2.50}$$

where

$$A^e_{(2i-1)\ (2j-1)} = \sum_{k=1}^{ip} \sum_{i=1}^{nnod} \sum_{j=1}^{nnod} \left(\frac{4}{3} \frac{\partial N_i}{\partial x_1} \frac{\partial N_j}{\partial x_1} + \frac{\partial N_i}{\partial x_2} \frac{\partial N_j}{\partial x_2} \right), \tag{2.51}$$

$$A^e_{(2i-1)\ 2j} = \sum_{k=1}^{ip} \sum_{i=1}^{nnod} \sum_{j=1}^{nnod} \left(-\frac{2}{3} \frac{\partial N_i}{\partial x_1} \frac{\partial N_j}{\partial x_2} + \frac{\partial N_i}{\partial x_2} \frac{\partial N_j}{\partial x_1} \right), \tag{2.52}$$

$$A^e_{2i\ (2j-1)} = \sum_{k=1}^{ip} \sum_{i=1}^{nnod} \sum_{j=1}^{nnod} \left(-\frac{2}{3} \frac{\partial N_i}{\partial x_2} \frac{\partial N_j}{\partial x_1} + \frac{\partial N_i}{\partial x_1} \frac{\partial N_j}{\partial x_2} \right), \tag{2.53}$$

$$A^e_{2i\ 2j} = \sum_{k=1}^{ip} \sum_{i=1}^{nnod} \sum_{j=1}^{nnod} \left(\frac{4}{3} \frac{\partial N_i}{\partial x_2} \frac{\partial N_j}{\partial x_2} + \frac{\partial N_i}{\partial x_1} \frac{\partial N_j}{\partial x_1} \right), \tag{2.54}$$

where i and j are node indexes from 1 to 7, A^e is a 14×14 matrix and the integrations k are done over the 6 velocity integration points,

$$Q^e_{i\ (2j-1)} = -\sum_{k=1}^{ip} \sum_{i=1}^{nnod} \eta \Pi_i \frac{\partial N_j}{\partial x_1}, \tag{2.55}$$

$$Q^e_{i\ 2j} = -\sum_{k=1}^{ip} \sum_{i=1}^{nnod} \eta \Pi_i \frac{\partial N_j}{\partial x_2}, \tag{2.56}$$

where i is the index for the pressure shape functions Π, with values from 1 to 3, j is the index for the velocity shape functions, with values from 1 to 7, Q^e is a 3×14 matrix, and the integration k is done over the 3 pressure integration points,

$$M^e = \sum_{k=1}^{ip} \sum_{i=1}^{nnod} \sum_{j=1}^{nnod} \eta \frac{1}{\kappa} \Pi_i \Pi_j, \tag{2.57}$$

where i and j are the indexes for the pressure shape functions from 1 to 3, M^e is a 3×3 matrix, and the integrations k are done over the 3 pressure integration points. Q^T is the transpose of Q. Then it is possible to write the mechanical system defined by Eqs. 2.25, 2.26 and 2.32 in FEM form as:

$$K_m^e u_m^e = Rhs_m^e, \tag{2.58}$$

where u_m^e is the unknowns with velocities v_{ij} at the beginning and the three pressures p_i at the end:

$$u_m^e = \begin{pmatrix} v_{11} \\ v_{21} \\ v_{12} \\ v_{22} \\ . \\ . \\ . \\ v_{17} \\ v_{27} \\ p_1 \\ p_2 \\ p_3 \end{pmatrix}, \tag{2.59}$$

where the first index represents the direction of the velocity, and the second represents the node for which the velocity is calculated. The right-hand side Rhs_m^e for the FEM form of the mechanical system is a vector with the body forces at the beginning and three zeros at the end that satisfies the Eq. 2.32:

$$Rhs_m^e = \begin{pmatrix} F_{11} \\ F_{21} \\ F_{12} \\ F_{22} \\ . \\ . \\ . \\ F_{17} \\ F_{27} \\ 0 \\ 0 \\ 0 \end{pmatrix}, \tag{2.60}$$

where the first index represents the direction of the body force, and the second represents the node in which the force is applied. The mechanical system Eq. 2.58 can also be written in terms of the matrices A, Q, M, and the velocity vector v, the pressure vector P and the body force vector F:

$$\begin{pmatrix} A & Q^T \\ Q & M \end{pmatrix} \begin{pmatrix} v \\ P \end{pmatrix} = \begin{pmatrix} F \\ 0 \end{pmatrix}. \tag{2.61}$$

Note that $Av + Q^T P = F$ and $Qv + MP = 0$, where P is a vector which components are p_1, p_2 and p_3. Then, it is possible to define P as:

$$P = -M^{-1}Qv. \tag{2.62}$$

Consequently:

$$(A - Q^T M^{-1} Q)v = F. \tag{2.63}$$

The global matrix becomes ill-conditioned through this procedure for bulk modulus corresponding to a very small divergences and incompressibility (Hughes, 2000). It is possible to solve this problem introducing a 'Uzawa-like' iteration which consist of changing the term $Q^T M^{-1} Q$ to the right-hand side term, multiplied by the velocity solved in the previous iteration v_{prev}, and solving again for the new iteration (Zienkiewicz et al., 1985):

$$(A - Q^T M^{-1} Q)v = F - (Q^T M^{-1} Q)v_{prev}. \tag{2.64}$$

Note that the volumetric viscosity κ, which can be taken out from M, works as a penalty factor in this formulation (Hughes, 2000).

The FEM also allows to make the code faster by employing isoparametric elements. Each element in the space can be mapped into a reference element with fixed local coordinates (ξ, μ), making the calculation of the local matrices faster. The change from local coordinates to global coordinates (x, y) is achieved by using the same shape functions that interpolate the physical fields:

$$x_1(\xi, \mu) = \sum_{i=1}^{nnodel} N_i(\xi, \mu) x_{1i}, \tag{2.65}$$

$$x_2(\xi, \mu) = \sum_{i=1}^{nnodel} N_i(\xi, \mu) x_{2i}, \tag{2.66}$$

where *nnodel* is the number of nodes in the element. It is possible to build a Jacobian matrix J which approximates the local coordinates values to the global ones:

$$J = \begin{pmatrix} \frac{\partial x_1}{\partial \xi} & \frac{\partial x_1}{\partial \mu} \\ \frac{\partial x_2}{\partial \xi} & \frac{\partial x_2}{\partial \mu} \end{pmatrix}. \tag{2.67}$$

The global coordinates shape functions are calculated from the locals multiplying by the inverse of the Jacobian:

$$\begin{pmatrix} \frac{\partial N}{\partial x_1} \\ \frac{\partial N}{\partial x_2} \end{pmatrix} = \begin{pmatrix} \frac{\partial x_1}{\partial \xi} & \frac{\partial x_1}{\partial \mu} \\ \frac{\partial x_2}{\partial \xi} & \frac{\partial x_2}{\partial \mu} \end{pmatrix}^{-1} \begin{pmatrix} \frac{\partial N}{\partial \xi} \\ \frac{\partial N}{\partial \mu} \end{pmatrix}. \tag{2.68}$$

2.5 Rock mechanical behaviour

Rocks mechanically behave as a visco-elasto-plastic material. In the case of both the viscous and the plastic behaviour the deformation is not recoverable, while elastic behaviour allows recovery of deformation once the stress ceases (Ranalli, 1994). This section reviews these three deformation mechanisms and explains the procedure followed to couple them into the numerical code.

2.5.1 Viscous behaviour and creep mechanisms

The viscous behaviour of rocks is represented by the so called flow laws or creep laws which can be both Newtonian and non-Newtonian. Rocks on the mantle deform mainly by two mechanisms: diffusion creep and dislocation creep, where creep refers to slow flow under constant stress (Ranalli, 1994). **Diffusion creep** occurs through diffusive mass transport between grain boundaries, for low stress level, small grain size, or both, and the strain rate increases linearly with stress (i.e. Newtonian deformation) (Karato and Wu, 1993). **Dislocation creep** occurs through the motion of crystalline dislocation within grains, for high stress level, large grain size, or both, and the strain rate increases nonlinearly with stress (i.e. non-Newtonian deformation) (Karato and Wu, 1993). Both mechanisms occur simultaneously for a given temperature and pressure, but the mechanism that gives the highest strain rate becomes the dominant creep mechanism (Karato and Wu, 1993). A nonlinear formulation (non-Newtonian) is needed in order to account for dislocation creep. By far the most important nonlinear stress-strain rate relation is the power-law creep equation, where the strain rate is related to the nth power of the stress (Ranalli, 1994). Factors, such as shear modulus μ, grain size d, pressure P, temperature T, and water fugacity fH_2O condition the rheology of the rocks. Empirical power-law equations that take into account some of these parameters to relate stress and strain rate are known as **flow laws**. Different flow laws imply different parameters and different calibrations. An example of flow law is the one described by Hirth and Kohlstedt, 2003 for olivine aggregates:

$$\dot{\varepsilon} = A\sigma_d^n d^{-m} f H_2 O^r exp(\alpha\phi) exp\left(-\frac{E^* + PV^*}{RT}\right), \tag{2.69}$$

where $\dot{\varepsilon}$ is the strain rate, A is the preexponential factor, σ_d is the differential stress, n is the stress exponent, d is the grain size, m is the grain size exponent, fH_2O is the water fugacity, r is the water fugacity exponent, α is the melt fraction factor, ϕ is the melt fraction, E^* is the activation energy, P is the pressure, V^* is the activation volume, R is the gas constant, and T is the temperature. For this particular case we can group most of the parameters into a new preexponential factor $B = Ad^{-m}fH_2O^r exp(\alpha\phi)$:

$$\dot{\varepsilon} = B\sigma_d^n exp\left(-\frac{E^* + PV^*}{RT}\right), \tag{2.70}$$

so that we obtain a more general flow law which can be representative of flow laws that take into account other parameters than the ones from Hirth and Kohlstedt, 2003, by grouping all this parameters inside a preexponential factor B. Table 2.1 summarize the different flow-law parameters used for the numerical studies contained in this thesis.

TABLE 2.1: Creep parameters. DIS and DIF refer to parameters for dislocation and diffusion creep respectively. Diffusion creep B is calculated using a grain size d of 6 mm. Wet olivine water fugacity fH_2O is 500 MPa (or C_{OH} in ppm H/Si) (Hirth and Kohlstedt, 2003).

Rock/mineral aggregate	Creep	$log(B)$ [$Pa^{-n}s^{-1}$]	n	E^* [kJ mol^{-1}]	Reference
Wet quartzite (upper crust and weak lower crust)	DIS	-28.0	4.0	223	Gleason and Tullis, 1995
Wet anorthite (intermediate lower crust)	DIS	-15.4	3.0	356	Rybacki and Dresen, 2000
Mafic granulite (strong lower crust)	DIS	-21.05	4.2	445	Wilks and Carter, 1990
Dry olivine (lithospheric mantle)	DIS	-15.56	3.5	530	Hirth and Kohlstedt, 2003
Wet olivine (asthenospheric mantle)	DIS	-15.05	3.5	480	Hirth and Kohlstedt, 2003
Dry olivine (lithospheric mantle)	DIF	-8.65	1	375	Hirth and Kohlstedt, 2003
Wet olivine (asthenospheric mantle)	DIF	-8.66	1	335	Hirth and Kohlstedt, 2003

Note that the values of strain rate $\dot{\varepsilon}$ and differential stress σ_d given by experiments are not equivalent to the root of the second invariant of the strain rate $\dot{\varepsilon}_{II}$ and the deviatoric stress τ_{II}. However, in numerical modelling it is convenient use both $\dot{\varepsilon}_{II}$ and τ_{II}, since the dynamic viscosity is calculated using Eq. 2.15. All chosen rheological parameters shown on table 2.1 were calculated from either uniaxial or triaxial experiments. In this type of

experiments σ_d is the differential stress such as:

$$\sigma_d = \sigma_1 - \sigma_3, \tag{2.71}$$

where σ_1 is the largest principal stress and σ_3 is the smallest (Fig. 2.3). The strain rate $\dot{\varepsilon}$ given in this type of studies is typically the axial strain rate $\dot{\varepsilon}_{11}$. The stress conditions of these experiments are such as:

$$\sigma_2 = \sigma_3 \neq \sigma_1, \tag{2.72}$$

where σ_2 and σ_3 smallest principal stresses are 0 in uniaxial experiments and correspond

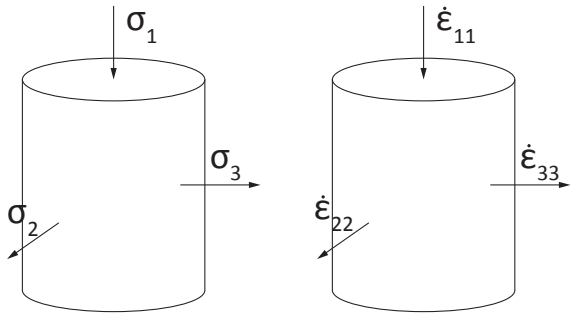

FIGURE 2.3: Uniaxial/triaxial test. σ_1, σ_2 and σ_3 represent principal stresses, and $\dot{\varepsilon}_{11}$, $\dot{\varepsilon}_{22}$ and $\dot{\varepsilon}_{33}$ are the strain rate components.

to the confining pressures in triaxial experiments. It is possible to define the deviatoric stress (Eq. A.8) as:

$$\tau = \begin{pmatrix} \sigma_1 - \frac{\sigma_1+2\sigma_3}{3} & 0 & 0 \\ 0 & \sigma_3 - \frac{\sigma_1+2\sigma_3}{3} & 0 \\ 0 & 0 & \sigma_3 - \frac{\sigma_1+2\sigma_3}{3}, \end{pmatrix} \tag{2.73}$$

so that the square root of the second invariant τ_{II} is:

$$\tau_{II} = \sqrt{\frac{1}{2}\left(\left(\frac{2}{3}\sigma_1 - \frac{2}{3}\sigma_3\right)^2 + 2\left(-\frac{1}{3}\sigma_1 + \frac{1}{3}\sigma_3\right)^2\right)}. \tag{2.74}$$

By using the definition of differential stress in Eq. 2.71:

$$\tau_{II} = \frac{1}{\sqrt{3}}\sigma_d, \tag{2.75}$$

or

$$\sigma_d = \sqrt{3}\tau_{II}. \tag{2.76}$$

Assuming incompressibility and uniform deformation along the axis 2 and 3 (Fig. 2.3), then:

$$\dot{\varepsilon}_{22} = \dot{\varepsilon}_{33} = -\frac{1}{2}\dot{\varepsilon}_{11}, \tag{2.77}$$

so that the square root of the second invariant of the strain rate $\dot{\varepsilon}_{II}$ can be defined as:

$$\dot{\varepsilon}_{II} = \sqrt{\frac{1}{2}\left(\dot{\varepsilon}_{11}^2 + 2\left(-\frac{1}{2}\dot{\varepsilon}_{11}\right)^2\right)}. \tag{2.78}$$

By simplifying we obtain:

$$\dot{\varepsilon}_{11} = \frac{2}{\sqrt{3}}\dot{\varepsilon}_{II}. \tag{2.79}$$

Then it is possible to write the generalized flow law Eq. 2.70 for triaxial and uniaxial tests in terms of τ_{II} and $\dot{\varepsilon}_{II}$ by using Eqs. 2.76 and 2.79:

$$\frac{2}{\sqrt{3}}\dot{\varepsilon}_{II} = B(\sqrt{3}\tau_{II})^n exp\left(-\frac{E^* + PV^*}{RT}\right), \tag{2.80}$$

or

$$\tau_{II} = 2^{\frac{1}{n}} 3^{-\frac{n+1}{2n}} B^{-\frac{1}{n}} \dot{\varepsilon}_{II}^{\frac{1}{n}} exp\left(\frac{E^* + PV^*}{nRT}\right). \tag{2.81}$$

By substituting Eq. 2.80 in Eq. 2.15 and neglecting PV^* due to its relatively small size in comparison with E^*, we can obtain the **dislocation** or **diffusion viscosity** η_{dd} for a certain $\dot{\varepsilon}_{II}$:

$$\eta_{dd} = FB^{-\frac{1}{n}} \dot{\varepsilon}_{II}^{\frac{1-n}{n}} exp\left(\frac{E^*}{nRT}\right), \tag{2.82}$$

where

$$F = \frac{1}{2^{\frac{n-1}{n}} 3^{\frac{n+1}{2n}}}. \tag{2.83}$$

In order to calculate the diffusion viscosity η_{dif} and the dislocation viscosity η_{dis}, we need to apply the flow-law parameters calculated from experiments (table 2.1) to Eq. 2.82.

Finally, it is possible to calculate a total creep viscosity η_c by considering rocks as Maxwell materials which implies that the total strain is represented by the summation of strains due to the different mechanisms involved in the deformation:

$$\dot{\varepsilon} = \dot{\varepsilon}_{dis} + \dot{\varepsilon}_{dif}. \tag{2.84}$$

It is possible to calculate $\dot{\varepsilon}_{dis}$ and $\dot{\varepsilon}_{dif}$ by using Eq. 2.12:

$$\dot{\varepsilon}_{dis} = \frac{\tau}{2\eta_{dis}}, \tag{2.85}$$

and

$$\dot{\varepsilon}_{dif} = \frac{\tau}{2\eta_{dif}}. \tag{2.86}$$

By substituting Eqs. 2.85 and 2.86 into Eq. 2.84:

$$\tau = 2\eta_c \dot{\varepsilon}, \tag{2.87}$$

where η_c is the creep viscosity defined as:

$$\eta_c = \frac{1}{\frac{1}{\eta_{dis}} + \frac{1}{\eta_{dif}}}. \tag{2.88}$$

2.5.2 Plasticity

Rocks not only behave as creeping materials, but plastically at low pressure and temperatures. **Plastic** behaviour implies that a critical stress σ_{yield} exist for a given material and after reaching this stress failure occurs, meaning that the material offers no resistance to flow (Ranalli, 1994; Gerya, 2010; de Souza Neto et al., 2008). Failure can occur through a fracture, which is known as **brittle** behaviour, or can occur along the whole body without causing any discontinuity, which is known as **plastic flow** (Ranalli, 1994). In order to include plastic behaviour in our code, we need to define a 'plastic' apparent viscosity η_p, for which we need to choose a failure or yield criterion. Many yield criterions are described in the literature such as Mohr-Coulomb, Von-Mises, and Drucker-Prager, which evaluate different stress states against different critical yield stresses. Here, we choose to use Drucker-Prager yield criterion which implies that failure occurs when the the root of the second invariant of the deviatoric stress reaches a yield stress σ_{yield} ($\tau_{II} \geq \sigma_{yield}$) calculated for a given pressure P, the material friction angle ϕ and cohesion c (de Souza Neto et al., 2008):

$$\sigma_{yield} = Psin\theta + c. \tag{2.89}$$

Then we can introduce the Prandtl-Reuss flow rule for plasticity:

$$\dot{\varepsilon}_p = G\frac{\tau}{2\tau_{II}}, \tag{2.90}$$

where G is a parameter calculated for the stress to remain on the yield stress (Moresi et al., 2003) (see section 2.5.4).

2.5.3 Elasticity

Rocks recover some deformation once stress ceases, in other words, they behave elastically (Ranalli, 1994). Elasticity is included into the rheology by adding an elasticity stress term to Eq. 2.12, such as:

$$\frac{\tau_{ij}}{2\eta_c} + \frac{\overset{\nabla}{\tau}_{ij}}{2\mu} = \dot{\varepsilon}_{ij}, \tag{2.91}$$

where η_c is the creep viscosity, μ is the elastic shear modulus, and $\overset{\nabla}{\tau}_{ij}$ is the objective material derivative of the deviatoric stress (Moresi et al., 2007). In this particular case, we use the Jaumann derivative as $\overset{\nabla}{\tau}_{ij}$, since it ensures that the objective derivative is deviatoric when the given stress is deviatoric (Moresi et al., 2003, 2007). The Jaumann objective derivative $\overset{\nabla}{\tau}_{ij}$ can be written as:

$$\overset{\nabla}{\tau}_{ij} = \frac{\partial \tau_{ij}}{\partial t} + \tau'_{ij}, \tag{2.92}$$

or by time discretazing the time derivative:

$$\overset{\nabla}{\tau}_{ij} = \frac{\tau_{ij} - \tau_{ij}^{old}}{\delta t} + \tau'_{ij}, \tag{2.93}$$

where τ_{ij} is at stress of the current time step, τ_{ij}^{old} the stress for the previous time step and τ'_{ij} is the instantaneous rate of change in the stress tensor associated with the transport, rotation and stretching by fluid motion (Moresi et al., 2007; Kaus et al., 2010). τ'_{ij} can be written as:

$$\tau'_{ij} = v_k \frac{\partial \tau_{ij}}{\partial x_k} - \omega_{ik}\tau_{kj}^{old} + \tau_{ik}^{old}\omega_{kj}, \tag{2.94}$$

where v represents velocities and ω_{ij} is the rigid-body rotation tensor (see Eq. A.12) (Moresi et al., 2007; Kaus, 2010). Since our model works with a Lagrangian grid the term $v_k \frac{\partial \tau_{ij}}{\partial x_k}$ can be neglected:

$$\tau'_{ij} = -\omega_{ik}\tau_{kj}^{old} + \tau_{ik}^{old}\omega_{kj}. \tag{2.95}$$

By substituting Eqs. 2.93 and 2.95 into Eq. 2.91 we obtain:

$$\tau_{ij} = 2\eta_{ve}\dot{\varepsilon}_{ij} + \chi_{ve}\tau_{ij}^{old_J}, \tag{2.96}$$

where

$$\eta_{ve} = \frac{1}{\frac{1}{\eta_c} + \frac{1}{\mu \Delta t}}, \tag{2.97}$$

$$\chi_{ve} = \frac{\eta_{ve}}{\mu \Delta t}, \tag{2.98}$$

and $\tau_{ij}^{old_J}$ represent the rotated stresses of the previous time step:

$$\tau_{ij}^{old_J} = \tau_{ij}^{old} + \delta t(\tau_{ik}^{old}\omega_{kj}^{old} - \omega_{ik}^{old}\tau_{kj}^{old}), \tag{2.99}$$

where τ_{ij}^{old} are deviatoric stresses from the previous time step (Kaus, 2010). Considering Eq. 2.96, it is possible to define η_{ve} as a relation between the stress and the strain rate:

$$\eta_{ve} = \frac{\tau_{ij} - \chi_{ve}\tau_{ij}^{old_J}}{2\dot{\varepsilon}_{ij}} = \eta - \frac{\chi_{ve}\tau_{ij}^{old_J}}{2\dot{\varepsilon}_{ij}}, \tag{2.100}$$

or

$$\eta = \eta_{ve} + \frac{\chi_{ve}\tau_{ij}^{old_J}}{2\dot{\varepsilon}_{ij}}. \tag{2.101}$$

where η is the viscosity that relates stress and strain rate for visco-elastic behaviour of rocks (Eq. 2.15). Then we can substitute Eq. 2.101 into Eqs. 2.21 and 2.22:

$$\frac{\partial}{\partial x_1}[2\eta_{ve}(\dot{\varepsilon}_{11} - \frac{1}{3}\dot{\varepsilon}_{kk}) + \chi_{ve}\tau_{11}^{old_J} - \frac{1}{3}\dot{\varepsilon}_{kk}\chi_{ve}\tau_{11}^{old_J}] + \frac{\partial}{\partial x_2}(2\eta_{ve}\dot{\varepsilon}_{12} + \chi_{ve}\tau_{12}^{old_J}) - \frac{\partial P}{\partial x_1} + \rho g_1 = 0, \tag{2.102}$$

for the x_1 axis and

$$\frac{\partial}{\partial x_1}(2\eta_{ve}\dot{\varepsilon}_{21} + \chi_{ve}\tau_{21}^{old_J}) + \frac{\partial}{\partial x_2}[2\eta_{ve}(\dot{\varepsilon}_{22} - \frac{1}{3}\dot{\varepsilon}_{kk}) + \chi_{ve}\tau_{22}^{old_J} - \frac{1}{3}\dot{\varepsilon}_{kk}\chi_{ve}\tau_{22}^{old_J}] - \frac{\partial P}{\partial x_2} + \rho g_2 = 0, \tag{2.103}$$

for the x_2 axis. For incompressible conditions the terms $\frac{1}{3}\dot{\varepsilon}_{kk}\chi_{ve}\tau_{11}^{old_J}$ and $\frac{1}{3}\dot{\varepsilon}_{kk}\chi_{ve}\tau_{22}^{old_J}$ can be neglected:

$$\frac{\partial}{\partial x_1}[2\eta_{ve}(\dot{\varepsilon}_{11} - \frac{1}{3}\dot{\varepsilon}_{kk})] + \frac{\partial}{\partial x_2}(2\eta_{ve}\dot{\varepsilon}_{12}) - \frac{\partial P}{\partial x_1} + \rho g_1 = -\chi_{ve}\frac{\partial \tau_{11}^{old_J}}{\partial x_1} - \chi_{ve}\frac{\partial \tau_{12}^{old_J}}{\partial x_2}, \tag{2.104}$$

for the x_1 axis and

$$\frac{\partial}{\partial x_1}(2\eta_{ve}\dot{\varepsilon}_{21}) + \frac{\partial}{\partial x_2}[2\eta_{ve}(\dot{\varepsilon}_{22} - \frac{1}{3}\dot{\varepsilon}_{kk})] - \frac{\partial P}{\partial x_2} + \rho g_2 = -\chi_{ve}\frac{\partial \tau_{21}^{old_J}}{\partial x_1} - \chi_{ve}\frac{\partial \tau_{22}^{old_J}}{\partial x_2}, \tag{2.105}$$

for the x_2 axis. Expanding these equations we obtain the elastic equivalents for the mechanical problem equations 2.25 and 2.26:

$$\frac{\partial}{\partial x_1}\left[\eta_{ve}\left(\frac{4}{3}\frac{\partial v_1}{\partial x_1} - \frac{2}{3}\frac{\partial v_2}{\partial x_2}\right)\right] + \frac{\partial}{\partial x_2}\left[\eta_{ve}\left(\frac{\partial v_1}{\partial x_2} + \frac{\partial v_2}{\partial x_1}\right)\right] - \frac{\partial P}{\partial x_1} = -\rho g_1 - \chi_{ve}\frac{\partial \tau_{11}^{old_J}}{\partial x_1} - \chi_{ve}\frac{\partial \tau_{12}^{old_J}}{\partial x_2}, \tag{2.106}$$

for the x_1 axis and

$$\frac{\partial}{\partial x_2}\left[\eta_{ve}\left(\frac{4}{3}\frac{\partial v_2}{\partial x_2} - \frac{2}{3}\frac{\partial v_1}{\partial x_1}\right)\right] + \frac{\partial}{\partial x_1}\left[\eta_{ve}\left(\frac{\partial v_1}{\partial x_2} + \frac{\partial v_2}{\partial x_1}\right)\right] - \frac{\partial P}{\partial x_2} = -\rho g_2 - \chi_{ve}\frac{\partial \tau_{21}^{old_J}}{\partial x_1} - \chi_{ve}\frac{\partial \tau_{22}^{old_J}}{\partial x_2}, \tag{2.107}$$

for the x_2 axis. Then, Eqs. 2.106 and 2.107 can be solved numerically by FEM by following the same procedure as for the only-viscous example in section 2.4. For elasticity benchmarking see section 2.8.

2.5.4 Effective viscosity

In order to couple plasticity with visco-elasticity (section 2.5.3) it is necessary to first evaluate the yield criterion at every element. If $\tau_{II} < \sigma_{yield}$ the element is not yielding and therefore, it will behave visco-elastically only. Then Eqs. 2.106 and 2.107 can be solved numerically by FEM, by using a **effective viscosity** $\eta_{eff} = \eta_{ve}$.

However, yielding may occur for given elements when yield criterion is met ($\tau_{II} \geq \sigma_{yield}$). Then it is necessary to calculate a new **effective viscosity** which contains the plastic term (Eq. 2.90) as well. To do this, Maxwell constitutive relation is taken into account (Ranalli, 1994; Moresi et al., 2003, 2007):

$$\frac{\tau}{2\eta_c} + \frac{\overset{\nabla}{\tau}}{2\mu} + G\frac{\tau}{2\tau_{II}} = \dot{\varepsilon}_v + \dot{\varepsilon}_e + \dot{\varepsilon}_p = \dot{\varepsilon}, \tag{2.108}$$

where $\dot{\varepsilon}_v$ is the strain rate due to creep, $\dot{\varepsilon}_e$ strain rate due to elasticity, and $\dot{\varepsilon}_p$ due to plasticity from Eq. 2.90. By substituting the objective derivative of the stress with the Jaumann derivative as in Eqs. 2.93, 2.94 and 2.95 we obtain:

$$\tau = \eta_{eff}\left(2\dot{\varepsilon} + \frac{1}{\mu\Delta t}\tau^{old_J}\right), \tag{2.109}$$

where the effective viscosity η_{eff} is defined as:

$$\eta_{eff} = \frac{1}{\frac{1}{\eta_c} + \frac{1}{\Delta t\mu} + \frac{G}{\tau_{II}}}, \tag{2.110}$$

and τ^{old_J} defined as in Eq. 2.99. Then, by following the same procedure as in section 2.5.3 (Eqs. 2.100-2.107) we obtain:

$$\frac{\partial}{\partial x_1}\left[\eta_{eff}\left(\frac{4}{3}\frac{\partial v_1}{\partial x_1} - \frac{2}{3}\frac{\partial v_2}{\partial x_2}\right)\right] + \frac{\partial}{\partial x_2}\left[\eta_{eff}\left(\frac{\partial v_1}{\partial x_2} + \frac{\partial v_2}{\partial x_1}\right)\right] - \frac{\partial P}{\partial x_1} = -\rho g_1 - \chi_{vep}\frac{\partial \tau_{11}^{old_J}}{\partial x_1} - \chi_{vep}\frac{\partial \tau_{12}^{old_J}}{\partial x_2}, \tag{2.111}$$

for the x_1 axis and

$$\frac{\partial}{\partial x_2}\left[\eta_{eff}\left(\frac{4}{3}\frac{\partial v_2}{\partial x_2} - \frac{2}{3}\frac{\partial v_1}{\partial x_1}\right)\right] + \frac{\partial}{\partial x_1}\left[\eta_{eff}\left(\frac{\partial v_1}{\partial x_2} + \frac{\partial v_2}{\partial x_1}\right)\right] - \frac{\partial P}{\partial x_2} = -\rho g_2 - \chi_{vep}\frac{\partial \tau_{21}^{old_J}}{\partial x_1} - \chi_{vep}\frac{\partial \tau_{22}^{old_J}}{\partial x_2}, \tag{2.112}$$

where χ_{vep} is defined as:

$$\chi_{vep} = \frac{\eta_{eff}}{\mu \Delta t}. \tag{2.113}$$

By grouping strain rate and old stress terms into an effective strain rate variable $\dot{\varepsilon}_{eff}$ it is possible to rewrite Eq. 2.109 as:

$$\tau = \eta_{eff} \dot{\varepsilon}_{eff}, \tag{2.114}$$

where

$$\dot{\varepsilon}_{eff} = 2\dot{\varepsilon} + \frac{1}{\mu \Delta t} \tau^{old_J}. \tag{2.115}$$

Then, we can write Eq. 2.114 in terms of roots of the second invariant of the stress and the effective strain rate $\dot{\varepsilon}_{IIeff}$ such as:

$$\tau_{II} = \eta_{eff} \dot{\varepsilon}_{IIeff}, \tag{2.116}$$

where

$$\dot{\varepsilon}_{IIeff} = \sqrt{(\varepsilon^2_{11eff} + \varepsilon^2_{22eff})/2 + \varepsilon^2_{12eff}}. \tag{2.117}$$

If the yield criterion is met, then the plastic factor G is such as that $\tau_{II} = \sigma_{yield}$ is satisfied (Moresi et al., 2003). Therefore, we can rearrange Eq. 2.116 to define η_{eff} for the visco-elasto-plastic scenario as:

$$\eta_{eff} = \frac{\sigma_{yield}}{\dot{\varepsilon}_{IIeff}}. \tag{2.118}$$

Then we can use η_{eff} to solve our generalized Stokes equations 2.111 and 2.112.

If needed, it is possible to calculate the plastic factor G by substituting Eq. 2.110 into 2.116 and considering that the root of the second invariant of the deviatoric stress τ_{II} is equal to the yield stress σ_{yield} at yielding (Moresi et al., 2003), so that:

$$G = \dot{\varepsilon}_{IIeff} - \sigma_{yield} \left(\frac{1}{\mu \delta t} + \frac{1}{\eta} \right). \tag{2.119}$$

2.5.5 Non-Newtonian iterations to calculate η_{eff}

Note that both, the creep viscosity η_c as defined in Eq. 2.88 and the effective viscosity η_{eff} when the yield criterion is met 2.118, depend on the strain rate, which is solved for a given viscosity. Therefore, the relationship between viscosity and strain rate is non-linear (Moresi et al., 2003; Gerya, 2010; Kaus, 2010). In order to solve for non-linear visco-elasto-plastic rheologies our code includes a loop for which an initial strain rate is calculated based on trial viscosities (i.e. viscosities of the previous time step). In the second

iteration the first iteration strain rate is used to calculate viscosity for a later recalculation of the strain rate. This iteration continues until a convergence criteria is met, which in our code is:

$$\dot{\varepsilon}_{conv} < 10^{-3}, \tag{2.120}$$

where

$$\dot{\varepsilon}_{conv} = \frac{max(|\dot{\varepsilon}_{II}^{it} - \dot{\varepsilon}_{II}^{it-1}|)}{\dot{\varepsilon}_{II}^{it-1}}, \tag{2.121}$$

where max is an operator to find the maximum value of $|\dot{\varepsilon}_{II}^{it} - \dot{\varepsilon}_{II}^{it-1}|$ among the elements, $\dot{\varepsilon}_{II}^{it}$ is the square root of the second invariant of the strain rate calculated for the current non-Newtonian iteration it and $\dot{\varepsilon}_{II}^{it-1}$ corresponds to the same type of strain rate calculated for the previous time step $it - 1$.

2.6 Strain softening

Faults and shear zones highly condition the geometry and the evolution of rifting. However, FEM does not allow, by definition, the occurrence of discontinuities. Solving the system with an apparent viscosity calculated with the Drucker-Prager yield criterion η_{eff} (Eq. 2.118), makes the model to reproduce the same amount of deformation that would be recovered from a real plastic behaviour, but it cannot reproduce brittle behaviour where part of the plastic deformation is concentrated in fault planes or shear zones. Therefore, it is necessary to develop an algorithm to simulate faults and/or shear zones. Fault planes and shear zones localize deformation because, once the yielding is achieved, deformation along the yielding plane is easier due to a cohesion loss (Buck, 1993). This can be approached as a weakening related with the strain, the so-called **brittle strain softening**. Other mechanisms, such as fluid pressure variations (Sibson, 1990), gouge formation and mineral transformations (Bos and Spiers, 2002) may reduce the brittle and frictional strength (Huismans and Beaumont, 2003). Additionally, strain softening can also occur in the viscous domain (**viscous strain softening**), due to a transition from dislocation to grain size sensitive creep (Braun et al., 1999; Karato et al., 1986; Poirier, 1980) that may reduce the effective viscosity (Huismans and Beaumont, 2003) and the development of crystallographic preferred orientations (CPO) along which the deformation becomes easier (Tommasi et al., 2000; Hansen et al., 2012). However, the contribution of these mechanisms to the total effect of the strain softening is poorly constrained. Therefore, a parametrization is applied in order to produce a strain related reduction of the apparent viscosity for both brittle and viscous domains.

By reducing both the friction angle θ and the cohesion c, the resulting apparent viscosity is also reduced (Eqs. 2.89 and 2.118). Here, we choose to apply strain softening for the brittle domain by reducing only the friction angle θ, where θ is a linear function of the square root of the second invariant of the historic strain ε_{II_h}, for the strain interval $(\varepsilon_{II_h}1, \varepsilon_{II_h}2)$:

$$\theta = (\varepsilon_{II_h} - \varepsilon_{II_h}1)\frac{\theta_2 - \theta_1}{\varepsilon_{II_h}2 - \varepsilon_{II_h}1} + \theta_1, \tag{2.122}$$

where θ_1 and θ_2 correspond to the maximum and minimum friction angle assumed possible respectively, $\theta_1 > \theta_2$, and $\varepsilon_{II_h}1 < \varepsilon_{II_h}2$ (Fig. 2.4). If $\varepsilon_{II_h} < \varepsilon_{II_h}1$, then $\theta = \theta_1$. If $\varepsilon_{II_h} > \varepsilon_{II_h}2$, then $\theta = \theta_2$.

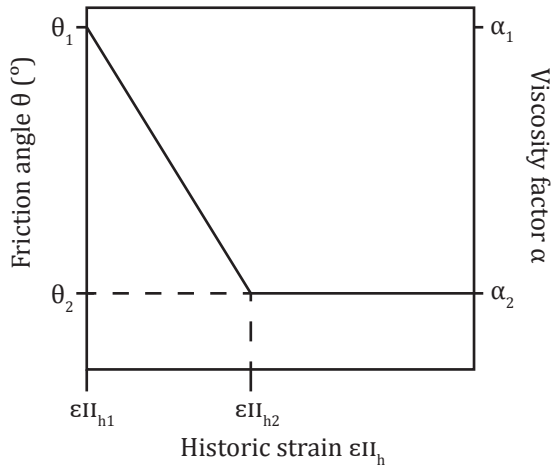

FIGURE 2.4: Strain softening function.

Strain softening for the viscous domain is applied introducing a α factor into Eq. 2.82 (Fig. 2.4). Then, it is possible to write the general creep formulation such as:

$$\eta_{creep} = \alpha^{-1} F B^{-\frac{1}{n}} \dot{\varepsilon}_{II}^{\frac{1}{n}-1} exp\left(\frac{E^*}{nRT}\right), \tag{2.123}$$

where α is a linear function of the second invariant of the historic strain ε_{II_h}, for the strain interval $(\varepsilon_{II_h}1, \varepsilon_{II_h}2)$:

$$\alpha = (\varepsilon_{II_h} - \varepsilon_{II_h}1)\frac{\alpha_2 - \alpha_1}{\varepsilon_{II_h}2 - \varepsilon_{II_h}1} + \alpha_1, \tag{2.124}$$

where α_1 and α_2 correspond to the minimum and maximum factor assumed possible respectively $(1 \leq \alpha_1 < \alpha_2)$. If $\varepsilon_{II_h} < \varepsilon_{II_h}1$, then $\alpha = \alpha_1$. If $\varepsilon_{II_h} > \varepsilon_{II_h}2$, then $\alpha = \alpha_2$.

The historic-strain interval $(\varepsilon_{II_h}1, \varepsilon_{II_h}2)$, the friction-angle interval (θ_1, θ_2), and the creep-factor interval (α_1, α_2) are parameters that need to be chosen for the strain softening approach.

2.7 Shear heating

Plastic and viscous deformation results in dissipation of the mechanical energy into heat. This heat is known as **shear heat** H_s and can be included in Eq. 2.33 inside the heat production term H, together with the radioactive heat production H_r (Gerya, 2010). The shear heating H_s is defined as:

$$Hs = \tau_{ij}\dot{\varepsilon}_{ij}^{ue\prime}, \tag{2.125}$$

where τ_{ij} and $\dot{\varepsilon}_{ij}^{ue\prime}$ are deviatoric stress and deviatoric inelastic strain rate, where ij denotes summation, so that in 2D:

$$Hs = \tau_{xx}\dot{\varepsilon}_{xx}^{ue} + \tau_{yy}\dot{\varepsilon}_{yy}^{ue} + 2\tau_{xy}\dot{\varepsilon}_{xy}^{ue}. \tag{2.126}$$

Our mechanical solver calculates total strain rate $\dot{\varepsilon}_{ij}$ from solved velocities (Eq. A.11), which are calculated based on effective viscosities η_{eff} and previous stresses. Therefore, it is necessary to calculate inelastic strain rate outside of the mechanical solver, before the thermal solver is run. Inelastic strain rate can be defined as:

$$\dot{\varepsilon}_{ij}^{ue} = \dot{\varepsilon}_{ij} - \dot{\varepsilon}_{ij}^{e}, \tag{2.127}$$

where $\dot{\varepsilon}_{ij}^{e}$ is the elastic strain rate (Moresi et al., 2007). The elastic strain rate can be written as:

$$\dot{\varepsilon}_{ij}^{e} = \frac{\overset{\nabla}{\tau}_{ij}}{2\mu}, \tag{2.128}$$

where $\overset{\nabla}{\tau}_{ij}$ is the objective material derivative of the deviatoric stress defined by Eq. 2.93. Then, it is possible to write the elastic strain rate in terms of the current-time-step stresses τ_{ij} and the Jaumann objective deviatoric stress for the previous step $\tau_{ij}^{old_J}$ (Eq. 2.99):

$$\dot{\varepsilon}_{ij}^{e} = \frac{1}{2\mu\Delta t}(\tau_{ij} - \tau_{ij}^{old_J}). \tag{2.129}$$

2.8 Elasticity benchmark

We chose to benchmark FEM visco-elasticity of our code (Sec. 2.5.3) against linear elasticity theory applied for the bending of a thin rigid plate. We chose two tests: 1) a **point load test** for which solution is given by a parametric equation, and 2) a **distributed load test** for which solution is given by a differential equation.

2.8.1 Bending of a rigid plate

Lithospheric plates are considered rigid plates resting over asthenospheric mantle rocks which behave as a fluid on geological time scales (Morgan, 1968). When a load is applied to a lithospheric plate deflection occurs. The plate sinks under the load while bulges rise at the margins of the negative relief due to the elastic response (Fig. 2.5) (Turcotte and Schubert, 1982). The general equation for the deflection ω of lateral-infinite thin rigid plate of thickness h under a load $q(x)$ is:

$$D\frac{d^4\omega}{dx^4} = q(x) - F_h\frac{d^2\omega}{dx^2}, \tag{2.130}$$

where D is the flexural rigidity defined as:

$$D \equiv \frac{Eh^3}{12(1-\nu^2)}, \tag{2.131}$$

where E is the Young's modulus, ν is the Poisson's ratio, and F_h is a horizontal force per unit length applied to the plate (Turcotte and Schubert, 1982). If the mantle below the plate is assumed fluid, then buoyant restoring forces are needed in the formulation:

$$D\frac{d^4\omega}{dx^4} + P\frac{d^2\omega}{dx^2} + \rho_m g\omega = q(x), \tag{2.132}$$

where ρ_m is the density of the fluid mantle (Turcotte and Schubert, 1982). Note that Eq. 2.132 is a differential equation where a load function of the coordinate x can be applied and then solved numerically. We use finite difference method to solve Eq. 2.132 for a distributed load in Sec. 2.8.3, assuming $F_h = 0$.

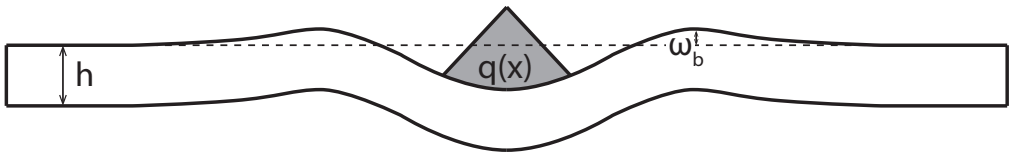

FIGURE 2.5: Deflection of a rigid plate under a load $q(x)$ where h is the thickness of the plate and ω_b is the maximum deflection at the bulges.

Eq. 2.132 can be simplified as described in Turcotte and Schubert (1982) by taking a point load where $q(x) = 0$ except for $x = 0$, assuming $F_h = 0$, and calculating the general solution for the differential equation. Then we obtain:

$$\omega = \frac{V_0\alpha^3}{8D}e^{-\frac{x}{\alpha}}\left(cos\frac{x}{\alpha} + sin\frac{x}{\alpha}\right) \qquad x \geq 0, \tag{2.133}$$

where V_0 is the point load, and α is the flexural parameter:

$$\alpha = \left(\frac{4D}{\rho_m g} \right)^{\frac{1}{4}}. \tag{2.134}$$

This analytical solution is only for positive values of x. However, the general solution is symmetric respect to 0, so it is possible to calculate the deflection ω for negative values of x by simply mirroring ω. This formulation is the one used in Sec. 2.8.2.

Note that all the formulations presented in this section are for plates whose thickness h tends to 0. In the case of finite differences solution the calculation is done for a infinitesimal thin layer where D is calculated for the choice of h so that the solution is similar. However, the analytical approach is obtained from integrating through an h (which is also assumed to be close to 0) so the solution for thick plates (> 10 km) will not give accurate results. Also note that the deflection calculated by these solutions occurs instantaneously, while in our FEM visco-elastic formulation a certain amount of deformation is calculated each time step. In order to compare both results our code will need to run through several time steps before the topography converges.

2.8.2 Point load

This visco-elastic test consists of a 2D box of $10^3 \times 400$ km where the bottom and lateral boundaries are fixed, and the top boundary is a free surface without stabilization algorithm (see Chapter 3) to avoid possible artificial effects. The experiment is divided into two layers of different linear viscosities and densities. The upper layer emulates a rigid plate of thickness $h = 2.5$, 5, or 10 km and density $\rho_2 = 2700$ kg/m^3, which viscosity $\mu_2 = 10^{24}$ Pa s is high enough to simulate a psuedo-rigid behaviour in contrast with the $\mu_1 = 10^{18}$ Pa s of the lower layer (pseudo-fluid) which $\rho_1 = 3200$ kg/m^3, equivalent to the mantle. A point load equivalent to a 100×2 km rock volume with density $\rho_L = 2700$ kg/m^3 is applied at the center of the model (0 km). The element resolution at the surface is 1 km. We chose a small time step $\delta t = 5$ yr in order to avoid topographic instabilities such as the ones described on Chapter 3. The model is run until the topography converges, where the criterion for convergence is 0.5 m difference between the previous and current time-step topographies. Note that the large dimension of the model is to attenuate the uprising of the topographies in areas not loaded due to the conservation of volume, so it is possible to compare with the solutions of Sec. 2.8.1, which are calculated for an infinite plate.

Results show a good agreement between topographies calculated with our FEM visco-elastic code and the analytical solution for $h = 2.5$ and 5 km (Fig. 2.6a and b). For the case where $h = 10$ km (Fig. 2.6c) the FEM results into a shallower negative topography than the

topography calculated by the analytical thin-plate solution. We calculate absolute errors along the topography (Fig. 2.6) from the differences between the topographies obtained from the FEM and the analytical solution. The relative errors calculated for the maximum absolute error are 2, 3 and 15% for $h = 2.5$, 5 and 10 km respectively. This relative errors are small enough for the thin plate tests to validate our elasticity approach. The large errors of the 10 km plate is the consequence of comparing our FEM model with an analytic approach for a thin plate, as 10 km is not thin enough for the analytic solution to accurately capture it.

2.8.3 Distributed load

The setup of this test is the same as the point load (Sec. 2.8.2) but with a distributed 2-km-high load along 100 km instead of a point load. A finite difference code developed by Marta Pérez-Gussinyé and Jason P. Morgan is used to solve the deflection in Eq. 2.132 along the surface to compare with the results from our code. As in the previous section, we chose to evaluate the solutions for plate thickenesses $h = 2.5$, 5 and 10 km.

Results show a very good agreement between the finite difference solution for elasticity for a rigid plate and our FEM visco-elastic approach (Fig. 2.7). Here the difference between the topographies in the visco-elastic code and the ones calculated with finite differeces are in the order of 10-30 meters. The relative differences (equivalent to relative errors in the previous section) at the coordinates where the absolute differences are larger are 4, 3 and 2% for $h = 2.5$, 5 and 10 km respectively. This decrease on the relative difference with h is probably due to smaller velocities for the time steps, and therefore, more stable solutions for thick plates in the visco-elastic code.

2.8.4 Conclusions

From the results shown on Secs. 2.8.2 and 2.8.3 we conclude that our elasticity algorithm included in our viscous code is a good enough approach to model processes at a lithospheric scale. We also conclude that the algorithm developed to include sediment loads in the mechanics of the model is correct since it is the same algorithm we used to apply the loads over the rigid plates.

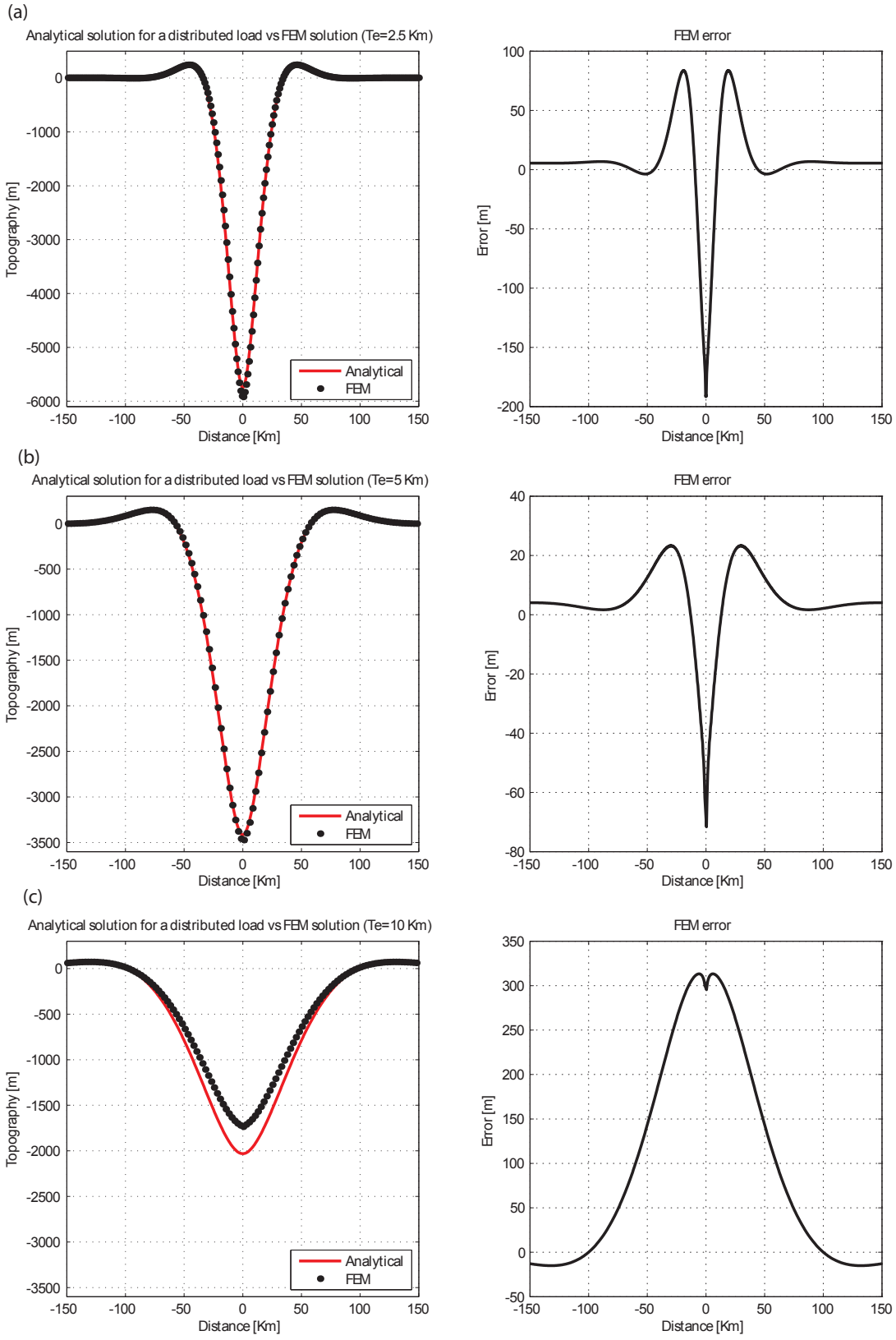

FIGURE 2.6: Point load over rigid plates of (a) 2.5, (b) 5, and (c) 10 km thickness. The red line represents the analytical solution and the black dots the FEM solution nodes. Note that the number of FEM nodes plotted has been cut down so that the analytical solution is visible in the plot. The plots on the right represent the difference between the FEM and the analytical solutions (absolute error).

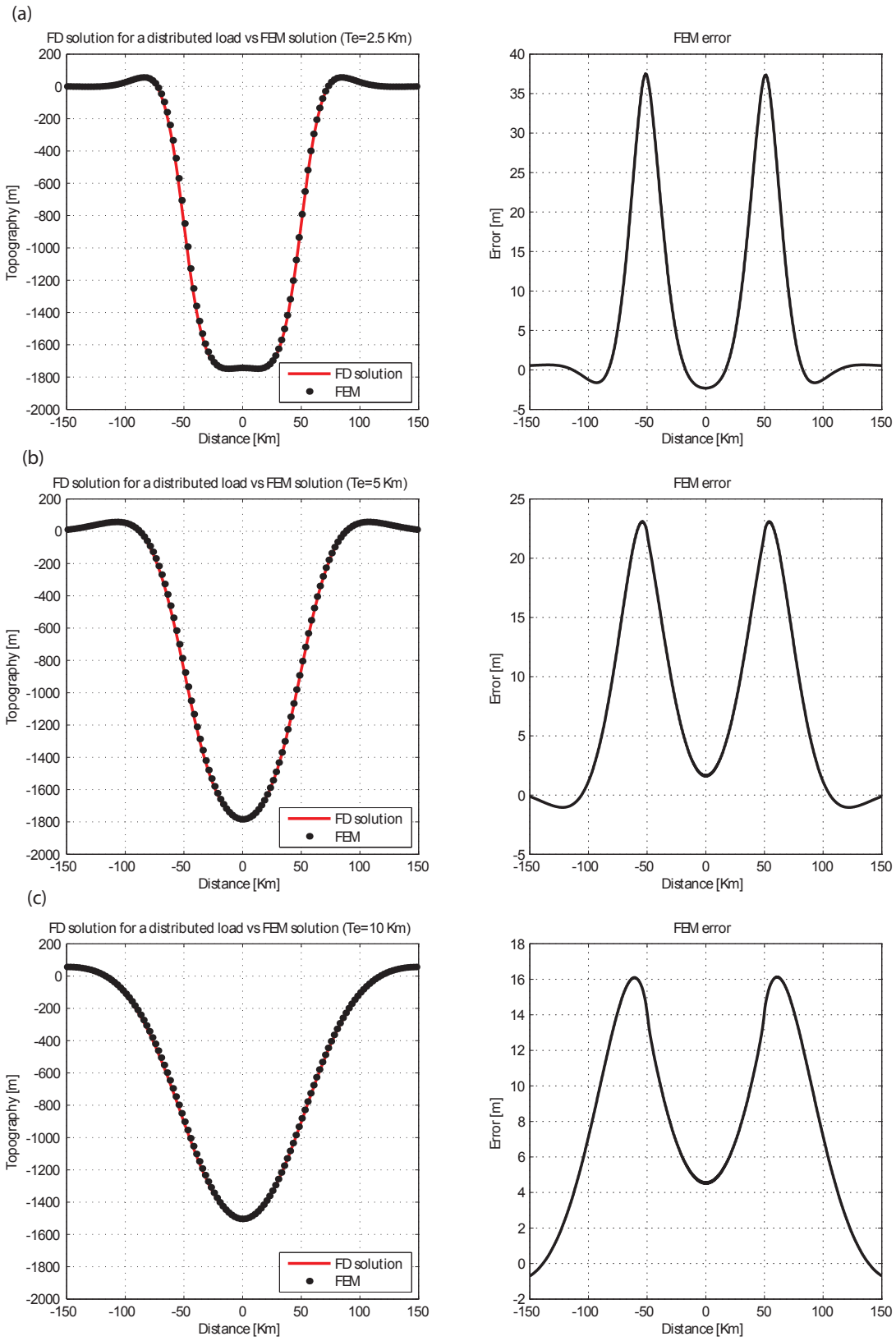

FIGURE 2.7: Distributed load over rigid plates of (a) 2.5, (b) 5, and (c) 10 km thickness. The red line represents the finite difference solution (FD) and the black dots the FEM solution nodes. Note that the number of FEM nodes plotted has been cut down so that the FD solution is visible in the plot. The plots on the right represent the difference between the FEM and the FD soutions (absolute error).

2.9 Code structure

The up-to-date formulation for the FEM geodynamic models has been explained in the previous sections. Most of this formulation was already included in the version of MILAMIN that I enhanced for this project. However, I needed to add strain softening, elasticity, shear heating, and a stress-free surface with a stabilization algorithm (describe in Chapter 3). The code is conceptually divided in three main sections that are:

Preprocessor

This section starts with the definition of the parameters and switches, and the declaration of the variables. It continues generating the initial mesh using a subroutine to generate the geometry of the model and another to call the triangle code (Shewchuk, 1996) to generate the grid based on the geometry. Then, it sets the initial boundary conditions for the model.

Processor

This section initializes the loop that runs along all the time steps. Firstly, checks the mesh and if it is very deformed it does remeshing using the same functions as the preprocessor. Then, it calls the mechanical and the thermal solvers.

Postprocessor

This section calculates some variables from the output of the solvers, for example the horizontal and vertical deviatoric stresses or the viscosity field, and plots the results of the model.

The **mechanical solver** starts by declaring the variables and initializes the strain rate iteration. It has two ways of solving the mechanical problem: one is coded in a more simplistic way, and the other one is less intuitive but more efficient. The complex procedure is based on building the matrices for K in blocks of 400 elements (Dabrowski et al., 2008). It is possible to choose between these different procedures from a switch, at the beginning of the main code. Then, the non-Newtonian iteration starts, calculate strain-softening parameters, updates the viscosities, load the shape functions and shape function derivatives, calculates the Jacobian, its determinant and its inverse. For the simplistic procedure it calculates the matrices A, Q, Q^T, M and the vector Rhs for each element, with integrating loops. For the block procedure it calculates the block matrices A, Q, Q^T, M and the block vector for the right-hand side Rhs, with integrating loops, and repeats for every block. Later, it changes from local coordinates to global coordinates using the inverse of the Jacobian and stores the data in the global matrices. Then, it generates the global stiffness sparse matrix, reorders the matrix, applies Cholesky factorization, sets

the boundary conditions and solves the system Eq. 2.63 by Uzawa iterations (Eq. 2.64). Finally, it calculates horizontal, vertical and maximum deviatoric stresses, horizontal, vertical and maximum strain, yield strength, historic strain, strain rate, second invariants of deviatoric stress and strain rate, recalculates the viscosities and checks convergence of the solution, closing the strain-rate loop. Once convergence is met (Eq. 2.120) stresses are rotated and saved to be used as old stresses $\tau_{ij}^{old_J}$ for elasticity (Eq. 2.99) in the future time step.

The **thermal solver** starts by declaring the variables and constants, loading the integration points, shape functions and derivatives of the shape functions for the local coordinates and indexing. Later, it initializes a blocking loop to build the stiffness matrix, integrates through the integration points, change from local to global coordinates and write the local stiffness matrices into the global stiffness matrix. Finally, it sets the boundary conditions and solves the system Eq. 2.48.

Here, I present the schematic flowcharts of our main code and the mechanical and temperature solvers, in order to clarify how the formulation is implemented.

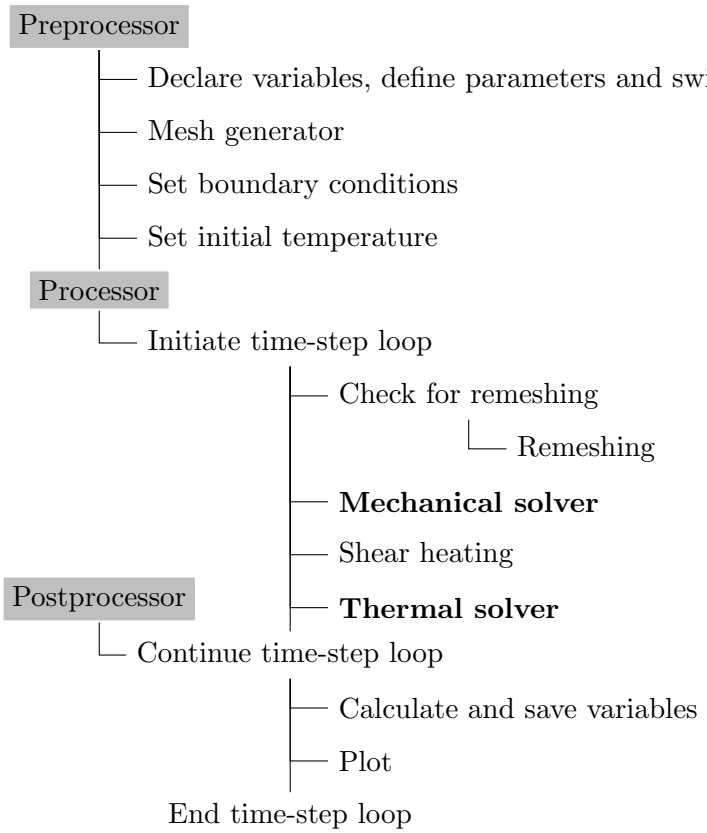

Mechanical solver

- Declare local variables
- Strain-rate iteration
  - Viscosity algorithm
    - Strain softening (Eqs. 2.122 and 2.124)
    - Calculate η_{eff} (Eqs. 2.88, 2.101, and 2.118)
  - Build stiffness matrix (A, Q, Q^T, M) and Rhs vector (F) (Sec. 2.2.5, 2.4 and 2.5.3)
  - Reorder A and Rhs
  - Cholesky factorization of A
  - Uzawa-iteration solver (Eq. 2.64)
    - Solve velocities $v = A^{-1}Rhs$
    - Calculate the divergence $Div = Q^T M^{-1}$
    - Recalculate $Rhs = Rhs - \kappa * Div * Q$
  - End of Uzawa-iteration
  - Calculate historic strain ε_{II_h} for future strain softening 2.8
  - Calculate stress σ, deviatoric stress τ, strain ε, rigid-body rotation ω, strain rate $\dot{\varepsilon}$ and second invariants τ_{II} and $\dot{\varepsilon}_{II}$

Check convergence (Eq. 2.120) and end the strain-rate iteration

Thermal solver

- Declare local variables
- Build stiffness matrix (K_T)(Sec. 2.3 and 2.4)
- Reorder K_T and Rhs
- Solve temperatures $T = K_T^{-1}Rhs$

Chapter 3

Methodology: Stabilization of a stress-free surface

M. Andrés-Martínez, J. P. Morgan, M. Pérez-Gussinyé, and L. Rüpke. A new free-surface stabilization algorithm for geodynamical modelling: Theory and numerical tests. *Physics of the Earth and Planetary Interiors*, 246:41–51, 2015. doi: 10.1016/j.pepi.2015.07.003. URL `http://dx.doi.org/10.1016/j.pepi.2015.07.003`

Authors contribution

JM, LR and MA designed the free surface stabilization algorithm. MA coded the algorithm in discussion with JM and MP. MA designed the tests and analysed the results in discussion with JM, MP and LR. MA wrote the full manuscript with the supervision of JM, MP and LR.

Notes

Results obtained by using the Kaus et al., 2010 algorithm (Fig. 7e) are calculated with $\alpha_K = 0.5$.

Physics of the Earth and Planetary Interiors 246 (2015) 41–51

Contents lists available at ScienceDirect

Physics of the Earth and Planetary Interiors

journal homepage: www.elsevier.com/locate/pepi

A new free-surface stabilization algorithm for geodynamical modelling: Theory and numerical tests

Miguel Andrés-Martínez [a,1], Jason P. Morgan [a,*], Marta Pérez-Gussinyé [a,*], Lars Rüpke [b,*]

[a] Royal Holloway University of London, Earth Sciences, Egham, United Kingdom
[b] GEOMAR – Helmholtz Centre for Ocean Research, Kiel, Germany

ARTICLE INFO

Article history:
Received 17 October 2014
Received in revised form 21 June 2015
Accepted 10 July 2015
Available online 20 July 2015

Keywords:
Free-surface stabilization
Geodynamic modelling

ABSTRACT

The surface of the solid Earth is effectively stress free in its subaerial portions, and hydrostatic beneath the oceans. Unfortunately, this type of boundary condition is difficult to treat computationally, and for computational convenience, numerical models have often used simpler approximations that do not involve a normal stress-loaded, shear-stress free top surface that is free to move. Viscous flow models with a computational free surface typically confront stability problems when the time step is bigger than the viscous relaxation time. The small time step required for stability ($<$ 2 Kyr) makes this type of model computationally intensive, so there remains a need to develop strategies that mitigate the stability problem by making larger (at least $\sim$10 Kyr) time steps stable and accurate. Here we present a new free-surface stabilization algorithm for finite element codes which solves the stability problem by adding to the Stokes formulation an intrinsic penalization term equivalent to a portion of the future load at the surface nodes. Our algorithm is straightforward to implement and can be used with both Eulerian or Lagrangian grids. It includes α and β parameters to respectively control both the vertical and the horizontal slope-dependent penalization terms, and uses Uzawa-like iterations to solve the resulting system at a cost comparable to a non-stress free surface formulation. Four tests were carried out in order to study the accuracy and the stability of the algorithm: (1) a decaying first-order sinusoidal topography test, (2) a decaying high-order sinusoidal topography test, (3) a Rayleigh–Taylor instability test, and (4) a steep-slope test. For these tests, we investigate which α and β parameters give the best results in terms of both accuracy and stability. We also compare the accuracy and the stability of our algorithm with a similar implicit approach recently developed by Kaus et al. (2010). We find that our algorithm is slightly more accurate and stable for steep slopes, and also conclude that, for longer time steps, the optimal α controlling factor for both approaches is $\sim$2/3, instead of the 1/2 Crank–Nicolson parameter inferred from a linearized accuracy analysis. This more-implicit value coincides with the velocity factor for a Galerkin time discretization applied to our penalization term using linear shape functions in time.

1. Introduction

Tectonics and mantle dynamics together with sedimentation and erosion build the Earth's surface topography (Anderson et al., 1973; McKenzie, 1977; Melosh and Raefsky, 1980; Hager et al., 1985; Willett, 1999; Beaumont et al., 2001; Koons, 2002; Finnegan et al., 2008; Braun, 2010). A topographical change translates into a change in the body forces governing the crustal and mantle dynamic processes. Additionally, there are feedbacks between surface erosion and topography (Ruddiman and Kutzbach, 1989; Braun, 2006) that make accurate topographic determinations desirable. The Earth's subaerial surface is a stress-free surface, which implies that both normal and shear stress should vanish at this interface (Harlow et al., 1965; De Bremaecker, 1976). Since surface and inner geodynamic processes are coupled, there is increasing interest in including stress-free surfaces and computationally similar submarine hydrostatic surfaces within geodynamic codes.

Several approaches to incorporate a free surface into geodynamical codes have been discussed during the last two decades. These include normal stress method, 'sticky-air' approaches, methods that treat the free surface as another variable of the flow problem, and a 'real' free surface. The normal-stress method remains most common because it is easiest to compute and also stable

* Corresponding authors.
E-mail addresses: miguel.andres-martinez.2011@live.rhul.ac.uk (M. Andrés-Martínez), jason.morgan@rhul.ac.uk (J.P. Morgan), marta.perez-gussinye@rhul.ac.uk (M. Pérez-Gussinyé), lruepke@geomar.de (L. Rüpke).
[1] Principal corresponding author.

http://dx.doi.org/10.1016/j.pepi.2015.07.003
0031-9201/

for time steps that are much larger than the viscous relaxation time of the system. It consists of an Eulerian top flat surface with free-slip boundary conditions for which stresses are calculated by solving the momentum equation, and where topography is post-calculated from normal stresses at the Eulerian surface nodes, by assuming that they are instantly compensated by the topographic load (McKenzie, 1977; Fleitout et al., 1986; Zhong et al., 1993, 1996). Although normal-stress methods are known to be computationally more efficient than real free surface ones, they are not able to solve the time-dependent relaxation of topography (Zhong et al., 1996; Crameri et al., 2012). If the relaxation time of a particular topographic wavelength is on the order of the time-scale of inner geodynamic processes, the relaxation of topography must also be considered. In this situation, a real free surface method is required to represent topographies that dynamically evolve with time (Zhong et al., 1996). The 'sticky-air' method consists of adding a low-viscous low-density layer at the top of the model, which is used as a proxy for air or water (Zaleski and Julien, 1990; Gerya and Yuen, 2003; Crameri et al., 2012), with the aim that the interface between the 'sticky-air' layer and the upper crust will behave similarly to a free surface. This method results into matrix singularities when the viscosity is too low, and introduces artefacts when the air/water layer is too viscous, because it can induce large stresses on the surface (Crameri et al., 2012). In practical use, any 'sticky-air' calculation should include post processing to determine that the sticky-air-to-surface interface is truly stress-free. Other methods treat the free surface as an additional independent variable and solve implicitly for it in conjunction with the Stokes equation (Kramer et al., 2012), or use implicit timestepping that has the nodal coordinates as part of the solution which can also yield a stable solution (Popov and Sobolev, 2008). Real free surface methods track the free surface in time and update it with the velocity calculated from solving the Stokes equation in the entire domain (Poliakov and Podladchikov, 1992). We chose to work with this method since it solves the time-dependent relaxation of topography and avoids artefacts associated with a 'sticky-air' layer without any additional calculation.

A stress-free surface, however, suffers from well-known instabilities when the time step is bigger than the viscous relaxation time (Zhong et al., 1996). Because the longest wavelength surface topography variations induce the most rapid rebound responses, we first consider the effects of surface topography with a wavelength of 1000 km, to approximate the effects of a large-scale Plate Tectonics-related topographic variation in a given problem. For a relevant viscosity of 10^{21} Pa s and surface density contrast of 2700 kg/m^3, the viscous relaxation time of such a topographical feature would be of order ~10 Kyr (Turcotte and Schubert, 1982). Thus, for time steps bigger than 10 Kyr topographic computations may become unstable. In Fig. 1 it is shown why instabilities arise for time steps bigger than the relaxation time. In our example, the initial topography is a valley underlain by a constant viscosity fluid. In the presence of gravity, this topography should relax to a flat surface. In most geodynamic codes, the velocities at the nodes are calculated for the beginning of a time step and assumed constant through the whole step. However, if the time step is large compared to the viscous relaxation time, the velocities should decrease within the time step. Hence, a large time step leads to an overestimation of the velocity and topography at the end of the time step. In some cases, the final topography will be larger than the isostatically balanced topography and in the next time step the estimated velocity will be directed downwards and create a new 'valley artefact'. In the subsequent time step this valley will become again a positive topography (due to overestimation of the average velocity in the numerical time step) and so on. Hence, the topography will oscillate around the value for correctly compensated isostatic relief. This instability could occur not only at the beginning of a simulation in which case we could always run the model for small time steps and then switch to bigger time steps when stability is achieved, but could also occur for later stages of simulations that account for complex rheologies and/or geometries.

One of the most common free-surface instabilities that is observed at geodynamic codes is the so called 'drunken sailor' instability. This instability occurs when the velocities for the surface are overestimated for a broad area on one part of the model, where in the opposite part the velocities are underestimated, and the resulting displacements overpass the isostatic equilibrium. Consequently, the topography of the previous step would be inverted. This phenomena could decay through a few time steps and then reach stability or, in case the overestimated velocities

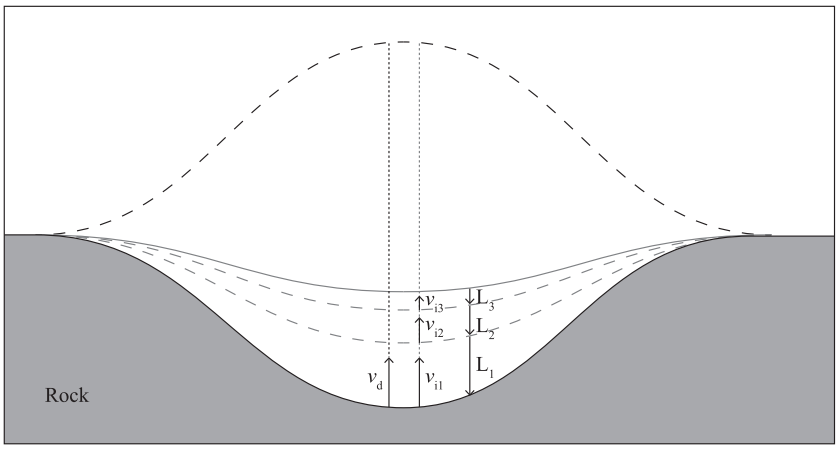

Fig. 1. Evolution of a valley-shape negative topography with different time steps. The solid black line represents the initial negative topography (mass defect). Theoretically, the negative topography should rise into a flat line due to buoyancy. Lets consider now two cases: (1) a single big time step (*TS*) for which the calculated velocity is v_d, where the dashed black line represents the positive unstable topography for the next time step, calculated with v_d; and (2) smaller time steps ts_1, ts_2, and ts_3, such as $TS = ts_1 + ts_2 + ts_3$, with respective calculated velocities v_{i1}, v_{i2} and v_{i3}, and load increments L_1, L_2 and L_3, the dashed gray lines represent smoother negative topographies at the end of the time steps ts_1 and ts_2, and the solid gray line represents a more realistic and stable topography at the end of ts_3, equivalent in time to the unstable topography of the case 1. For the case 1, the load increments are not considered into the body forces, so the resulting integrated displacement is bigger than the integrated displacement through the small time steps, for which body forces are updated with the load increments at the beginning of each *ts*. The instability of the free surface is the consequence of a time step bigger than the viscous relaxation time, which often leads to an overestimation of the velocities at the beginning of the next time step.

produce a displacement on the surface bigger than the initial topography, it will lead to the instability of the whole model.

Instabilities at a free surface will not occur for small enough time steps, since the new topography and the corresponding changes in body forces implied by it are included with sufficient accuracy in successive calculations. In our example, both the topography and upward velocity would be slowly reduced through the successive time steps leading to a stable solution (Fig. 1). Kramer et al. (2012) estimate that time steps to obtain a stable solution need to be at least one order of magnitude less than the time step in an identical simulation but employs a free-slip boundary. For simplistic viscous tests we have developed, ~2000 year steps are small enough to prevent numerical instabilities for a layer with a viscosity of 10^{21} Pa s. Although smaller time steps allow more accurate tracking of the topography, they are computationally expensive.

For this reason, it is desirable to develop algorithms that allow real free surface codes to run stable for relatively big time steps ($\geqslant$10 Kyr). Here, we present a new free-surface stabilization algorithm (FSSA). It consists of adding a penalizing load to the real free surface, calculated implicitly from a fraction of the increment in height of the surface between the initial and the following steps. A similar FSSA algorithm was developed by Kaus et al. (2010). Their algorithm takes into account the surface traction terms derived from the time discretization of the momentum equations. Though their mathematical formulation is different, these terms also penalize the velocities as a function of the surface displacement along a time step in a similar way to our FSSA. Therefore, we have coded and tested both algorithms in order to check whether there are particular cases for which one algorithm gives a more accurate solution and/or allows a larger time step than the other while preserving stability. The results presented here were calculated with a modified version of MILAMIN (Dabrowski et al., 2008), which is a Lagrangian finite element method (FEM) solver for large 2D problems.

2. Methodology

Velocities and pressures are the unknowns of the mechanical problem in these geodynamic simulations. Velocities can be solved by using the Stokes equation for the viscous flow for incompressible flow:

$$\frac{\partial \tau_{ij}}{\partial x_j} - \frac{\partial P}{\partial x_i} = -\rho g_i, \tag{1}$$

where the deviatoric stress τ_{ij} can be written in terms of velocities in 2D, so for the x direction Stokes equation is:

$$\frac{\partial}{\partial x}\left[\eta\left(\frac{4}{3}\frac{\partial v_x}{\partial x} - \frac{2}{3}\frac{\partial v_y}{\partial y}\right)\right] + \frac{\partial}{\partial y}\left[\eta\left(\frac{\partial v_x}{\partial y} + \frac{\partial v_y}{\partial x}\right)\right] - \frac{\partial P}{\partial x} = -\rho g_x, \tag{2}$$

and for the y direction:

$$\frac{\partial}{\partial y}\left[\eta\left(\frac{4}{3}\frac{\partial v_y}{\partial y} - \frac{2}{3}\frac{\partial v_x}{\partial x}\right)\right] + \frac{\partial}{\partial x}\left[\eta\left(\frac{\partial v_x}{\partial y} + \frac{\partial v_y}{\partial x}\right)\right] - \frac{\partial P}{\partial y} = -\rho g_y, \tag{3}$$

where η is the viscosity, v_x and v_y are the velocities along the x and y directions respectively, P is the pressure, ρ is the density, and g_x and g_y are the accelerations along the x and y directions respectively (Dabrowski et al., 2008). The right-hand side of Eqs. (2) and (3) are the terms arising from the body force vector field. In this work we choose the positive y direction to be in the direction of the gravity vector, so that the acceleration g_x is 0 and g_y is Earth's gravity. In our code this is defined to be negative, so the horizontal body forces are zero and the vertical body forces are negative. Another equation is needed in order to solve for the pressure P. Using the relation between the mean stress changes and the volumetric strain rates we obtain:

$$\frac{\partial v_x}{\partial x} + \frac{\partial v_y}{\partial y} + \frac{P}{\kappa} = 0, \tag{4}$$

where κ is a 'penalty' volumetric viscosity coefficient analogous to the bulk modulus in linear elasticity (Hughes, 2000). For incompressible conditions $\frac{\partial v_x}{\partial x} + \frac{\partial v_y}{\partial y} = 0$. Therefore, $P\kappa^{-1} \approx 0$, so we assign κ a very big value ($10^6 \eta_{max}$) using it as a penalty factor (Hughes, 2000). We introduce a discretization for velocity and pressure into Eqs. (2)–(4) using global shape functions N and Π, and we use the Galerkin method to derive the weak form. Then, we can rewrite this system of differential equations in the matrix form:

$$\begin{pmatrix} A & Q^T \\ Q & -\kappa^{-1}M \end{pmatrix}\begin{pmatrix} v \\ P \end{pmatrix} = \begin{pmatrix} F \\ 0 \end{pmatrix}, \tag{5}$$

where

$$A = \int_{\Omega^e} (\eta^e B^T D B) d\Omega, \tag{6}$$

$$Q = -\int_{\Omega^e} (\Pi B_{vol}) d\Omega, \tag{7}$$

$$M = \int_{\Omega^e} (\Pi \Pi^T) d\Omega, \tag{8}$$

$$B = \begin{pmatrix} \frac{\partial N_1}{\partial x}(x,y) & 0 & \dots \\ 0 & \frac{\partial N_1}{\partial y}(x,y) & \dots \\ \frac{\partial N_1}{\partial y}(x,y) & \frac{\partial N_1}{\partial x}(x,y) & \dots \end{pmatrix}, \tag{9}$$

$$D = \begin{pmatrix} \frac{4}{3} & -\frac{2}{3} & 0 \\ -\frac{2}{3} & \frac{4}{3} & 0 \\ 0 & 0 & 1 \end{pmatrix}, \tag{10}$$

$$B_{vol} = \begin{pmatrix} \frac{\partial N_1}{\partial x}(x,y) & 0 & \dots \\ 0 & \frac{\partial N_1}{\partial y}(x,y) & \dots \end{pmatrix}, \tag{11}$$

$$F = \int_{\Omega^e} (\rho g) d\Omega, \tag{12}$$

where η^e is the viscosity over the element, B defines the FE strain rate matrix, $\eta^e D$ is the constitutive tensor in Voigt notation, v and P are the velocity and pressure unknowns, F contains the body forces per volume and the boundary integrals over all forces acting on the modelling domain Ω with boundaries S, and Ω^e is an element domain (Hughes, 2000). It is possible to formally solve for pressure $P = \kappa M^{-1} Q v$ and then simplify this system of equations to equations only for vector v:

$$K v = F, \tag{13}$$

where $K \equiv A + \kappa Q^T M^{-1} Q$ is the penalized stiffness matrix for incompressible flow (Hughes, 2000; Zienkiewicz et al., 1985). Here, we use Crouzeix–Raviart triangular elements with quadratic velocity shape functions enhanced by a cubic bubble function and discontinuous linear interpolation pressure (Crouzeix and Raviart, 1973). Meshes were generated employing the Triangle Mesh Generator developed by Shewchuk (1996) (http://www.cs.cmu.edu/~quake/triangle.html, version 1.6, 2005).

2.1. Free-surface approach

For a surface node at the beginning of a time step n, we can define an increment to the surface height Δh_{n+1} for this node. We assume that the x-location of this interpolation for h_{n+1} is fixed to the current x-location for each surface node. In this case, the topographic change during this time step is given by:

$$\Delta h_{n+1} = \Delta h^x_{n+1} + \Delta h^y_{n+1}, \tag{14}$$

$$\Delta h_{n+1} = -\delta t \left(\frac{\bar{\delta h}}{\delta x}\right) v_x + \delta t\, v_y, \tag{15}$$

where δt is the time step, v_x and v_y are the time-averaged x- and y-velocity components calculated at this node along top surface, and $\left(\frac{\bar{\delta h}}{\delta x}\right)$ is an approximation to the slope of the top surface during the time step (Fig. 2). The negative sign of the horizontal term is needed to determine the change in relief due to positive (rightwards) advection of a positive (up to the right) slope (Fig. 3a–d).

To stabilize the displacement calculated with a large time step, we chose to damp the velocity solution by adding, during that time step, a portion of the load that would correspond to a fraction of the estimated displacement Δh_{n+1}. At the end of the time step this can be expressed as:

$$\Delta \bar{h}_n = \alpha \left(-\beta \delta t \left(\frac{\bar{\delta h}}{\delta x}\right) v_x + \delta t\, v_y \right), \tag{16}$$

where α is a number between 0 and 1 to control what fraction of v_x and v_y contribute to $\Delta \bar{h}_n$, and β is also a number between 0 and 1 to control the contribution of v_x alone. The force produced by the load $\Delta \bar{h}_n$ is:

$$F_{FS} = -\int_S \rho g_y \alpha \beta \delta t \left(\frac{\bar{\delta h}}{\delta x}\right) v_x dx + \int_S \rho g_y \alpha \delta t\, v_y dx. \tag{17}$$

where ρ is the density of the rock for the subaerial case, or density contrast between the rock and the water for the submarine case, and g_y is gravity. Here we assume that the slope is relatively constant along the time step, so $\left(\frac{\bar{\delta h}}{\delta x}\right) \approx \left(\frac{\delta h}{\delta x}\right)_n$. Separating the x and y terms of the F_{FS} and incorporating this force into the standard weak formulation (Hughes, 2000, p. 25):

$$F^{yx}_{FS^i} = -\rho g_y \alpha \beta \delta t \left(\frac{\delta h}{\delta x}\right)_n \int_S N_i N_j v_{xj} dS, \tag{18}$$

$$F^{yy}_{FS^i} = \rho g_y \alpha \delta t \int_S N_i N_j v_{yj} dS, \tag{19}$$

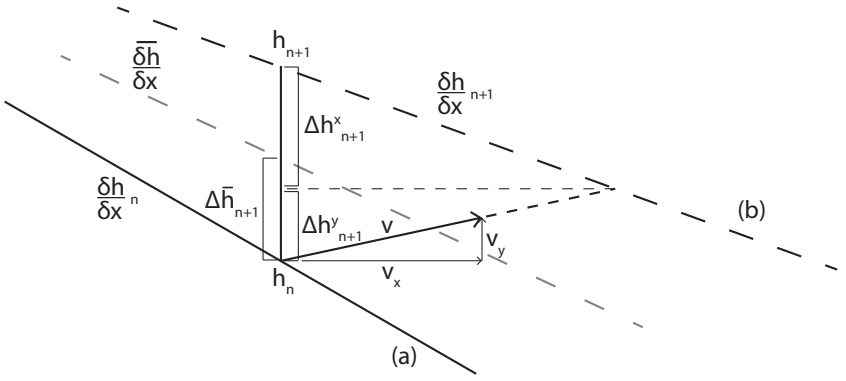

Fig. 2. Increments in height Δh at a surface node (a) before and (b) after a time step at the same horizontal location: v represents the velocity at the beginning of the time step, h_n and h_{n+1} are the height at the beginning and end of the time step respectively, Δh^x_{n+1} and Δh^y_{n+1} are the height increments after the time step, calculated using v_x and v_y components of the velocity respectively, $\left(\frac{\delta h}{\delta x}\right)_n$, $\left(\frac{\delta h}{\delta x}\right)_{n+1}$ and $\left(\frac{\bar{\delta h}}{\delta x}\right)$ are the surface slopes at the beginning, at the end, and an average approximation during of the time step respectively, and $\Delta \bar{h}_n$ is the portion of the height increment for the end of the time step, obtained for a given choice of the α and β controlling factors.

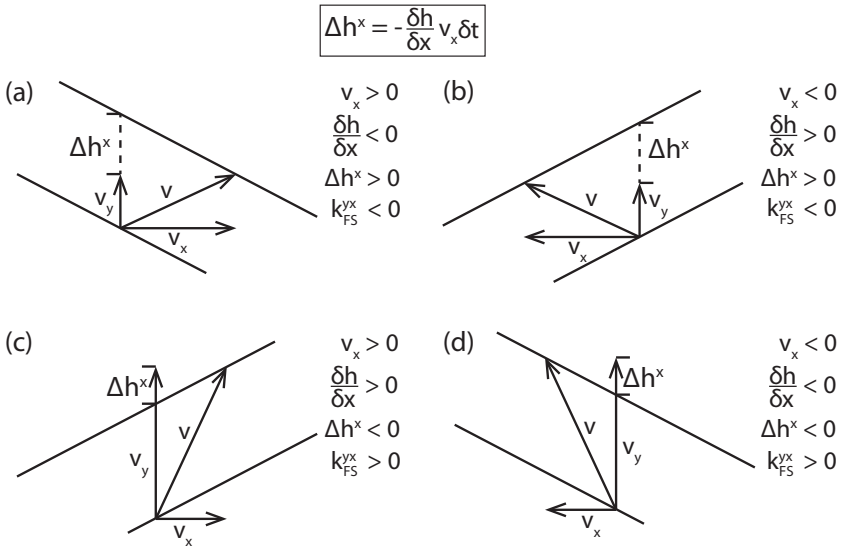

Fig. 3. Different configurations of positive vertical velocities v_y with positive and negative horizontal velocities v_x and positive and negative slopes $\frac{\bar{\delta h}}{\delta x}$: (a) and (b) horizontal velocities v_x result in positive vertical displacements of the surface Δh^x, for the given slopes that should be penalized with a negative k^{yx}_{FS} term, while (c) and (d) horizontal velocities v_x for the given slopes result in negative displacements of the surface Δh^x that should be penalized with a positive k^{yx}_{FS}. Note that the term k^{yx}_{FS} is opposite in sign to the displacement Δh^x. This change in sign is due to the negative sign of the gravity.

where F_{FS}^{yx} and F_{FS}^{yy} are the different terms of the force along the y axes (first superscript) due to the displacements along the x and y axis (second superscript) respectively, i is the global index of all nodes at the free surface, and N are the shape functions evaluated along the surface. Note that these penalization forces will always work in the opposite sense of the surface displacement since the gravity g is defined to be negative (Fig. 3). In order to stabilize the free surface we add both forces into the right hand side of Eq. (13), which is equivalent to add the average load due to $\Delta\bar{h}_n$ over the time step:

$$K v = F + F_{FS}^{yx} + F_{FS}^{yy}. \tag{20}$$

Since F_{FS}^{yx} and F_{FS}^{yy} are expressed in weak formulation it is possible to write:

$$K v = F + K_{FS}^{x} v_x + K_{FS}^{y} v_y, \tag{21}$$

where K_{FS}^{x} and K_{FS}^{y} are stiffness-shape terms which include ρ, g_y, the parameters α and β, and the shape functions N. We can therefore rewrite the Eq. (21) as:

$$[K - K_{FS}^{x} - K_{FS}^{y}] v = F. \tag{22}$$

The system of Eq. (22) is now solved for the velocities (and pressures) which leads to a more stable and accurate solution for the velocities along the free surface. Note that we are using the vertical and horizontal velocities of each surface node to calculate the future vertical displacement at the current horizontal location of the node for the topographic variation during the time step (Fig. 2). Therefore, this is an Eulerian formulation. This is justified because the correction is applied at the node location as the solver is used for this configuration of the mesh. Also note that although we developed this formulation for the top surface where the largest density contrast is expected, it can also be applied to any internal interface across which there is a density contrast.

In order to implement the proposed algorithm into a FEM code, it is necessary to build the K_{FS}^{x} and K_{FS}^{y} matrices. These additional matrices incorporate typical forms in the usual stiffness matrix K. Here we show a 2D example of the stiffness-matrix structure for an element K_e:

$$K_e = \begin{pmatrix} k_{11}^{xx} & k_{11}^{xy} & k_{12}^{xx} & k_{12}^{xy} & . & . & k_{1n}^{xx} & k_{1n}^{xy} \\ k_{11}^{yx} & k_{11}^{yy} & k_{12}^{yx} & k_{12}^{yy} & . & . & k_{1n}^{yx} & k_{1n}^{yy} \\ k_{21}^{xx} & k_{21}^{xy} & k_{22}^{xx} & k_{22}^{xy} & . & . & k_{2n}^{xx} & k_{2n}^{xy} \\ k_{21}^{yx} & k_{21}^{yy} & k_{22}^{yx} & k_{22}^{yy} & . & . & k_{2n}^{yx} & k_{2n}^{yy} \\ . & . & . & . & k_{ij}^{xx} & k_{ij}^{xy} & . & . \\ . & . & . & . & k_{ij}^{yx} & k_{ij}^{yy} & . & . \\ k_{n1}^{xx} & k_{n1}^{xy} & k_{n2}^{xx} & k_{n2}^{xy} & . & . & k_{nn}^{xx} & k_{nn}^{xy} \\ k_{n1}^{yx} & k_{n1}^{yy} & k_{n2}^{yx} & k_{n2}^{yy} & . & . & k_{nn}^{yx} & k_{nn}^{yy}, \end{pmatrix} \tag{23}$$

where n is the number of nodes in the element. The first superscript of k indicates the direction of the force resulting from multiplying k by its respective v in Eq. (13). The second superscript indicates the direction of the velocity v which is multiplying k, and the subscripts i and j indicates the shape functions involved in the calculation of the component. Our penalizing force F_{FS} has both F_{FS}^{yx} and F_{FS}^{yy} components that are applied in the y direction, and are calculated from the velocities v_x and v_y at the surface nodes. Therefore, K_{FS}^{x} and K_{FS}^{y} matrices will be 0 everywhere, except for the components $k_{FS^{ij}}^{yx}$ and $k_{FS^{ij}}^{yy}$ at surface nodes:

$$k_{FS^{ij}}^{yx} = -\rho g_y \alpha \beta \delta t \left(\frac{\delta h}{\delta x}\right)_n \int_S N_i N_j dS, \tag{24}$$

$$k_{FS^{ij}}^{yy} = \rho g_y \alpha \delta t \int_S N_i N_j dS. \tag{25}$$

The annexe includes an example of coded $k_{FS^{ij}}^{yx}$ and $k_{FS^{ij}}^{yy}$ for a 2D FEM model.

The stiffness matrix for a flow solver is typically symmetric so it is possible to apply the computationally efficient Cholesky decomposition method to solve it. The matrix K_{FS}^{y} is also symmetric, so that subtracting it from the stiffness matrix would have little effect on computing time. However, K_{FS}^{x} is not symmetric, since its non-zero values are located off-diagonal in the lower-triangular matrix (Eq. (23)), so subtracting it from the stiffness matrix would make a symmetric Cholesky decomposition impossible. LU decomposition could be applied in this case, but this would considerably degrade the performance of the code. We have chosen to use an iterative operator split into symmetric and asymmetric matrices that can use Cholesky decomposition for inversion of a symmetric matrix with multiple back-substitutions. This approach is ~100 times faster than a full LU decomposition for the resolution used in our experiments (10–30 km). In this iterative solution the symmetric matrix K_{FS}^{y} is subtracted from the stiffness matrix, then Cholesky factorization is applied to this matrix. The system of equations is solved in which the right hand-side of the system consist of the body forces F plus our correcting free surface force term F_{FS}^{yx} or $K_{FS}^{x} v_{it-1}$:

$$[K - K_{FS}^{y}] v_{it} = F + K_{FS}^{x} v_{it-1}, \tag{26}$$

where it is the number of the current iterative approximation to the solution at this time step. The first iteration v_{it-1} is assumed to be 0, so F_{FS}^{yx} is also 0. In each new iteration v_{it-1} is updated using the velocities calculated in the previous iteration. The loop runs until the solution converges. Typically, FEM codes for a incompressible flow also use an 'Uzawa' iterative solution algorithm in order to achieve incompressibility. Here, 'Uzawa' is the name used by Zienkiewicz et al. (1985) to describe their proposed 'iterative improvement' of a penalty formulation for incompressible flow. Other geodynamics papers use the overused term 'Uzawa' to mean different, but related, numerical algorithms. We merge both iterations by applying two loops, an outer loop which updates the velocities from the previous iteration and adds $K_{FS}^{x} v_{it-1}$ to the right-hand side Rhs of the Eq. (13), and an inner loop which iterates to obtain incompressibility:

---

*Loop*1 *it* = 1 : *m*
  Operator split, asymmetric matrix terms moved to Rhs:
  $Rhs = F + K_{FS}^{x} v_{it-1}$
  Zienkiewicz et al. (1985) **'Uzawa iteration':**
  *Loop*2 *uz* = 1 : *n*
    $u = [K - K_{FS}^{y}]^{-1}\ Rhs$
    $Div = Q' M^{-1}$
    $Rhs = Rhs - \kappa Div Q$
  end
end

---

where m and n are the number of iterations for each loop, Div is the divergence, κ is the pressure-formulation penalty factor, and Q and M are the parts of the stiffness matrix indicated in Eqs. (7) and (8) respectively. Note that the matrix $K - K_{FS}^{y}$ is formed and Cholesky-factorized only once per time step so that all Rhs and incompressibility-preserving subiterations only involved relatively cheap and fast Cholesky back-substitutions analogous to the back-substitutions in a typical Uzawa algorithm for incompressibility.

3. Results

Four experiments were conducted in order to test the stability and the accuracy of the above algorithm and also to explore which α and β parameters are 'best' for practical use. These experiments

exhibit both 'drunken sailor' instabilities and/or meshing problems when the time step is too large. The experiments are: (a) a decaying first-order sinusoidal topography test, (b) a decaying high-order sinusoidal topography test, (c) a Rayleigh–Taylor instability test, and (d) a steep-slope test. The test for the topography of a half-sinusoidal initial relief consists of a single layer experiment with constant viscosity and an initial top-surface relief imposed as a half-sinusoid. Theoretically, this topography should evolve towards a flat surface. This experiment is appropriate for testing the stability and the accuracy of our algorithm since it introduces the longest wavelength, highest amplitude form of the 'drunken sailor' instability. For time steps >14 Kyr for the given 10^{21} Pa s viscosity this instability occurs for a simple free surface. The 50th-harmonic test is a variation of the previous test but with a much shorter wavelength sinusoidal topography. For this topographic variation the predicted relaxation time is bigger (Turcotte and Schubert, 1982). However, this test is convenient since it allows us to check the accuracy of our FSSA for steep-slopes and its ability to reduce the numerical artefact involving a self-intersecting top surface (Fig. 4). The Rayleigh–Taylor instability test is a two-layer viscous flow experiment, in which the upper layer is more viscous and denser than the lower layer, resulting in a Rayleigh–Taylor instability beneath the free surface. The instability is triggered by relief on the interface between the two layers, which helps the upper layer to start sinking where it is thicker, and the lower layer to start rising where the upper layer is thinner. The solution of the Rayleigh–Taylor instability is highly sensitive to the top-surface topography, so that a badly constrained free surface also induces the 'drunken sailor' instability which does not allow the Rayleigh–Taylor instability to evolve properly. Finally, the steep-slope test is a single-layer viscous experiment that has a steep slope in its initial topography. Theoretically the slope should become smoother through time and finally become a stable flat top surface. Although this experiment does not lead to a drunken-sailor type instability, the horizontal component of the velocity affects the slope of the top surface so it is a suitable experiment to better evaluate the effects of the K_{fs}^{x} correction terms. Table 1 summarizes the parameters used in the different experiments.

In order to investigate the accuracy of our algorithm, we compare the experiments to a reference solution determined for a very small time step of 100 yr and a 'simple' free surface. Based on the tests we made for solutions run with small 100 yr and 200 yr time steps (see Table 2), the reference solution appears likely to be better than 1×10^{-2} m accuracy (RMS error) for all tests, and that we chose to use $\alpha=0$ for the reference solution so that we would not use a FSSA for the reference solution. We next discuss the accuracy comparing the topographies generated with the FSSA tests with this reference solution. We found it also necessary to determine the biggest stable time step for the non-FSSA approach, since it defines for which δt the tests become unstable without FSSA, and is useful as a reference when discussing the improved stability of the FSSA approaches.

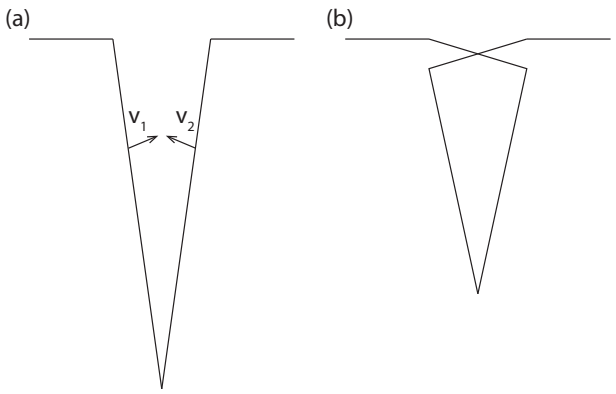

Fig. 4. Self-intersection of surface topography created by a surface valley with very steep slopes. In this case the surface velocities v_1 and v_2 in (a) induce large horizontal displacements during a time step leading to a numerical artefact in which the top-surface intersects itself after a Lagrangian time step as shown in (b).

Table 1
Experiment parameters.

Test	Viscosity η [Pa s]	Geometry parameters [km]	Geometry
Decaying-half-sinusoid of top-surface relief	10^{21}	500×500 A = 10	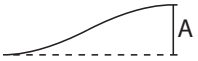
Multiple harmonics of top-surface relief	10^{21}	500×500 A = 10 $\lambda=10$	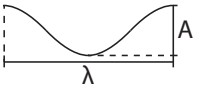
Rayleigh–Taylor instability beneath a free top surface	$\eta_1=10^{21}$ $\eta_2=10^{20}$	500×500 A = 10	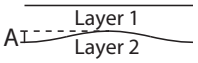
Steep-slope along a free top surface	10^{21}	5×0.1 A = 2 $\Theta=30^{\circ}$	

3.1. Decaying-half-sinusoidal test

Decaying-half-sinusoidal tests with $\alpha=1$, 0.75, 0.7, 2/3, 0.6, 0.5 and 0.25, and $\beta=1$ and 0, were run for time steps $\delta t=0.5$, 1, 2, 2.5, 4, 5, 10 and 20 Kyr. These results show that introducing the penalization for the horizontal component of the velocity K_{fs}^{x} ($\beta=1$) produces almost the same surface relief as the computationally faster tests that just include the vertical penalization K_{fs}^{y} (*e.g.* $\beta=0$). The experiment starts to become unstable without FSSA for $\delta t>14$ Kyr. For small time steps (<5 Kyr) $\alpha=0.5$ yields the most accurate results, while $\alpha=0.7$, 2/3 and 0.6 give the most accurate results for FSSA approach with $\delta t\geqslant20$ Kyr (Figs. 5 and 6).

3.2. Decaying 50th-harmonic-sinusoidal relief test

This test was run for $\delta t=10$, 20, 50, 100 and 400 Kyr, for $\alpha=1$, 0.75, 0.7, 2/3, 0.6, 0.5 and 0.25, and for $\beta=1$ and 0. The highest accuracy was achieved for $\alpha=0.25$ and 0.5 for the smallest time steps, and for $\alpha=0.7$, 2/3 and 0.6 for $\delta t=400$ Kyr (Fig. 7a and b). Root-mean-square errors (RMS) show that using $\beta=0$ gives results that are slightly more accurate than $\beta=1$ for these tests.

3.3. Rayleigh–Taylor instability test

Rayleigh–Taylor instability tests with $\alpha=1$, 0.75, 0.7, 2/3, 0.6, 0.5 and 0.25, and $\beta=1$ and 0 for $\delta t=10$ and 20 Kyr, show similar results to that of decaying-sinusoidal surface topography. Both $\delta t=10$ and 20 Kyr lead to an instability without FSSA stabilization. Even with FSSA, the free surface becomes unstable for $\alpha=0.25$ when $\delta t=10$ Kyr, and for $\alpha=0.25$ and 0.5 when $\delta t=20$ Kyr. Again, results indicate a better accuracy for a 10 Kyr time step with $\alpha=0.5$, while $\alpha=0.6$ produces the most accurate results followed by $\alpha=2/3$ (Fig. 7c and d) for larger time steps. Topographies calculated with $\beta=0$ and 1 do not differ significantly from each other. The RMS error with respect to the 100 yr non-FSSA reference solution shows that the calculations done with $\beta=0$ are again slightly more accurate than those calculated with $\beta=1$ (Fig. 7c and d).

Table 2
Topographical RMS differences between tests with different small δt and α, after 1 Myr. Note that the differences are smaller than the ones shown in Fig. 7, that compares larger time steps with a reference of $\delta t = 100$ yr and $\alpha = 0$.

Small δt comparisons	$(\delta t_{100}\alpha_0 - \delta t_{100}\alpha_{0.5})$ [m]	$(\delta t_{200}\alpha_0 - \delta t_{100}\alpha_0)$ [m]	$(\delta t_{200}\alpha_{0.5} - \delta t_{100}\alpha_{0.5})$ [m]
Decaying-half-sinusoid relief	7.196×10^{-3}	7.195×10^{-3}	5.746×10^{-7}
50th-harmonic-sinusoidal relief	8.595×10^{-2}	1.133×10^{-1}	7.503×10^{-2}
Rayleigh–Taylor instability	5.040×10^{-3}	4.177×10^{-4}	9.159×10^{-3}
Steep-slope	3.198×10^{-3}	3.241×10^{-3}	1.927×10^{-3}

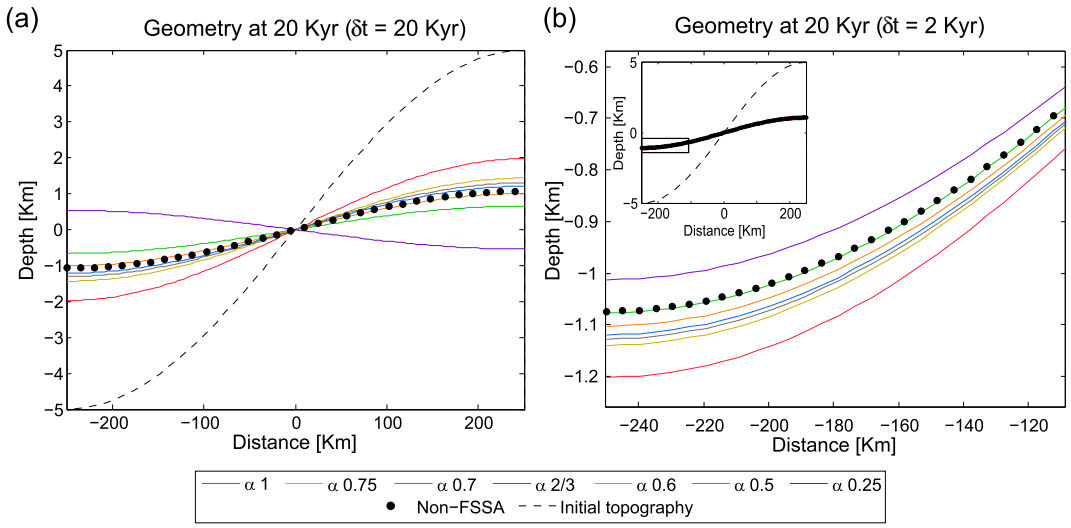

Fig. 5. Topographies generated after 20 Kyr, calculated with (a) a time step of 20 Kyr and (b) a time step of 2 Kyr for different α, with $\beta = 1$. (a) The topographies generated for different choices of α after the first 20 Kyr time step show remarkable differences from one to another; $\alpha = 0.25$ leads to instability since the topography is inverted after a single step, with $\alpha = 0.6$ and 2/3 calculations yield the most accurate results. $\alpha = 0.6$ is more likely than higher values to trigger instability in future steps, since it results into an small overestimate of the surface displacement. (b) The topographies generated with the more stable FSSA approximation and a ten-fold smaller time step differ by less than 200 m from one to another. The most accurate results for small time-steps are obtained with $\alpha = 0.5$.

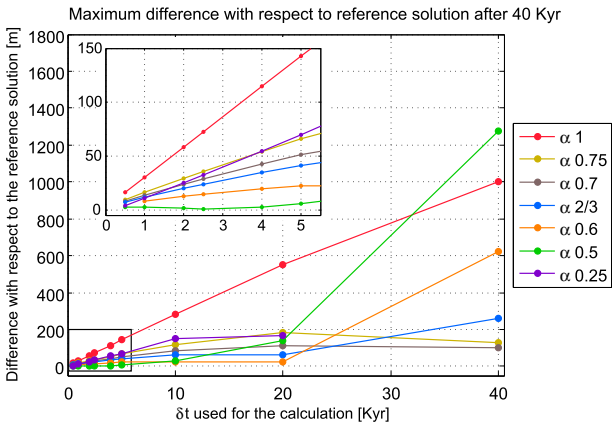

Fig. 6. Maximum absolute differences between the topography calculated for FSSA approximations with different α and δt, and the topography calculated with a very small $\delta t = 100$ yr using no FSSA. $\alpha = 0.5$ is most accurate for smaller time steps where the method is numerically stabler, while $\alpha = 0.7$, 2/3 and 0.6 are more accurate for larger time steps that result numerical instabilities in experiments without FSSA stabilization ($\delta t > 14$ Kyr).

3.4. Steep-slope test

The steep-slope test has been run for $\delta t = 20$ Kyr with $\alpha = 1$, 0.75, 0.7, 2/3, 0.6, 0.5 and 0.25 and $\beta = 1$ and 0. Calculations done with $\alpha = 0.5$, 0.6 and 2/3 result in the most accurate outcomes (Fig. 8a). Fig. 7e shows that $\alpha = 2/3$ gives better results after 6 Myr, whereas $\beta = 0$ gives the most accurate results for the first 12 Myr while $\beta = 1$ gives the most accurate results after 14 Myr of surface evolution.

4. Discussion

As mentioned above, our formulation differs conceptually from that previously presented by Kaus et al. (2010). They also applied an implicit penalizing load to the stiffness matrix, but did this using the surface traction terms derived from the time discretization of the momentum equation, which translated into using a normal-to-the-surface velocity vector $(v_x n_x, v_y n_y)$ instead of out 'Eulerian' approach using velocity directions at the node (Fig. 2). Their equivalent penalizing terms $k^{yx}_{K^{ij}}$ and $k^{yy}_{K^{ij}}$ can be defined as:

$$k^{yx}_{K^{ij}} = n_x \rho g \alpha_K \delta t \int_S N_i N_j dS, \tag{27}$$

$$k^{yy}_{K^{ij}} = n_y \rho g \alpha_K \delta t \int_S N_i N_j dS, \tag{28}$$

where α_K is their FSSA controlling factor, for which they showed 0.5 is the optimal value among 0, 0.5 and 1 (Kaus et al., 2010). Their algorithm is formulated to be applied at every element boundary, while we apply it only at the free surface. Their penalization terms cancel out between elements of equal densities, so the penalization is only effective at the free surface or at interfaces where changes in density occur. This results in better estimates for multilayer models even if free slip is imposed at the surface. Since only one of our tests was multilayered, we chose to apply the stabilization algorithm only at the surface, but it too would be easy to implement at internal density interfaces, but not as a general correction for all

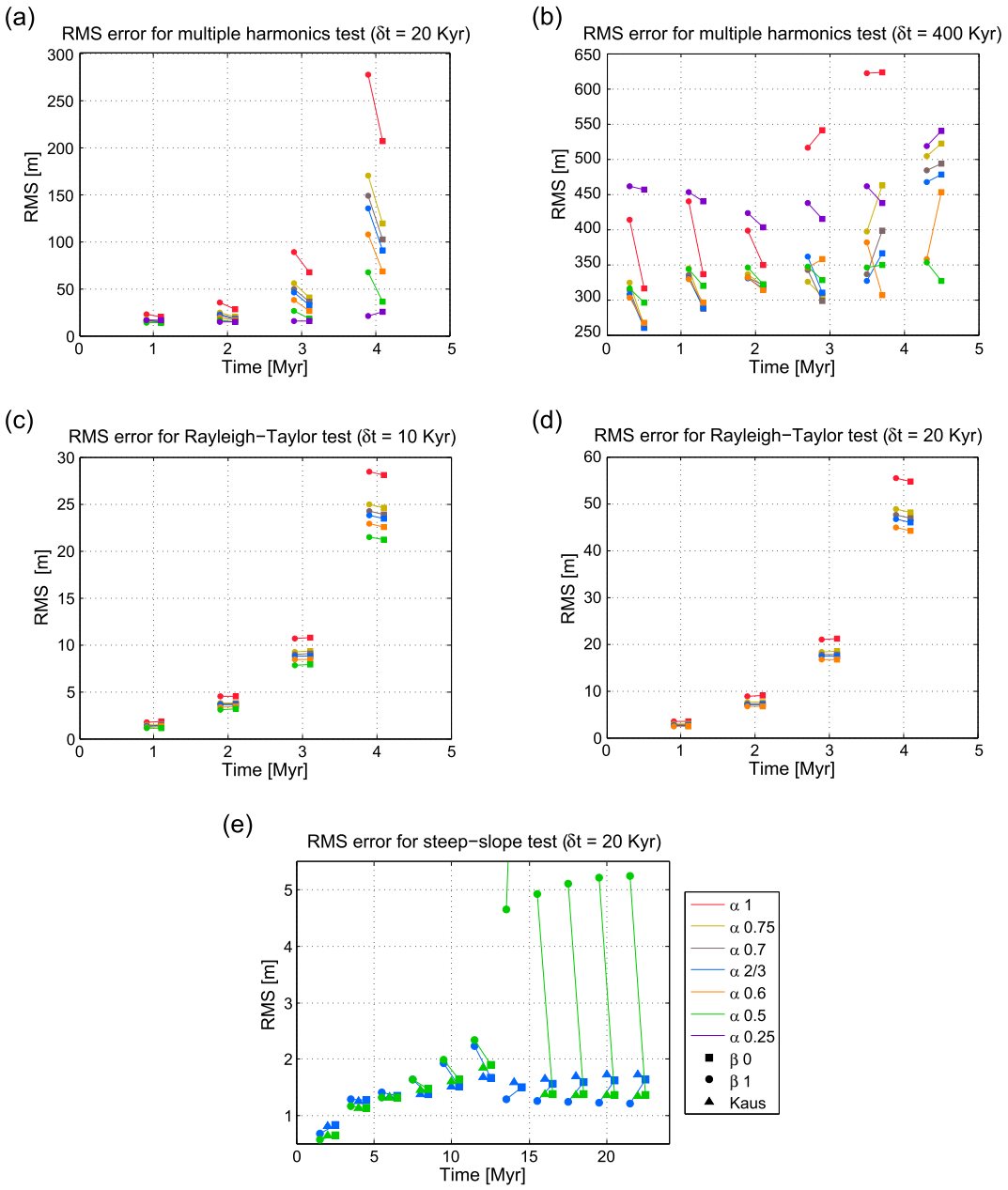

Fig. 7. Root-mean-square errors obtained from the difference between the topographies calculated with FSSAs for various α and β, and the non-FSSA reference solution calculated using $\delta t = 100$ yr for: (a) and (b) decaying 50th-harmonic sinusoidal relief for $\delta t = 20$ and 400 Kyr respectively, (c) and (d) the Rayleigh–Taylor instability test for $\delta t = 10$ and 20 Kyr respectively, and (e) the steep-slope test for $\delta t = 20$ Kyr. RMS differences for $\alpha = 0.25$ for (c) and $\alpha = 0.25$ and 0.5 for (d) are not plotted because these tests result in an unstable numerical solution.

elements. Assuming that the slope of the surface can be defined as $\frac{\partial h}{\partial x} = -\frac{n_x}{n_y}$, then their formulation is equivalent to ours (Eqs. (24) and (25)) multiplied by n_y. In order to improve the performance of their algorithm, they assumed $n_x \approx 0$, as is true for small slopes. In this case, $k^{yx}_{k^{ij}} = 0$ and the resulting penalized stiffness matrix is symmetric. However, processes that typically transform topography, such as erosion and faulting, can produce steep-enough slopes for models to require the horizontal term to increase numerical stability.

We also included Kaus et al. (2010) FSSA into our tests for comparison, and to test for the 'best practice' values for α_K. We ran the same tests as for our FSSA, with $\alpha_K = 1$, 0.75, 0.7, 2/3, 0.6, 0.5 and 0.25. The results show that $\alpha_K = 0.5$ produces the most accurate solutions for smaller time steps, while $\alpha_K = 1$ produces the most stable solutions, as suggested by Kaus et al. (2010). However, for the decaying-sinusoidal topography and Rayleigh–Taylor tests, we find that $\alpha = 0.6$ and 2/3 are the best for accuracy with their approach when using time steps bigger than the maximum stable time step for a non-FSSA approach. Except for the steep-slope test (Fig. 7e) where our algorithm produces slightly more accurate results for the $\delta t = 20$ Kyr test after 14 Myr of time-run for $\alpha = 2/3$ and both $\beta = 1$ and 0 (being $\beta = 1$ results the most accurate), there are no major differences between the results produced with the Kaus et al. (2010) FSSA and our FSSA in accuracy.

Based on the results of these tests, we suggest that for large FSSA-stabilized time steps, one should use $\alpha = 2/3$ for 'best practice' results (best accuracy and stability together) for both our and Kaus et al. (2010) algorithms. Note that a 2/3 value would be obtained for a standard finite-element Galerkin discretization in time with linear shape functions in time, as opposed to a standard

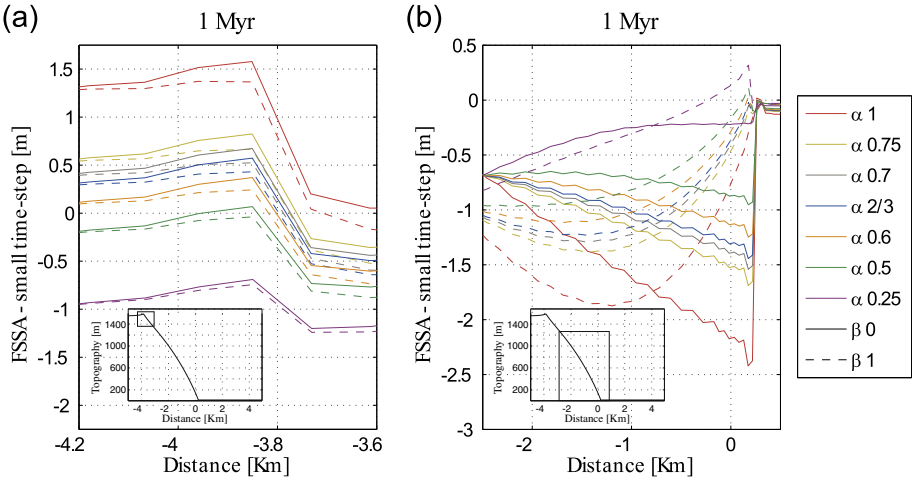

Fig. 8. Steep-slope relief differences between topographies calculated with FSSA methods using different α and β parameters and $\delta t = 20$ Kyr and a reference non-FSSA solution with a 100 yr time step during a 1 Myr time run. Note that for the upper topographic inflexion (a) the tests $\alpha = 0.5$, 0.6 and 2/3, and $\beta = 0$ and 1 are more accurate. Note also that $\beta = 1$ tests for any α results in more accurate topographies at the end of the slope (b), where the horizontal velocities are bigger.

finite-difference approximation in time that is normally used. The finite-element-like Galerkin time-discretization results in a factor of 2/3 that multiplies the unknown at the end of the time step, while the factor obtained from a finite-difference Crank–Nicolson formulation (less stable but theoretically more accurate at smaller time steps) is 1/2. Applying a Galerkin discretization in time using linear shape functions $M(t)$ in Eq. (20), following the scheme described in Warzee (1974), one obtains:

$$\int_{time} M_s \left[K \sum_{u=0}^{r} M_v v_u - \delta t A \sum_{u=0}^{r} M_u v_u - F(t) \right] dt = 0, \tag{29}$$

where $\delta t A \sum M_u v_u$ is equivalent to the penalization term $F_{FS}, A_{ij} = -\rho g \left(\frac{\delta h}{\delta x}\right) \int_S N_i N_j dS$ for the horizontal penalization term, and $A_{ij} = \rho g \int_S N_i N_j dx$ for the vertical penalization term. Integrating through a time step δt:

$$K\left(\frac{1}{3}u_0 + \frac{2}{3}u_1\right) - \delta t A\left(\frac{1}{3}v_0 + \frac{2}{3}v_1\right) - \left(\frac{1}{3}F_0 + \frac{2}{3}F_1\right) = 0, \tag{30}$$

where the subindexes 0 and 1 indicate whether the variables are calculated for the beginning or the end of the time step, respectively. Therefore, 2/3 would also be the parameter for the Galerkin time discretization of our stabilization term, coinciding with the 'best practice' α found in our numerical tests.

Results often show worse RMS errors with the penalized horizontal stabilization term ($\beta = 1$) than without it ($\beta = 0$) (Fig. 7). This can be anticipated since $\beta = 1$ introduces an additional load at the top of the surface (as well as $\alpha > 0$), which for cases where the time step is small and/or the surface is stable implies that the error could be increased in the calculations as a byproduct of greater stability. However, for $\alpha = 2/3, \beta = 1$ gives smaller RMS at the last stages of the multiple harmonics test with $\delta t = 400$ Kyr (Fig. 7b), and the last stages of the steep-slope test for $\delta t = 20$ Kyr (Fig. 7e). This two tests produce the highest surface horizontal displacements from the set of tests we run and, therefore we conclude that, for near-optimal α, $\beta = 1$ can improve the accuracy of models that have a tendency for lateral instability.

In order to study stability of the different FSSAs these tests were pushed to values of δt for which they become numerically unstable with $\alpha = \alpha_K = 0.5$ and 2/3 (Table 3). Results show that both our and the Kaus et al. (2010) algorithms can be used for a time step at least 2 times bigger than the maximum for a non-FSSA test for the worst-case decaying half-sinusoid and steep-slope tests, and at least one order of magnitude more than the non-FSSA for the other situations. $\alpha = \alpha_K = 2/3$ allows bigger time steps than $\alpha = \alpha_K = 0.5$, except for the 50th-harmonic sinusoid test. There are no major differences in the maximum time step, independent

Table 3
Stability tests. δt represents the time step from which the different tests start to be unstable or having mesh problems, t_b is the run time for which the tests break, and the capital letters indicate the way the tests fail, where DS stands for 'drunken sailor' instability, SIS for the self-intersecting surface artefact instability (Fig. 4) and MESH for an artefact in which inner nodes become displaced outside of the border of the evolving Lagrangian mesh.

Test	Total run-time interval	Non-FSSA (max δt)	Kaus $\alpha_K = 0.5$	Kaus $\alpha_K = 2/3$	$\alpha = 0.5$ $\beta = 0$	$\alpha = 2/3$ $\beta = 0$	$\alpha = 2/3$ $\beta = 0.5$	$\alpha = 2/3$ $\beta = 1$
Decaying-half-sinusoid relief	5 Myr	DS δt 14 Kyr t_b 14 Kyr	DS δt 27 Kyr t_b 27 Kyr	DS δt 40 Kyr t_b 40 Kyr	DS δt 27 Kyr t_b 27 Kyr	DS δt 40 Kyr t_b 40 Kyr	DS δt 40 Kyr t_b 40 Kyr	DS δt 40 Kyr t_b 40 Kyr
50th-harmonic-sinusoidal relief	20 Myr	DS δt 30 Kyr t_b 1.11 Kyr	SIS δt 620 Kyr t_b 19.84 Kyr	SIS δt 570 Kyr t_b 18.81 Kyr	SIS δt 610 Kyr t_b 19.52 Kyr	SIS δt 510 Kyr t_b 18.87 Kyr	SIS δt 500 Kyr t_b 19 Kyr	SIS δt 500 Kyr t_b 19 Kyr
Rayleigh–Taylor instability	7 Myr	DS δt 5 Kyr t_b 50 Kyr	DS δt 16 Kyr t_b 720 Kyr	DS δt 35 Kyr t_b 525 Kyr	DS δt 16 Kyr t_b 752 Kyr	DS δt 35 Kyr t_b 525 Kyr	DS δt 35 Kyr t_b 525 Kyr	DS δt 35 Kyr t_b 525 Kyr
Steep-slope	100 Myr	MESH δt 2.7 Kyr t_b 5.4 Kyr	MESH δt 4.7 Kyr t_b 9.4 Kyr	MESH δt 5.6 Kyr t_b 11.2 Kyr	MESH δt 4.7 Kyr t_b 9.4 Kyr	MESH δt 5.6 Kyr t_b 11.2 Kyr	MESH δt 5.9 Kyr t_b 11.8 Kyr	SIS δt 4.3 Kyr t_b 12.9 Kyr

of the FSSA or choice of β parameter for the decaying-half-sinusoid and Rayleigh–Taylor instability tests. However, the Kaus et al. (2010) FSSA allows a slightly bigger time step (570 Kyr in contrast to 510 Kyr) for the decaying 50th-harmonic sinusoid test for $\alpha = 2/3$, without inducing a self-intersecting surface artefacts, while our FSSA results into the maximum time step without meshing problems (5.9 Myr in contrast to 5.6 Myr) for $\beta = 0.5$, and the worse results (4.3 Myr) for $\beta = 1$.

In order to solve the asymmetric system our FSSA combines Cholesky factorization with Uzawa-like iterations, as previously explained. In order to converge, the FSSA with the vertical and horizontal penalty terms needs ~5 times more 'backsolve' operations than the vertical-only penalized form. We expect that for different resolutions than the ones used here, and even for 3D, the number of backsolve operations needed for convergence would vary little for similar viscosities since the convergence of Uzawa-like iterations only weakly depends on the number of unknowns (Zienkiewicz et al., 1985). Consequently, the solver for the asymmetric system is spending approximately 5 times more 'backsolve' operations than the one for the symmetric system. However, the performance is still good in contrast with a solver that applies LU factorization, since LU can spend more than 100 times the computing-time (for the given resolution) than the forward Cholesky factorization, which is the most time-intensive portion of the Cholesky forward-backsolve solution process.

The algorithm presented here is formulated and tested for finite element discretization. However, many experiments within the modelling community are done with staggered finite difference codes. These models also suffer from free surface instabilities (Duretz et al., 2011), so a free-surface stabilization algorithm is also required. A generalized formulation of our FSSA is obtained by applying a body force penalization term to Eq. (1) at the surface (and/or density interfaces) cells:

$$\frac{\partial \tau_{ij}}{\partial x_j} - \frac{\partial P}{\partial x_i} = -\rho g_i + F_{FS}, \tag{31}$$

where

$$F_{FS} = \frac{\delta \rho}{\delta y} g_y \alpha \delta t \left(-\beta \frac{\delta \bar{h}}{\delta x} v_x + v_y \right), \tag{32}$$

where $\frac{\delta \rho}{\delta y}$ is the vertical density change across the free surface or density interface. This generalized formulation of our FSSA can be implemented in finite difference codes.

Here, we have demonstrated that: (1) the damping factor $\alpha = 2/3$ works best in the limit of maximum stable time steps both for Kaus et al. (2010) and our FSSAs, and (2) the horizontal term of the stabilization algorithm is not necessary for steep slopes (up to 30°), meaning that Kaus et al. (2010) approach, where the horizontal term is neglected, is a good approach since it still makes little practical difference to include the horizontal term for extreme topographies. We also present an operator-split method for implementing the horizontal term that retains symmetric stiffness matrix, in case readers do wish to economically use this approach for very steep slopes. Future work to be addressed in a follow-up paper would include: (1) a more exhaustive examination of the relative performance (CPU time versus accuracy and stability) of proposed free-surface stabilization algorithms; (2) a study of the stability radius for the semi-implicit time integrators; and (3) comparison with additional methods of free surface stabilization such as the implicit algorithm proposed by Kramer et al. (2012) or methods in which the surface is updated during every strain iteration of a non-Newtonian solution so that instabilities are mitigated without need for an explicit stabilization algorithm (i.e. Popov and Sobolev (2008)).

5. Conclusions

Numerical flow models with free surfaces need a free-surface stabilization algorithm (FSSA) in order to be stable at relatively large time steps ($\geqslant$10 Kyr) that allow for a reasonably small compute time. We have developed a FSSA algorithm which adds to the mechanical system a load calculated implicitly from a portion of the difference in surface relief between the beginning and end of a time step. This FSSA allows time steps 2–20 times larger than the free surface models without stabilization, and produces accurate results ($< 1\%$ relative error) for the viscosities and time steps used in these tests. The magnitude of the additional implicit surface load during a time step is controlled by parameters α and β, where α corresponds to the total controlling factor of the load (with values between 0 and 1), which β controls only the horizontal term of the load (with values also between 0 and 1). In addition, we have implemented an Uzawa-like iteration in this algorithm that allows us to solve the asymmetric system resulting from $\beta = 1$ in compute time comparable to that for the symmetric solution with $\beta = 0$.

Different viscous experiments were carried out in order to numerically assess the 'best-practice' values for α and β. For time steps close to the stability limit for models without a FSSA, $\alpha = 0.5$ results in the most accurate free surface approximation, while for time steps larger than those stable in models without a FSSA, $\alpha = 2/3$ is found to be the best option for both our FSSA and the FSSA described by Kaus et al. (2010), because it generally yields the most accurate and stable results.

Including the horizontal term in our FSSA ($\beta = 1$) gives generally slightly less accurate results than omitting it ($\beta = 0$), except for the steep-slope test after several million years. The maximum time steps achieved with stability for our and the Kaus et al. (2010) FSSAs are very similar for all tests explored here. Although the multiple-harmonic topography test and the steep-slope test never become unstable before they experience mesh- deformation -related problems in our Lagrangian tests, the Kaus et al. (2010) algorithm allows slightly bigger time steps without mesh-deformation-related problems for the 50th-harmonic -sinusoidal relief test, while our algorithm with $\beta = 0.5$ allows the use of slightly larger time steps for the steep-slope test. Although our FSSA with $\beta = 1$ should intuitively give more stable results for steep slopes than the FSSAs without the horizontal stabilization term, as it is, in theory, a more complete approximation, our tests did not demonstrate a significant improvement over FSSA approximations with $\beta = 0$. We did see that it leads to more accurate results for the latest stages of the relaxation of a initial steep-slope, with only a minor increase in computational time with respect to FSSA methods that neglect this additional term. Our final recommendation: use FSSA, with $\alpha = 2/3$.

Acknowledgments

We would like to acknowledge Dave May and Boris Kaus for very exhaustive and constructive reviews, which have greatly improved the quality of this manuscript. We also thank Royal Holloway University for supporting this research through a Reid Scholarship.

Appendix A. Supplementary material

Supplementary data associated with this article can be found, in the online version, at http://dx.doi.org/10.1016/j.pepi.2015.07.003.

References

Anderson, R.N., McKenzie, D., Sclater, J.G., 1973. Gravity, bathymetry and convection in the earth. Earth Planet. Sci. Lett., 18 http://dx.doi.org/10.1016/0012-821X(73)90095-2.

Beaumont, C., Jamieson, R., Nguyen, M., Lee, B., 2001. Himalayan tectonics explained by extrusion of a low-viscosity crustal channel coupled to focused surface denudation. Nature 414, 738–742. http://dx.doi.org/10.1038/414738a.

Braun, J., 2006. Recent advances and current problems in modelling surface processes and their interaction with crustal deformation. Geol. Soc. Lond. Spec. Publ. 253, 307–325.

Braun, J., 2010. The many surface expressions of mantle dynamics. Nat. Geosci. 3, 825–833.

Crameri, F., Schmeling, H., Golabek, G.J., Duretz, T., Orendt, R., Buiter, S.J.H., May, D.A., Kaus, B.J.P., Gerya, T.V., Tackley, P.J., 2012. A comparison of numerical surface topography calculations in geodynamic modelling: an evaluation of the sticky air method. Geophys. J. Int., 189 http://dx.doi.org/10.1111/j.1365-246X.2012.05388.x.

Crouzeix, M., Raviart, P.A., 1973. Conforming and nonconforming finite element methods for solving the stationary stokes equations I. Reveu française d'automatique, informatique, recherche opérationnelle Mathématique tome 7, 33–75.

Dabrowski, M., Krotkiewski, M., Schmid, D.W., 2008. Milamin: matlab-based finite element method solver for large problems. Geochem. Geophys. Geosyst., 9

De Bremaecker, J., 1976. Relief and gravity anomalies over a convecting mantle. Geophys. J. Int. 45, 349–356. http://dx.doi.org/10.1111/j.1365-246X.1976.tb00330.x.

Duretz, T., May, D.A., Gerya, T.V., Tackley, P.J., 2011. Discretization errors and free surface stabilization in the finite difference and marker-in-cell method for applied geodynamics: a numerical study. Geochem. Geophys. Geosyst. 12. http://dx.doi.org/10.1029/2011GC003567, n/a–n/a.

Finnegan, N.J., Hallet, B., Montgomery, D.R., Zeitler, P.K., Stone, J.O., Anders, A.M., Yuping, L., 2008. Coupling of rock uplift and river incision in the namche Barwa–Gyala peri massif, tibet. Geol. Soc. Am. Bull., 120 http://dx.doi.org/10.1130/B26224.1.

Fleitout, L., Froidevaux, C., Yuen, D., 1986. Active lithospheric thinning. Tectonophysics, 132. http://dx.doi.org/10.1016/0040-1951(86)90037-5.

Gerya, T.V., Yuen, D.A., 2003. Rayleigh–Taylor instabilities from hydration and melting propel cold plumes at subduction zones. Earth Planet. Sci. Lett. 212, 47–62. http://dx.doi.org/10.1016/S0012-821X(03)00265-6.

Hager, B.H., Clayton, R.W., Richards, M.A., Comer, R.P., Dziewonski, A.M., 1985. Lower mantle heterogeneity, dynamic topography and the geoid. Nature 313, 541–545.

Harlow, F., Shannon, J., Welch, J., 1965. Liquid waves by computer. Science (New York, NY) 149, 1092–1093. http://dx.doi.org/10.1126/science.149.3688.1092.

Hughes, T.J.R., 2000. The Finite Element Method: Linear Static and Dynamic Finite Element Analysis. Dover Publications, Mineola, NY, ID: 301049178.

Kaus, B.J., Mühlhaus, H., May, D.A., 2010. A stabilization algorithm for geodynamic numerical simulations with a free surface. Phys. Earth Planet. Inter., 181 http://dx.doi.org/10.1016/j.pepi.2010.04.007.

Koons, P.O., 2002. Mechanical links between erosion and metamorphism in Nanga Parbat, Pakistan Himalaya. Am. J. Sci., 302 http://dx.doi.org/10.2475/ajs.302.9.749.

Kramer, S.C., Wilson, C.R., Davies, D.R., 2012. An implicit free surface algorithm for geodynamical simulations. Phys. Earth Planet. Inter. 194195, 25–37. http://dx.doi.org/10.1016/j.pepi.2012.01.001.

McKenzie, D., 1977. Surface deformation, gravity anomalies and convection. Geophys. J. Roy. Astron. Soc. 48, 211–238.

Melosh, H.J., Raefsky, A., 1980. The dynamical origin of subduction zone topography. Geophys. J. Roy. Astron. Soc. 60, 333–354.

Poliakov, A., Podladchikov, Y., 1992. Diapirism and topography. Geophys. J. Int., 109 http://dx.doi.org/10.1111/j.1365-246X.1992.tb00117.x.

Popov, A., Sobolev, S., 2008. SLIM3D: a tool for three-dimensional thermomechanical modeling of lithospheric deformation with elasto-visco-plastic rheology. Phys. Earth Planet. Inter., 171 http://dx.doi.org/10.1016/j.pepi.2008.03.007.

Ruddiman, W.F., Kutzbach, J.E., 1989. Forcing of late cenozoic northern hemisphere climate by plateau uplift in southern asia and the american west. J. Geophys. Res., 94 http://dx.doi.org/10.1029/JD094iD15p18409.

Shewchuk, J., 1996. Triangle: engineering a 2D quality mesh generator and Delaunay triangulator. In: Lin, M., Manocha, D. (Eds.), Applied Computational Geometry Towards Geometric Engineering, Lect. Notes Comput. Sci., vol. 1148. Springer, Berlin, Heidelberg, pp. 203–222. http://dx.doi.org/10.1007/BFb0014497.

Turcotte, D., Schubert, G., 1982. Geodynamics. John Wiley & Sons.

Warzee, G., 1974. Finite element analysis of transient heat conduction application of the weighted residual process. Comput. Meth. Appl. Mech. Eng., 3 http://dx.doi.org/10.1016/0045-7825(74)90028-0.

Willett, S.D., 1999. Orogeny and orography: the effects of erosion on the structure of mountain belts. J. Geophys. Res., 104 http://dx.doi.org/10.1029/1999JB900248.

Zaleski, S., Julien, P., 1990. Numerical simulation of salt diapir formation in small and extended geometries. Report, Total-Compagnie Francaise des Petroles.

Zhong, S., Gurnis, M., Hulbert, G., 1993. Accurate determination of surface normal stress in viscous flow from a consistent boundary flux method. Phys. Earth Planet. Inter. 78, 1–8.

Zhong, S., Gurnis, M., Moresi, L., 1996. Free-surface formulation of mantle convection-i, basic theory and application to plumes. Geophys. J. Int. 127, 708–718.

Zienkiewicz, O., Vilotte, J., Toyoshima, S., 1985. Iterative method for constrained and mixed approximation. an inexpensive improvement of FEM performance.

1 Annexe

Listing 1: Example of Matlab source-code lines where k_{ij}^{yx} and k_{ij}^{yy} are built (Eqs. 20 and 21). Ax_fse and Ay_fse correspond to the integration terms of k_{ij}^{yx} and k_{ij}^{yy} respectively, $nnode\_el\_fs$ is the number of surface nodes per element, nip_fs number of integration points for the surface problem, N_fs shape functions, Ipw_fs weight functions for the integration, Dx_e is the total length of the triangular element (since every triangular element consist of 2 surface elements $dS = Dx\_e/2$), Ax_fse_col and Ay_fse_col are the k_{ij}^{yx} and k_{ij}^{yy}, inc_rho is the density contrast (ρ), $G(2)$ the gravity (g), $alpha$ and $beta$ the control parameters (α and β), $dhdx$ the slope ($\partial h/\partial x$), and dt the time step. Symbol $'$ in Matlab is the command to calculate the transpose of the preceding matrix. Note that the integration terms of Eqs. 20 and 21 are written in the form $A_{ij} = \int_S N_i N_j dS$ which is equivalent to the matricial form $A = \int_S N \cdot N^T dS$.

```
% Initialize the matrices for the penalization of A
Ax_fse = zeros(nnod_el_fs,nnod_el_fs);
Ay_fse = zeros(nnod_el_fs,nnod_el_fs);

for ip_fs = 1:nip_fs % Integration loop
    Ax_fse = Ax_fse + N_fs{ip_fs}*N_fs{ip_fs}'*...
        Ipw_fs(ip_fs)*Dx_e(i)/2; % Ni*Nj*w*dx
    Ay_fse = Ay_fse + N_fs{ip_fs}*N_fs{ip_fs}'*...
        Ipw_fs(ip_fs)*Dx_e(i)/2; % Ni*Nj*w*dx
end

Ax_fse_col = Ax_fse(:)*inc_rho(i)*G(2)*alpha*beta*-(dhdx
    )*dt;
    % Afs for x = inc_density*g*beta*dhdx*dt*integral(Ni
        *Nj*dx)
Ay_fse_col = Ay_fse(:)*inc_rho(i)*G(2)*alpha*dt;
    % Afs for y = inc_density*g*alpha*dt*integral(Ni*Nj*
        dx)
```

Chapter 4

Passive margin asymmetry and its polarity in the presence of a craton

M. Andrés-Martínez, M. Pérez-Gussinyé, M. Neto-Araujo, and J. P. Morgan. Passive margin asymmetry in the presence of a craton. *Planned for submission to Nature Geosciences*, 2016b

Authors contribution

MP, MN, and MA designed the research. MA programmed the GMT codes to generate the maps and to measure and plot margin widths and distances to the craton, in discussion with MP. MA developed the numerical geodynamic code in discussion with MP and JM. MA designed the tests and analysed the results in discussion with MP and JM. MA wrote the manuscript in collaboration with MP. JM reviewed the manuscript.

Passive margin asymmetry and its polarity in the presence of a craton

Miguel Andrés-Martínez[a,*], Marta Pérez-Gussinyé[a,b,c,**], Mario Neto-Araujo[d], Jason Phipps Morgan[a,**]

[a] *Royal Holloway University of London, Earth Sciences*
[b] *MARUM - Center for Marine Enviromental Sciences*
[c] *Bremen University, Geosciences*
[d] *PETROBRAS*

Abstract

When continental lithosphere is extended to break-up it forms two conjugate passive margins. In many instances these margins are asymmetric: while one is wide and extensively faulted, the conjugate thins more abruptly and exhibits little faulting. Recent observational studies have suggested that this asymmetry results from the formation of an oceanward-younging sequential normal fault array on the future wide margin. Numerical models have shown that fault sequentiality arises as a result of asymmetric uplift of the hot mantle towards the hanging wall of the active fault, which weakens this area and promotes the formation of a new oceanward fault. In numerical models the polarity of the asymmetry is random. It results from spontaneous preferential localization of strain in a given fault, a process reinforced by strain weakening effects. Slight changes in the experiments initial grid result in an opposite polarity of the asymmetry. However, along a long stretch of the South Atlantic margins, from the Camamu-Gabon to the North Santos-South Kwanza conjugates, the polarity is not random and is very well correlated with the distance of the rift to nearby cratons. Here, we use numerical experiments to show that the presence of a thick cratonic root inhibits asthenospheric flow from underneath the craton towards the adjacent fold belt, while flow from underneath the fold belt towards the craton is favoured. This enhances and promotes sequential faulting towards the craton and results in a wide faulted margin located in the fold belt and a narrow conjugate margin in the craton side, thereby determining the polarity of the asymmetry, as observed in nature.

Keywords: rifting, margin architecture, cratons, numerical modelling

Magma poor rifted margins present a wide variety of architectures and geometries from the relatively narrow Newfoundland-Iberia asymmetric conjugates (∼150 Km wide), to the hyper-extended margins of the central South Atlantic where conjugate margin width may span 1000 Km (e.g. North Santos-South Kwanza). Along the magma-poor region of the South Atlantic (Blaich et al., 2011), where extension was perpendicular to the margin (Davison, 1997; Meisling et al., 2001), the degree of asymmetry as well as margin width varies substantially (Fig. 1). To the North, in the Camamu-Gabon sector, the conjugate margins are asymmetric. The Brazilian Camamu conjugate, located close to the onshore San Francisco craton, is much narrower than the Gabon one. In the central sector, the Campos-Kwanza conjugates are fairly symmetric. Here, both

*Principal corresponding author
**Corresponding authors
Email addresses: m.andres-martinez.2011@live.rhul.ac.uk (Miguel Andrés-Martínez), marta.perez-gussinye@rhul.ac.uk (Marta Pérez-Gussinyé), marioaraujo@petrobras.com.br (Mario Neto-Araujo), jason.morgan@rhul.ac.uk (Jason Phipps Morgan)

margins developed far away from cratons. Southwards, the North Santos margin is much wider than its conjugate the South Kwanza, which developed offshore of the Congo craton. Thus, margin width and the proximity to a craton at the time of break-up are clearly correlated (Fig. 1). Where the rift developed close to a craton, the margin closer to the craton is narrow, while the opposite margin is wider.

Figure 1: **Width of Central South Atlantic conjugate margins and distance from the edge of the margin to the cratons.**

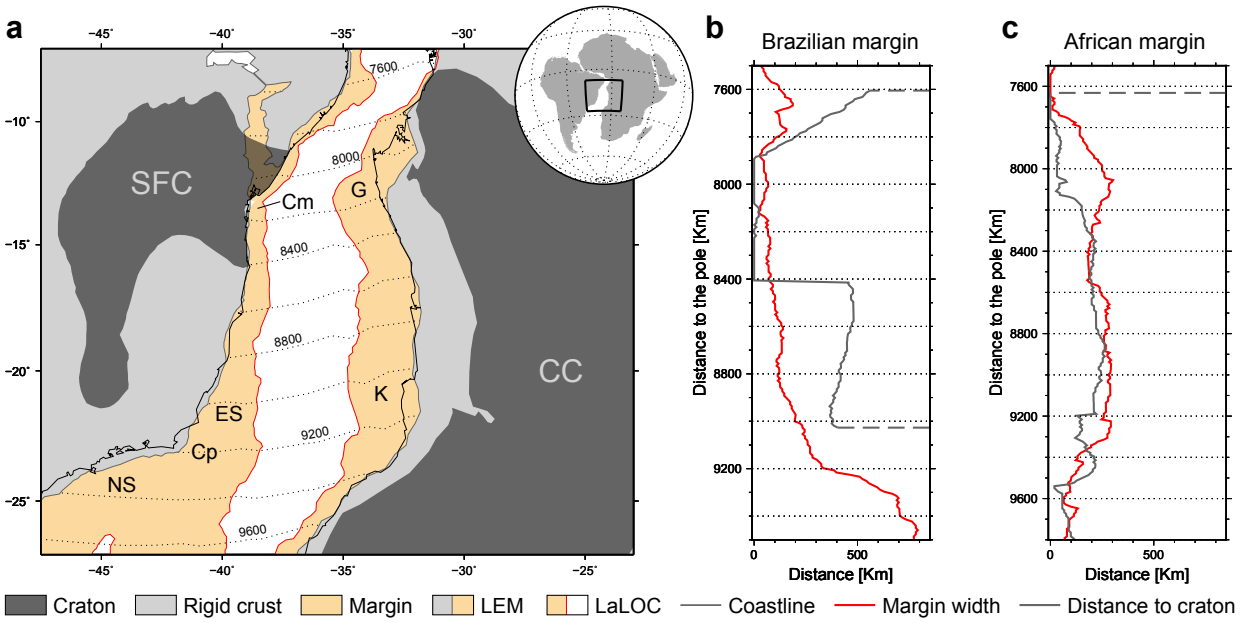

Figure 1: **a**, Map of the central sector of the South Atlantic conjugate margins using Pérez-Díaz and Eagles, 2014 reconstruction at 106 Myr. Dots represent flowlines which labels are distance in km to the Central-Africa respect South-America rotation pole from 106 Myr to present. SFC—Sao Francisco Craton, CC—Congo Craton, Cm—Camumu, ES—Espirito Santo, Cp—Campos, NS—North of Santos, G—Gabon, K—Kwanza basins. Rigid crust (light grey) as crust not deformed by rifting, and landward limit of the oceanic crust (LaLOC) from Heine et al., 2013. Note that the further the craton to the landward edge of the margin (LEM), the wider the margin. **b**, **c**, Margin width (red lines) and distance from the craton to the LEM measured along flowlines Pérez-Díaz and Eagles, 2014 model. At the Brazilian margin, **b**, where Sao Francisco craton is by the coast the margin is very narrow (<50 km), while southwards the craton is far from the LEM and the margin is wider. North of Sao Francisco craton the extension is transtensional so we do not evaluate this data. Along the African margin, **c**, there is a clear direct relationship between the width of the margin and the distance from the craton to the LEM.

The mechanisms of asymmetry generation at extensional margins have been long debated. Early observational studies suggested that asymmetry may be generated by large and long-lived detachments faults that may cross-cut through the entire lithosphere from the onset of extension (Wernicke, 1985; Lister and Davis, 1989). Numerous factors have been proven to influence asymmetry such as of crustal rheologies (Kusznir and Park, 1987; Buck, 1991; Buiter et al., 2008; Huismans and Beaumont, 2003), plastic thickness (Lavier and Buck, 2002), strain weakening (Buck and Lavier, 2001; Huismans and Beaumont, 2002), extension velocities (Huismans and Beaumont, 2002; Brune et al., 2014), anisotropic weakness in the mantle due to precursor structures (Tommasi et al., 2009; Hansen et al., 2012), and heterogeneities, both in the crust and mantel lithosphere (Dunbar and Sawyer, 1988; Corti et al., 2003; Nielsen and Hopper, 2004).

Recent studies have suggested that asymmetry formation may be a late stage process during rifting which occurs when a fault direction becomes dominant. This promotes the development of an array of faults that are sequential in time and consistently dip in that dominant direction, thereby generating two asymmetric margins. The margin where sequential faulting occurs becomes the wide margin, and the conjugate is the narrow one (Ranero and Pérez-Gussinyé, 2010; Brune et al., 2014; Pérez-Gussinyé, 2013). Numerical models show that a fault direction becomes dominant when upper crustal faults are strongly coupled to mantle deformation, so that a fault/shear zone penetrating at depth, leads to asymmetric up-welling of the mantle, heating and weakening of the hanging wall of that active fault, where the future fault will occur (Brune et al., 2014). This process feeds back onto itself thereby generating an array of sequential faults that dip consistently in one direction. Sequential faulting occurs as long as there is lower crust that is weak enough to flow into the tip of the active fault, thereby inhibiting mechanical breakup of the crust by faulting. However, a too weak rheology will allow for decoupling of crustal and mantle deformation and consequent symmetric crustal deformation. Hence, asymmetry formation strongly depends on lower crustal viscosity.

Here, we use numerical models to study margin asymmetry related to the presence of cratons. Our models are seeded by a slight temperature increase in the lower crust which dissipates with time (see Methods). This temperature anomaly leads to an initial viscosity decrease in this location, so that the starting deformation pattern are two conjugate shear zones dipping towards the initial weak seed. This initial set up favours symmetry in the absence of viscous strain softening (VSS) as observed in Figure 2a. Half extension velocities of 5 mm/yr are applied at the boundaries of the model. This velocities are in the order of the ones proposed by (Heine et al., 2013) for the South Atlantic central sector, calculated from the 127-140 Ma stage pole for South America relative to a fixed African plate. These velocities are also in the order of the ones estimated for the Southern Sea extension during the formation of the continent ocean transition (Direen et al., 2012).

Our tests show that increasing degrees of VSS (pre-exponential factor ranges from 1 to 15 and 1 to 30, see Methods) lead to increasing margin asymmetry (Fig. 2b and c). This is a consequence of the non-linear character of the VSS which greatly enhances localization of strain at shear zones present at viscous domains such as the lower crust. If one shear zone at the lower crust accommodates slightly more deformation than its conjugate one, weakening will occur faster at the former and eventually it will dominate deformation leading to asymmetry.

However, margin asymmetry does not exclusively depend on the amount of VSS but also on rock type, temperature field, crustal thickness and strain rate. For example, Figures 2c and 2d show that for the same amount of VSS a 40 km thick crust with mafic granulite lower crust will produce asymmetric margins, while a 35 km crust with the same rheology will produce symmetric margins. This is because, a 35 km crust accounts for a stronger viscosity at its base (since the temperature at 35 km is less than at 40 km), so lower crustal flow does not inhibit mechanical breakup of the crust, resulting in two narrow symmetric margins. When the crust is 40 km, the low viscosity at the deep lower crust allows one fault to become dominant and sequential faulting to be triggered. Unfortunately, the exact amount of VSS is not well constrained by observations or laboratory experiments. Here, we use VSS pre-exponential factors varying linearly with the strain from 1 to 30, as for the models in Figures 2c and d, as these are in the order of typically values used in other modelling works (e.g. Huismans and Beaumont, 2003; Warren and Beaumont, 2008; Brune et al., 2012, 2014).

Figure 2: **Numerical experiments**

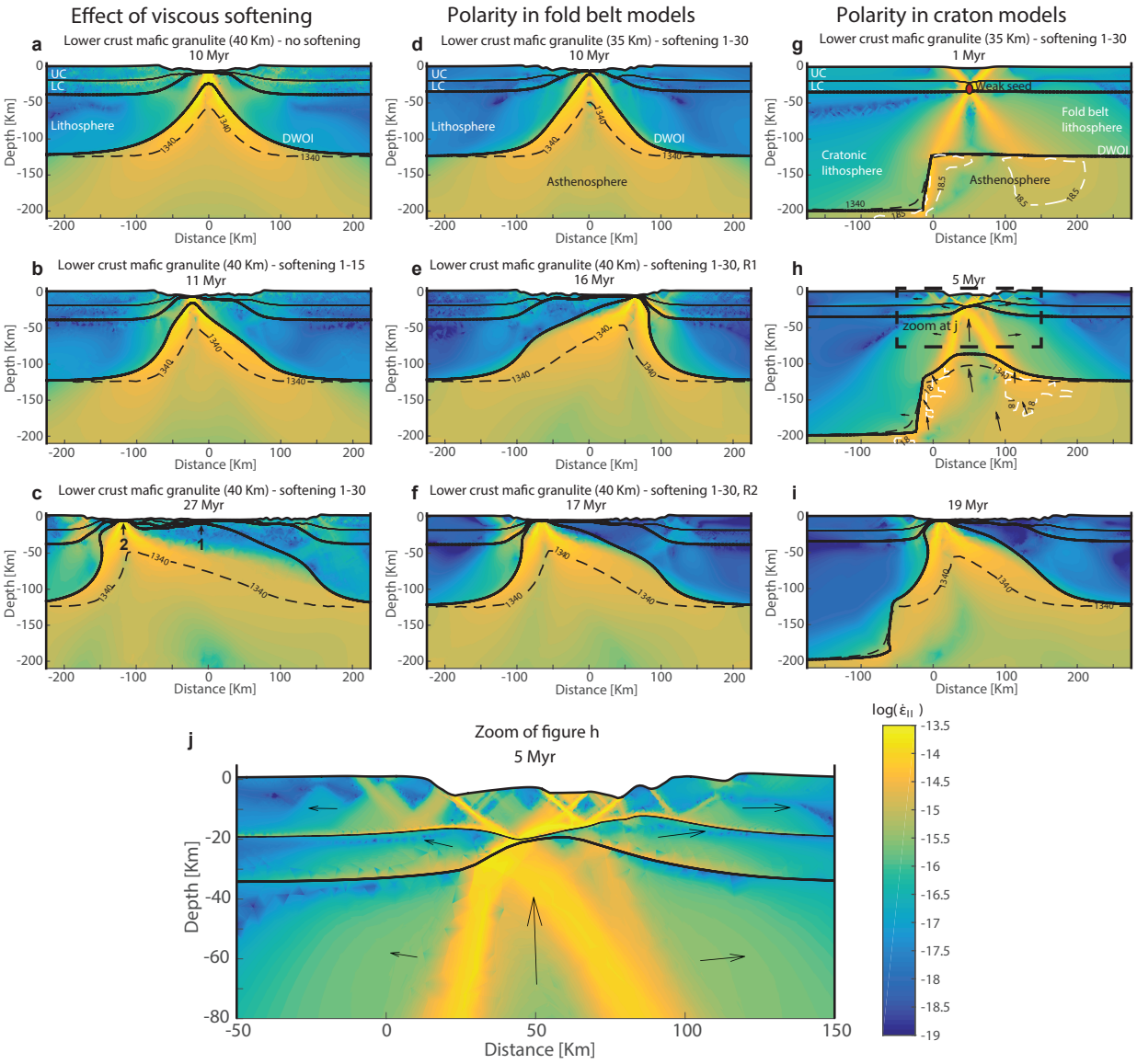

Figure 2: Strain rate fields of different numerical experiments with mafic granulite lower crustal rheologies. Discontinue black lines represent the 1340°C isotherm. UC stands for upper crust, LC for lower crust and DWOI for dry-wet olivine interface. **a, b, c,** Experiments without craton and 40 km crustal thickness for maximum VSS values of 1 (no softening), 15 and 30. Note that asymmetry increases with increasing maximum VSS factor. In **c**, 1 represents an area of crust thinned by sequential faulting previous to the rifting migration to 2, which adds a thicker crustal block (between 1 and 2) to the wide margin. **d,** Experiment with 35 km crust and a maximum VSS factor of 30 resulting into symmetric conjugates. **e, f,** Experiments with 40 km crust, identical parameters, but randomly differentiated meshes. Note that geometries and length of the margins are similar but polarity of the asymmetry is inverted. **g, h, i,** Evolution of a 35-km-crust experiment with a cratonic lithosphere at the left side. White lines represent isoviscosity lines with viscosities given in logarithm on base 10. **j,** zoom of (**h**). The craton favours localization of the deformation in the closest shear zone (**g**) and asymmetric up-welling of the asthenosphere (**h**), which results into asymmetric margins, in contrast with the equivalent experiment without craton (**d**). Note that the narrowest margin develops close to the craton since sequential faulting develops in this direction due to the asymmetric up-welling of the fold-belt lithospheric mantle and asthenosphere.

When the crustal and lithospheric geometry and rheology along the modelled section, are laterally constant, the polarity of the asymmetry cannot be predicted a priori. Experiments with exactly the same starting set-up and boundary conditions but a slightly different finite element grid result in opposite polarities (Fig. 2e and f). However, the presence of a craton near the incipient rift would produce a laterally heterogenous lithosphere. Figures 2g-i show time steps of a numerical experiment used to exemplify how the presence of a craton may trigger asymmetric margins, where the narrow margin develops near the craton while the wide one is in the opposite side. This occurs because the shear zone at the lower crust that dips towards the craton becomes dominant since the cratonic lithosphere is stronger than the fold belt one, hence it localizes deformation more effectively and, as it strains, it is able to pull the asthenosphere initially located beneath the fold belt upwards (Figs. 2g-i). In the contrary, the shear zone that dips towards the fold belt is more diffuse, and as it deforms it cannot pull the underlying asthenosphere upwards, as the craton root forms a barrier to asthenospheric flow in this direction.

To test that the craton determines the polarity of the asymmetry we ran experiments with laterally homogeneous crustal and lithospheric structure (from here on called no-craton tests), and tests with a craton and a fold belt (from here on called craton tests). As margin architecture is dependent on lower crustal rheology (Kusznir and Park, 1987; Buck, 1991; Huismans and Beaumont, 2003; Buiter et al., 2008), we used two different rheologies, the strong mafic granulite and the weaker wet anorthite (tests with an unlikely rheology of wet quartzite are also presented in the Supp. Info.), and also two different crustal thicknesses, 35 and 40 km. We ran tests with initial weak seeds located at different distances from the craton (50, 100, 150 and 300 km), to analyse the impact of the distance from the rift to the craton on asymmetry formation and polarity. Experiments are run 6 times with identical parameters for randomly differentiated meshes in order to test for consistency of the results. Small variations in the mesh affect mainly to the polarity of the asymmetry, but the length of the conjugated margins and their final architecture remain similar (Figs. 2e and f). In Figure 3 we show the paired mode of conjugated margin lengths of these 6 experiments for no-craton tests. For craton tests we show the paired mode and we used shading to show the spread of the results.

In no-craton tests with 35 km thick crust the resulting margins, have very similar width, thus are symmetric (Figs. 3a and b). In craton tests with 35 km thick crust, when the rift initializes at 50 and 100 km from the craton border (i.e. weak seed at 50 and 100 km), the margin located further from the craton is wider than the one located close to the craton. For strong mafic granulite, which favours asymmetry formation more strongly than weaker wet anorthite, the asymmetry is more marked. When the rift intitalizes at 150 km or more from the craton, the craton does not exert any influence in the crustal deformation and margins become symmetric again. Therefore, we conclude that the presence of a craton close enough to the rift location, can trigger asymmetry in cases where no asymmetry is observed in the absence of a craton and also determines the polarity of this asymmetry.

No-craton tests with 40 km crust result in asymmetric margins (Figs. 3c and d), but the polarity of this asymmetry is random (as exemplified in Figs. 2e-f). As before, the asymmetry is more marked in the mafic granulite than in the wet anorthite experiments. For craton tests and 40 km thick crust, the degree of asymmetry is similar or slightly larger when the rift initializes at 50 and 100 km from the craton. At these distances the craton determines margin polarity, with the narrow margin being always on the craton side. For rifting initiation 150 km away from the craton for anorthite, and 300 km for mafic granulite, the

Figure 3: **Margin width vs distance to craton**

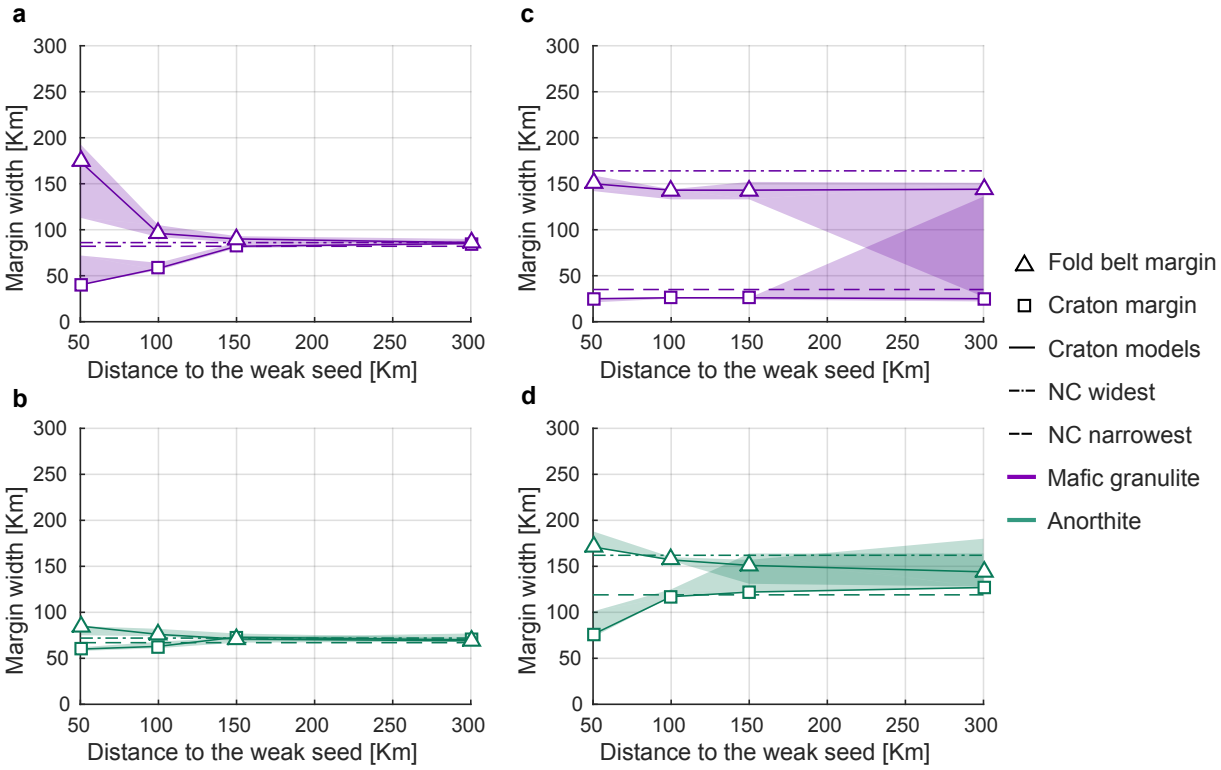

Figure 3: Margin width versus the distance between the initiation of rifting and the craton (50, 100, 150 and 300 km). Results from experiments with cratons are plotted in solid lines. No-craton experiments (NC) results are plotted in discontinuous lines. NC results of this experiments are plotted in terms of widest and narrowest margins independently of their polarity. Shaded areas correspond to maximum variations on the margin width found with randomly-differentiated meshes. **a,b,** Margin widths for different lower crustal rheologies and 35 km crustal thickness. **d,e,** Margin widths for different lower crustal rheologies and 40 km crustal thickness. Note that the narrowest margin always develops near the craton when the rifting initiates close enough to the craton. For results of wet quartzite see Supp. Info.

polarity of the asymmetry becomes random, which implies that the craton does not influence polarity any more.

In this work we find that polarity of the asymmetry is random when a laterally homogeneous initial set up is chosen. We also conclude that 1) cratons will influence the polarity of the asymmetry, with the narrow margin developing in the side of the craton and the wide margin in the opposite side, as observed in the South Atlantic and also South of Australia, next to the Yilgarn craton, (see Supp. Info.), and 2) cratons are capable of triggering asymmetric rifting even when lower crustal rheologies and crustal thickness are not favourable for asymmetry in their absence (Fig. 3a and b). For these effects to occur initiation of the deformation should take place close enough to the craton ($\leq$100 km) so that the craton-dipping shear zone in the mantle is forced to localize more deformation than the conjugate. Additionally, strong to intermediate lower crustal rheologies are needed for coupling of crustal and mantle deformation so that asymmetric extension can be sustained. We have shown that cratons influence margin architecture and polarities when rifting initiates at distances $\leq$100 km, which coincide well with the observations in the South Atlantic and also South of Australia, although margins are wider and degree of asymmetry is smaller than in the South Atlantic example (see Supp. Info.). Cratons may also influence subduction geometry (Manea et al., 2012; Pérez-Gussinyé et al., 2008). Some conjugate magma-rich margins developed near a craton, such as SE Greenland, also showcase an asymmetric architecture. However, these margins show inverse polarity to the one observed at magma-poor ones. At magma-rich margins the crust is asymmetrically accreted by magmatic bodies, where larger volumes of magmatic bodies are observed near the craton (Hopper et al., 2003). However, numerical models have not yet been able to reproduce this magmatic asymmetry (Nielsen and Hopper, 2004). Further work is needed in our code, such as implementation of melting, depletion-dependent viscosities and temperature- and depletion-dependent densities, before approaching the craton influence in the development of volcanic margins.

Methods

Maps and distances along flowlines

In this study we relate asymmetry of conjugate margins and margin width with the distance from the initiation of rifting to a craton. In order address this we have measured width of margins and distance from cratons to the landward edge of the margin (LEM) for the South Atlantic and the Australian margin of the Southern ocean.

In the case of the South Atlantic, we used a compilation of data made by Heine et al., 2013, based on seismic, potential field and map data. From this data set we extracted: (a) the rigid crust data which stands for areas of the crust that have not been deformed by the South Atlantic rifting, which edges we defined as LEM, and (b) the landward limit of the oceanic crust (LaLOC). Sao Francisco and Congo craton maps were obtained from Trompette, 1994. Cratonic domains in the maps include Paleoproterozoic rocks since they typically present deep lithospheric roots similar to those of the Archean domains (Hoffman, 1990). We measured width of the margins, from LaLOC to LEM, and distance to cratons, from LEM to the edge of the cratons, along the flowlines of the South Atlantic kinematic paleoreconstruction model by Pérez-Díaz and Eagles, 2014 (Fig. 1a). We also measured margin width and distance to craton along flowlines of the

Heine et al., 2013 paleoreconstruction with similar results (see Supp. Info.).

Numerical model

For the numerical experiments we developed a 2D finite element visco-elasto-plastic code based on MILAMIN mechanical and temperature solvers (Dabrowski et al., 2008). It uses the Stokes equation with incompressibility condition and the heat conservation equation to solve velocities, pressures and temperatures at Crouzeix-Raviart triangular elements with quadratic shape functions enhanced by a cubic bubble function and discontinues linear-interpolation pressure (Crouzeix and Raviart, 1973). Here, rock is treated as a non-Newtonian fluid and, therefore, viscosity is non-linear. Stokes solution is then achieved by a loop where viscosities are updated by using the previous iteration strain rate. Viscosity is calculated on a parallel scheme which includes diffusion and dislocation creep, and plastic (by Drucker-Prager yielding) terms. Elasticity is implemented following the Moresi et al., 2003 formulation. The boundary conditions are half-extension velocities applied to the lateral boundaries of the model box with consequent up-welling of the deep bottom boundary (400 km depth to avoid artefacts at the lithosphere). Dynamic topography is generated by a free surface top boundary where we applied a free-surface stabilization algorithm (Andrés-Martínez et al., 2015; Kaus et al., 2010) so that topographies can be generated in a stable way for relatively big time steps (10 Kyr).

Rheology and parametrizations

The numerical model domain is divided in four layers of different rheologies: (1) wet quartzite upper crust (Gleason and Tullis, 1995), (2) lower crust for which we use strong mafic granulite (Wilks and Carter, 1990), intermediate strength wet anorthosite (Rybacki and Dresen, 2000), or weak wet quartzite lower crust (Gleason and Tullis, 1995) (see Supp. Info. for wet quartzite results), (3) dry olivine lithospheric mantle (Hirth and Kohlstedt, 2003), and (4) wet olivine asthenosphere (Hirth and Kohlstedt, 2003).

Strain weakening is implemented by: (a) linear reduction of the friction angle of the Druker-Prager yield criterion dependent on the root of accumulated second strain invariant for windows from 0 to 1 strain, and 30 to 15° friction angle, which simulates brittle weakening of faults, and (2) linear increase of the pre-exponential factor in the creep flow laws (Hirth and Kohlstedt, 2003) for a strain window from 0 to 1, in distinct ranges of factors varying from 1 to 15 and 1 to 30, which simulates olivine weakening by grain reduction (Karato and Wu, 1993) and crystallographic preferred orientations (CPO) (Tommasi et al., 2009; Hansen et al., 2012). This last type of strain-dependent weakening is referred here as viscous strain softening (VSS). Note that the larger the pre-exponential factor range the more effective the VSS.

Weak seeds are needed in order to initialize deformation in numerical models. We chose to use 2D-Gaussian temperature weak seed of 10×20 km size and +100 °C maximum temperature increment, which allows the experiments to nucleate rifting in regions of interest with the advantage of vanishing after a number of time steps by diffusion.

See Table 1 in Supp. Info. for a complete list of parameters.

Simulation of a craton

Cratons are simulated in our model thermally and by their volatile content. The thermal boundary condition used in our model is a constant temperature of 1350 °C below 125 km depth, which represents the thermal lithosphere-asthenosphere boundary (LAB). Here, we approximate the asthenospheric temperature to be constant since its geotherm is adiabatic due to convection. Cratons are simulated by placing the thermal LAB at 200 km (Evans et al., 2011; Ritsema and van Heijst, 2000), so that the thermal gradient at the craton is lower than the one of mobile belts. The same depths apply for the dry-wet olivine interface (Fullea et al., 2011; Khoza et al., 2013). LAB transition between cratonic and mobile belt lithosphere occurs at 80° (Ritsema and van Heijst, 2000). Craton crustal thicknesses observed in nature vary from 35 to 50 km and in fold belt crusts from 40 to 55 km (Durrheim and Mooney, 1994; Niu and James, 2002; Ford et al., 2010). Crust at cratons is inferred to be mostly felsic with the exception of areas affected by plumes, while at mobile belts is found to be slightly more mafic (Nguuri et al., 2001; Kgaswane et al., 2009). For simplicity, we choose to use same thickness of the crust and same crustal rheology for both cratons and mobile belts. We vary crustal thicknesses in cratons and fold belts between 35 and 40 km

Numerical experiments

We run 150 experiments with cratons next to mobile belts where we systematically vary: (1) rheology of the lower crust (mafic granulite, anorthite, and wet quartzite, results from wet quartzite shown in Supp. Info.), (2) crustal thickness of 35 and 40 km, and (3) position of the weak seed respect to the craton (0, 50, 100, 150, 300 km) to initialize rifting at different distances from the craton and study its influence on the asymmetry and polarity. We also run 30 experiments on laterally homogeneous mobile belt lithosphere alone varying: (1) rheology of the lower crust, and (2) crustal thickness. This last experiments seek to understand which combination of parameters would result in symmetric margins when a craton is not present, so that we can study for which combination of parameters the presence of craton is determinant for the development of conjugate margin asymmetry. Slightly different meshes can result in different solutions due to non-linearities in the formulation, and will specially affect polarity of the asymmetry. All parameter combinations are run over 6 different meshes in order to prove that cratons actually condition the polarity of the asymmetry. See Experiments evolution in Supp. Info. for results with mafic granulite, anorthite and wet quartzite lower crust and the experiments without craton.

References

M. Andrés-Martínez, J. P. Morgan, M. Pérez-Gussinyé, and L. Rüpke. A new free-surface stabilization algorithm for geodynamical modelling: Theory and numerical tests. *Physics of the Earth and Planetary Interiors*, 246:41–51, 2015. doi: 10.1016/j.pepi.2015.07.003. URL http://dx.doi.org/10.1016/j.pepi.2015.07.003.

O. A. Blaich, J. I. Faleide, and F. Tsikalas. Crustal breakup and continent-ocean transition at South Atlantic conjugate margins. *Journal of Geophysical Research: Solid Earth*, 116(B1), 2011.

S. Brune, A. A. Popov, and S. V. Sobolev. Modeling suggests that oblique extension facilitates rifting and continental break-up. *Journal of Geophysical Research: Solid Earth*, 117(B8), 2012. doi: 10.1029/2011JB008860. URL http://dx.doi.org/10.1029/2011JB008860.

S. Brune, C. Heine, M. Pérez-Gussinyé, and S. V. Sobolev. Rift migration explains continental margin asymmetry and crustal hyper-extension. *Nature Communications*, 5, 2014. doi: 10.1038/ncomms5014. URL http://dx.doi.org/10.1038/ncomms5014.

W. R. Buck. Modes of continental lithospheric extension. *Journal of Geophysical Research: Solid Earth*, 96(B12):20161–20178, 1991. doi: 10.1029/91JB01485. URL http://dx.doi.org/10.1029/91JB01485.

W. R. Buck and L. L. Lavier. A tale of two kinds of normal fault: the importance of strain weakening in fault development. *Geological Society, London, Special Publications*, 187(1):289–303, 2001. doi: 10.1144/GSL.SP.2001.187.01.14. URL http://dx.doi.org/10.1144/GSL.SP.2001.187.01.14.

S. J. H. Buiter, R. S. Huismans, and C. Beaumont. Dissipation analysis as a guide to mode selection during crustal extension and implications for the styles of sedimentary basins. *Journal of Geophysical Research: Solid Earth*, 113(B6), 2008. doi: 10.1029/2007JB005272. URL http://dx.doi.org/10.1029/2007JB005272.

G. Corti, J. V. Wijk, M. Bonini, D. Sokoutis, S. Cloetingh, F. Innocenti, and P. Manetti. Transition from continental break-up to punctiform seafloor spreading: How fast, symmetric and magmatic. *Geophysical Research Letters*, 30(12), 2003. doi: 10.1029/2003GL017374. URL http://dx.doi.org/10.1029/2003GL017374.

M. Crouzeix and P.-A. Raviart. Conforming and nonconforming finite element methods for solving the stationary Stokes equations I. *Reveu française d'automatique, informatique, recherche opérationnelle. Mathématique*, 7(3):33–75, 1973.

M. Dabrowski, M. Krotkiewski, and D. W. Schmid. MILAMIN: MATLAB-based finite element method solver for large problems. *Geochemistry, Geophysics, Geosystems*, 9(4), 2008.

I. Davison. Wide and narrow margins of the Brazilian South Atlantic. *Journal of the Geological Society*, 154(3):471–476, 1997. doi: 10.1144/gsjgs.154.3.0471. URL http://dx.doi.org/10.1144/gsjgs.154.3.0471.

N. G. Direen, H. M. J. Stagg, P. A. Symonds, and I. O. Norton. Variations in rift symmetry: cautionary examples from the Southern Rift System (Australia-Antarctica). *Geological Society, London, Special Publications*, 369(1):453–475, 2012. doi: 10.1144/SP369.4. URL http://dx.doi.org/10.1144/SP369.4.

J. Dunbar and D. Sawyer. Continental rifting at pre-existing lithospheric weaknesses. *Nature*, 1988. doi: 10.1038/333450a0. URL http://dx.doi.org/10.1038/333450a0.

R. J. Durrheim and W. D. Mooney. Evolution of the Precambrian lithosphere: Seismological and geochemical constraints. *Journal of Geophysical Research: Solid Earth*, 99(B8):15359–15374, 1994. doi: 10.1029/94JB00138. URL http://dx.doi.org/10.1029/94JB00138.

R. L. Evans, A. G. Jones, X. Garcia, M. Muller, M. Hamilton, S. Evans, C. J. S. Fourie, J. Spratt, S. Webb, H. Jelsma, and D. Hutchins. Electrical lithosphere beneath the Kaapvaal craton, southern Africa. *Journal of Geophysical Research: Solid Earth*, 116(B4), 2011. doi: 10.1029/2010JB007883. URL http://dx.doi.org/10.1029/2010JB007883.

H. A. Ford, K. M. Fischer, D. L. Abt, C. A. Rychert, and L. T. Elkins-Tanton. The lithosphere-asthenosphere boundary and cratonic lithospheric layering beneath Australia from Sp wave imaging. *Earth and Planetary Science Letters*, 300(3-4): 299–310, 2010. doi: 10.1016/j.epsl.2010.10.007. URL http://dx.doi.org/10.1016/j.epsl.2010.10.007.

J. Fullea, M. R. Muller, and A. G. Jones. Electrical conductivity of continental lithospheric mantle from integrated geophysical and petrological modeling: Application to the Kaapvaal Craton and Rehoboth Terrane, southern Africa. *Journal of Geophysical Research: Solid Earth*, 116(B10), 2011. doi: 10.1029/2011JB008544. URL http://dx.doi.org/10.1029/2011JB008544.

G. C. Gleason and J. Tullis. A flow law for dislocation creep of quartz aggregates determined with the molten salt cell. *Tectonophysics*, 247(1):1–23, 1995. doi: 10.1016/0040-1951(95)00011-B. URL http://dx.doi.org/10.1016/0040-1951(95)00011-B.

L. N. Hansen, M. E. Zimmerman, and D. L. Kohlstedt. Laboratory measurements of the viscous anisotropy of olivine aggregates. *Nature*, 492(7429):415–418, 2012. doi: 10.1038/nature11671. URL http://dx.doi.org/10.1038/nature11671.

C. Heine, J. Zoethout, and R. D. Müller. Kinematics of the South Atlantic rift. *Solid Earth*, 4(2):215–253, 2013. doi: 10.5194/se-4-215-2013. URL http://dx.doi.org/10.5194/se-4-215-2013.

G. Hirth and D. Kohlstedt. Rheology of the upper mantle and the mantle wedge: A view from the experimentalists. In J. Eiler, editor, *Inside the subduction factory*, pages 83–105. AGU, 2003. ISBN 0-87590-997-3.

P. F. Hoffman. Geological constraints on the origin of the mantle root beneath the Canadian Shield. *Philosophical Transactions of the Royal Society of London A: Mathematical, Physical and Engineering Sciences*, 331(1620):523–532, 1990.

J. R. Hopper, T. Dahl-Jensen, W. S. Holbrook, H. C. Larsen, D. Lizarralde, J. Korenaga, G. M. Kent, and P. B. Kelemen. Structure of the SE Greenland margin from seismic reflection and refraction data: Implications for nascent spreading center subsidence and asymmetric crustal accretion during North Atlantic opening. *Journal of Geophysical Research: Solid Earth*, 108(B5), 2003.

R. Huismans and C. Beaumont. Symmetric and asymmetric lithospheric extension: Relative effects of frictional-plastic and viscous strain softening. *Journal of Geophysical Research: Solid Earth*, 108(B10), 2003.

R. S. Huismans and C. Beaumont. Asymmetric lithospheric extension: The role of frictional plastic strain softening inferred

from numerical experiments. *Geology*, 30(3):211–214, 2002.

S. I. Karato and P. Wu. Rheology of the upper mantle: A synthesis. *Science*, 260(5109):771–778, 1993.

B. J. Kaus, H. Mühlhaus, and D. A. May. A stabilization algorithm for geodynamic numerical simulations with a free surface. *Physics of the Earth and Planetary Interiors*, 181(1):12–20, 2010. doi: 10.1016/j.pepi.2010.04.007.

E. M. Kgaswane, A. A. Nyblade, J. Julià, P. H. G. M. Dirks, R. J. Durrheim, and M. E. Pasyanos. Shear wave velocity structure of the lower crust in southern Africa: Evidence for compositional heterogeneity within Archaean and Proterozoic terrains. *Journal of Geophysical Research: Solid Earth*, 114(B12), 2009. doi: 10.1029/2008JB006217. URL http://dx.doi.org/10.1029/2008JB006217.

T. D. Khoza, A. G. Jones, M. R. Muller, R. L. Evans, M. P. Miensopust, and S. J. Webb. Lithospheric structure of an Archean craton and adjacent mobile belt revealed from 2-D and 3-D inversion of magnetotelluric data: Example from southern Congo craton in northern Namibia. *Journal of Geophysical Research: Solid Earth*, 118(8):4378–4397, 2013. doi: 10.1002/jgrb.50258. URL http://dx.doi.org/10.1002/jgrb.50258.

N. J. Kusznir and R. G. Park. The extensional strength of the continental lithosphere: its dependence on geothermal gradient, and crustal composition and thickness. *Geological Society, London, Special Publications*, 28(1):35–52, 1987. doi: 10.1144/GSL.SP.1987.028.01.04. URL http://dx.doi.org/10.1144/GSL.SP.1987.028.01.04.

L. L. Lavier and W. R. Buck. Half graben versus large-offset low-angle normal fault: Importance of keeping cool during normal faulting. *Journal of Geophysical Research: Solid Earth*, 107(B6), 2002. doi: 10.1029/2001JB000513. URL http://dx.doi.org/10.1029/2001JB000513.

G. S. Lister and G. A. Davis. The origin of metamorphic core complexes and detachment faults formed during Tertiary continental extension in the northern Colorado River region, USA. *Journal of Structural Geology*, 11(1):65–94, 1989.

V. C. Manea, M. Pérez-Gussinyé, and M. Manea. Chilean flat slab subduction controlled by overriding plate thickness and trench rollback. *Geology*, 40(1):35–38, 2012.

K. E. Meisling, P. R. Cobbold, and V. S. Mount. Segmentation of an obliquely rifted margin, Campos and Santos basins, southeastern Brazil. *AAPG bulletin*, 85(11):1903–1924, 2001.

L. Moresi, F. Dufour, and H. B. Mühlhaus. A Lagrangian integration point finite element method for large deformation modeling of viscoelastic geomaterials. *Journal of Computational Physics*, 184(2):476–497, 2003. ISSN 0021-9991. doi: 10.1016/S0021-9991(02)00031-1. URL http://www.sciencedirect.com/science/article/pii/S0021999102000311.

T. K. Nguuri, J. Gore, D. E. James, S. J. Webb, C. Wright, T. G. Zengeni, O. Gwavava, and J. A. Snoke. Crustal structure beneath southern Africa and its implications for the formation and evolution of the Kaapvaal and Zimbabwe cratons. *Geophysical Research Letters*, 28(13):2501–2504, 2001. doi: 10.1029/2000GL012587. URL http://dx.doi.org/10.1029/2000GL012587.

T. K. Nielsen and J. R. Hopper. From rift to drift: Mantle melting during continental breakup. *Geochemistry, Geophysics, Geosystems*, 5(7), 2004.

F. Niu and D. E. James. Fine structure of the lowermost crust beneath the Kaapvaal craton and its implications for crustal formation and evolution. *Earth and Planetary Science Letters*, 200(1):121–130, 2002.

L. Pérez-Díaz and G. Eagles. Constraining South Atlantic growth with seafloor spreading data. *Tectonics*, 33(9):1848–1873, 2014. doi: 10.1002/2014TC003644. URL http://dx.doi.org/10.1002/2014TC003644.

M. Pérez-Gussinyé. A tectonic model for hyperextension at magma-poor rifted margins: an example from the West Iberia–Newfoundland conjugate margins. *Geological Society, London, Special Publications*, 369(1):403–427, 2013.

M. Pérez-Gussinyé, A. R. Lowry, J. P. Morgan, and A. Tassara. Effective elastic thickness variations along the Andean margin and their relationship to subduction geometry. *Geochemistry, Geophysics, Geosystems*, 9(2), 2008. doi: 10.1029/2007GC001786. URL http://dx.doi.org/10.1029/2007GC001786.

C. R. Ranero and M. Pérez-Gussinyé. Sequential faulting explains the asymmetry and extension discrepancy of conjugate margins. *Nature*, 468(7321):294–299, 2010.

J. Ritsema and H. van Heijst. New seismic model of the upper mantle beneath Africa. *Geology*, 28(1):63–66, Jan. 2000.

E. Rybacki and G. Dresen. Dislocation and diffusion creep of synthetic anorthite aggregates. *Journal of Geophysical Research: Solid Earth*, 105(B11), 2000. doi: 10.1029/2000JB900223. URL http://dx.doi.org/10.1029/2000JB900223.

A. Tommasi, M. Knoll, A. Vauchez, J. W. Signorelli, C. Thoraval, and R. Logé. Structural reactivation in plate tectonics controlled by olivine crystal anisotropy. *Nature Geoscience*, 2(6):423–427, 2009. doi: 10.1038/ngeo528. URL http://dx.doi.org/10.1038/ngeo528.

R. Trompette. *Geology of Western Gondwana (2000 - 500 Ma): Pan-African-Brasiliano Aggregation of South America and Africa*. Taylor & Francis, 1994. ISBN 9789054101659.

C. Warren and C. Beaumont. Formation and exhumation of ultra-high-pressure rocks during continental collision: Role of detachment in the subduction channel. *Geochemistry, Geophysics, Geosystems*, 9(4), 2008. doi: 10.1029/2007GC001839. URL http://dx.doi.org/10.1029/2007GC001839.

B. Wernicke. Uniform-sense normal simple shear of the continental lithosphere. *Canadian Journal of Earth Sciences*, 22(1): 108–125, 1985.

K. Wilks and N. Carter. Rheology of some continental lower crustal rocks. *Tectonophysics*, 182(1-2):57–77, October 1990.

Supplementary Information

1 Maps, margin width and distance to cratons

1.1 South Atlantic conjugates

A figure on the South Atlantic conjugate margins equivalent to Fig. 1 in the article is presented here as Fig. 1. The difference between Fig. 1 and the one in the article is that in the former the pole of rotation used is the one suggested by Heine et al., 2013. Although margin widths and distance to cratons are slightly different, the relationship between the polarity of the margin asymmetry and the proximity to the craton remains constant, so that the narrowest margin of a pair occurs on the side where a craton is closer to the landward edge of the margin.

1.2 Australia-Antarctica conjugates

Asymmetry can be observed as well in the Australian margin of the Southern ocean (Fig. 2). There, Yilgarn and Gawler cratons expand west and east of Australia respectively, near the coast (Myers, 1995; Fitzsimons, 2003). In the conjugate Antarctic margin, Archean and Paleoproterozoic rocks associated to the Terre Adélie craton are observed at at the coasts of Terre Adélie and King George V Land (Ménot et al., 2007; Fitzsimons, 2003). However, the extension of the Terre Adélie craton is not well constrained since it is covered by the Antarctic ice cap. Therefore we choose to exclude the Antarctic margin from this study. Two phases of rifting are observed in the South Australia-Antarctica conjugates: a Jurassic phase (165-145 Ma) where rifting is broad, and a Cretaceous-Paleogene phase (93.5-50 Ma) where rifting is narrow (Ball et al., 2013). Seismic sections and gravity data show little deformation associated with the initial phase along sectors of the Gawler shelf (next to the Gawler craton), while West of the Archean-Mesoproterozoic limit initial phase stretching is broad (Totterdell et al., 2003; Ball et al., 2013). Different deformation sectors recognised at the Australian margin are probably conditioned by prerift mechanical heterogeinities such as the Yilgarn and Gawler cratons (Ball et al., 2013). Asymmetry of conjugated margins is mainly observed in the East and West sectors (Stagg and Reading, 2007; Ball et al., 2013), while the central sector remains highly symmetric (Direen et al., 2011, 2012). The western Australian margin is narrower (∼350 km) where the Yilgarn craton is close to the coast while it widens towards the east (∼450 km) (Fig. 2b). Similarly, the margin next to Gawler craton is narrower. However, in this sector the extension is oblique to the margin and, therefore, we cannot address the mechanical influence of the craton in the rifting by using a 2D approach.

Figure 1: **Width of South Atlantic conjugate margins, and distance from the edge of the margin to the cratons using the rotation pole defined in Heine et al., 2013**

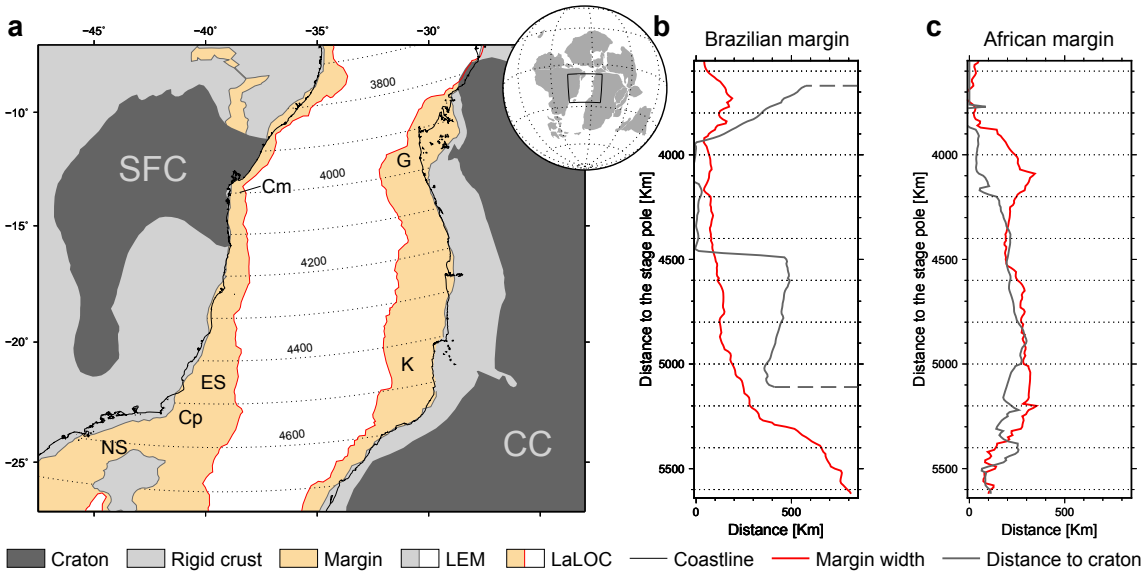

Figure 1: **a**, Map of the central sector of the South Atlantic conjugate margins using Heine et al., 2013 reconstruction at 105 Myr. Dots represent flowlines which labels are distance in km to the Central-Africa respect South-America rotation pole from 105 Myr to present. SFC—Sao Francisco Craton, CC—Congo Craton, Cm—Camumu, ES—Espirito Santo, Cp—Campos, NS—North of Santos, G—Gabon, K—Kwanza basins. Rigid crust (light grey) as crust not deformed by rifting and landward limit of the oceanic crust (LaLOC) from Heine et al., 2013. Note that the further the craton to the landward edge of the margin (LEM), the wider the margin. **b**, **c**, Margin width (red lines) and distance from the craton to the LEM measured along flowlines Heine et al., 2013 model. The relationship between polarity of the asymmetry and the distance from the craton to the LEM remains similar to the one shown in the Fig. 1 in the article, even if the rotation poles used to calculate the distances are different.

Figure 2: **Width of South Australian-Antarctic conjugate margins and distance from the edge of the margin to the cratons.**

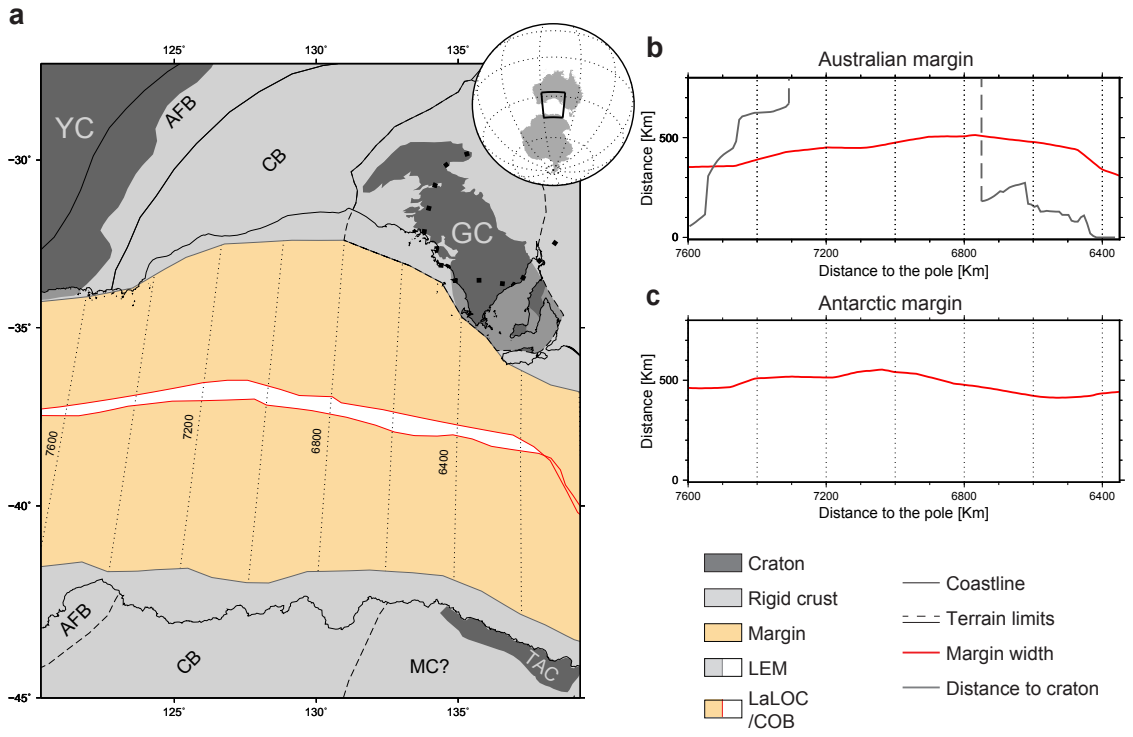

Figure 2: **a**, Map of the Australian-Antarctic margin conjugates reconstructed at 45 Myr by using the White et al., 2013 model. YC—Yilgarn Craton, GC—Gawler Craton, MW—Mawson Craton, TAC—Terre Adélie Craton, AFB—Albany-Fraser Belt and CB—Coompana Block. **c**, Width of the Australian margin and distance from the LEM to the cratons. **b** Width of the Antarctic margin. Note that next to Yilgarn craton the Australian margin is ∼100 km narrower than its Antarctic conjugate. Eastward of the Yilgarn craton the conjugate pair becomes symmetric. Asymmetry occurs again closer to the Gawler Craton, although we choose to not evaluate this area in our study since deformation is not perpendicular to the opening direction and the lack of control on the cratonic presence at the Antarctic side due to the ice sheet.

2 Model parameters

Table 1: Model parameters. Rheological parameters from Rybacki and Dresen, 2000; Wilks and Carter, 1990; Hirth and Kohlstedt, 2003. Remaining parameters from Turcotte and Schubert, 2002. Diffusion creep B is calculated using a grain size d of 6 mm. Wet olivine water fugacity fH_2O is 500 MPa (in C_{OH} ppm H/Si).

Rock/ mineral aggregate	Wet quartzite (upper crust and weak lower crust)	Wet anorthite (intermedium lower crust)	Mafic granulite (strong lower crust)	Dry olivine (lithospheric mantle)	Wet olivine (asthenospheric mantle)
Dislocation pre-exponential factor $log(B)$ [$Pa^{-n}s^{-1}$]	-28.0	-15.4	-21.05	-15.56	-15.05
Dislocation exponent n	4.0	3.0	4.2	3.5	3.5
Dislocation activation energy E^* [kJ mol^{-1}]	223	356	445	530	480
Diffusion pre-exponential factor $log(B)$ [Pa s^{-1}]	-	-	-	-8.65	-8.66
Diffusion exponent n	-	-	-	1	1
Diffusion activation energy E^* [kJ mol^{-1}]	-	-	-	375	335
Shear modulus μ [GPa]	UC 36 LC 40	40	40	74	74
Thermal conductivity k [W m^{-1} K^{-1}]	UC 2.1 LC 2.5	2.5	2.5	3.3	3.3
Heat capacity C_p [J $Kg^{-1}K^{-1}$]	1200	1200	1200	1200	1200
Radiogenic heat production H_p [$\mu W m^{-3}$]	UC 1.3 LC 0.2	0.2	0.2	0	0
Densities ρ [Kg m^{-3}]	UC 2700 LC 2850	2850	2850	3300	3300

3 Wet quartzite lower crust results

For completeness, we chose to run equivalent experiments to those described in the main text for an unlikely weak wet quartzite rheology for the lower crust. Figure 3 shows results for this model. In the 35 km crust experiment we observe higher asymmetry, for both craton and no-craton tests, in comparison with anorthite models (Fig. 3a). This is explained by a combination of asymmetric upwelling of the mantle combined with crustal deformation related to a widely extended channel of low viscosity developed at the base of the crust (see Sec. 4). This lower crustal channel develops due to the extremely weak wet quartzite viscosity at the base of the crust, and acts as a detachment for crustal faulting. However, this channel is laterally limited by the craton, where basal crustal temperatures are slightly colder than the equivalent ones in the fold belt. Therefore, a larger number of faults rooting in this low viscosity channel develop in the fold belt side enhancing asymmetry.

Experiments with wet quartzite lower crust and 40 km crustal thickness develop a larger and thicker low viscosity channel than the equivalent ones with 35 km (see Sec. 4). This allows for complete decoupling of mantel and crustal deformation. Even if shear zones close to cratons localize deformation faster at initial phases of rifting, their conjugates are forced to remain active to accommodate wide crustal

Figure 3: **Margin width vs distance to craton for wet quartzite lower crusts**

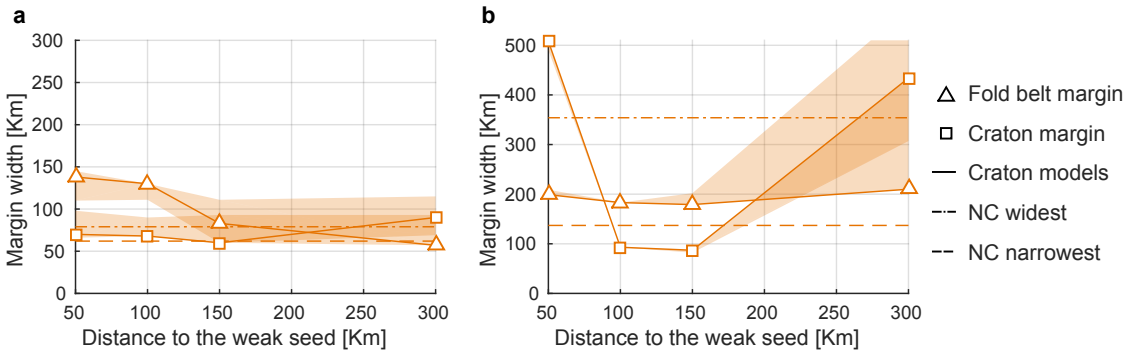

Figure 3: Margin width versus the distance between the initiation of rifting and the craton (50, 100, 150 and 300 km) for experiments run with wet quartzite lower crust. Results from experiments with cratons are plotted in solid lines. No-craton experiments (NC) results are plotted in discontinuous lines. NC results of this experiments are plotted in terms of widest and narrowest margins independently of their polarity. Shaded areas correspond to maximum variations on the margin width found with randomly-differentiated meshes. **a,** Margin widths for 35 km crustal thickness.**b,** Margin widths for 40 km crustal thickness. Note that the narrowest margin develops near the craton when the rifting initiates close enough to the craton except in the case with 40 km crust. This is due to a decoupling between mantle and crustal deformation aided by a wide channel of low viscosity developed at the base of the crust.

deformation, and eventually weaken enough to allow for symmetric up-welling of the asthenosphere. In later phases of rifting (>20 Myr) a low viscosity pocket occurs and allows sequential faulting to take over on wide extension and asymmetry develops. Consequently, polarity of the asymmetry is random even for the tests with cratons, except for the experiment where rifting is initiated at 50 km from the craton, where polarity of the asymmetry is opposite to the one for the rest of parameter combinations (Fig. 3b). The polarity for this particular case is a consequence of the low viscosity channel not being able to develop in the cratonic crust similarly to tests with 35 km crust. Here the difference is that there is no deformation coupling between crust and mantle and, therefore, up-welling of the asthenosphere is symmetric while crustal thinning occurs asymmetrically and the rifting migrates away from the craton.

Consequently we conclude that asymmetry does not depend exclusively on the presence of a craton but also on the rheology of the lower crust. In order to have such a relationship between the polarity of the margin asymmetry and distance to the craton, the lower crust needs to be strong enough to allow coupling of mantle and crustal deformations.

4 Experiments evolution and final margin architectures

In this section we introduce figures of some of the most relevant models which margin widths and distances to craton where used to produce Fig. 3 in the article. Colours represent square root second invariant of the strain rate $\dot{\varepsilon}_{II}$.

4.1 GRANULITE 35 KM CRUST (Fig. 4)

4.1.1 Symmetry with no craton

This type of model allows for a strong coupling of upper and lower crust in the brittle deformation domain. Consequently, the result is large-offset faults and a very symmetric geometry with short margins.

4.1.2 Craton test - weak seed at 50 km

This model results in a strong asymmetry although equivalent models without craton are symmetric. The polarity of the asymmetry is such as that the narrow margin develops close to the craton and the widest margin in the opposite side. Asymmetry is favoured since early stages of the model (see 4 Myr). This is because the mantle shear zone closer to the craton is favoured due to the asymmetric up-welling of the asthenosphere. Since the lower crust is very strong and deforms by creep only at depths near the Moho, the asymmetric character of the deformation in the mantle is transmitted to the crust which initially favours one fault among the two initial conjugates and finally induces a low viscosity pocket in the lower crust by strain softening which is translated into sequential faulting (Brune et al., 2014).

4.1.3 Symmetric craton test - weak seed 300

When the craton is a distance of 300 km from the rift axis, its influence in the deformation of the mantle is small and consequently the resulting conjugated margins are symmetric.

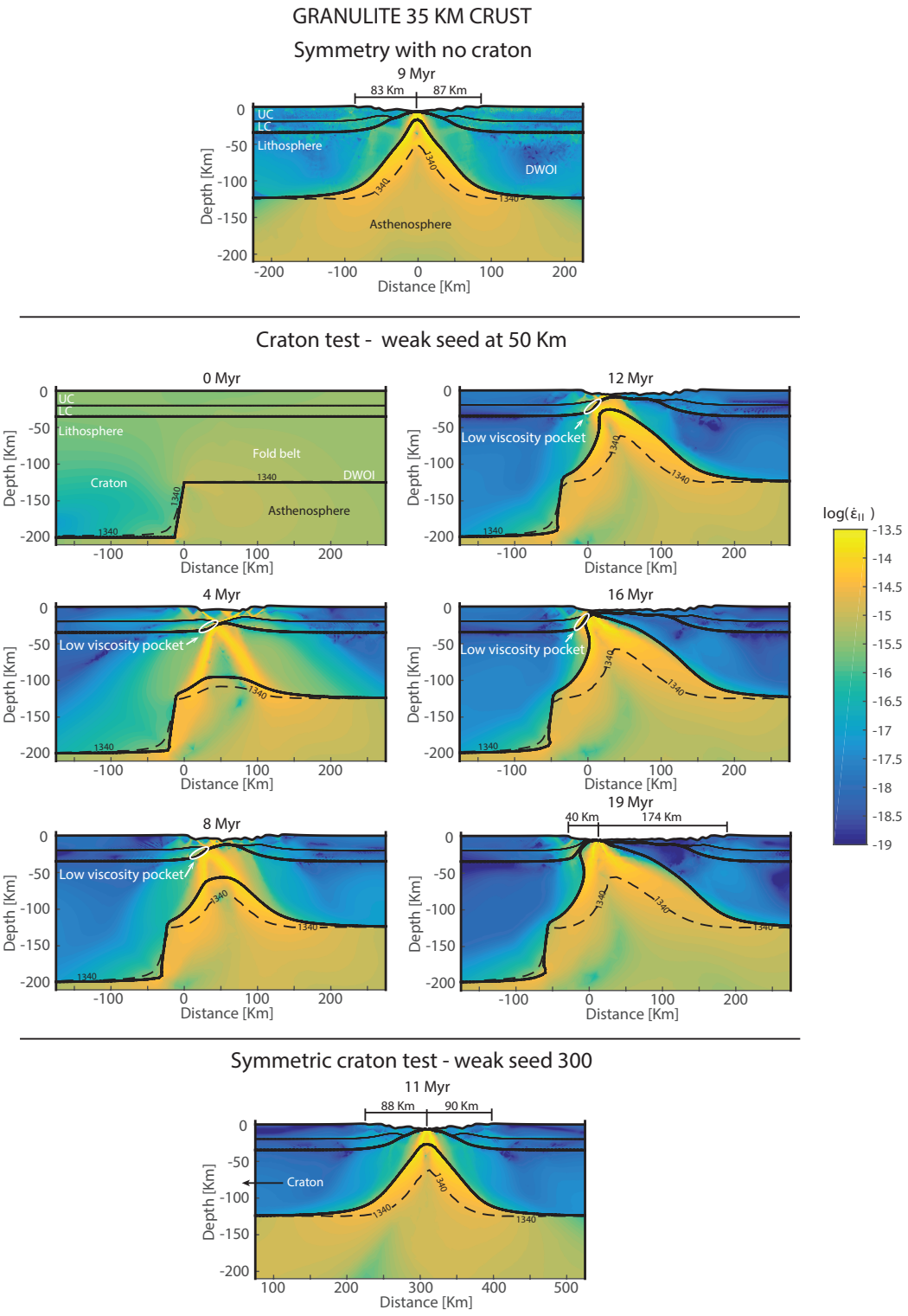

Figure 4: Evolution and architectures of granulite lower crust (35 km thick)

4.2 GRANULITE 40 KM CRUST (Fig. 5)

4.2.1 No craton with different polarities

The models presented have asymmetric conjugate margins. Although the lower crust is strong, it is 5 km thicker than models with 35 km. This allows the lower crust to accommodate larger deformations and, as an effect of the non-linearity of the viscous strain softening, one of the two initial conjugate faults will be favoured, resulting in subsequent asymmetry. The favouring of one initial fault over its conjugate is triggered by natural-heterogeinity-scale errors associated with the spactial discretization. Since meshes for tests are generated with small random variations, the polarity of the asymmetry observed here is also random.

4.2.2 Craton test - weak seed at 50 km

Results are very similar to tests without craton in terms of asymmetry and length of the narrow and wide margins. However, polarity of the asymmetry is always such as that the narrow margin develops near the craton and the wide margin opposite to it. This is again due to an asymmetric up-welling of the mantle triggered by the craton stiffness, which favours one lower crustal shear zone over its conjugate.

This type of test with craton never reaches a 0 km crust (breakup) because the lower-crustal low-viscosity pocket becomes too dominant in the presence of a craton. Tests without a craton account for a weak shear zone in the upper mantle which partially accommodates the bending produced by the deformation on the low viscosity pocket. When mantle and lower crust are cold enough (become strong enough) the low-viscosity pocket looses control of the deformation, localization occurs faster on the mantle shear zone and breakup is reached. Similar low-viscosity pocket and associated mantle shear zone is observed in tests with craton (see 16 Myr), but the mantle shear zone will eventually disappear allowing for the low-viscosity pocket to continue controlling deformation and breakup not be reached. However, we found that geometries of the margins and their widths are very similar to the ones observed in tests with no-craton when we consider the breakup to occur just before the mantle shear zone disappears. This results typically in a crust with minimum thickness of 3 km, where we assume the breakup is located.

4.2.3 Craton tests with different polarities - weak seed 300

When a craton is far enough from the rift axis, the polarity of the asymmetry becomes random as in models with no craton.

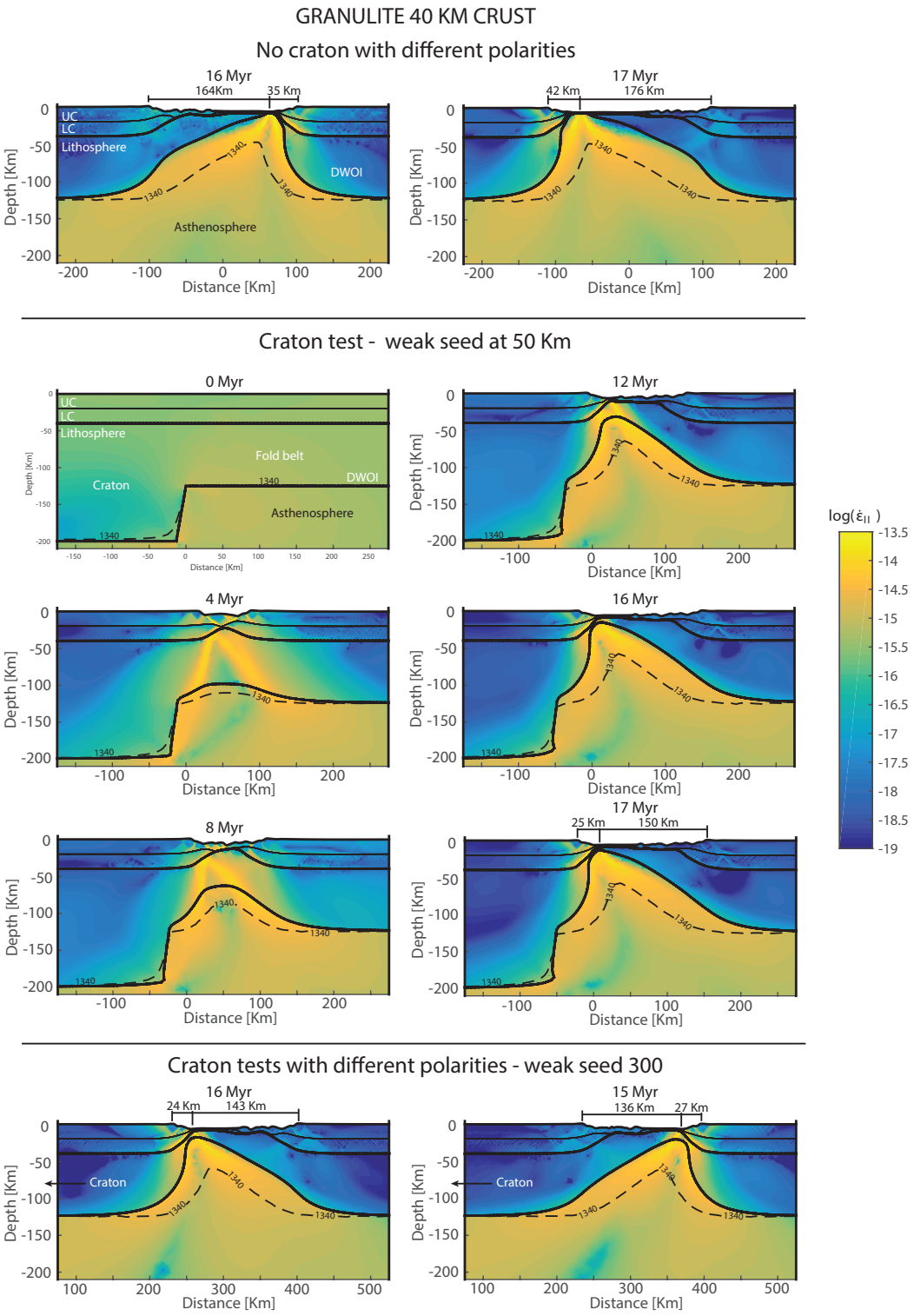

Figure 5: Evolution and architectures of granulite lower crust (40 km thick)

4.3 ANORTHITE 35 KM CRUST (Fig. 6)

4.3.1 Symmetry with no craton

Like the granulite 35 km crust models, anorthite 35 km crust models result in symmetric margins due to a strong crust which behaves mainly brittly.

4.3.2 Craton test - weak seed at 50 km

The presence of a craton near the rift axis seems to favour a slight asymmetry by the same mechanisms observed in models with granulite 35 km crust. The reduction in asymmetry occurs due to the weaker lower crusts which couple less effectively upper crustal deformation with lower crustal deformation, and therefore, the lower-crustal low-viscosity pocket is not as dominant as tests with granulite lower crust.

4.3.3 Symmetric craton test - weak seed 150

Models where rifting initiates 150 km away from the craton result in symmetric margins.

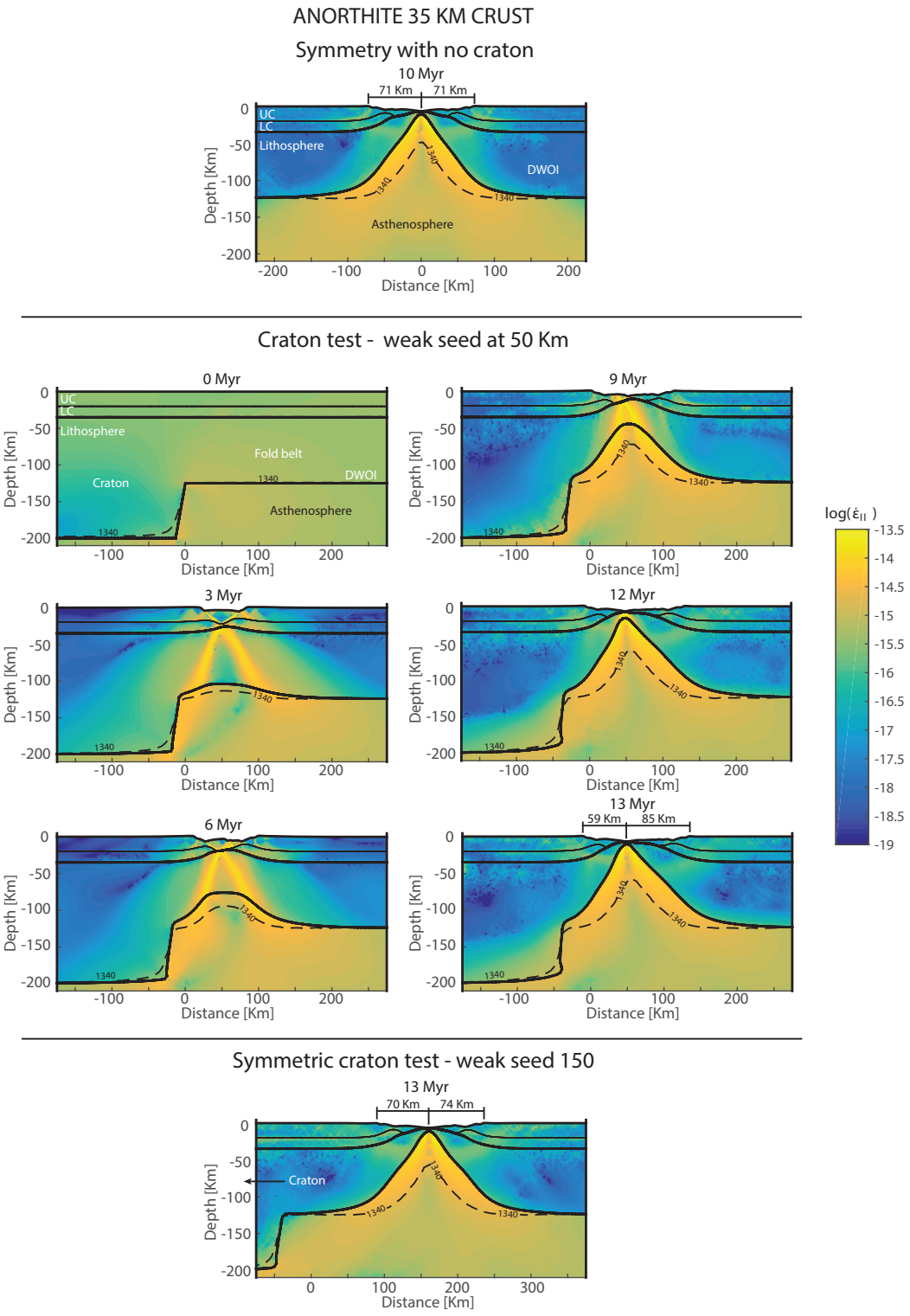

Figure 6: Evolution and architectures of anorthite lower crust (35 km thick)

4.4 ANORTHITE 40 KM CRUST (Fig. 7)

4.4.1 No craton with different polarities

In an initial phase wide extension occurs symmetrically along the model due to a smaller coupling of the deformation in the upper crust and lower crust than in tests with granulite. Eventually, when the crust becomes thin enough, strong coupling occurs and a pocket of low-viscosity is developed in the lower crust that results in sequential faulting and asymmetry. Here, the asymmetry of the width of the margins is small. However, there is a large asymmetry in the geometry of the lithosphere. This is due to the fact that the thinned lithosphere developed during the first phase is attached to one of the margins while the sequential faulting develops at the edge of this thinned lithosphere. Again, polarity of the asymmetry is random in tests without a craton.

4.4.2 Craton test - weak seed at 50 km

Asymmetry in tests with cratons is similar to the one shown in tests without a craton. However, the polarity of the asymmetry is always such as that the narrow margin develops near the craton and the wide margin opposite to it. This occurs because the low-viscosity pocket that appears in the second phase of extension is favoured by an asymmetric up-welling of the mantle (see 5 and 10 Myr).

4.4.3 Craton tests with different polarities - weak seed 150

When rifting develops far away from the influence of the craton the polarity of the asymmetry becomes random as in tests with no craton.

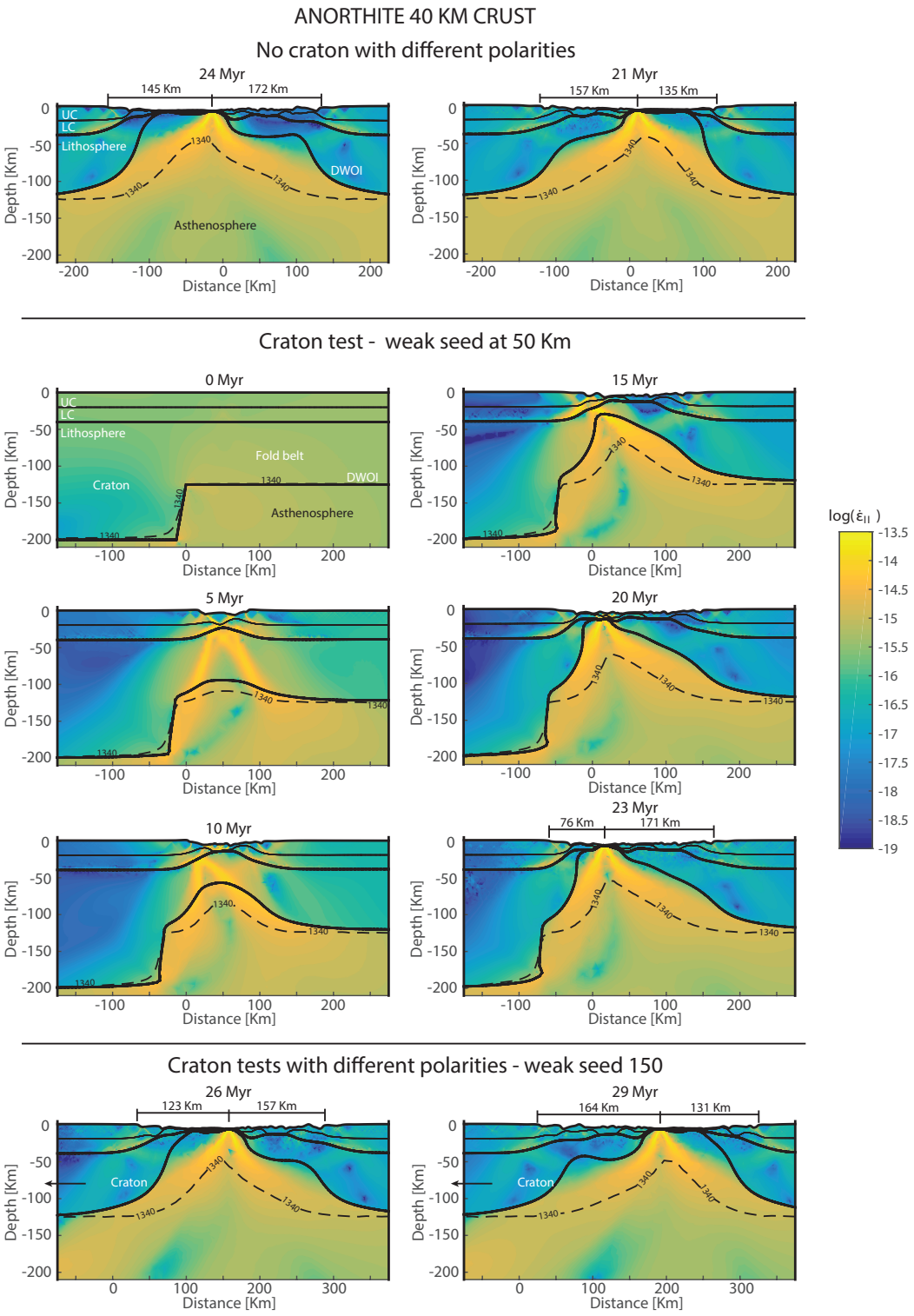

Figure 7: Evolution and architectures of anorthite lower crust (40 km thick)

4.5 QUARTZITE 35 KM CRUST (Fig. 8)

4.5.1 No craton with different polarities

Very little asymmetry is observed in these models. This is due to a very weak lower crust with creep behaviour. Consequently, extension spans along a broad area not allowing for any shear zone in the lower crust to dominate.

4.5.2 Craton test - weak seed at 50 km

Slight asymmetry is observed in tests with cratons. In these tests this is not due to an asymmetric up-welling of the mantle. In this case lower temperatures of the lower crust at the craton limit the development of a low-viscosity channel, while a low viscosity channel extends far away from the rift axis inside the fold belt (see 8, 12, 16, 19 Myr). This allows for faults to root further away from the rift axis in the fold belt side which increases the margin width.

4.5.3 Craton tests with different polarities - weak seed 150

When rifting takes place far away from the craton the polarity of the asymmetry becomes random.

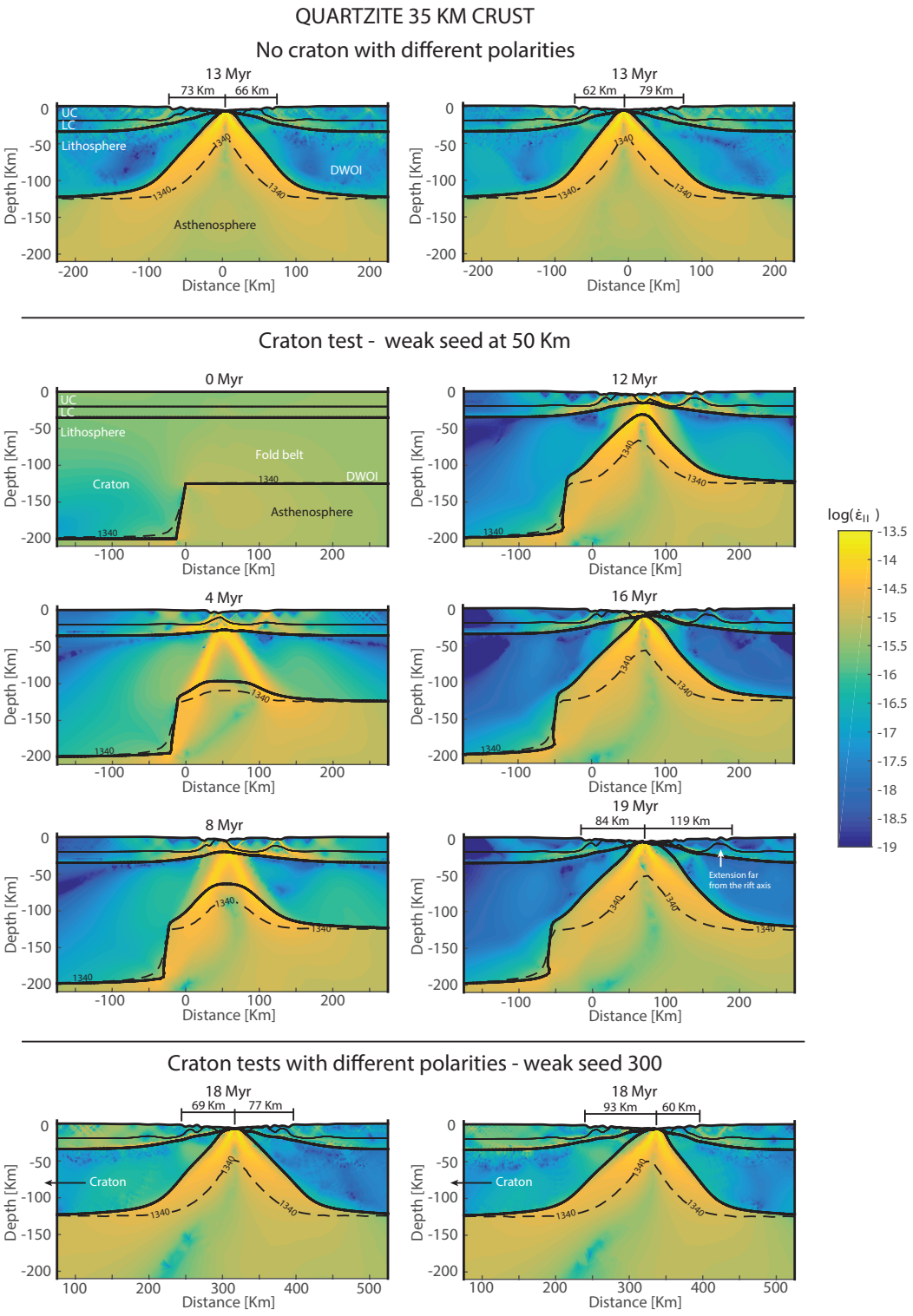

Figure 8: Evolution and architectures of quartzite lower crust (35 km thick)

4.6 QUARTZITE 40 KM CRUST (Fig. 9)

4.6.1 No craton with different polarities

Strong asymmetry is observed in this models. In an initial phase the extension is wide and symmetric. Eventually, a fault is favoured and one of the branches of the channel of low viscosity develops into a smaller low viscosity pocket which dominates deformation until breakup.

4.6.2 Craton test - weak seed at 50 km

In tests with cratons the larger branch of the low viscosity channel developed under the fold belt allows for decoupling between mantle and crustal deformation (see 12 and 24 Myr). As a consequence a lot of strain is accommodated by this branch which results in a large viscosity pocket dipping towards the fold belt which dominates deformation until breakup. This results in a polarity of the asymmetry opposite to what we observed in the previous models, thus the widest margin developed in the craton side and the shortest opposite to it. Note that in this case the mantle and crustal deformations are completely decoupled so that the factor responsible for rift migration is the contrast in crustal strength at the border of the craton, and not the asymmetric mantle flow.

4.6.3 Craton tests with different polarities - weak seed 150

Different geometries and polarities of the asymmetry are observed in tests where the craton is far away from the rift axis.

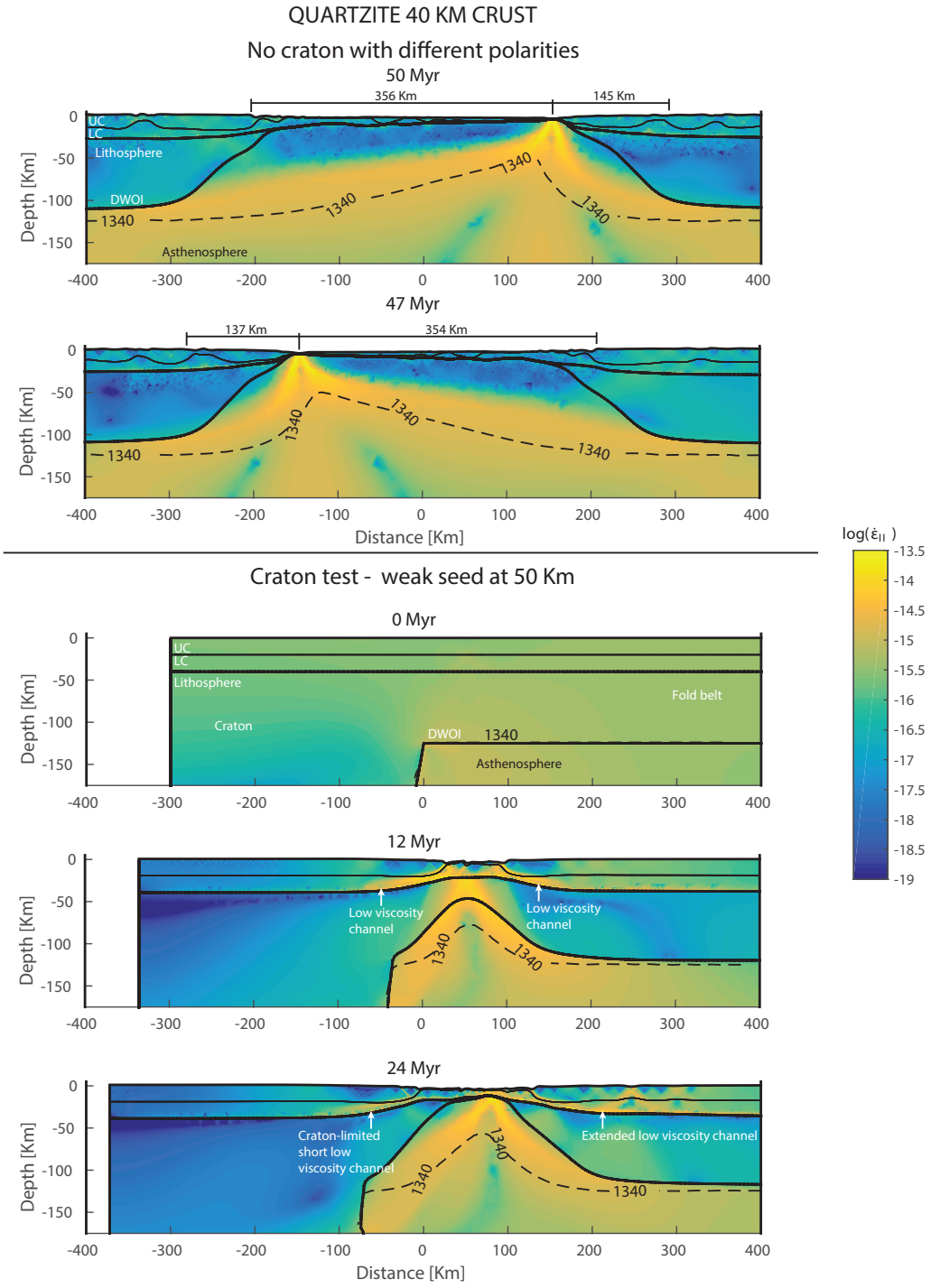

Figure 9: Evolution and architectures of quartzite lower crust (40 km thick)

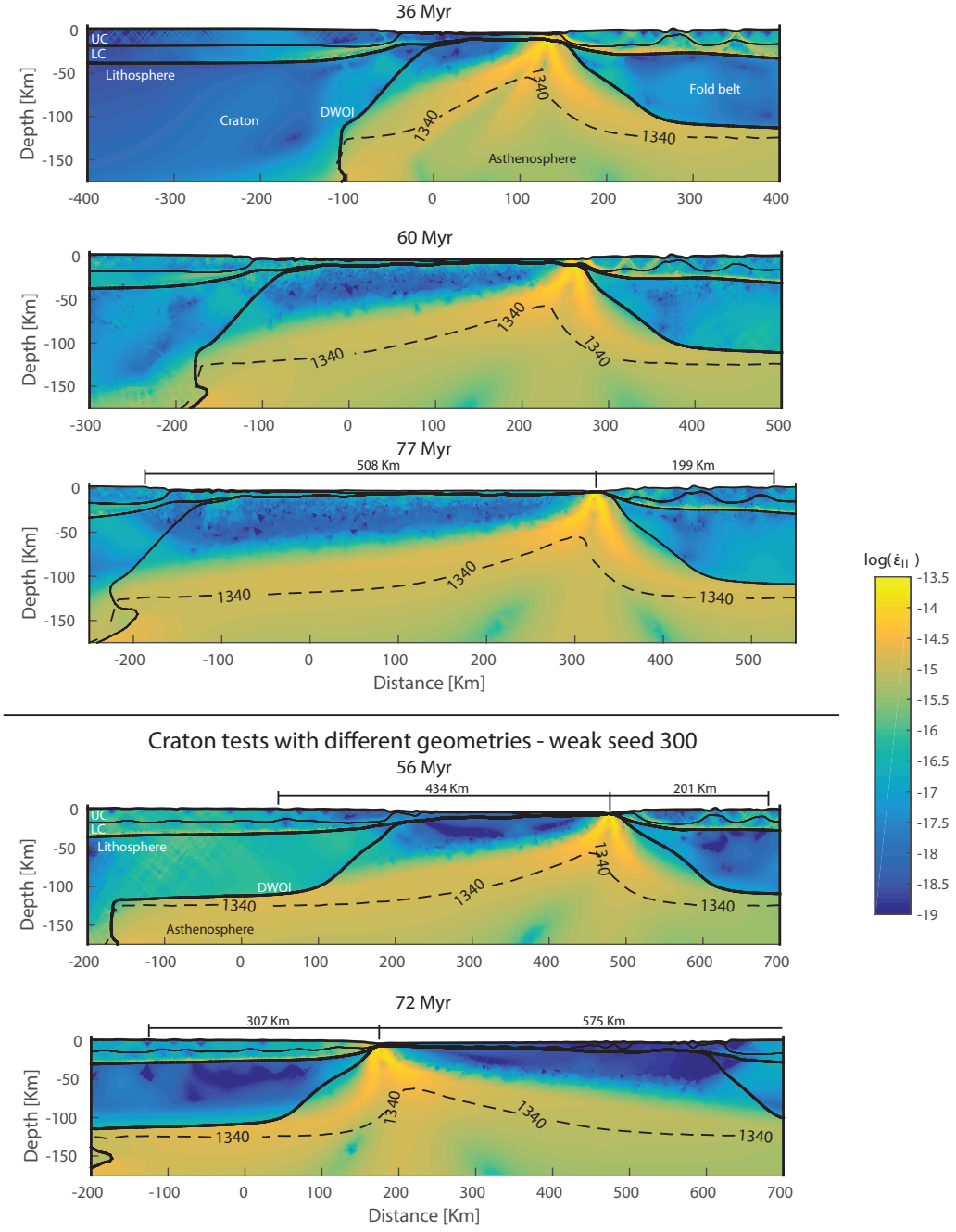

Figure 9: Evolution and architectures of quartzite lower crust (40 km thick)

References

P. Ball, G. Eagles, C. Ebinger, K. McClay, and J. Totterdell. The spatial and temporal evolution of strain during the separation of Australia and Antarctica. *Geochemistry, Geophysics, Geosystems*, 14(8):2771–2799, 2013. doi: 10.1002/ggge.20160. URL http://dx.doi.org/10.1002/ggge.20160.

S. Brune, C. Heine, M. Pérez-Gussinyé, and S. V. Sobolev. Rift migration explains continental margin asymmetry and crustal hyper-extension. *Nature Communications*, 5, 2014. doi: 10.1038/ncomms5014. URL http://dx.doi.org/10.1038/ncomms5014.

N. G. Direen, H. M. J. Stagg, P. A. Symonds, and J. B. Colwell. Dominant symmetry of a conjugate southern Australian and East Antarctic magma-poor rifted margin segment. *Geochemistry, Geophysics, Geosystems*, 12(2), 2011. doi: 10.1029/2010GC003306. URL http://dx.doi.org/10.1029/2010GC003306.

N. G. Direen, H. M. J. Stagg, P. A. Symonds, and I. O. Norton. Variations in rift symmetry: cautionary examples from the Southern Rift System (Australia-Antarctica). *Geological Society, London, Special Publications*, 369(1):453–475, 2012. doi: 10.1144/SP369.4. URL http://dx.doi.org/10.1144/SP369.4.

I. Fitzsimons. Proterozoic basement provinces of southern and southwestern Australia, and their correlation with Antarctica. *Geological Society, London, Special Publications*, 206(1):93–130, 2003.

C. Heine, J. Zoethout, and R. D. Müller. Kinematics of the South Atlantic rift. *Solid Earth*, 4(2): 215–253, 2013. doi: 10.5194/se-4-215-2013. URL http://dx.doi.org/10.5194/se-4-215-2013.

G. Hirth and D. Kohlstedt. Rheology of the upper mantle and the mantle wedge: A view from the experimentalists. In J. Eiler, editor, *Inside the subduction factory*, pages 83–105. AGU, 2003. ISBN 0-87590-997-3.

R. Ménot, G. Duclaux, J. Peucat, Y. Rolland, S. Guillot, M. Fanning, J. Bascou, D. Gapais, A. Pecher, et al. Geology of the Terre Adélie craton (135–146 e). In *Antarctica: A Keystone in a Changing World–Online Proceedings of the 10th ISAES, edited by AK Cooper and CR Raymond et al., USGS Open-File Report*, volume 1047, 2007.

J. S. Myers. The generation and assembly of an Archaean supercontinent: evidence from the Yilgarn craton, Western Australia. *Geological Society, London, Special Publications*, 95(1):143–154, 1995. doi: 10.1144/GSL.SP.1995.095.01.09. URL http://dx.doi.org/10.1144/GSL.SP.1995.095.01.09.

E. Rybacki and G. Dresen. Dislocation and diffusion creep of synthetic anorthite aggregates. *Journal of Geophysical Research: Solid Earth*, 105(B11), 2000. doi: 10.1029/2000JB900223. URL http://dx.doi.org/10.1029/2000JB900223.

H. Stagg and A. Reading. Crustal architecture of the oblique-slip conjugate margins of George V Land and southeast Australia. In *Proceedings of Antarctica: A Keystone in a Changing World.*

Online Proceedings for the 10th International Symposium on Antarctic Earth Sciences. US Geological Survey, Open-File Report, volume 1047, pages 1–6, 2007.

J. Totterdell, B. Bradshaw, and J. Willcox. Structural and tectonic setting of the Great Australian Bight. In G. W. O'Brien, E. Paraschivoiu, and J. E. Hibburt, editors, *Petroleum Geology of South Australia*, volume 5, pages 1–57. Primary Ind. and Resour., South Australia, 2003.

D. Turcotte and G. Schubert. *Geodynamics*. Cambridge University Press, 2002. ISBN 9780521666244.

L. T. White, G. Gibson, and G. S. Lister. A reassessment of paleogeographic reconstructions of eastern Gondwana: Bringing geology back into the equation. *Gondwana Research*, 24(3):984–998, 2013.

K. Wilks and N. Carter. Rheology of some continental lower crustal rocks. *Tectonophysics*, 182(1-2): 57–77, October 1990.

Chapter 5

Rheological implications of sediment transport for continental rifting and its impact in margin geometry and major unconformities

M. Andrés-Martínez, M. Pérez-Gussinyé, J. Armitage, and J. P. Morgan. Rheological implications of sediment transport for continental rifting and its impact in margin geometry and mayor unconformities. *Planned for submission in*, 2016a

Authors contribution

MA designed the research in discussion with MP and JM. JA programmed the surface processes function. MA programmed the tectonic model and coupled it with the surface processes function in discussion with MP and JM. MA programmed the time-line processing and plotting functions in discussion with MP. MA interpreted the seismic sections in discussion with MP. MA designed the tests and analysed the results in discussion with MP and JM. MA wrote the manuscript with the supervision of MP, JA and JM.

Rheological implications of sediment transport for continental rifting and its impact in margin geometry and major unconformities

Miguel Andrés-Martínez[a,*], Marta Pérez-Gussinyé[a,b,c,**], John Armitage[d,**], Jason Phipps Morgan[a,**]

[a] *Royal Holloway University of London, Earth Sciences*
[b] *MARUM - Center for Marine Enviromental Sciences*
[c] *Bremen University, Geosciences*
[d] *Institut de Physique du Globe de Paris*

Abstract

The inner dynamics of the Earth such as mantle convection, geochemical reactions and isostasy have been typically interpreted as the main engine of plate tectonics and crustal deformation. However, nowadays it is well established that processes transporting material along the surface of the Earth influence the inner dynamics. Surface processes play a key role particularly during rifting, where great subsidence rates occur at synrift basins while shoulder uplift provides rock to be eroded for later infilling of these basins. Erosion implies unloading of the crust which favours uplift, and sedimentation at basins results in loading which favours subsidence. Consequently, erosion and sedimentation amplify stresses and the flexural response of the lithosphere in situations with extensive faulting. These changes to the stress field may be large enough to result in changes in the evolution of rifting and its modes of extension. Additionally, higher subsidence rates and thermal blanketing due to sediments may result in higher geotherms and consequently, a weaker/more-viscous behaviour of the crustal rocks. This would also have a large impact on the deformation style during extension. Here, we explore the interactions between surface processes and tectonics using numerical modelling. Experiments are run with the absence of sediment transport and with different sediment transport regimes for 35 and 40 km crustal thicknesses. Tests with higher transport coefficient show more effective localization of deformation into upper crustal faults which results in effective crustal thinning, larger blocks and longer-lived faults. Our experiments also prove that more effective surface processes reduce the length of margins generated by sequential faulting. For our end member situations, high sedimentation rates lead to pure shear extension of the crust induced by high temperatures, which finally results in broad extension and symmetric margins. Furthermore, our model allows for the recovery of predicted sediment stratigraphic patterns. Major unconformities that separate synrift from sag-basin-type sediments are observed in these pseudo-strata patterns. Here, we also address the meaning of these major unconformities and their relationship to the time of breakup.

Keywords: surface/tectonic interplays, sedimentation, uncomformities, numerical modelling

*Principal corresponding author
**Corresponding authors
Email addresses: m.andres-martinez.2011@live.rhul.ac.uk (Miguel Andrés-Martínez), marta.perez-gussinye@rhul.ac.uk (Marta Pérez-Gussinyé), (John Armitage), jason.morgan@rhul.ac.uk (Jason Phipps Morgan)

1. Introduction

Rifting is an extraordinarily complex system in which many processes and interplays take place. These processes range from erosion and sedimentation at the surface, to deeper processes such as faulting, flexure due to loading/unloading, lithospheric and crustal thinning, mineral phase changes, convection, mantle exhumation and melting.

Nowadays it is widely accepted that surface processes can have an effect on both shallow and deeper Earth dynamics. For example, numerical models that allow for dynamic topography solve a sinking slab problem better than models with free-slip top surface (Kaus et al., 2010). It has also been observed that shoulder uplift in passive margins can persist more than 50 Myr after breakup which has been explained by the tradeoffs between flexural bending, unloading at the shoulder due to erosion and loading at the marginal basins due to sedimentation (Weissel and Karner, 1989; Redfield and Osmundsen, 2012). During rifting an input of sediments from farfield sources have proven to favour narrow rifting (Bialas and Buck, 2009), and also to control the mode transition from asymmetric basins to symmetric due to loading of the hanging wall (Buiter et al., 2008). Additionally, Clift et al., 2015 proved that an increase of sediment influx related to a climate change during postrift is capable of inducing ductile lower crustal flow and consequent larger subsidence rates than expected from thermal subsidence.

Examples in nature seem to support such interplays between surface processes and tectonics. Here, we compare the West Iberian Margin (WIM) with the Great Australian Bight (GAB), both of them representative of ultra-slow magma-poor margins, although they differ in the amount of synrift deposition.

The WIM shows little synrift sediment infilling (Boillot et al., 1988). The crystalline crust is overlain by a succession of sandstones, conglomerates and Thitonian carbonates of possible prerift origin, and a synrift succession of at least 1 km thickness at half-graben depocenters and an estimated maximum of 2 km by seismic imaging of line IAM11 (Fig. 1a). Seismic sections also show a large number of crustal blocks limited by faults that thin the crust smoothly by sequential faulting (Ranero and Pérez-Gussinyé, 2010). Although these faults account for great offsets little sediment infilling is observed.

The GAB exhibits thicker synrift sediments which together with postrift exceed 15 km thickness at the depocenter of Ceduna basin (Stagg et al., 1990). Synrift sediments date from Late Jurassic-Early Cretaceous and are deposited at half-grabens which bounding faults dip southwards (Totterdell et al., 2000). Based on seismic imaging (line AGS0199 0900) maximum 5 km thickness of synrift sediments are estimated to be deposited at a major depocenter (Fig. 1b). This major depocenter is found along the GAB bounded by large offset faults such as the Wallaroo Fault System (Talwani et al., 1979; Falvey and Mutter, 1981; Totterdell et al., 2000). Abrupt necking of the crust is inferred from sonobuoy data in the vicinity of these faults (Talwani et al., 1979; Direen et al., 2012).

The observations at the WIM and GAB suggest that sediment loading influences the crustal architecture at margins. Margins with larger sediment loads such as the GAB have major faults due to higher stresses resulting in abrupt thinning of the crust. Margins with little sediment loads contain a larger number of faults leading to a smooth thinning of the crust.

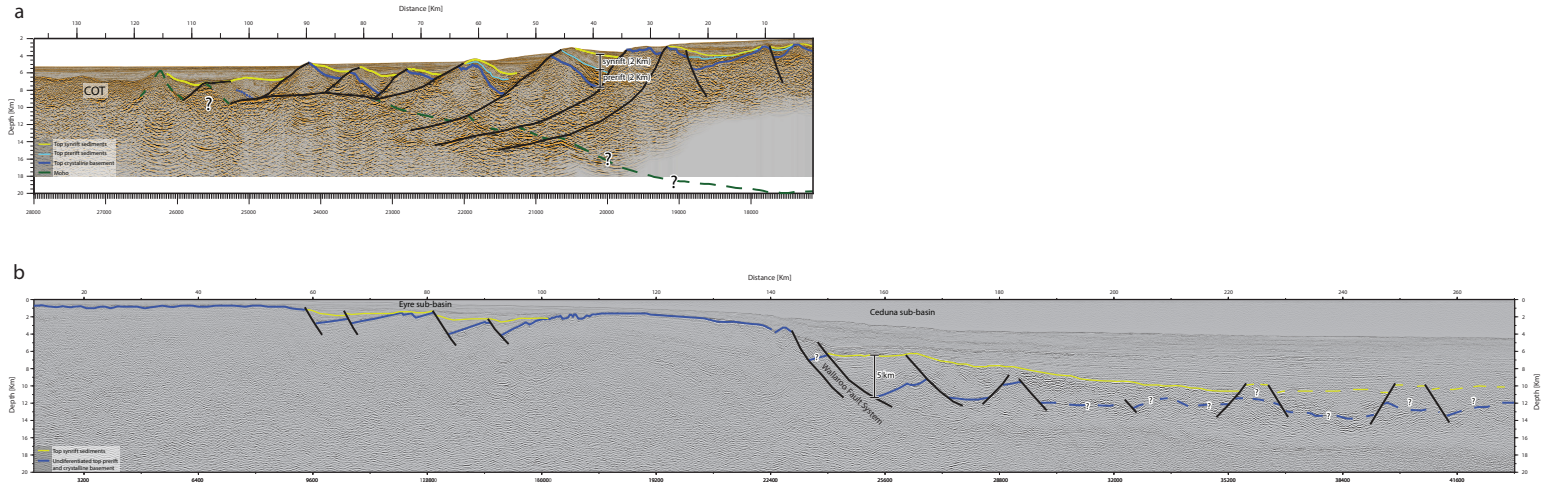

Figure 1: Depth-migrated profiles of West Iberia and South Australia non-volcanic passive margins. a) West Iberian Margin seismic section, line IAM11 modified from (Ranero and Pérez-Gussinyé, 2010). Synrift sediments do not exceed the 2 km thickness at the largest depocenter. Crust is smoothly thinned by the presence of numerous faults. b) Great Bight Basin seismic section, line AGS0199 0900 (Pérez-Gussinyé et al., in prep.). Profile includes Eyre and Ceduna sub-basins. Note that sediments contenporary of the Wallaroo fault system have a thickness of at least 5 km at the depocenter.

On the other hand, regional scale unconformities are observed and commonly associated with breakup (Falvey, 1974). The breakup unconformity is typically explained as a result of thermal relaxation of upwelled asthenosphere with the consequent increase on mantle density which allows for regional subsidence after synrift faulting. However, other different processes could likewise result in the erosion of synrift sediments and later broad subsidence required for the formation of the breakup unconformities, such as: phase changes in lower crustal or mantle lithospheric rocks (Podladchikov et al., 1994; Armitage and Allen, 2010), necking of the lithosphere with consequent flexural relaxation (uplifting of basins and overdeeping in the flanks) (Braun and Beaumont, 1989), and erosion during the final uplift phase associated with a last pulse of mantle upwelling with later subsidence (Falvey, 1974). Furthermore, the tectonic meaning of the breakup unconformities remains controversial. Postrift sequences onlapping synrift observed in some sectors of proximal margins turn into synrift-like geometries in distal sectors (i.e. at the Great Australian Bight) (Gillard et al., 2015). This is interpreted to be the result of rift migration and polyphase rifting. This interpretation invalidates concepts such as a time-synchronous 'breakup unconformity', and prerift, synrift and postrift as time-synchronous terms (Ranero and Pérez-Gussinyé, 2010; Pérez-Gussinyé, 2013; Gillard et al., 2015).

This work will therefore address two main questions relating to surface processes and tectonics: 1) do surface processes have an important impact on passive margin architecture and how does loading/unloading affect faults, temperature field and crustal rheology, and 2) what are the possible tectonic settings that lead to 'breakup-like' unconformities and do they actually coincide in time with breakup.

In order to approach both the effect of surface processes on the development of margin architecture and the tectonic meaning of breakup unconformities we have developed a new 2D visco-elasto-plastic geodynamic model based on MILAMIN mechanical and thermal solvers (Dabrowski et al., 2008). This code simulates dynamic topography by using a stress-free surface, and accounts for strain softening, shear heating and surface processes. Erosion and sedimentation are modelled as a function of sediment transport. Lines in the sediments of same depositional age are tracked along the model so that stratigraphy and unconformities can be recovered from the model.

2. Methodology

2.1. Tectonic model

Here, we model a 2D section of the continental lithosphere and upper asthenosphere using numerical codes. This 2D volume of virtual rock is divided in three layers of different properties: 1) upper crust (UC), 2) lower crust (LC), and 3) mantle. Mantle is subsequently divided by a 35 km transition into lithospheric dry mantle and asthenospheric wet mantle, where rheologies are calculated based on depletion values and tracked with the material flow along time. Then, the model domain is subjected to half-extension velocities on the sides to simulate far-field stretching. In order to solve deformation due to extension, temperatures and pressures inside the section we use a visco-elasto-plastic finite element code based on MILAMIN solvers (Dabrowski et al., 2008).

We solve Stokes equation for the incompressible viscous flow and elasticity written in terms of velocities

(Moresi et al., 2003; Kaus, 2010), to calculate velocities, stresses and strains due to the given extension:

$$\frac{\partial}{\partial x_i}\left[\eta_{eff}\left(\frac{4}{3}\frac{\partial v_i}{\partial x_i}-\frac{2}{3}\frac{\partial v_j}{\partial x_j}\right)\right]+\frac{\partial}{\partial x_j}\left[\eta_{eff}\left(\frac{\partial v_i}{\partial x_j}+\frac{\partial v_j}{\partial x_i}\right)\right]-\frac{\partial P}{\partial x_i}=-\rho g_i-\chi_{vep}\frac{\partial \tau_{ii}^{old_J}}{\partial x_i}-\chi_{vep}\frac{\partial \tau_{ij}^{old_J}}{\partial x_j}, \quad (1)$$

where η_{eff} is the effective viscosity, v is the velocity vector, x represents the axis of the coordinate system, P is the pressure, ρ density, g is the gravity vector, τ^{old_J} are the Jaumann-rotated previous time step stresses and χ_{vep} is the elastic factor defined as:

$$\chi_{vep}=\frac{\eta_{eff}}{\mu\Delta t}, \quad (2)$$

where μ is the elastic shear modulus. In order to introduce incompressibility we couple the barometric equation of the state into the system:

$$\bigtriangledown\cdot v+\frac{P}{\kappa}=0, \quad (3)$$

where κ is equivalent to the bulk modulus and is chosen to be a large value ($10^6\times max(\eta_{eff})$) to be used as a penalty factor for the pressure formulation (Hughes, 2000).

Temperatures are solved by the heat conservation equation:

$$\rho C_p\frac{DT}{Dt}=k\frac{\partial T}{\partial x_i}+H, \quad (4)$$

where C_p is the heat capacity, T is temperature, t is time, k the thermal conductivity and H is the volumetric heat production composed by radioactive and shear heating components.

The effective viscosity η_{eff} is calculated by following the scheme described in Moresi et al., 2003, so that our formulation accounts for diffusion and dislocation creeps (Hirth and Kohlstedt, 2003), elasticity and plasticity:

$$\eta_{eff}=\frac{1}{\frac{1}{\eta_c}+\frac{1}{\Delta t\mu}+\frac{G}{\tau_{II}}}, \quad (5)$$

where Δt is the given time step, G is the plastic flow potential, τ_{II} is the square root of the second invariant of the deviatoric stress and η_c is the creep viscosity such as:

$$\eta_c=\frac{1}{\frac{1}{\eta_{dis}}+\frac{1}{\eta_{dif}}}. \quad (6)$$

In Eq. 6, dislocation η_{dis} and diffusion η_{dif} creep viscosities are defined by the flow rule:

$$\eta_{dis/dif}=FB^{-\frac{1}{n}}\dot{\varepsilon}_{II}^{\frac{1-n}{n}}exp\left(\frac{E^*}{nRT}\right), \quad (7)$$

which parameters for both mechanisms and rocks are shown in table 1.

After the discretization of the spatial domain we use the finite element method to numerically solve Eqs. 1, 3 and 4. Here, we use a high resolution triangular grid (1 km UC, 5 km LC and mantle) tracked along with the material (Lagrangian mesh). When high deformations take place in a Lagrangian mesh (i.e. in shear zones), this may result in extremely non-equilateral triangles, in which case the finite element method may not return an accurate solution for the system. In order to avoid this issue a remesh with a

Table 1: Model parameters. Rheological parameters from Wilks and Carter, 1990; Gleason and Tullis, 1995; Hirth and Kohlstedt, 2003. Remaining parameters from Turcotte and Schubert, 2002. Diffusion creep B is calculated using a grain size d of 6 mm. Wet olivine water fugacity fH_2O is 500 MPa (in C_{OH} ppm H/Si).

Rock/ mineral aggregate	Wet quartzite (upper crust)	Mafic granulite (strong lower crust)	Dry olivine (lithospheric mantle)	Wet olivine (asthenospheric mantle)
Dislocation pre-exponential factor $log(B)$ [Pa^{-n} s^{-1}]	-28.0	-21.05	-15.56	-15.05
Dislocation exponent n	4.0	4.2	3.5	3.5
Dislocation activation energy E^* [kJ mol^{-1}]	223	445	530	480
Diffusion pre-exponential factor $log(B)$ [Pa s^{-1}]	-	-	-8.65	-8.66
Diffusion exponent n	-	-	1	1
Diffusion activation energy E^* [kJ mol^{-1}]	-	-	375	335
Shear modulus μ [GPa]	36	40	74	74
Thermal conductivity k [W m^{-1} K^{-1}]	2.1	2.5	3.3	3.3
Heat capacity C_p [J kg^{-1} K^{-1}]	1200	1200	1200	1200
Radiogenic heat production H_p [μ W m^{-3}]	1.3	0.2	0	0
Densities ρ [kg m^{-3}]	2700	2850	3300	3300

subsequent variable resampling takes place when extremely distorted triangles appear.

Additionally, the model includes a stress-free surface at the top of the model with a free-surface stabilization algorithm (Andrés-Martínez et al., 2015) in order to accurately model dynamic topography and to avoid instabilities typically associated with free surfaces. The model also accounts for strain weakening where previously deformed materials are weaker than non-deformed materials. This allows for the simulation of faults and shear zones because deformation will localize into weakened bands which will become increasingly weaker and narrow. Strain weakening is justified for the plastic behaviour of rocks due to a cohesion loss when yielding criteria is met. This loss in cohesion is associated with fault planes since they represent a discontinuity to the rock's integrity. Fluids penetrate faults from the surface, increasing the fluid pressure, decreasing the friction angle and also inducing mineral transformations, which together are used to justify the friction angle softening (Bos and Spiers, 2002; Handy and Stünitz, 2002). Here, we choose to use friction angle softening alone, because cohesion contributes only a small amount to the yield stress in comparison with the friction coefficient which is multiplied by the pressure. Softening is applied as a linear function of the historic strain invariant (Huismans and Beaumont, 2007), so that for no deformation the friction angle is 30° and for historic strains $\geq$1 the friction angle is 15°. Furthermore, we include viscous weakening by linear increasing of the pre-exponential factor of the dislocation creep law B (Eq. 7), which accounts for weakening due to grain size reduction by dislocation mechanism and crystallographic preferred orientations (Karato and Wu, 1993; Hansen et al., 2012). The viscous strain weakening rule is such that the pre-exponential factor remains the same for no deformation and it linearly varies with deformation up to 30 times larger than the original value when the historic (or accumulated) strain is $\geq$1.

Together, free surface and strain weakening allow for the developing of faults and associated relief,

subsidence and elastic response of the topography to the tectonic and geomorphological loading and unloading. Consequently, accommodation space for sedimentation and positive topographies for erosion are made available, which is critical for this study.

Additional rules included in our model are shear heating, and density dependency on temperature and the degree of depletion in the mantle. The degree of depletion is defined by an initial profile tracked with the material along time. The initial depletion profile has values of 0 for depths below 160 km, from 160 to 60 km depletion varies linearly towards 0.1 values, and above 60 km depletion remains constant at 0.1. Lithospheric mantle and asthenosphere are mechanically differentiated by dry and wet olivine rheologies respectively (table 1). We use wet olivine rheologies where the depletion is 0, and dry olivine where the depletion is above 0.04 (above 125 km depth in initial profiles) (Morgan et al., 1995; Morgan, 1997; Hirth and Kohlstedt, 2003). These rheologic parameters linearly vary with the depletion profile in the lithosphere-asthenosphere transition, where dry olivine contribution increases with increasing depletion and wet olivine contribution increases with decreasing depletion. For simplicity, melting and depletion dependency on melting are not implemented, which we consider a valid assumption in this context of ultra-slow magma-starved rifting.

Half-extension velocities of 5 mm/yr (ultra-slow) are applied as lateral boundary conditions for the model while subsequent half extension rates are applied at the bottom boundary (upwelling of the asthenosphere by pure shear approach) for the mechanical problem. In order to avoid strong influence of the boundary conditions in the deformation styles we use a relatively large modelling domain (500×400 km). Additionally, we impose a weak seed at the middle of the domain to nucleate rifting far from the boundaries so that we avoid boundary-related artefacts in the deformation. The weak seed is a 10×20 km region with the center located at 30 km depth and where temperature is increased at the initial time step by 100°C following a 2D Gaussian function. This increase of temperature makes viscosity smaller in that region. Once the model is started the seed is allowed to thermally relax so that it only helps for the nucleation of rifting but does not contribute to later phases.

Thermal boundary conditions are 0°C at the surface (including sediment surface), and 1350°C below 125 km where heat transport is assumed to occur adiabatically by convection.

2.2. Geomorphologic model

Topographic variations can be due to both tectonic deformation and the downslope transport of rocks along the surface towards areas of lower relief. For transport to happen, basement rocks need to loose cohesion by transforming into sediment through erosion and weathering. Therefore, to model sediment transport it is necessary to define how material from the basement is transferred by erosion or weathering to the sediment/regolith mobile layer. One possible assumption is to consider a constant sediment thickness so that the sediment production (i.e. erosion) dominates landscape evolution. This type of assumption is known as detachment-limited model (Kirkby, 1971; Carson and Kirkby, 1972; Howard, 1994; Dietrich et al., 2003). As the sediment production can be defined as a function of the slope, steep slopes will be eroded faster than low ones, which leads to landscapes similar to the river profiles, with steeper slopes towards the drainage divides. However, this model does not allow for sedimentation. A second possibility is to assume that there is always availability of sediment/regolith at the surface of the model and consequently, that the sediment transport dominates landscape evolution. Then, we can define a diffusion-concentrative equation

for sediment transport in 1D such as:

$$\frac{Dh}{Dt} = U - \frac{\partial q_s}{\partial x}, \tag{8}$$

where h is the topography, t is time, U is uplift, q_s represents the sediment flux and x the horizontal coordinate (Culling, 1960; Smith and Bretherton, 1972). This implies that the temporal topographic variation for an element depends only in the uplift and in the difference between the sediment flux into the element and the out flux and, consequently, that the landscape evolution is a function of the sediment transport spatial variation. This approach is known as the transport-limited model (Kirkby, 1971; Carson and Kirkby, 1972; Howard, 1994; Dietrich et al., 2003). Here we choose this approach for our landscape evolution model since it allows for sedimentation to occur.

It is possible to define the sediment transport flux q_s in terms of water flux q_w such as:

$$q_s = -(K + kq_w^n)\frac{\partial z}{\partial x}, \tag{9}$$

where K is the slope diffusivity, k is the transport coefficient, and $n \geq 1$ is the power law that defines the type of relationship between the sediment transport and the water flux (Smith and Bretherton, 1972; Simpson and Schlunegger, 2003). Therefore, our model accounts for hillslope diffusion processes where the topography will tend to a dispersive diffusion (Culling, 1960) and fluvial transport processes which result on concentrative diffusion due to water run off (Graf, 1984). For simplicity in the solution we choose a linear relationship between sediment transport and water flux ($n = 1$). The water flux can be related to the water discharge/effective rainfall α such as:

$$\frac{\partial}{\partial x}(\mathbf{n}q_w) = -\alpha, \tag{10}$$

where $\mathbf{n}$ is an unit vector directed down the surface gradient (Smith and Bretherton, 1972). By assuming a constant α and integrating Eq. 10 over the surface in the downstream direction, then we obtain:

$$q_w = \alpha x_d, \tag{11}$$

where x_d is the downstream distance from the drainage divide. By substituting Eqs. 9 and 11 into 8 we obtain the 1D sediment mass conservation equation for combined hillslope and discharge-dependent fluvial transport:

$$\frac{Dh}{Dt} = U + \frac{\partial}{\partial x}\left((K + k\alpha x_d)\frac{\partial h}{\partial x}\right), \tag{12}$$

where downstream distance x_d is calculated at each time step as the distance from the topographic highs to the valley floors. Because q_w is dependent to the length of the drainage, the model mimics 1D landscapes similar to river profiles when the fluvial processes are dominant.

Note that Eq. 8 is defined in an Eulerian frame of reference. However, our model works under a Lagrangian frame. In order to transfer this equation into a Lagrangian frame of reference it is necessary to consider the definition of the material time derivative (Malvern, 1969):

$$\frac{Dh}{Dt} = \frac{\partial h}{\partial t} + v \cdot \nabla h, \tag{13}$$

where $\frac{Dh}{Dt}$ is the material time derivative, $\frac{\partial h}{\partial t}$ is the variation of the topography along time for a given

particle, v is the velocity and ∇h is the gradient of the topography which in 1D is equivalent to $\frac{\partial h}{\partial x}$. Then we can obtain $\frac{\partial h}{\partial t}$ in 1D for a given particle (Lagrangian frame) such as:

$$\frac{\partial h}{\partial t} = U - \frac{\partial q_s}{\partial x} - v_x \frac{\partial h}{\partial x}. \tag{14}$$

Here, the tectonic uplift U works like a source term. However, in our model surface processes are run over a static topography, which is obtained from the Stokes solution at the last time step (see section 2.3). Therefore, the uplift source term is not needed ($U = 0$). In our model the product of topographic slopes and velocities is relatively small in comparison with $\frac{\partial q_s}{\partial x}$. This allows us to neglect the term $v_x \frac{\partial h}{\partial x}$ which is convenient for simplicity. Then, the change in topography with time in our Lagrangian mesh can be defined as:

$$\frac{\partial h}{\partial t} = -\frac{\partial q_s}{\partial x}. \tag{15}$$

Substituting the sediment flux q_s as done in Eq. 12 one obtains the transport equation that we use in our model:

$$\frac{\partial h}{\partial t} = \frac{\partial}{\partial x}\left((K + k\alpha x_d)\frac{\partial h}{\partial x}\right). \tag{16}$$

Table 2 shows the parameters used in Eq. 16 for the numerical experiments done in this study.

Table 2: Sediment transport parameters

	Values			Reference
Surface processes time step δt_s [Kyr]	1			
Hill-slope diffusion K [m^2 yr^{-1}]	1			Flemings and Jordan, 1989, Martin and Church, 1997, Armitage et al., 2015
Discharge transport coefficient k	Low transport 10^{-3}	Intermedium transport 10^{-2}	High transport 1	Paola et al., 1992; Marr et al., 2000, Armitage et al., 2014
Precipitation rate α [m yr^{-1}]	1			Huffman et al., 2009

2.3. Coupling of tectonics and surface processes

Coupling between inner Earth dynamics and landscape evolution is done by first solving the tectonic model defined by Eqs. 1 and 4 for a time step δt, then advecting topography for δt with the solved velocities and finally solving for sediment transport (Eq. 16). This approach implies that sediment transport during δt occurs over a tectonically static topography previously calculated for the current time step. Therefore, this approach neglects the feedbacks between the load redistribution caused by the landscape model and the tectonic model during a given time step. This approach is valid because the wavelength and amplitude of the topographic changes due to sediment transport are sufficiently small that their relaxation time is large compared with the size of the flow solver time step δt (10 Kyr).

For stability reasons, we choose to run the sediment transport model for a number of smaller time steps δt_s (1 Kyr) which in total sum the tectonic time step δt. Once the new topography is calculated from the

sediment transport function, y-coordinates of the top nodes of the triangular grid are updated.

Variables for nodes and integration points of surface elements are resampled every time step after the topography update. In the case nodes or integration points are located out of the old mesh due to sedimentation (Fig. 2), then their temperature is set to be the top boundary condition value (0°C), historic strain and rotated stress values are set to 0, and viscosity and strain rate are set to be the average of the closest element in order to ensure model stability. Temperature boundary conditions remain at the top boundary independently of the nature of the exposed rock (basement or sediment).

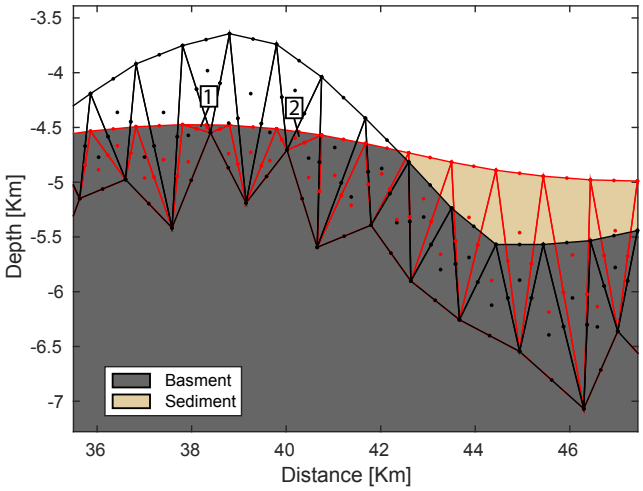

Figure 2: Topography after surface processes. Black triangles and dots represent surface elements and nodes of the old mesh before erosion/sedimentation. Red triangles and dots represent elements and nodes of the new mesh after erosion/sedimentation function is applied. In 1 and 2 erosion is large enough for the update of the topography to result in bad elements (non-Delaunay triangles). In this case a remesh is necessary. However, this example represents a extreme case, while in our models most of the time steeps need no remeshing since nor the erosion or the sedimentation make such large changes in the surface elements.

Additionally, we use tracers to follow previous time-step topographies (PTST) throught the time. Here, we choose to track PTSTs separated by a time lapse of 100 Kyr, since following every time step PTST (10 Kyr) is computationally very expensive. PTST are equivalent to time-lines in the sediments, meaning surfaces inside the sediments of syncronous depositional time. Once the model run finishes, we use a post-processing script to evaluate where erosion has occured in every PTST, so that we can plot sediment time-lines.

In summary, the scheme used here for coupling landscape evolution model and tectonics for a given time step δt is as follows:

1. Run the flow and thermal solvers (tectonic model) (Eqs. 1, 3 and 4) for δt, and obtain velocities, pressures and temperatures
2. Advect nodes with calculated velocities generating a new 'tectonic topography'
3. Advect previous time-step topographies (PTST), equivalent to sediment time-lines
4. Run the landscape evolution model for the new 'tectonic topography' for i number of δt_s time steps, where $\delta t_s = \delta t / i$
5. Update model topography with the final 'landscape-model topography'
6. Resample variables for updated elements

This scheme for coupling tectonics and landscape evolution is equivalent to the one used in Collignon et al., 2014.

Ideally, sediments should have different mechanical properties than the ones of the basement. However, this would imply that in our model we should include an extra high-resolution discontinuous layer to represent sediments. The resolution of this extra layer should be sufficiently high to have Delaunay triangles even if the sediment layer is as thin as a few meters (which is the case at the initial steps of the model). These extremely high resolutions are to be avoided because of the high computation time spent in Stokes solution. Some strategies to reduce the number of small elements could be used, such as to only generate an independent sediment layer when the sediment thickness is on the scale of the resolution set for the crust (1 km).

However, for simplicity, we assume that the sediment mechanical properties are the same as the upper crust (wet quartzite, table 1) and we include sediments into the upper crustal layer. This assumption is valid for shallow to intermediate depth sediments that deform in the elasto-plastic or brittle regime since the apparent viscosity is controlled by the yield criterion and not by the flow law parameters. However, deeper sediments at temperatures between 200-400°C are expected to deform by grain boundary diffusion creep driven by pressure solution (Rutter and Elliott, 1976; McClay, 1977). This deformation mechanism would result in larger strain rates for smaller stresses and therefore, lower apparent viscosities (Rutter and Elliott, 1976).

Lower effective viscosities of the sediments may change deformation inside sediments probably allowing for more distributed deformation at the sediment layer and detachment levels where viscosities are low. However, it is out of the scope of this manuscript to accurately model sediment deformation during diagenesis. Instead, we focus on basement deformation affected by sediment loads and thermal blanketing. Therefore, considering the difficulties previously mentioned, we choose to model sediments including them in the same layer as the upper crust and using the same flow parameters (wet quartzite).

3. Results

3.1. Tests without surface processes

First we display the results of models without surface processes to illustrate the general behaviour of the model and because they also serve as an end member case for this study. The evolution of two tests is shown in Fig. 3 where the initial crustal thickness is 35 and 40 km and where the lower crust is modelled with a mafic granulite rheology (Wilks and Carter, 1990).

At rifting initiation two main initial faults or shear zones nucleate at the weak seed, near the Moho, in both the 35 and 40 km crust models (Figs. 3a and f). While upper crust shear zones dip inwards in both models the behaviour of the lower crust is different. In the 35 km crust model the lower crustal shear zones dip inward, while in the 40 km crust model shear zones dip outward. This is related to the distance between the weak seed and the low-viscosity channel at the base of the crust (see the isoviscosity line at Figs. 3a and f). Minor upper crustal faults are also generated in the surrounding areas of the main shear zones. These minor faults root on a slightly smaller viscosity layer present at the base of the upper crust. The crustal block between the two conjugate main shear zones is subjected to strong subsidence which results in a graben geometry.

At 3 Myr the mode of extension changes from two symmetric dominant conjugated shear zones to multiple upper crustal faults that develop outwards of the initial main shear zones (Figs. 3b and g). These faults

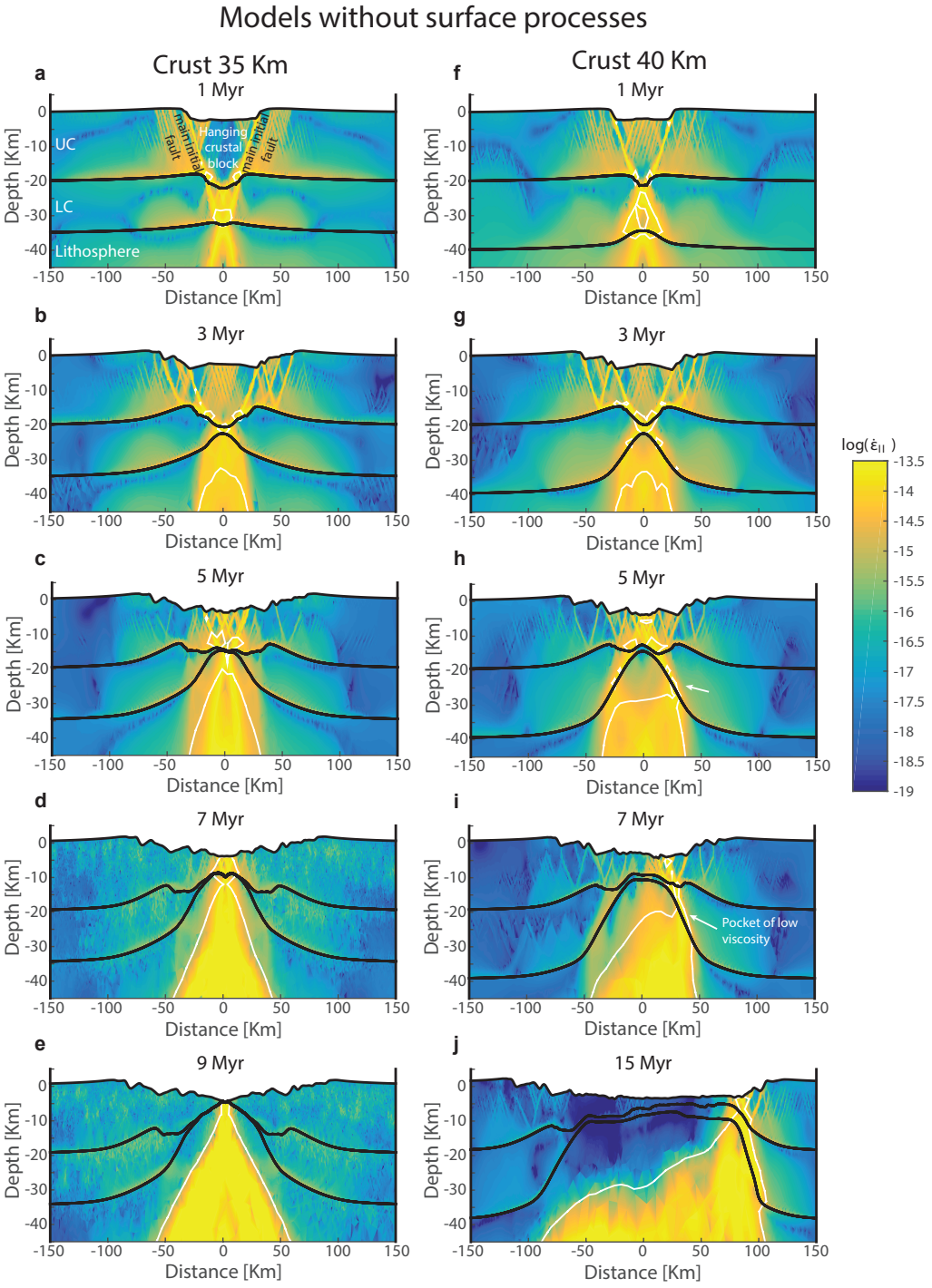

Figure 3: Strain rate evolution of rifting in the absence of surface processes for a mafic granulite lower crust. a, b, c, d and e illustrate the rifting evolution of a model with initial 35 km thick crust. f, g, h, i and j recover the rifting evolution of a model with initial 40 km thick crust. The white line represents a isoline of viscosity 10^{21} Pa s.

present symmetric dips with respect to the center of the model. The hanging crustal block located between the two groups of upper crustal faults of opposite dips starts to fault in the center due to high bending stresses. The upper crustal faults root on a detachment level at the base of the upper crust. These faults accommodate extension produced by the former main symmetric shear zones that are the main extensional feature in the lower crust. Now both shear zones at the lower crust dip outwards of the model, separating the two lower-crustal hanging walls from the mantle wedge below the extended upper crustal block. In both the 35 and 40 km crust models, the lower crustal shear zones have greatly thinned the lower crust in the region of localized deformation. Note that central lower crustal thickness is very similar in both 35 and 40 km crust models at 3 Myr, although the 40 km model has initially 5 km extra of lower crust to thin. This occurs because deeper lower crust implies higher temperatures and consequently a weaker rheology, which allows for accommodation of larger deformations in proportionally narrower regions.

After 5 Myr the outer-graben groups of faults are abandoned in favor of the faults that nucleated in the hanging wall of the graben (Figs. 3c and h). This occurs mainly because the hanging wall has been highly stressed by bending associated with the bounding graben faults. In the case of 35 km crust, the lower crust has been removed completely from the center of the rift, the lower crustal shear zones are very attenuated, and upper crustal faulting is strongly coupled with extension in the upper mantle (Fig. 3c). In the case of the 40 km crust the extension of the upper crust couples with the outward-dipping shear zones of the lower crust, which start to deflect upper mantle deformation into two extensional domains (Fig. 3h). This occurs because the initially weaker lower crust near the Moho has undergone larger deformations and consequently has suffered further weakening. The strong weakening present at these shear zones stops the deformation from migrating to the center of the model and conditions the extension of the upper mantle to locate at two different extensional regions at the base of the lower crustal shear zones near the Moho.

Symmetric deformation continues at the center of the model for the 35 km crust test until crustal breakup occurs at 9 Myr (Figs. 3d and e). In this case, rifting resulted in two symmetric conjugate margins.

In the 40 km crust model, after 5 Myr, one of the two crustal shear zones are favoured due to the non-linear nature of strain weakening coupled with small random numerical errors, breaking the symmetry of the system. At 7 Myr the favoured shear zone becomes dominant coupling mantle and crustal deformation. This leads to asymmetric up-welling of the mantle and heating with consequent weakening at the tip of the active fault. Hence, the next fault will form in the hanging wall of the currently active fault because it is nearest to the weakened region. This process repeats itself leading to sequential faulting and the formation of asymmetric margins (Ranero and Pérez-Gussinyé, 2010; Pérez-Gussinyé, 2013; Brune et al., 2014).

In conclusion, the difference in margin geometry and symmetry/asymmetry among the 35 and the 40 km crust models in absence of surface processes is due to different final modes of extension, where in the 35 km model final extension concentrates in a narrow region of intense multi-dipping faulting while 40 km model last-phase extension is driven by sequential faulting.

3.2. Influence of the sediment transport coefficient into the margin architecture

Our landscape evolution model depends on hill-slope diffusion, transport coefficient and water discharge parameters (Sec. 2.2). For simplicity we chose to test only different transport coefficients k (Eq. 16). For each crustal thickness (35 and 40 km) we ran three models with different transport coefficients $k = 10^{-3}, 10^{-2}$ and 1. $k = 10^{-3}$ represents an end member where surface processes are active but transport is very ineffective

and consequently erosion and sedimentation. The opposite end member is $k = 1$ where transport is very efficient and erosion and sedimentation diffuse negative and positive topographies very fast.

3.2.1. Crustal thickness of 35 km

Figure 4 shows rifting evolution of the models with 35 km crust. For the first 3 Myr, the model with transport coefficient $k = 10^{-3}$ gives similar results to the equivalent without surface processes in terms of crustal and mantle deformation (Fig. 4a and b). This model develops rift shoulders where escarpments of faults are slightly diffuse. Note that half graben basins develop where the main initial faults intersect the top boundary of the model. Similarly to the model without surface processes, deformation concentrates within a small region at the center of the hanging crustal block between the two main faults at 5 Myr. This leads to fast necking of the upper crust and breakup at 10 Myr (Fig. 4f). As observed in the tests without surface processes, the resulting conjugate margins are symmetric and their width is also similar (∼90 km). However, the number of faulted blocks of size between 5 and 15 km is smaller than in the models without surface processes (9 vs 14), while larger blocks between 15 and 25 km occur in the model with surface processes and $k = 10^{-3}$ (Fig. 5a, b, c and d).

The model with $k = 10^{-2}$ shows a crustal evolution deformation analogous to the models without surface processes and with $k = 10^{-3}$. However, sediments deposited at the half grabens in the vicinity of the main faults are thicker due to the higher transport rate. This adds an extra load to the hanging walls that leads to higher offsets at the main faults and bending of the crustal block between them (Fig. 4i). Due to the larger bending stresses, the narrow rifting phase at the hanging crustal block occurs earlier and takes place over a wider region (Fig. 4i). The resulting margins at the end of the rifting are symmetric and the thinned crust is of similar length (∼85 km) to the tests with less erosion/sedimentation. However, the number of large crustal blocks separated by faults (15-25 km) is slightly bigger and the total number of faulted blocks is smaller (Fig. 5e and f). This is a consequence of the extra loading at hanging walls produced by faster infilling of synrift basin. Higher stresses due to sediment loading (Fig. 6) lead to larger offsets at faults that result in higher weakening, allowing faults to accommodate more extension and to remain active for longer periods of time.

High transport ($k = 1$) drastically changes the modes of extension operating in the second phase of rifting. Transport of larger amounts of sediments for greater distances results in high deposition rates along the whole hanging crustal block between the main faults. Instead of two half grabens, a large graben basin develops on top of the hanging crustal block due to uniform sediment loading (Figs. 4m and n). The uniform sediment layer prevents the hanging crustal block from bending as described by Buiter et al., 2008. Rift shoulders are not created because they are rapidly removed by high erosion rates. Thinning of the lower crust is rapidly compensated by subsidence of the hanging crustal block. Therefore, mantle is not needed to fill the space generated by fast extension on the lower crust and the Moho remains flat until 7 Myr (Figs. 4m, n and o). At 7 Myr lower crust has been completly removed from the center of the model and upper crust is in contact with the mantle at depths of ∼32 km (Fig. 4p). Consequently, former upper crustal rocks are exposed to Moho temperatures (Fig. 7c and e). Additionally, the thermal blanketing due to the thick package of sediments contributes to higher crustal temperatures. High temperatures of upper crustal rocks result in lower viscosities of the central part of the model and necking of the crust by mantle upwelling (Fig. 7e and f). Up-welled mantle further increase the thermal gradient and a wide region of viscous behaviour is formed at the basal to intermediate crust (Figs. 4q and 7g and h). This leads to a change in

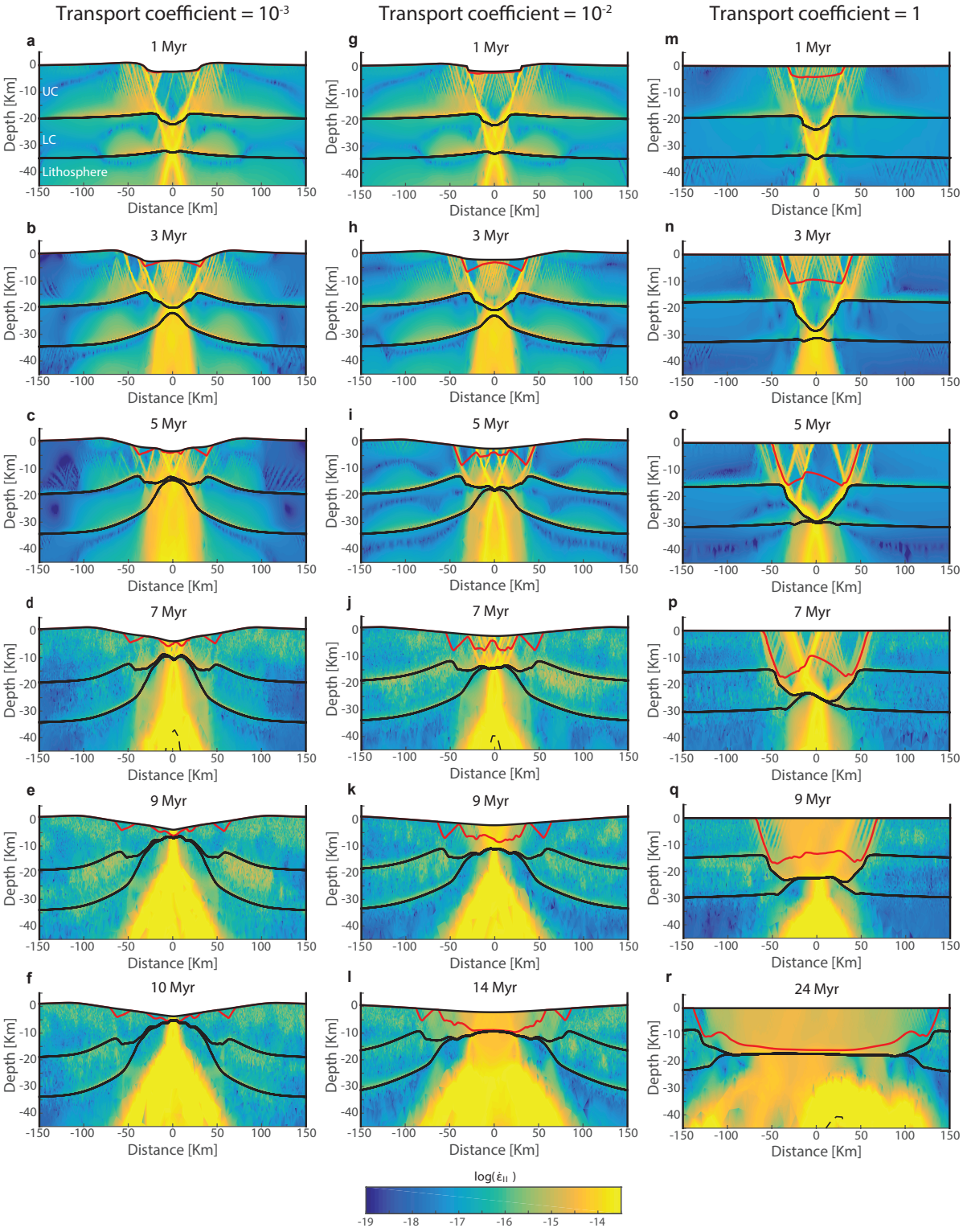

Figure 4: Strain rate evolution of rifting of 35 km crust with different transport coefficients. a, b, c, d, e and f illustrate the rifting evolution of a model with transport coefficient $k = 10^{-3}$ (low erosion/sedimentation rates). g, h, i, j, k and l recover the rifting evolution of a model with $k = 10^{-2}$. m, n, o, p, q and r show the evolution of a model with $k = 1$ (high erosion/sedimentation rates). The red lines represent the interface between basement and sediments.

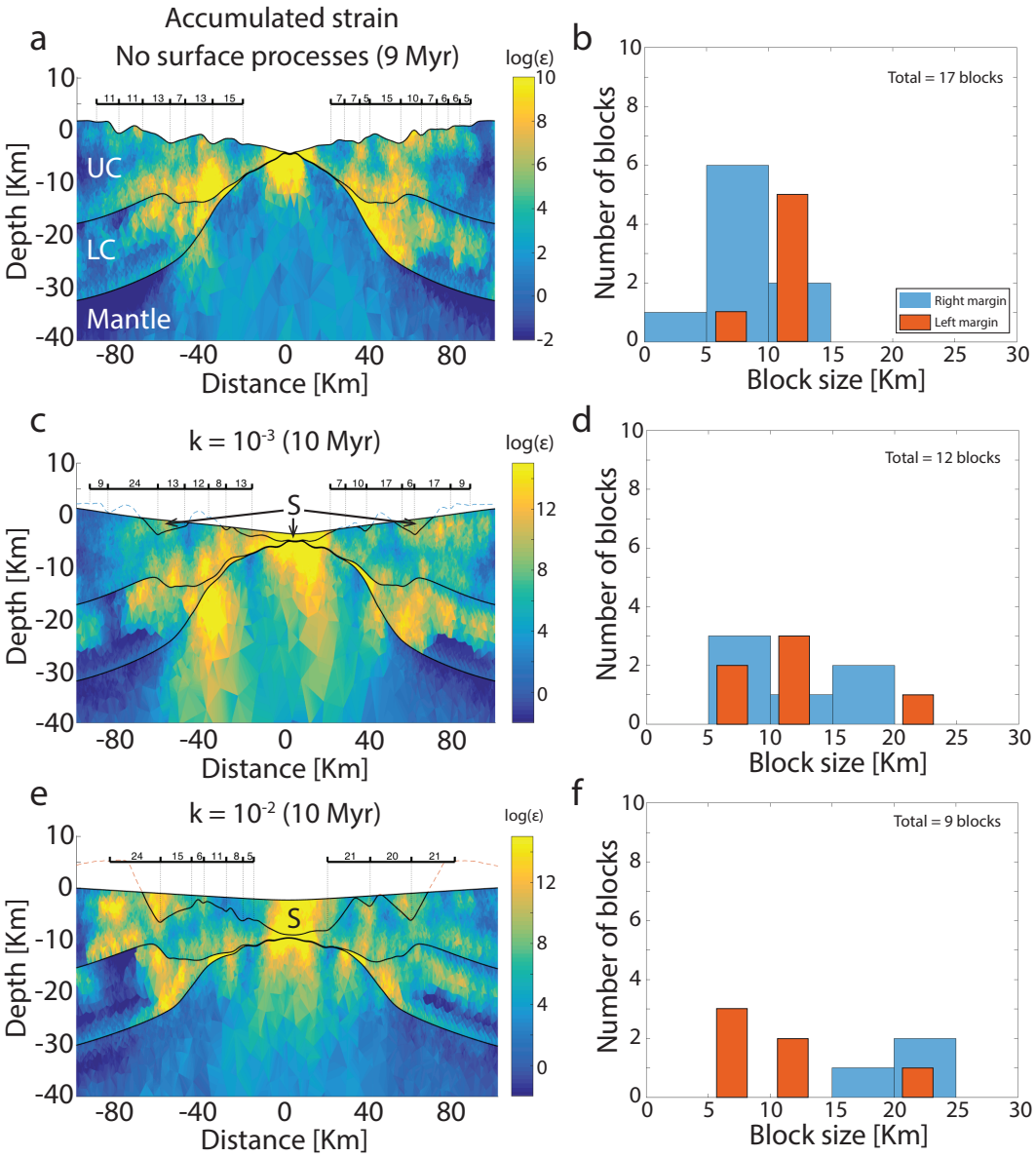

Figure 5: Size of faulted blocks of 35 km crust experiments. a, c and e colors represent the root of the second invariant of the accumulated (historic) strain for different magnitudes of sediment transport. UC, LC and S stand for upper crust, lower crust and sediments respectively. Faulted block size is measured by observing fault development along rift evolution and by picking locations where wiggles in the topography intersect faults (high strain bands). Note that in areas near the center of the rift this type of measurement is not possible due to the insufficient resolution of the model and/or pure shear deformation. Discontinuous lines represent eroded top basement interface. b, d and f are histograms representing the number of blocks grouped in 5 km size intervals. Note that the total number of blocks decrease with increasing sediment transport. Also, the number of blocks between 5 and 10 km is reduced with increasing transport while larger blocks increase their number.

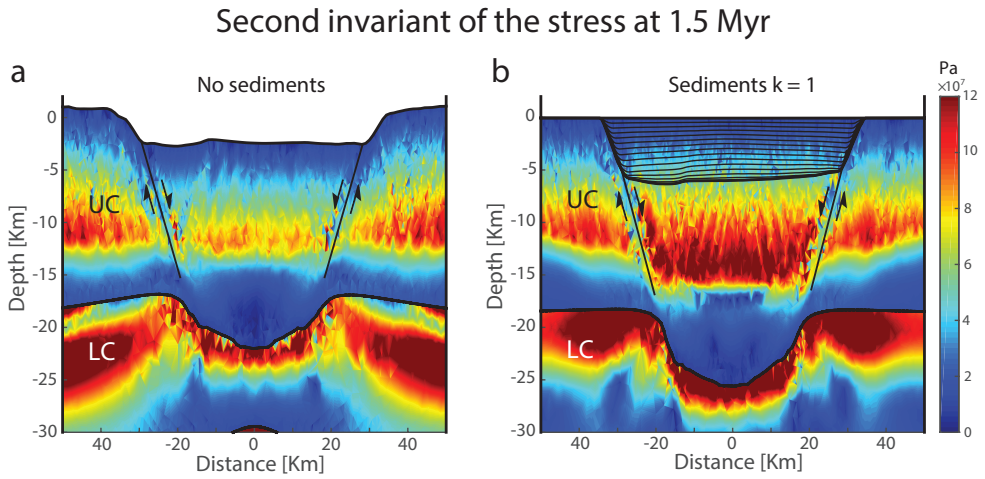

Figure 6: Square root of the second invariant of the deviatoric shear stress at 1.5 Myr. a) Test without sediments. b) Test with sediments where the transport coefficient is $k = 1$ (very efficient transport). Black thin lines represent 100 Kyr time lines inside the sediments. In both cases shear stresses at the faults are low due to the strain weakening. Note that both hanging and foot walls are subjected to greater stresses at b) due to the sediment load.

the mode of extension of the upper crust and sediments from symmetric extension dominated by two main conjugate faults (Fig. 4p) to symmetric extension by multiple faults (Fig. 4q), and finally pure shear that slowly attenuates the crust along a wide region. Consequently, extension results into two symmetric wide thinned crustal domains overlain by 15 km package of sediments at crustal breakup (24 Myr) (Fig. 4r).

3.2.2. Crustal thickness of 40 km

Figure 8 shows the evolution of 40 km crust tests with different transport coefficients. The model with transport coefficient $k = 10^{-3}$ showcase similar modes of extension (symmetric rifting followed by sequential faulting), asymmetry and margin architecture when compared to the model without surface processes (Fig. 8a, b, c, d, e and f). However, this model reaches crustal breakup at 12 Myr while the model without surface processes remains in sequential faulting mode during the whole time span for these experiments (40 Myr) (Fig. 3j). The widest margin is smaller in this case (∼140 km) in comparison to the model without surface processes (>200 km). A shorter margin forms due to larger offsets at longer-lived sequential upper crustal faults caused by the effect of sediment loads on the stresses and fault weakening. The resulting larger offsets at upper crustal faults exceed deformation at the lower-crustal low-viscosity pocket allowing for effective thinning of the crust and eventually breakup. The number of 5-10 km faulted blocks is larger in this case than for the experiment with no surface processes (10 vs 8) which is against the overall conclusions of this study (Fig. 9a, b, c and d). However, note that this is because the ductile deformation style of the model without surface processes prevents us from being able to measure blocks in the hyper-extended crust. If brittle behaviour would dominate rifting in the last phase, additional small blocks should be observed in the distal margin as predicted by Pérez-Gussinyé, 2013. Furthermore, 15-25 km blocks exist in the model with sediment transport $k = 10^{-3}$, while they are absent in the model with no surface processes. Therefore, we see an increase of the maximum block size with increasing sedimentation rates, which is in agreement with the general conclusions of our study.

The model with $k = 10^{-2}$ also results in asymmetric margins by sequential faulting (Fig. 8d, e and f).

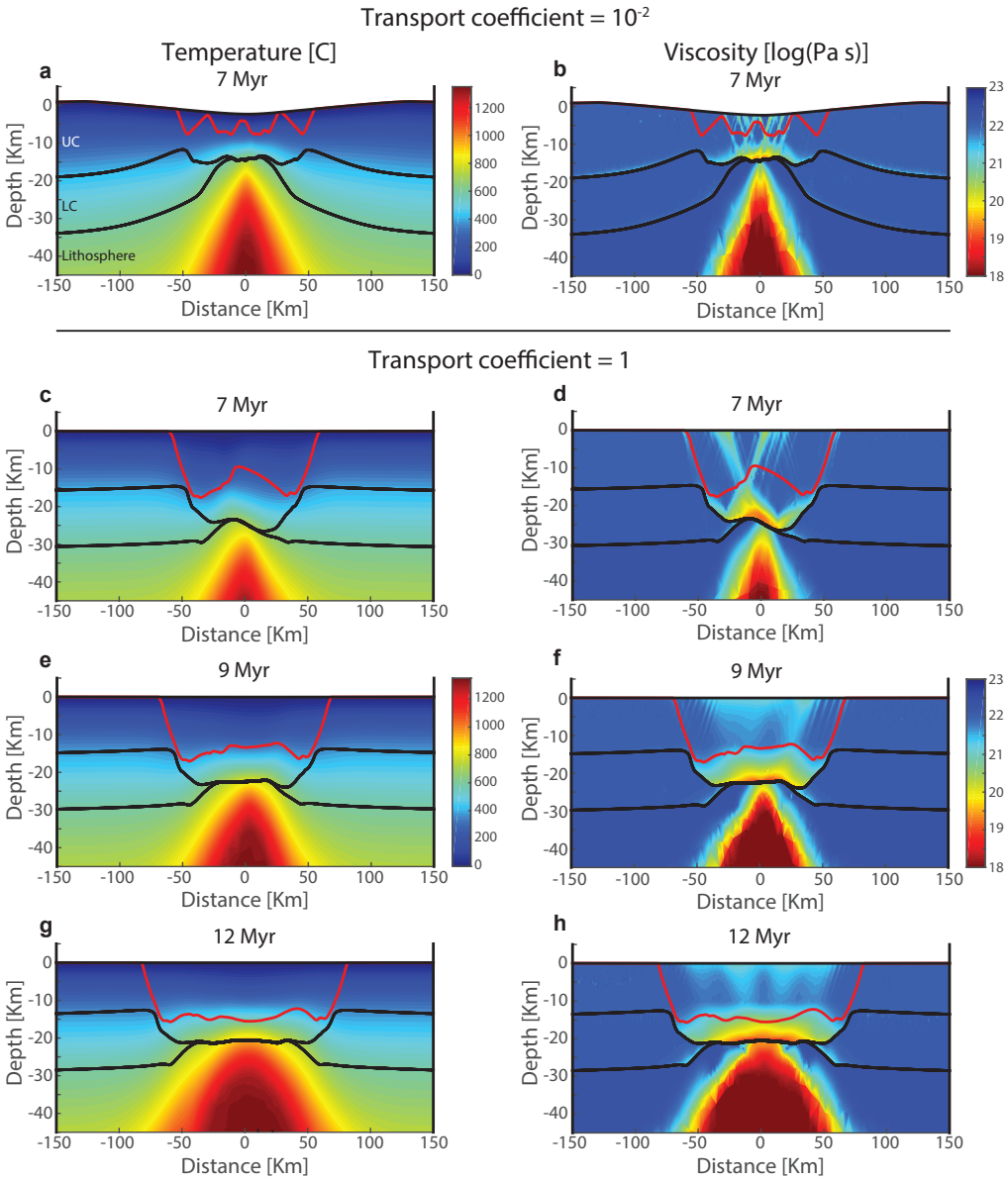

Figure 7: Temperatures and viscosities of models with 35 km crust. a and b, temperature and viscosity fields for the experiment with $k = 10^{-2}$ at 7 Myr. c, d, e, f, g and h temperature and viscosity fields for a model with $k = 1$ at different time steps after changing to multi-faulting/pure shear mode of extension. Note that at the base of the crust temperatures are at least 150°C higher at the $k = 1$ test than the $k = 10^{-2}$ test and consequently viscosities are lower at the former.

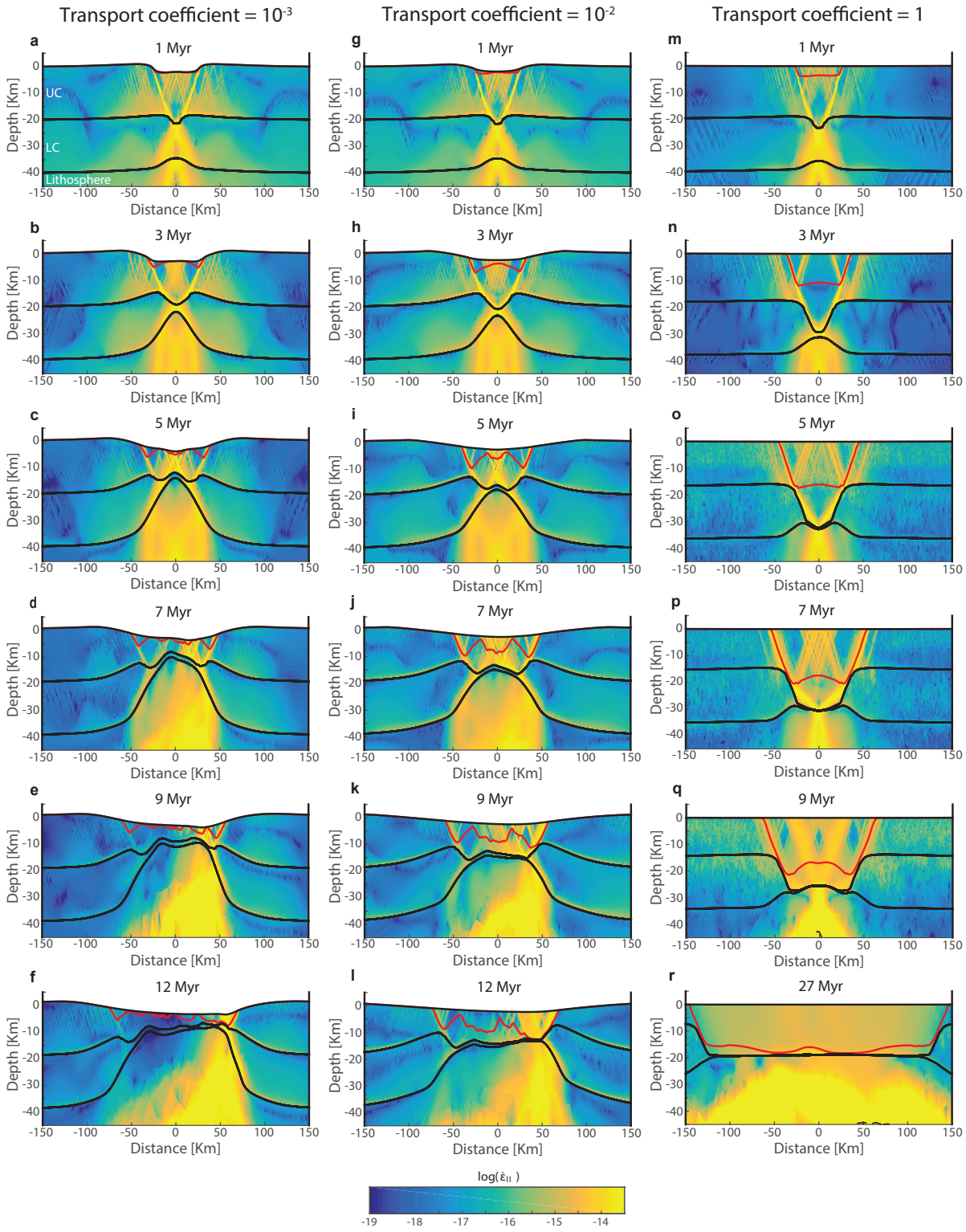

Figure 8: Strain rate evolution of rifting of 40 km crust with different transport coefficients. a, b, c, d, e and f illustrate the rifting evolution of a model with transport coefficient $k = 10^{-3}$ (low erosion/sedimentation rates). g, h, i, j, k and l recover the rifting evolution of a model with $k = 10^{-2}$. m, n, o, p, q and r show the evolution of a model with $k = 1$ (high erosion/sedimentation rates). The red lines represent the interface between basement and sediments.

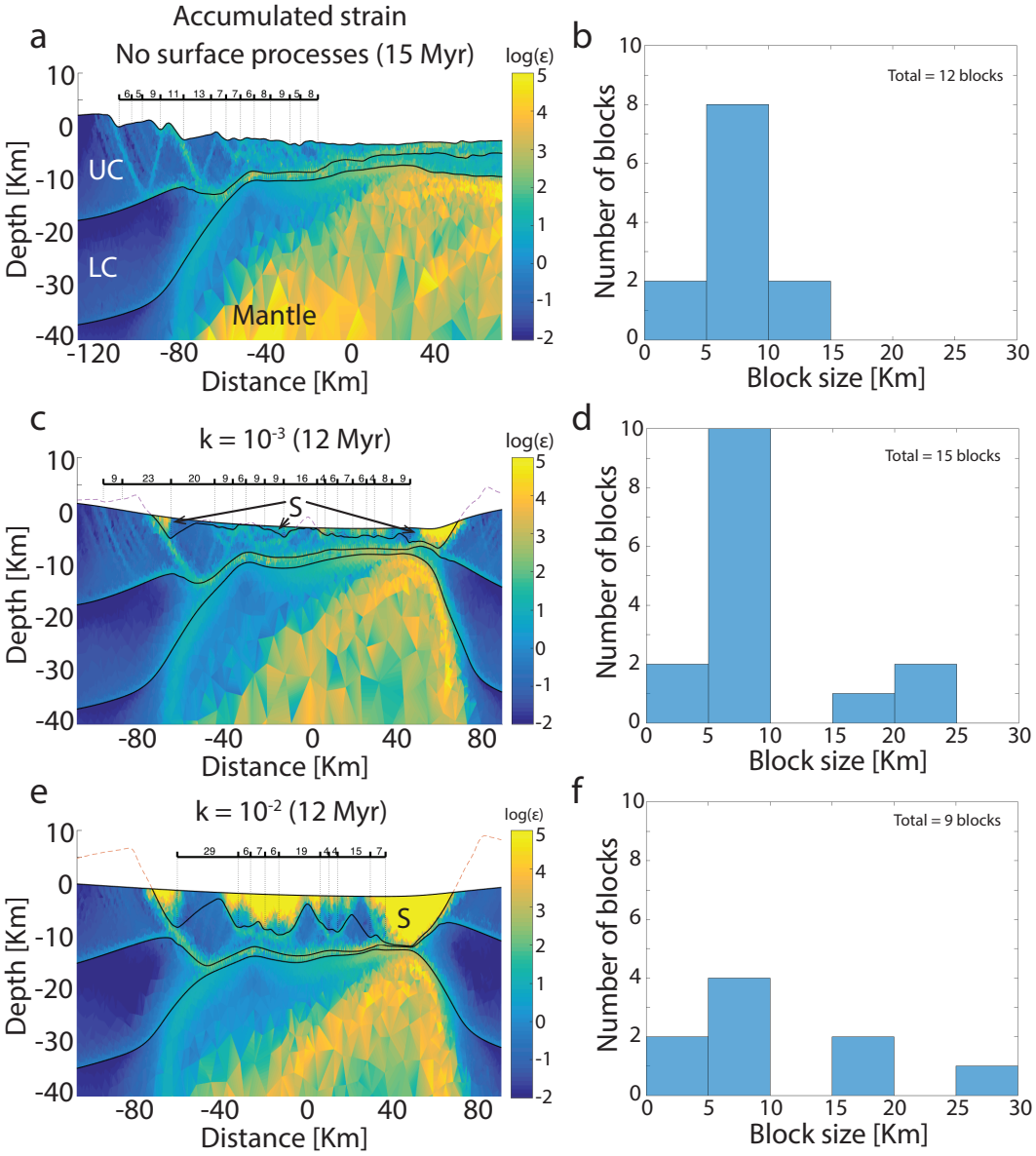

Figure 9: Size of faulted blocks of 40 km crust experiments. a, c and e colors represent the root of the second invariant of the accumulated (historic) strain for different magnitudes of sediment transport. UC, LC and S stand for upper crust, lower crust and sediments respectively. Faulted block size is measured as described in Fig. 5. In this case we choose to only measure block sizes in the left margins since the right margins have little amount of faulted blocks. In (a), last phase of rifting occurs by ductile deformation of the crust which leads to no faulted blocks, but instead a wide domain of thin and highly deformed crust. b, d and f are histograms representing the number of blocks grouped in 5 km size intervals. In this case the total number of blocks decreases with increasing sediment transport in (d) and (f), while the experiment without surface processes (b) have a smaller number of blocks than the one with $k = 10^{-3}$. This is because the sediment loads favour strain localization which allows the crust to behave brittlely until breakup and blocks to be measure along the whole margin, while in (a) that is not possible due to the ductile deformation of the last rifting phase. Note that the number of large blocks and their size increase with increasing sediment transport.

However, the larger loads of sediments deposited on the hanging walls of the faults lead to larger offsets and larger-in-size and smaller-in-number faulted blocks (Fig. 9e and f). Larger localization of the deformation in the faults produce more effective thinning of the crust which makes the widest margin even narrower (∼130 km) than the one modelled with $k = 10^{-3}$ (Figs. 8f, l, 9e and f).

The experiment with $k = 1$ displays almost identical modes of extension and crustal geometry compared to the analogous model with 35 km crust (Fig. 8m, n, o, p, q and r). Note that equivalent models without surface processes and with $k = 10^{-3}$ and 10^{-2} result in asymmetric margins (Figs. 3j, 8f and l) while this model creates symmetric margins with extremely attenuated crusts (Fig. 8r). The change from asymmetry to symmetry is due to pure shear dominating the last phase of rifting instead of sequential faulting. Pure shear takes over extension from 7 Myr, first by dominating deformation at the necked crust near the moho, and then by taking place along the whole thickness of the hanging crustal block and the overlaying sediment layer. By 9 Myr the center of the model has been greatly weakened by high deformation and extension by pure shear is more effective in this region resulting in two symmetric thinned crustal domains (Fig. 8r).

3.3. Sediment time lines and breakup unconformity

Our model allows for the recovery of time lines in the sediments. Time lines represent relief at the top of the sediments at a given time. Therefore, they limit packages of sediments deposited in this time interval. We view these as a computational approximation of stratal packages. These lines are tracked along with sediment deformation and can be eroded, which allows for observation of unconformities and synrift/postrift-like sediment geometries (i.e. wedging, onlapping and sag-type basins).

As previously discussed in Sec. 3.2.1, the model with 35 km crust and low transport rates ($k = 10^{-3}$) results in symmetric margins by subsidence of the hanging crustal block with consequent deposition on the half grabens in the vicinity of the main faults and later narrower extension located at the middle of the hanging crustal block. This migration and localization of the deformation towards the center of the model results in sediments younging towards the center of the model (Fig. 10a). Furthermore, sag-basin-type sediments are deposited in proximal areas of the margin that unconformably overlay older sediments. The deposition of such type of sediments, typically associated to postrift phase, occurs contemporaneously to rifting at more distal parts of the margins.

More effective transport in the 35 km crust experiment ($k = 10^{-2}$) does not generate sag-basin-type deposition at the proximal margin as illustrated in Fig. 10b. Instead, all new sediments are deposited where deformation is taking place and old sediments are eroded. Therefore, we do not observe an equivalent to the breakup unconformity before crustal breakup time (Fig. 10b). In this case we would expect that sag-basin-type deposition will occur after crustal breakup and that a consistent-in-time breakup unconformity will be formed.

In experiments where asymmetric margins occur by sequential faulting (i.e. 40 km crust and $k = 10^{-3}$) sediments young towards the last active fault in the wide margin. In the particular case of 40 km and $k = 10^{-3}$, three sag basins developed onlapping old synrift sediments by the time of crustal breakup (Fig. 10c). Additionally, the age of the basal sag-basin sediments also youngs towards the distal part of the margin.

In conclusion, models show that unconformities separating synrift from sag-basin sediments do not necessarily date the regional breakup, but instead involve the migration of rift deformation into other sectors of the margin. If this migration is sequential in a certain direction an unconformity can occur so

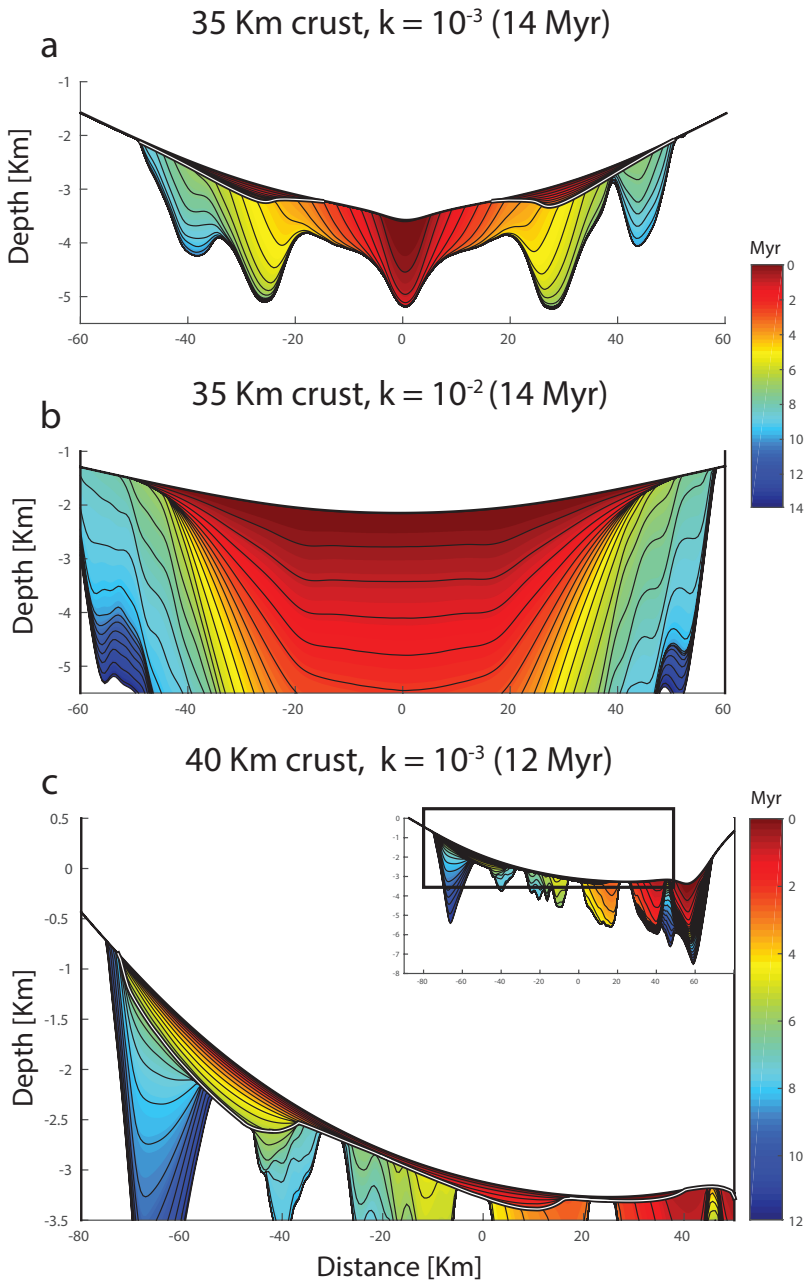

Figure 10: Sediment ages and time lines at crustal breakup for: a) a model with initial 35 km crust and transport coefficient of $k = 10^{-3}$, b) initial crustal thickness of 35 km and $k = 10^{-2}$, and c) initial 40 km crust and $k = 10^{-3}$. Colours represent age of sediments. Time lines are drawn every 500 Kyr. White lines represent unconformities separating synrift from sag-basin-type sediments.

that it separates synrift from sag-basin sediments which progressively youngs towards proximal sectors of the margin.

4. Discussion

We can now start to couple complex rheological deformation models with surface processes. However, these models are still very simplistic. Here, we have shown results of a model where complex multi-layered non-linear rheologies interplay with a landscape evolution model which accounts for hill-slope diffusion and sediment transport. Sediments are included in the mechanical and thermal solvers which implies a great improvement for investigating the impact of sediment loading and thermal blanketing in the tectonics. Additionally, time lines within the sediments are tracked with time, which allows us to examine the unconformities associated with rifting.

However, this model is still limited by the uncertainties involved in the parametrizations that we used. In particular, sediment transport parameters are poorly constrained due to the regional character of this study and due to the one-dimensional approximation, while surface processes in nature always work along a two-dimensional heterogeneous surface. Furthermore, the sediment transport-limited model is not able to reproduce erosive patterns typical of high uplift areas where detachment of exposed rock mainly controls the landscape evolution (Dietrich et al., 2003). Also the assumption that there is always availability of soil or sediments for transport may not be valid in regions where high uplift exceeds the regolith production rate (Dietrich et al., 2003). Geomorphological studies often assume that all these approaches are valid due to the large scale character of the study, where individual events of erosion and deposition become averaged out (Paola et al., 1992). Furthermore, small uplift rates are observed in the models so that it is unlikely that uplift exceeds regolith production. Small uplift also implies that rock detachment mechanisms at the surface is unlikely to dominate landscape evolution. A major limitation of this geomorphologic model is that it does not account for sea or water filling of depressions. Beneath water the mechanisms governing sediment transport differ from those for fluvial transport, and therefore, a water body introduced into the model would result in a lateral change in the transport coefficient. This implies that sea level should be a factor to consider in future studies of margin development since we observe that different transport coefficients have an effect on the final margin geometry.

These models also lack of melting, lack pre-existing structures, assume that rifting occurs under a single phase of constant velocity extension, and have the limitations on the surface processes algorithm previously mentioned. Nonetheless, we find similarities between the structures predicted by these models and those observed at the non-volcanic margins of West Iberia (WIM) and Great Australian Bight (GAB). Models that tend to asymmetry and sequential faulting in the absence of surface processes show similar deformation histories and margin architectures as the WIM. The West Iberia Margin experienced low sedimentation rates contemporary of the crustal faulting. Here, we have shown that sequential faulting is inhibited by large amount of sediments so that the small infill at the WIM can be linked to its final stage of sequential faulting. On the contrary, there is a significant sediment accumulation in the Great Australian Bight synchronous to the deformation at major faults that thin the crust very effectively (Talwani et al., 1979; Stagg et al., 1990; Direen et al., 2012). This also agrees with our models in which high sedimentation rates favour localization of deformation at pre-existing faults, effective thinning of the crust along these large offset faults, and a large increase in the stability of these faults.

We conclude that effective transport favours symmetry since longer lived faults result in bending of the hanging wall which triggers formation of conjugate faulting to release stresses. Our results agree with previous models from Buiter et al., 2008 that predict sedimentation should favour symmetric deformation.

Furthermore, some margins showcase extremely attenuated hyper-extended crusts at a later phase of rifting (i.e. South Atlantic). Extension mechanisms in these sectors of the margins are currently a subject of debate since little faulting has been observed (Aslanian et al., 2009). It is possible that deformation takes place along very small offset faults that are not imaged by seismic sections due to signal attenuation by the thick sediment packages. Here, we propose that this potential distributed stretching of the crust is analogous of the model where we observe pure shear at attenuated crusts overlain by large sediment thicknesses. This mode of extension could be triggered by a change on sediment transport or simply by deposition of larger volumes of sediments due to slow and/or multi-phase rifting.

Additionally, we suggest that changes in modes of extension can be triggered by an increment of sediment input in the rift system influenced by a catchment of an up-stream basin. An example of this is the Amazon drainage system that 10.5 Myr ago captured the Pebas system due to a faster Andean mountain building phase (Figueiredo et al., 2009; Sacek, 2014). The implications of this is that even far field tectonic processes may have some control on margin architecture due to their effects on the transport of mass along Earth's surface.

Regarding the well-known unconformities that separate synrift-like from sag-fill sediments, we conclude that they form due to thermal subsidence, and not necessarily be related to breakup but instead to a rift migration (Ranero and Pérez-Gussinyé, 2010; Pérez-Gussinyé, 2013) and consequent migration of the hot mantle up-welling. From our results we agree with Gillard et al., 2015 about the need to revisit well-accepted stratigraphic terms such as breakup unconformity, prerift, synrift and postrift, since these terms can obscure our understanding when processes such as rift migration and poly-phase rifting are present.

5. Conclusions

The transport of sediments can greatly influence deformation due to rifting. Sediment loads at faulted hanging walls increase stresses which favour deformation localization, larger offsets and faulted blocks and faults active for longer periods of time. One of the effects of this localization is that sequential faulting is penalized by a more effective thinning of the crust. This implies that, in cases where margin asymmetry is controlled by sequential faulting, an increase of sediment infill will lead to a reduction of the degree of margin asymmetry. Consequently, margins with little sediment infill such as the West Iberian Margin are expected to have undergone larger extension by numerous faults that are sequential in time oceanwards. On the contrary, for margins with large amount of sediment input such as the Great Australian Bight, deformation is expected to localize at large offset faults along which crust is thinned very effectively.

Furthermore, sinking of crust due to extreme sedimentation rates in areas of extension helps to expose crustal rocks to high temperatures for which the rheology of these rocks will change from plastic to weak viscous flow. This results in a change from finite localized faulting to multi-faulting of the crust and sediments along a broad region and/or pure shear deformation. Here, we propose this as a potential mechanism for hyper-extension observed at margins such as the ones in the South Atlantic.

Finally, our models show breakup-like unconformities separating synrift from sag-fill-type sediments. We observe that these unconformities do not necessarily date the breakup but instead date the localization

of extension in a narrower region or a lateral continuous migration of rifting (i.e. by sequential faulting), in which case sag-basin sediments young towards the direction of the migration. This is observed at the West Iberian Margin where 'synrift' sediments young oceanwards, or at the Great Australian Bight where sequences onlap synrift-like sediments in proximal sectors of the margin while the same sequences show synrift-like geometries in more distal sectors. The results of these simple model patterns are incompatible with standard rift terminology like, 'synrift', 'postrift' and 'breakup unconformity'.

References

M. Andrés-Martínez, J. P. Morgan, M. Pérez-Gussinyé, and L. Rüpke. A new free-surface stabilization algorithm for geodynamical modelling: Theory and numerical tests. *Physics of the Earth and Planetary Interiors*, 246:41–51, 2015. doi: 10.1016/j.pepi.2015.07.003. URL http://dx.doi.org/10.1016/j.pepi.2015.07.003.

J. Armitage, R. Duller, and S. Schmalholz. The influence of long-wavelength tilting and climatic change on sediment accumulation. *Lithosphere*, 6(5):303–318, 2014. doi: 10.1130/L343.1. URL http://dx.doi.org/10.1130/L343.1.

J. J. Armitage and P. A. Allen. Cratonic basins and the long-term subsidence history of continental interiors. *Journal of the Geological Society*, 167(1):61–70, 2010. doi: 10.1144/0016-76492009-108. URL http://dx.doi.org/10.1144/0016-76492009-108.

J. J. Armitage, P. A. Allen, P. M. Burgess, G. J. Hampson, A. C. Whittaker, R. A. Duller, and N. A. Michael. Sediment transport model for the Eocene Escanilla sediment-routing system: Implications for the uniqueness of sequence stratigraphic architectures. *Journal of the Geological Society*, 85(12):1510–1524, 2015. ISSN 1527-1404. doi: 10.2110/jsr.2015.97.

D. Aslanian, M. Moulin, J. Olivet, P. Unternehr, L. Matias, F. Bache, M. Rabineau, H. Nouzé, F. Klingelheofer, I. Contrucci, and C. Labails. Brazilian and African passive margins of the central segment of the South Atlantic Ocean: Kinematic constraints. *Tectonophysics*, 468(1):98–112, 2009. doi: 10.1016/j.tecto.2008.12.016. URL http://dx.doi.org/10.1016/j.tecto.2008.12.016.

R. W. Bialas and R. W. Buck. How sediment promotes narrow rifting: Application to the Gulf of California. *Tectonics*, 28(4), 2009. doi: 10.1029/2008TC002394.

G. Boillot, E. Winterer, et al. Drilling on the Galicia margin: retrospect and prospect. In *Proceedings of the Ocean Drilling Program, Scientific Results*, volume 103, pages 809–828, 1988.

B. Bos and C. J. Spiers. Frictional-viscous flow of phyllosilicate-bearing fault rock: Microphysical model and implications for crustal strength profiles. *Journal of Geophysical Research: Solid Earth*, 107(B2), 2002. doi: 10.1029/2001JB000301. URL http://dx.doi.org/10.1029/2001JB000301.

J. Braun and C. Beaumont. A physical explanation of the relation between flank uplifts and the breakup unconformity at rifted continental margins. *Geology*, 17(8):760–764, 1989. doi: 10.1130/0091-7613(1989)017⟨0760:APEOTR⟩2.3.CO;2. URL http://dx.doi.org/10.1130/0091-7613(1989)017<0760:APEOTR>2.3.CO;2.

S. Brune, C. Heine, M. Pérez-Gussinyé, and S. V. Sobolev. Rift migration explains continental margin asymmetry and crustal hyper-extension. *Nature Communications*, 5, 2014. doi: 10.1038/ncomms5014. URL http://dx.doi.org/10.1038/ncomms5014.

S. J. H. Buiter, R. S. Huismans, and C. Beaumont. Dissipation analysis as a guide to mode selection during crustal extension and implications for the styles of sedimentary basins. *Journal of Geophysical Research: Solid Earth*, 113(B6), 2008. doi: 10.1029/2007JB005272. URL http://dx.doi.org/10.1029/2007JB005272.

M. A. Carson and M. J. Kirkby. *Hillslope form and process*. Cambridge University Press Cambridge, 1972.

P. D. Clift, S. Brune, and J. Quinteros. Climate changes control offshore crustal structure at South China Sea continental margin. *Earth and Planetary Science Letters*, 420:66–72, 2015. ISSN 0012-821X. doi: 10.1016/j.epsl.2015.03.032.

M. Collignon, B. J. P. Kaus, D. A. May, and N. Fernandez. Influences of surface processes on fold growth during 3-D detachment folding. *Geochemistry, Geophysics, Geosystems*, 15(8):3281–3303, 2014. doi: 10.1002/2014GC005450. URL http://dx.doi.org/10.1002/2014GC005450.

W. Culling. Analytical theory of erosion. *The Journal of Geology*, pages 336–344, 1960.

M. Dabrowski, M. Krotkiewski, and D. W. Schmid. MILAMIN: MATLAB-based finite element method solver for large problems. *Geochemistry, Geophysics, Geosystems*, 9(4), 2008.

W. E. Dietrich, D. G. Bellugi, L. S. Sklar, J. D. Stock, A. M. Heimsath, and J. J. Roering. Geomorphic transport laws for predicting landscape form and dynamics. *Prediction in geomorphology*, pages 103–132, 2003.

N. G. Direen, H. M. J. Stagg, P. A. Symonds, and I. O. Norton. Variations in rift symmetry: cautionary examples from the Southern Rift System (Australia-Antarctica). *Geological Society, London, Special Publications*, 369(1):453–475, 2012. doi: 10.1144/SP369.4. URL http://dx.doi.org/10.1144/SP369.4.

D. A. Falvey. The development of continental margins in plate tectonic theory. *APPEA Journal-Australian Petroleum Production and Exploration Association*, 14(1):95–106, 1974.

D. A. Falvey and J. C. Mutter. Regional plate tectonics and the evolution of Australia's passive continental margins. *BMR Journal of Australian Geology and Geophysics*, 6:1–29, 1981.

J. Figueiredo, C. Hoorn, P. Van der Ven, and E. Soares. Late Miocene onset of the Amazon river and the Amazon deep-sea fan: Evidence from the Foz do Amazonas Basin. *Geology*, 37(7):619–622, 2009.

P. Flemings and T. Jordan. A synthetic stratigraphic model of foreland basin development. *Journal of Geophysical Research: Solid Earth*, 94(B4):3851–3866, 1989. doi: 10.1029/JB094iB04p03851.

M. Gillard, J. Autin, G. Manatschal, D. Sauter, M. Munschy, and M. Schaming. Tectonomagmatic evolution of the final stages of rifting along the deep conjugate Australian-Antarctic magma-poor rifted margins: Constraints from seismic observations. *Tectonics*, 34(4):753–783, 2015. doi: 10.1002/2015TC003850. URL http://dx.doi.org/10.1002/2015TC003850.

G. C. Gleason and J. Tullis. A flow law for dislocation creep of quartz aggregates determined with the molten salt cell. *Tectonophysics*, 247(1):1–23, 1995. doi: 10.1016/0040-1951(95)00011-B. URL http://dx.doi.org/10.1016/0040-1951(95)00011-B.

W. H. Graf. *Hydraulics of sediment transport*. Water Resources Publication, 1984.

M. R. Handy and H. Stünitz. Strain localization by fracturing and reaction weakening – a mechanism for initiating exhumation of subcontinental mantle beneath rifted margins. *Geological Society, London, Special Publications*, 200(1):387–407, 2002. doi: 10.1144/GSL.SP.2001.200.01.22. URL http://dx.doi.org/10.1144/GSL.SP.2001.200.01.22.

L. N. Hansen, M. E. Zimmerman, and D. L. Kohlstedt. Laboratory measurements of the viscous anisotropy of olivine aggregates. *Nature*, 492(7429):415–418, 2012. doi: 10.1038/nature11671. URL http://dx.doi.org/10.1038/nature11671.

G. Hirth and D. Kohlstedt. Rheology of the upper mantle and the mantle wedge: A view from the experimentalists. In J. Eiler, editor, *Inside the subduction factory*, pages 83–105. AGU, 2003. ISBN 0-87590-997-3.

A. D. Howard. A detachment-limited model of drainage basin evolution. *Water Resources Research*, 30(7):2261–2285, 1994.

G. Huffman, R. Adler, D. Bolvin, and G. Gu. Improving the global precipitation record: GPCP version 2.1. *Geophysical Research Letters*, 36(17), 2009. ISSN 1944-8007. doi: 10.1029/2009GL040000.

T. J. R. Hughes. *The finite element method: linear static and dynamic finite element analysis*. Dover Publications, Mineola, NY, 2000. ISBN 0486411818 9780486411811. ID: 301049178.

R. S. Huismans and C. Beaumont. Roles of lithospheric strain softening and heterogeneity in determining the geometry of rifts and continental margins. *Geological Society, London, Special Publications*, 282(1):111–138, 2007. doi: 10.1144/SP282.6. URL http://dx.doi.org/10.1144/SP282.6.

S. I. Karato and P. Wu. Rheology of the upper mantle: A synthesis. *Science*, 260(5109):771–778, 1993.

B. J. Kaus, H. Mühlhaus, and D. A. May. A stabilization algorithm for geodynamic numerical simulations with a free surface. *Physics of the Earth and Planetary Interiors*, 181(1):12–20, 2010. doi: 10.1016/j.pepi.2010.04.007.

B. J. P. Kaus. Factors that control the angle of shear bands in geodynamic numerical models of brittle deformation. *Tectonophysics*, 484(1):36–47, 2010.

M. J. Kirkby. Hillslope process-response models based on the continuity equation. *Special Publication Institute of British Geographers*, 3:15–30, 1971.

L. E. Malvern. *Introduction to the Mechanics of a Continuous Medium*. Prentice-Hall, 1969.

J. Marr, J. Swenson, C. Paola, and V. Voller. A two-diffusion model of fluvial stratigraphy in closed depositional basins. *Basin Research*, 12(3-4):381–398, 2000. doi: 10.1111/j.1365-2117.2000.00134.x.

Y. Martin and M. Church. Diffusion in landscape development models: on the nature of basic transport relations. *Earth Surface Processes and Landforms*, 22(3):273–279, 1997.

K. R. McClay. Pressure solution and Coble creep in rocks and minerals: a review. *Journal of the Geological Society*, 134(1):57–70, 1977.

L. Moresi, F. Dufour, and H. B. Mühlhaus. A Lagrangian integration point finite element method for large deformation modeling of viscoelastic geomaterials. *Journal of Computational Physics*, 184(2):476–497, 2003. ISSN 0021-9991. doi: 10.1016/S0021-9991(02)00031-1. URL http://www.sciencedirect.com/science/article/pii/S0021999102000311.

J. P. Morgan. The generation of a compositional lithosphere by mid-ocean ridge melting and its effect on subsequent off-axis hotspot upwelling and melting. *Earth and Planetary Science Letters*, 146(1):213–232, 1997.

J. P. Morgan, J. W. Morgan, and E. Price. Hotspot melting generates both hotspot volcanism and a hotspot swell? *Journal of Geophysical Research: Solid Earth*, 100(B5):8045–8062, 1995.

C. Paola, P. L. Heller, and C. L. Angevine. The large-scale dynamics of grain-size variation in alluvial basins, 1: Theory. *Basin Research*, 4(2):73–90, 1992.

M. Pérez-Gussinyé. A tectonic model for hyperextension at magma-poor rifted margins: an example from the West Iberia–Newfoundland conjugate margins. *Geological Society, London, Special Publications*, 369(1):403–427, 2013.

M. Pérez-Gussinyé, D. Klaeschen, and J. Totterdell. Margin architecture and oceanization of the Australian Bay Bight. In preparation for *Tectonics*.

Y. Y. Podladchikov, A. N. B. Poliakov, and D. A. Yuen. The effect of lithospheric phase transitions on subsidence of extending continental lithosphere. *Earth and Planetary Science Letters*, 124(1):95–103, 1994.

C. R. Ranero and M. Pérez-Gussinyé. Sequential faulting explains the asymmetry and extension discrepancy of conjugate margins. *Nature*, 468(7321):294–299, 2010.

T. F. Redfield and P. T. Osmundsen. The long-term topographic response of a continent adjacent to a hyperextended margin: A case study from Scandinavia. *Geological Society of America Bulletin*, 125(1-2):184–200, 2012. doi: 10.1130/B30691.1. URL http://dx.doi.org/10.1130/B30691.1.

E. Rutter and D. Elliott. The kinetics of rock deformation by pressure solution [and discussion]. *Philosophical Transactions of the Royal Society of London A: Mathematical, Physical and Engineering Sciences*, 283(1312):203–219, 1976.

V. Sacek. Drainage reversal of the Amazon river due to the coupling of surface and lithospheric processes. *Earth and Planetary Science Letters*, 401:301–312, 2014. doi: 10.1016/j.epsl.2014.06.022. URL http://dx.doi.org/10.1016/j.epsl.2014.06.022.

G. Simpson and F. Schlunegger. Topographic evolution and morphology of surfaces evolving in response to coupled fluvial and hillslope sediment transport. *Journal of Geophysical Research: Solid Earth*, 108(B6), 2003. doi: 10.1029/2002JB002162. URL http://dx.doi.org/10.1029/2002JB002162.

T. R. Smith and F. P. Bretherton. Stability and the conservation of mass in drainage basin evolution. *Water Resources Research*, 8(6):1506–1529, 1972. doi: 10.1029/WR008i006p01506. URL http://dx.doi.org/10.1029/WR008i006p01506.

H. Stagg, J. Willcox, D. Needham, G. OBrien, C. Cockshell, A. Hill, B. Thomas, and L. Hough. Basins of the Great Australian Bight region-geology and petroleum potential: Continental margins program folio 5. *Bureau of Mineral Resources, Geology and Geophysics and Department of Mines and Energy, South Australia*, 1990.

M. Talwani, J. Mutter, R. Houtz, and M. Konig. The crustal structure and evolution of the area underlying the magnetic quiet zone on the margin south of Australia: Rifted margins. In *Geological and Geophysical Investigations of Continental Margins*, pages 151–175. AAPG Special Volumes, 1979.

J. Totterdell, J. Blevin, H. Struckmeyer, B. Bradshaw, J. Colwell, and J. Kennard. A new sequence framework for the Great Australian Bight: Starting with a clean slate. *APPEA Journal-Australian Petroleum Production and Exploration Association*, 40(1):95–120, 2000.

D. Turcotte and G. Schubert. *Geodynamics*. Cambridge University Press, 2002. ISBN 9780521666244.

J. K. Weissel and G. D. Karner. Flexural uplift of rift flanks due to mechanical unloading of the lithosphere during extension. *Journal of Geophysical Research: Solid Earth*, 94(B10):13919–13950, 1989.

K. Wilks and N. Carter. Rheology of some continental lower crustal rocks. *Tectonophysics*, 182(1-2):57–77, October 1990.

Chapter 6

Discussion

6.1 Introduction

The aim of this thesis is to address margin development and architecture using numerical modelling techniques. For this purpose, I have worked on a pre-existing numerical code to bring it to a state-of-the-art level and beyond. My major additions to this code are a free surface stabilization algorithm to simulate dynamic topography, elasticity, plasticity, strain weakening to simulate faults and shear zones, shear heating, and coupling with a sediment transport function to model surface processes. In this chapter I evaluate the outcomes of this thesis from the point of view of the limitations of the numerical model and the parameters used. I also evaluate where these model and model results contrast with observations and models from other authors. Finally, I propose several areas where future work can be carried out.

6.2 Critical evaluation

6.2.1 Model limitations

One of the main limitations of our models is that Earth is a highly heterogeneous system, while our experiments are in general laterally homogeneous. Additionally, different deformation mechanisms and chemical processes act at completely different scales, from the mineral lattice, mineral boundaries, and mineral aggregates to the overall mechanisms of deformation inside shear zones, faults and fault gouges. Numerical modelling uses parametrizations to represent these processes. Although this implies an oversimplification of the Earth system, reproducing the exact mechanisms that shape geology at all their

scales, and their interplays would be extremely laborious and computationally intractable. In this section I discuss the limitations related to the approaches I made in order to model the extension of the lithosphere.

6.2.1.1 Rheologies

Rheologies strongly influence the behaviour of a mechanical model. The rheologies used in this thesis are taken from laboratory experiments obtained from triaxial set-ups (Wilks and Carter, 1990; Gleason and Tullis, 1995; Rybacki and Dresen, 2000; Hirth and Kohlstedt, 1996). However, experimental values are obtained at relatively low deviatoric stresses (in the maximum order of 100 MPa) and high strain rates (from 10^{-1} to 10^{-5} s^{-1}). In our models these values are applied to simulate the mechanics of deep lithospheric and asthenospheric rocks which may be subjected to stresses on the order of ∼100 MPa and higher and lower strain rates. Consequently, the use of these parameters in at least one order of magnitude higher than for the stresses they were calculated implies a degree of uncertainty on the model outcome, especially when it is highly conditioned by deep processes.

That is the case in Chapter 4, where asymmetric deep mantle flow induced by the presence of a craton triggers asymmetry during margin development and conditions the polarity of the asymmetry of conjugated margins. Tests without a craton show that rheological changes in the lower crust of the model only influence the degree of the asymmetry but not its polarity. However, the main outcome of chapter 4 is that the presence of a craton near rifting favours asymmetry and conditions polarity. This outcome remains probably true for olivine rheologies different than the ones used here as it is proven that what conditions the asymmetric mantle flow is the contrast between stiff cold cratonic lithosphere adjacent to hotter and weaker fold belt lithosphere and asthenosphere, and not the rheology itself. This contrast is justified since it is observed from tomographic experiments and isostasy models (i.e. Turcotte and Schubert, 1982; Ritsema and van Heijst, 2000; Evans et al., 2011).

Another limitation related to the rheology is that most of the parameters are calculated for monomineralic rocks while rocks in nature are typically polymineralic and have a fabric. Values are measured in monomineralic rocks for simplicity, and it is justified since weaker and most abundant mineral phases are proven to dominate deformation (Karato and Wu, 1993). Including the contribution to deformation of secondary but abundant mineral phases, such as feldespar in the upper crust and pyroxenes and amphiboles, implies using rheological parameters calculated for a large variety of mineral combinations and rocks.

This results in a vast parameter space to be explored, which is beyond the scope of this thesis.

6.2.1.2 Peierls creep

Peierls creep is a type of plasticity mechanism that acts at low temperatures (<1200 K) and stresses above 500 MPa (Kameyama et al., 1999). This type of mechanism is not included into our model since the up-welling of the asthenosphere provides enough heat to prevent it. However, this mechanism is thought to be important in subducting slabs where larger stresses are expected at lower temperatures (Kameyama et al., 1999).

6.2.1.3 Deformation seeds

As mentioned in Chapters 4 and 5, weak seeds are needed in order to nucleate deformation in desired regions of the model. With this, it is possible to avoid artefacts on the deformation that will take place if rifting nucleates near the boundaries of the model. Additionally, this allows us to initiate rifting at different distances from a craton in Chapter 4. In nature deformation is expected to nucleate around heterogeneities such as hotter areas, regions in the crust of weaker lithologies, old orogenic sutures, etc. In this thesis I use a thermal seed at the lower crust, which consist of a 2D Gaussian temperature increase of 100°C. Many other authors use low viscous/yield-stress seeds associated with a small region of low viscosity (i.e. Buck, 1991; Duretz et al., 2016; Buiter et al., 2008; Huismans and Beaumont, 2011). The decision of using a thermal instead of a viscous/yield-stress seed was made based on the fact that higher temperature results as well in a lower viscosity, with the difference that this seed relaxes with time due to heat diffusion, which is desirable since it will not affect deformation at later stages of rifting.

Duretz et al., 2016 shows the big impact of the type of weak seed used in extension modes, by testing different weak seeds placed at different depths. Such a variability is also observed in the models used here. As a large part of the thesis is focused on asymmetry controls I opt for placing the weak seed at the lower crust which favours symmetry (Brune, personal communication), so that the causes of the asymmetry can be evaluated without the need of taking into account the weak seed.

6.2.1.4 Temperature-dependent density

In Chapter 4 the density does not depend on temperature. This approach was made in order to avoid associated small scale convection. Small scale convection is capable

of removing the cratonic lithosphere if other processes that penalize convection are not applied, such as depletion-dependent density (Nielsen and Hopper, 2004). As cratonic lithosphere is expected to be preserved along long periods of time, temperature-dependent density was not included in the experiments on Chapter 4 so that the implementation of more complex processes that allow for craton preservation was avoided.

In later work the development of a depletion-dependent density algorithm by Elena Ros-Bernabeu, Marta Pérez-Gussinyé and Jason P. Morgan, allowed for slower small scale convections that are in better agreement with observations. Consequently, both temperature- and depletion-dependent density functions were included for my most recent models showed in Chapter 5.

6.2.1.5 Strain weakening

A major limitation of the models shown here is their approximation of strain softening. As mentioned in previous chapters, strain softening is generated by gouge production, the presence of fluids at faults, mineralization, reduction in grain size and the formation of crystallographic preferred orientations (CPO) (Karato and Wu, 1993; Bos and Spiers, 2002; Handy and Stünitz, 2002; Hirth and Kohlstedt, 2003; Huismans and Beaumont, 2007; Hansen et al., 2012). The fact that so many processes can contribute to this type of weakening makes difficult to quantitatively describe strain softening. Rigorous parametric numerical studies have been carried out in addressing the influence of strain softening on extension (Sibson, 1990; Rice, 1992; Ridley, 1993; Streit, 1997; Ingebritsen and Manning, 1999; Bos and Spiers, 2002; Handy and Stünitz, 2002). However, these numerical experiments allow for model control but not for direct strain-softening parameter calibration. Field studies suggest that strain softening is on the order of the models presented in this thesis, but to my knowledge exact parameters and weakening-strain dependency degree have yet to be quantitatively described. Therefore, further field and laboratory research is needed to constrain strain softening, and bring modelling of shear zone dynamics to the levels of uncertainty of other rheologic approximations.

In spite of the limitations referred here in the uncertainty on strain softening parameters, a viscous strain softening algorithm could be improved by the use of temperature-dependent Arrhenius crystal growth (Turcotte and Schubert, 2002). This will add to the rock the capacity to heal which will allow for a more confident use of strain softening in the diffusion-creep regime that will be limited to lower temperature regions.

Strain is the relationship between an initial length before deformation and the final length after deformation. Consequently, when resolution is high a given deformation can easily

produce larger strains than in lower resolutions. This implies that strain softening acts differently depending on the resolution of the mesh. In the code presented here further improvements could be addressed by adding a strain softening scaling with the mesh size (Buck and Lavier, 2001), or by the use of an adaptive mesh where the resolution of a certain area depends on the amount of strain rate.

Additionally, a reduction of the friction angle in the plastic formulation as described in Chapter 2 reduces the effective viscosity but does not result in an effective reduction of the fault angle respect the principal stresses. In order to account for these effects an anisotropic formulation of viscosity is needed as described in Moresi and Mühlhaus, 2006. Furthermore, weakening along crystal preferred orientations results in anisotropic dislocation-creep viscosity (Hansen et al., 2012). Here, I chose to not implement anisotropic viscosity and anisotropic strain softening due to lack of time to explore the parametric space associated with this effect.

6.2.1.6 Extension rates

Experiments run for this thesis were always calculated for half extension velocities of 5 mm/yr. However, continents rift in a wide range of velocities (∼3-50 mm/yr). Furthermore, different extension velocities have proven to result into different types of rifting evolution and margin architectures (Brune et al., 2014). Therefore, further research is needed in this direction.

6.2.1.7 Magmatism and serpentinization

Magmatism and serpentinization are important processes involved in the formation of the continent-ocean transition and the oceanization. As this thesis addresses rifting at non-volcanic margins and their architectures I do not include such processes in the modelling. However, I am aware that melting highly influences mantle rheologies (Morgan et al., 1995; Hirth and Kohlstedt, 2003), even in the low percentages present in the non-volcanic margins during rifting. Also, water brought by faults into the mantle can potentially result in the serpentinization of peridotites below the crust. Serpentinization implies an increase in the peridotite volumes (Gresens, 1967; O'Hanley, 1992) whose impacts on upper crustal extension remains an open question. These two processes and their implications were out of the scope of this thesis and are being addressed by other members of my research group.

6.2.1.8 Erosion and sediments

Limitations in the modelling of surface process are related to parametrizations and the simplicity of the assumptions made. I consider a major issue the lack of sea-floor transport and sedimentation environment. Submarine sediment transport processes are different in the mechanisms and time and space scales from the continental transport processes. Consequently, at least different transport coefficients should be used when sediments reach the sea. There is also a relevant ongoing discussion on how sea level changes can correlate the stratigraphy globally and the magnitude of the sea level change needed for such correlations, for which varying sea levels are a desirable implementation.

6.2.1.9 2D versus 3D

Oblique rifting is very common in Earth and it has been proven to be a more efficient way of stretching the crust (Brune et al., 2012). Additionally, it is unlikely that extension takes place exactly perpendicular to precursor structures which might result into very important three-dimensional effects (Brune et al., 2012; Tommasi et al., 2009; Sacek and Ussami, 2013). Furthermore, for surface processes to be two-dimensional as in nature 3D lithospheric models are needed. However, non-linear visco-elasto-plastic rheologies imply a computational challenge for high resolutions in 3D. For this reason this thesis addresses 2D numerical modelling so that a larger amount of processes can be simultaneously modelled.

6.2.2 Outlook

This thesis addresses how different factors influence margin architecture. Special emphasis has been put on how cratons interfere with margin development, how surface processes affect margin geometry and asymmetry of conjugates and how crustal faulting and mantle dynamics translate into major unconformities in margin sediments.

All these questions are closely related to the style of crustal faulting. In order to realistically simulate faulting a free surface is needed at the top of the model, so that foot-walls can uplift, hanging-walls subside and bending can take place. Free surfaces in numerical models have been typically avoided in the past because small time steps leads to computationally expensive runs while large time steps leads to surface instabilities. Strategies to approach free surfaces such as 'sticky-air' (Zaleski and Julien, 1990; Gerya and Yuen, 2003; Crameri et al., 2012), normal-stress method (McKenzie, 1977; Fleitout et al., 1986; Zhong et al., 1993, 1996) or implicitly solving for topography in conjuction with Stokes equation (Kramer et al., 2012) can suppress instabilities but result in surface artefacts

or do not solve the time-dependent relaxation of the topography. In order to accurately model topography a free-surface stabilization algorithm (FSSA) has been developed. The FSSA adds a penalization term to the stiffness matrix equivalent to a fraction of the future load due to the change in topography during the time step (see Chapter 3). This penalization is controlled by a factor α for which we found optimal results (large time steps with stability) for a value of 2/3. Previous stabilization algorithm by (Kaus et al., 2010) is shown to give similar results as ours in terms of stability and computational efficiency when used with a corresponding α of 2/3 (instead of the 1/2 originally proposed by them). The new FSSA together with the finding of the 2/3 optimal penalization factor will not only be an important contribution to future modelling of continental extension, but for modelling dynamic topographies at all geological contexts.

In addition to the FSSA, further implementations were required to make the models as realistic as possible. Therefore, I have worked in developing algorithms for reproducing strain softening, visco-elasto-plastic rheology and shear heating. These implementations discussed in Chapter 2 allowed for experiments of sufficient complexity to address passive margin development.

The first set of experiments were designed to address margin asymmetry when rifting initiates in the vicinity of a craton (discussed on Chapter 4). Many authors have approached asymmetry of conjugate passive margins and have proven for it to be related to crustal rheologies, strain softening, extension velocities and lithospheric/crustal heterogeneities (Kusznir and Park, 1987; Dunbar and Sawyer, 1988; Buck, 1991; Buck and Lavier, 2001; Huismans and Beaumont, 2002, 2003; Corti et al., 2003; Nielsen and Hopper, 2004; Buiter et al., 2008; Tommasi et al., 2009; Hansen et al., 2012; Brune et al., 2014). In those studies the polarity of asymmetry is random. However, observations from the central sector of the South Atlantic conjugates and the Southern Sea show a clear relationship between the polarity of the margin and the distance from its landward edge to the craton. This relationship is such that narrow margins develop next to cratons while wide margins develop in conjugates where there is no craton or it is distant from the margin edge. These observations motivate experiments where initiation of rifting is triggered at different horizontal distances away from the craton inside a fold belt. The experimental results match with the correlation between polarity of the asymmetry and distance to craton observed in nature, when rift initiation occurs in the craton influence zone ($\sim$100 km). This polarity of the asymmetry occurs due to: 1) a stronger lithosphere near the craton which allows for fast localization of deformation, and 2) asymmetric up-welling of the fold belt mantle due to the shadowing effect exerted by the thick and stiff cratonic lithosphere. When the asymmetric deformation at the mantle is coupled with crustal faulting extension migrates towards the craton, leaving a wide margin behind and mechanically 'eroding' and

shortening the margin next to the craton. Although there are several limitations related to this model as mentioned in the previous section, a large parametric space has been explored (different rheologies, viscous softening and crustal thicknesses) and the results always proved the influence of the craton in the asymmetry and its polarity. I consider this a very important finding since it completes the knowledge on margin asymmetry development by adding a reliable prediction for its polarity and also points out the need of integrating the precursor geology into models to narrow down the window between the reality and the experiments.

The second set of experiments presented in this thesis (Chapter 5) targets the influence of surface processes into modes of extension and final margin geometry. For this experiments a surface processes function based on sediment transport was coupled to the tectonic model. Experiments show that larger sediment transport coefficients provide greater sediment inputs to the synrift basins which result in larger stresses at hanging walls due to the sediment loading. Larger stresses translate into larger offsets at faults, increasing weakening and sustaining deformation at the faults for longer periods of time. The result is margins with fewer faults, larger blocks and very effective and abrupt thinning of the crust. These results agree with observations at the Great Australian Bight margin where thick synrift sediment packages are found along small number of blocks bounded by large offset faults that thin the crust very effectively (Talwani et al., 1979; Falvey and Mutter, 1981; Stagg et al., 1990; Totterdell et al., 2000; Direen et al., 2012). Experiments also show that very large transport coefficients favour pure shear/multi-faulting of the crust leading to the formation of symmetric hyper-extended margins. Sediment loading also results in large crustal subsidence. Mode of extension changes to pure shear when lower crustal viscosities drop due to high temperatures at the greater depths. This implies that a large increase on sediment input could trigger a change from a finite faulting mode of extension towards distributed deformation along an attenuated crust. This deformation mechanism represents a potential candidate to explain hyper-extended margins such as the ones from the central sector of the South Atlantic and Norway (Aslanian et al., 2009; Lundin and Doré, 2011; Redfield and Osmundsen, 2012). Low sediment transport coefficients imply smaller sediment rates at hanging walls and allow for short-lived faults and rift migration. The analogue for this type of architecture is the West Iberian Margin where little synrift sedimentation allows for several sequential faults that smoothly thin the crust (Ranero and Pérez-Gussinyé, 2010; Pérez-Gussinyé, 2013). Additionally, when margin asymmetry depends on sequential faulting or rift migration, models show that larger sedimentation rates favour symmetry by load-triggered localization of the deformation and consequent inhibition of strain migration. Previous numerical models addressing continental extension either omitted surface processes or approached them in a very simplistic way. Although

surface processes modelled in Buiter et al., 2008 were approached simplistically, they found that sediment input triggers change in deformation from congugate-asymmetric faulting to symmetric faulting, in agreement with my results.

Furthermore, the more realistic sediment transport function used in Chapter 5 allows the recovery of time lines (or pseudo strata) in the sediments. This algorithm is shown to be sufficient to address regional scale sedimentation events. Time lines can be deformed and eroded by the tectonic model so that unconformities can develop. Careful examination of these unconformities show that they are not necessarily related to the breakup time, but that they can occur due to thermal subsidence when rift migrates. This agrees with observations at the West Iberia Margin where distal-younging sediments are explained by sequential faulting (Ranero and Pérez-Gussinyé, 2010; Pérez-Gussinyé, 2013), and in the Great Bight Basin where a wide rifting phase is followed by a narrow distal phase, and where sediment sequences that showcase postrift onlap on the proximal margin present synrift structures at distal parts (Gillard et al., 2015). Thermal subsidence due to rift migration and related unconformities provide a new context in which major unconformities need to be interpreted. This also points out at the need of revising concepts such as prerift, synrift, postrift and breakup unconformity.

Numerical models have proven to be an excellent tool for answering questions related to details of margin development, faulting history and surface-to-deep interactions. Most relevant new findings of this thesis are that: 1) asymmetry is expected to be influenced by the presence of cratonic lithospheres which can be key to define its polarity, 2) surface processes can greatly impact extension modes, rifting history and margin asymmetry, 3) greater sedimentation rates favour deformation localization and longer-lived faults which has a great impact on the geometry of the margin, and 4) large unconformities separating 'synrift-type' sediments from onlapping sag infills are not necessarily associated to breakup time but instead to thermal subsidence triggered by rift migration.

This thesis expands our knowledge of passive margins and at the same time provides some useful information that can be applied to other tectonic contexts. For example, the new free-surface stabilization algorithm and α factor can be used to calculate more accurate topographies in any geological context. Conclusions drawn from chapter 4 highlight the role of lithospheric heterogeneities in the crustal deformation and allows us to predict the polarity of the asymmetry at passive margins. A relevant implication is that wherever this model might fail to predict polarity, an anomalous crust and/or lithospheric mantle are expected. Finally, orogens resulting from continent-continent collisions such as the Alps or the Himalayas often preserve margin segments. These segments display old margin

geometries and sediments. This thesis provides new information about under which rheological conditions given basement and/or sediment geometries are expected. Identifying these geometries in the collisional context and relating them to the expected rheologies can therefore provide valuable information about the strength of the materials participating in the collision, the other end of the Wilson cycle.

6.3 Future work

Many questions arise from the exploration done in this PhD thesis. Some of these questions are related to computational issues associated to the modelling of the crust and lithosphere and on parametric uncertainty. Other questions relate to unexplored phenomena and feedback between processes taking place during continental extension.

From the technical point of view a better meshing function is desirable. A new grid should be adaptive, implying that regions of special interest (i.e. zones of high strain rates or sediments) will be generated with better resolution, while areas away from deformation will have lower resolution. This would greatly enhance the performance of the code and, at the same time, would allow for high resolution near faults that is particularly interesting for consistent strain softening without the need of the scaling described at Sec. 6.2.1.5.

More realistic weak seeds are also needed. Current weak seeds available in the code initialize rifting by two main conjugate faults. In nature this could be the case if rifting is initialized by a point heterogeneity. However, initial phases of wide rifting described for several margins suggest that localization of the deformation may occur in a later phase of extension. In order to simulate this effect weak noise can be introduced in the rheological model (i.e. randomly reducing the initial friction angle). Maximum amplitude of the noise can be distributed as a spatial Gaussian function so that the maximum would imply the most likely location for rifting to localize, while random noise will prevent extreme localization at the beginning of the run time.

I consider that the most important limitations of these models are the uncertainties involved in the parameters used. Further composition studies as inferred from seismic tomography, refraction experiments and MT data would be needed in order to better scale laboratory experiments. Another strategy to approach this is to start using multi-scale modelling where parameters for the tectonic model are obtained from chemical/crystallographic models that run for given stresses, temperatures and pressures (i.e. Lebensohn and Tomé, 1993; Tommasi et al., 2009; Wimert and Hier-Majumder, 2012).

Another major area of research are the approximations for strain weakening modelling. Strain weakening algorithms can be greatly improved by adding anisotropic viscosities and healing as pointed out in Sec. 6.2.1.5. Also further work on strain weakening parameters and functions can be done by using field examples for calibration of the models.

Surface process modelling requires refinement as well. As commented in Sec. 6.2.1.8, the results shown in this thesis do not take into account the presence of a sea. Implementing the sea as a load over the crust and as a reduction of transport coefficients in the geomorphic model would bring the model closer to reality and would allow for a new set of experiments for which the influence of sea level changes into the margin development can be explored. Another potential field of study is to test if spatial variation of the discharge (i.e. larger precipitations rates in some regions of the model) have an impact on the asymmetry of conjugate margins, linking climate to tectonics.

Magmatism and serpentinization are processes that are expected to have great impact on margin evolution. Studying how such processes interplay with sediments and lithospheric heterogeneities can open a broad field to be explored from a modelling perspective.

Finally, I found of particular interest 3D modelling where oblique tectonics can be addressed and surface processes can be modelled to reproduce actual sedimentary systems such as rivers, graben depositional environments, alluvial fans and deltas. However, even 3D models will still confront limitations since their results will still be general and difficult to apply to a particular region. In this aspect, I think that Montecarlo simulations could be a great tool to grasp 1-to-1 correlations between the numerical models and the highly heterogeneous geology of the Earth.

Chapter 7

Conclusions

- A new free-surface stabilization algorithm has been developed in order to efficiently simulate stable topographies with geodynamic numerical models.
- This algorithm penalizes the stiffness matrix at the surface to reduce velocity overestimations that lead to instability.
- This method and previously developed similar ones, need a controlling parameter to stabilize the free-surface. This parameter has been proven to be optimal at values of 2/3, which coincides with the velocity factors for a Galerkin time discretization of the penalization term.
- The presence of cratonic lithosphere in the vicinity of a fold belt lithosphere rifting region ($\leq$ 100 km) can result in asymmetric conjugate margins even if similar rheological parameters give symmetric conjugates when the craton is not present.
- When asymmetry occurs, the narrowest margin develops near the craton while the wide margin develops on the opposite margin. This polarity needs of strong enough lower crusts to allow coupling of the deformation from crust to mantle.
- Margin asymmetry and its polarity are the result of: 1) high localization of the deformation at lower-crustal craton-dipping shear zone due to its lower temperature in contrast with its conjugate and 2) asymmetric up-welling of the fold-belt mantle due to the shadowing effect exerted by the cratonic lithosphere.
- Surface processes have an important impact on margin architecture.
- Large sedimentation rates synchronous to faulting result in overloading of the hanging-walls, large stresses, large fault offsets, large fault weakening, abrupt thinning of the crust and little number of faults that bound large crustal blocks. These effects can

inhibit or reduce margin asymmetry in comparison with parametrically-equivalent margins subjected to smaller sedimentation rates.

- An excess of sediment loads can lead to a change in mode of extension from any type of finite faulting to pure shear/multi-faulting. This is because large loads translate into large crustal subsidences that expose lower crustal rocks to hot mantle temperatures at the same time that the thick sediment cover amplifies this effect by thermal blanketing. Consequently, lower crustal rocks weaken and flow easily, distributing extension along a broad crustal region which will evolve into a very attenuated crust.

- Models show that major unconformities developed at margins are not necessarily synchronous to the breakup time. Instead, they are found to be the consequence of thermal subsidence after rift migration. This points out at the need of revising the breakup associated terminology commonly applied to stratigraphic interpretation of seismic sections.

Appendix A

Stress, strain and momentum equation

A.0.1 Stress

Traction is defined as the force f per unit area. If we assume an infinitesimal small surface S then the traction T is:

$$T = \lim_{\delta S \to 0} \frac{\partial f}{\partial S}. \tag{A.1}$$

Tractions need not to be normal to the surface and can be resolved either into normal and tangential components or into Cartesian components. The SI unit of traction is the Pascal (Pa), equivalent to one Newton per square metre (Nm^{-2}). In continuum mechanics, the traction is considered by convention to be positive when acting in the same general direction as the outer normal to the surface (tension), and negative in the opposite case (compression) (Ranalli, 1994). In geology and rock mechanics the sign convention is typically the opposite (compression as positive and tension as negative). Most of the modelling literature uses the continuum mechanics convention and, consequently, I choose to use the same.

Consider now a small cube with its faces oriented perpendicular to the coordinate axes x_1, x_2 and x_3 (Fig. A.1). Then it is possible to define the tractions T_1, T_2 and T_3 for the faces normal to the axis x_1, x_2 and x_3:

$$T_1 = (\sigma_{11}, \sigma_{12}, \sigma_{13}), \tag{A.2}$$

$$T_2 = (\sigma_{21}, \sigma_{22}, \sigma_{23}), \tag{A.3}$$

$$T_3 = (\sigma_{31}, \sigma_{32}, \sigma_{33}), \tag{A.4}$$

where σ_{ij} represents the component of the traction applied on the face perpendicular to

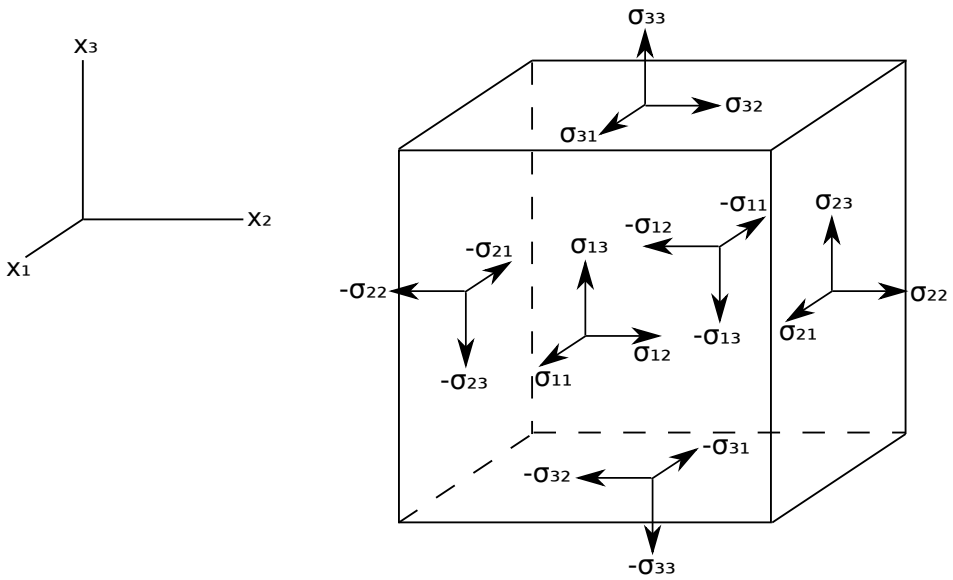

FIGURE A.1: Stress components exerted on the faces of an infinitesimal cube. The sign of the components indicates whether the stress component is the result of a force (positive) or a counterforce (negative).

the i axis, in the j direction. The three tractions together form the stress tensor σ_{ij}:

$$\sigma_{ij} = \begin{pmatrix} \sigma_{11} & \sigma_{12} & \sigma_{13} \\ \sigma_{21} & \sigma_{22} & \sigma_{23} \\ \sigma_{31} & \sigma_{32} & \sigma_{33} \end{pmatrix}. \tag{A.5}$$

Consequently, **stress** is the tensor formed of tractions acting on the faces of a infinitesimal cubic volume inside a continuum. Stress can also be defined as the internal distribution and intensity of force acting at any point within a continuum in response to various internal and external loads applied to the continuum (Malvern, 1969). In 3D space the stress tensor is represented by a 3×3 matrix which units of its components are the same ones of its component tractions (Pa in SI). Normal stresses are located in the diagonal of the matrix and shear stresses are located in the off-diagonal part. Due to the condition of force balance in absence of internal sources of angular momentum the stress matrix is symmetric relative to the main diagonal (Malvern, 1969), so:

$$\sigma_{ij} = \sigma_{ji}. \tag{A.6}$$

Pressure P is defined to be the average of the normal stresses:

$$P = -(\sigma_{11} + \sigma_{22} + \sigma_{33})/3. \tag{A.7}$$

The negative sign in the Eq. A.7 is assigned as a convention, assuming that pressure is positive under compression. The deviatoric stresses τ_{ij} are defined as the deviations of the stresses from the pressure:

$$\tau_{ij} = \sigma_{ij} + P\delta_{ij}, \tag{A.8}$$

where δ_{ij} is the Kronecker delta which is $\delta_{ij} = 1$ when $i = j$ and $\delta_{ij} = 0$ when $i \neq j$. Therefore, the off-diagonal deviatoric components are equal to the off-diagonal components of the stress.

A.0.2 Strain and strain rate

Lets assume two particles P and Q inside a continuous domain D which coordinates are respectively x_i and $x_i + dx_i$ (Fig. A.2). After displacement the particles coordinates will change into $P'(x_i + u_i)$ and $Q'(x_i + dx_i + u_i + du_i)$, where u_i and $u_i + du_i$ would be the displacements of the particles P and Q respectively. If u_i is a continuous function of the coordinates and its displacement gradient $\partial u_i/\partial x_j$ is also continuous and very small, the displacements of contiguous particles would differ only by an infinitesimal amount (Ranalli, 1994). Then the difference on displacement du_i can be defined as a function of the initial difference in location dx_j:

$$du_i = \frac{\partial u_i}{\partial x_j} dx_j. \tag{A.9}$$

Is is possible to split the displacement gradient in two parts:

$$\frac{\partial u_i}{\partial x_j} = \frac{1}{2}\left(\frac{\partial u_i}{\partial x_j} + \frac{\partial u_j}{\partial x_i}\right) + \frac{1}{2}\left(\frac{\partial u_i}{\partial x_j} - \frac{\partial u_j}{\partial x_i}\right), \tag{A.10}$$

where i and j are the coordinate indices 1, 2 and 3 and x_1, x_2 and x_3 are the spatial coordinates. The first term corresponds to the strain tensor ε_{ij}:

$$\varepsilon_{ij} = \frac{1}{2}\left(\frac{\partial u_i}{\partial x_j} + \frac{\partial u_j}{x_i}\right), \tag{A.11}$$

which describes the changes in shape and volume of the domain D, and the second term corresponds to the rigid-body rotation tensor ω_{ij}:

$$\omega_{ij} = \frac{1}{2}\left(\frac{\partial u_i}{\partial x_j} - \frac{\partial u_j}{x_i}\right), \tag{A.12}$$

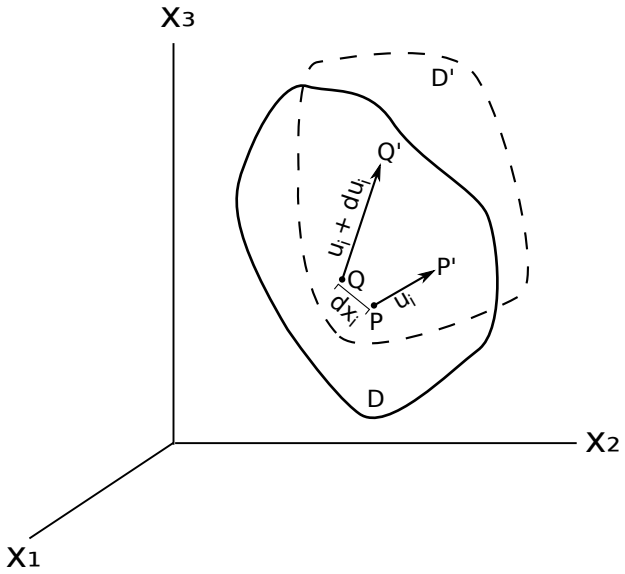

FIGURE A.2: Displacements of two proximate particles P and Q inside a continuum domain D. The initial coordinates of the particles are respectively x_i and $x_i + dx_i$, and the displacements for each one are respectively u_i and $u_i + du_i$.

which describes rigid-body displacements and rotations (Malvern, 1969). Note that the strain tensor is symmetric while the rigid-body rotation tensor is antisymmetric. In the models presented in this thesis the domain is represented by the mantle and the crust, where rotations are small enough for the rigid-body rotation tensor to be neglected in the dynamic formulation, although it is important to consider rotations where tensorial properties are needed to be tracked.

The **strain** tensor characterizes the amount of deformation inside a continuum evaluating the change of coordinates for a point along the space. Strain is dimensionless and it is defined by a 3×3 matrix:

$$\varepsilon_{ij} = \begin{pmatrix} \frac{\partial u_1}{\partial x_1} & \frac{1}{2}\left(\frac{\partial u_1}{\partial x_2} + \frac{\partial u_2}{\partial x_1}\right) & \frac{1}{2}\left(\frac{\partial u_1}{\partial x_3} + \frac{\partial u_3}{\partial x_1}\right) \\ \frac{1}{2}\left(\frac{\partial u_2}{\partial x_1} + \frac{\partial u_1}{\partial x_2}\right) & \frac{\partial u_2}{\partial x_2} & \frac{1}{2}\left(\frac{\partial u_2}{\partial x_3} + \frac{\partial u_3}{\partial x_2}\right) \\ \frac{1}{2}\left(\frac{\partial u_3}{\partial x_1} + \frac{\partial u_1}{\partial x_3}\right) & \frac{1}{2}\left(\frac{\partial u_3}{\partial x_2} + \frac{\partial u_2}{\partial x_3}\right) & \frac{\partial u_3}{\partial x_3} \end{pmatrix}, \tag{A.13}$$

where the diagonal terms represent the elongations in the directions of the coordinate axes and the off-diagonal components are related with angular deformation.

Then, we can define the **strain rate** $\dot{\varepsilon}_{ij}$, which accounts for the amount of deformation through time inside a continuum, through the x_i axes:

$$\dot{\varepsilon}_{ij} = \frac{\partial \varepsilon_{ij}}{\partial t}, \tag{A.14}$$

or, in the matricial form:

$$\dot{\varepsilon}_{ij} = \begin{pmatrix} \frac{\partial v_1}{\partial x_1} & \frac{1}{2}\left(\frac{\partial v_1}{\partial x_2} + \frac{\partial v_2}{\partial x_1}\right) & \frac{1}{2}\left(\frac{\partial v_1}{\partial x_3} + \frac{\partial v_3}{\partial x_1}\right) \\ \frac{1}{2}\left(\frac{\partial v_2}{\partial x_1} + \frac{\partial v_1}{\partial x_2}\right) & \frac{\partial v_2}{\partial x_2} & \frac{1}{2}\left(\frac{\partial v_2}{\partial x_3} + \frac{\partial v_3}{\partial x_2}\right) \\ \frac{1}{2}\left(\frac{\partial v_3}{\partial x_1} + \frac{\partial v_1}{\partial x_3}\right) & \frac{1}{2}\left(\frac{\partial v_3}{\partial x_2} + \frac{\partial v_2}{\partial x_3}\right) & \frac{\partial v_3}{\partial x_3} \end{pmatrix}, \tag{A.15}$$

where v_i represents the velocities in the i directions 1, 2 and 3. The strain rate unit in the SI is s^{-1}.

The deformation produced by the change in volume is defined by the volumetric strain $(\varepsilon_{11} + \varepsilon_{22} + \varepsilon_{33})/3$. The **deviatoric strain** is the result of subtracting the volumetric strain from the strain tensor:

$$\varepsilon'_{ij} = \varepsilon_{ij} - \frac{1}{3}\varepsilon_{kk}\delta_{ij}. \tag{A.16}$$

Similarly, it is possible to define the **deviatoric strain rate** which is the change in deformation without taking into account the change in volumetric strain:

$$\dot{\varepsilon}'_{ij} = \dot{\varepsilon}_{ij} - \frac{1}{3}\dot{\varepsilon}_{kk}\delta_{ij}. \tag{A.17}$$

A.0.3 The momentum equation

Newton's second law states that a force f exerted on a body of mass m will result in an acceleration a of the body directly proportional to the force and on its direction:

$$f = ma. \tag{A.18}$$

The acceleration describes the velocity changes with time:

$$a = \frac{\partial v}{\partial t}, \tag{A.19}$$

where v is the velocity and t is the time. Both the force and the acceleration are vectors which can be defined in the three components of the space:

$$f_j = ma_j \quad \text{or} \quad f_j = m\frac{\partial v_j}{\partial t}, \tag{A.20}$$

where j represents the three dimensions of the space 1, 2 and 3. Eq. A.20 can be applied to a continuum, considering each material point as a very small Lagrangian volume (Fig. A.3). The total force applied into the j direction would be the result of adding the gravity force mg_j to the outside forces in the j direction, exerted over the boundaries of the body (Malvern, 1969):

$$f_j = f_{jA} + f_{jB} + f_{jC} + f_{jD} + f_{jE} + f_{jF} + mg_j, \tag{A.21}$$

where g_j is the gravity acceleration in the j direction, $f_{jA}-f_{jF}$ are stress-related forces

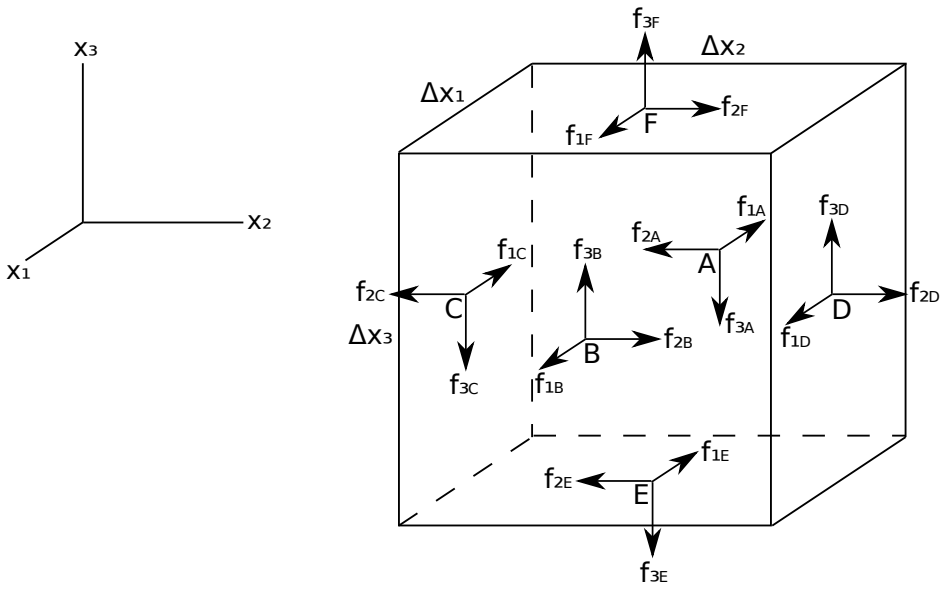

FIGURE A.3: Forces applied into a Lagrangian volume on its boundaries $A - F$.

acting from outside of the Lagrangian volume, and A, B, C, D, E and F represent the boundaries of the body in which the forces are exerted. If Δx_1, Δx_2 and Δx_3 are the dimensions of the Lagrangian volume, then the stress-related forces for the different boundaries can be defined as:

$$f_{jA} = -\sigma_{1jA}\Delta x_2 \Delta x_3, \tag{A.22}$$

$$f_{jB} = +\sigma_{1jB}\Delta x_2 \Delta x_3, \tag{A.23}$$

$$f_{jC} = -\sigma_{2jC}\Delta x_1 \Delta x_3, \tag{A.24}$$

$$f_{jD} = +\sigma_{2jD}\Delta x_1 \Delta x_3, \tag{A.25}$$

$$f_{jE} = -\sigma_{3jE}\Delta x_1 \Delta x_2, \tag{A.26}$$

$$f_{jF} = +\sigma_{3jF}\Delta x_1 \Delta x_2, \tag{A.27}$$

where σ_{ijA} to σ_{ijF} are the components of the stresses for the faces perpendicular to the i directions, defined at the different boundaries A to F. The sign on the right hand side of the Eqs. A.22 – A.27 differentiate forces (positive sign) from counterforces (negative sign). Combining Eqs. A.20 and A.21:

$$f_{jA} + f_{jB} + f_{jC} + f_{jD} + f_{jE} + f_{jF} + mg_j = ma_j. \tag{A.28}$$

Substituting A.22 – A.27 into A.28:

$$(\sigma_{1jB} - \sigma_{1jA})\Delta x_2\Delta x_3 + (\sigma_{2jD} - \sigma_{2jC})\Delta x_1\Delta x_3 + (\sigma_{3jF} - \sigma_{3jE})x_1x_2 + mg_j = ma_j. \tag{A.29}$$

Normalizing Eq. A.29 with the Lagrangian volume V:

$$V = \Delta x\Delta y\Delta z, \tag{A.30}$$

and defining the stress component increments:

$$\Delta\sigma_{1j} = (\sigma_{1jB} - \sigma_{1jA}), \tag{A.31}$$

$$\Delta\sigma_{2j} = (\sigma_{2jD} - \sigma_{2jC}), \tag{A.32}$$

$$\Delta\sigma_{3j} = (\sigma_{3jF} - \sigma_{3jE}), \tag{A.33}$$

we can obtain the momentum equation in the Lagrangian form for the j directions:

$$\frac{\Delta\sigma_{1j}\Delta x_2\Delta x_3}{V} + \frac{\Delta\sigma_{2j}\Delta x_1\Delta x_3}{V} + \frac{\Delta\sigma_{3j}\Delta x_1\Delta x_2}{V} + \frac{m}{V}g_j = \frac{m}{V}a_j, \tag{A.34}$$

or

$$\frac{\Delta\sigma_{1j}}{\Delta x_1} + \frac{\Delta\sigma_{2j}}{\Delta x_2} + \frac{\Delta\sigma_{3j}}{\Delta x_3} + \rho g_j = \rho a_j, \tag{A.35}$$

where ρ is the average material density of the Lagrangian volume. If Δx_1, Δx_2 and Δx_3 tend towards zero and by considering Eq. A.19, then, Eq. A.35 turns into the differential momentum equation in the Lagrangian form which describes the conservation of momentum for a continuous medium in the gravity field:

$$\frac{\partial\sigma_{1j}}{\partial x_1} + \frac{\partial\sigma_{2j}}{\partial x_2} + \frac{\partial\sigma_{3j}}{\partial x_3} + \rho g_j = \rho\frac{\partial v_j}{\partial t}, \tag{A.36}$$

or,

$$\frac{\partial\sigma_{ij}}{\partial x_j} + \rho g_i = \rho\frac{\partial v_i}{\partial t}. \tag{A.37}$$

The stress derivatives with respect to the coordinates represent the forces exerted over the surfaces of an infinitesimal cubic volume, the density times the gravity represents

the body force and the density times the derivative of the velocity with respect to time (acceleration) represents the inertial forces.

Bibliography

C. Amante and B. Eakins. Arc-minute global relief model: procedures, data sources and analysis (ETOPO1), 2009.

M. Andrés-Martínez, J. P. Morgan, M. Pérez-Gussinyé, and L. Rüpke. A new free-surface stabilization algorithm for geodynamical modelling: Theory and numerical tests. *Physics of the Earth and Planetary Interiors*, 246:41–51, 2015. doi: 10.1016/j.pepi.2015.07.003. URL `http://dx.doi.org/10.1016/j.pepi.2015.07.003`.

M. Andrés-Martínez, M. Pérez-Gussinyé, J. Armitage, and J. P. Morgan. Rheological implications of sediment transport for continental rifting and its impact in margin geometry and mayor unconformities. *Planned for submission in*, 2016a.

M. Andrés-Martínez, M. Pérez-Gussinyé, M. Neto-Araujo, and J. P. Morgan. Passive margin asymmetry in the presence of a craton. *Planned for submission to Nature Geosciences*, 2016b.

J. Armitage, T. Henstock, T. Minshull, and J. Hopper. Lithospheric controls on melt production during continental breakup at slow rates of extension: Application to the North Atlantic. *Geochemistry, Geophysics, Geosystems*, 10(6), 2009.

J. Armitage, J. Collier, and T. Minshull. The importance of rift history for volcanic margin formation. *Nature*, 465, 2010.

J. J. Armitage, T. J. Henstock, T. A. Minshull, and J. R. Hopper. Modelling the composition of melts formed during continental breakup of the Southeast Greenland margin. *Earth and Planetary Science Letters*, 269(1):248–258, 2008.

J. J. Armitage, D. J. Ferguson, S. Goes, J. O. Hammond, E. Calais, C. A. Rychert, and N. Harmon. Upper mantle temperature and the onset of extension and break-up in Afar, Africa. *Earth and Planetary Science Letters*, 418:78–90, 2015.

D. Aslanian, M. Moulin, J. Olivet, P. Unternehr, L. Matias, F. Bache, M. Rabineau, H. Nouzé, F. Klingelheofer, I. Contrucci, and C. Labails. Brazilian and African passive

margins of the central segment of the South Atlantic Ocean: Kinematic constraints. *Tectonophysics*, 468(1):98–112, 2009. doi: 10.1016/j.tecto.2008.12.016. URL `http://dx.doi.org/10.1016/j.tecto.2008.12.016`.

B. H. Baker, P. A. Mohr, and L. A. J. Williams. Geology of the eastern rift system of Africa. *Geological Society of America Special Papers*, 136:1–68, 1972.

R. W. Bialas and R. W. Buck. How sediment promotes narrow rifting: Application to the Gulf of California. *Tectonics*, 28(4), 2009. doi: 10.1029/2008TC002394.

O. A. Blaich, J. I. Faleide, and F. Tsikalas. Crustal breakup and continent-ocean transition at South Atlantic conjugate margins. *Journal of Geophysical Research: Solid Earth*, 116 (B1), 2011.

G. Boillot and N. Froitzheim. Non-volcanic rifted margins, continental break-up and the onset of sea-floor spreading: some outstanding questions. *Geological Society, London, Special Publications*, 187(1):9–30, 2001.

B. Bos and C. J. Spiers. Frictional-viscous flow of phyllosilicate-bearing fault rock: Microphysical model and implications for crustal strength profiles. *Journal of Geophysical Research: Solid Earth*, 107(B2), 2002. doi: 10.1029/2001JB000301. URL `http://dx.doi.org/10.1029/2001JB000301`.

J. Braun, J. Chry, A. Poliakov, D. Mainprice, A. Vauchez, A. Tomassi, and M. Daignires. A simple parameterization of strain localization in the ductile regime due to grain size reduction: A case study for olivine. *Journal of Geophysical Research: Solid Earth*, 104 (B11):25167–25181, 1999. ISSN 2156-2202. doi: 10.1029/1999JB900214.

S. Brune, A. A. Popov, and S. V. Sobolev. Modeling suggests that oblique extension facilitates rifting and continental break-up. *Journal of Geophysical Research: Solid Earth*, 117(B8), 2012. doi: 10.1029/2011JB008860. URL `http://dx.doi.org/10.1029/2011JB008860`.

S. Brune, C. Heine, M. Pérez-Gussinyé, and S. V. Sobolev. Rift migration explains continental margin asymmetry and crustal hyper-extension. *Nature Communications*, 5, 2014. doi: 10.1038/ncomms5014. URL `http://dx.doi.org/10.1038/ncomms5014`.

W. Buck. Effect of lithospheric thickness on the formation of high- and low- angle normal faults. *Geology*, 21(10):933–936, 1993. ISSN 00917613. doi: 10.1130/0091-7613(1993)021⟨0933:EOLTOT⟩2.3.CO.

W. R. Buck. Modes of continental lithospheric extension. *Journal of Geophysical Research: Solid Earth*, 96(B12):20161–20178, 1991. doi: 10.1029/91JB01485. URL `http://dx.doi.org/10.1029/91JB01485`.

W. R. Buck and L. L. Lavier. A tale of two kinds of normal fault: the importance of strain weakening in fault development. *Geological Society, London, Special Publications*, 187 (1):289–303, 2001. doi: 10.1144/GSL.SP.2001.187.01.14. URL `http://dx.doi.org/10.1144/GSL.SP.2001.187.01.14`.

S. J. H. Buiter, R. S. Huismans, and C. Beaumont. Dissipation analysis as a guide to mode selection during crustal extension and implications for the styles of sedimentary basins. *Journal of Geophysical Research: Solid Earth*, 113(B6), 2008. doi: 10.1029/2007JB005272. URL `http://dx.doi.org/10.1029/2007JB005272`.

P. D. Clift, S. Brune, and J. Quinteros. Climate changes control offshore crustal structure at South China Sea continental margin. *Earth and Planetary Science Letters*, 420:66–72, 2015. ISSN 0012-821X. doi: 10.1016/j.epsl.2015.03.032.

G. Corti, J. V. Wijk, M. Bonini, D. Sokoutis, S. Cloetingh, F. Innocenti, and P. Manetti. Transition from continental break-up to punctiform seafloor spreading: How fast, symmetric and magmatic. *Geophysical Research Letters*, 30(12), 2003. doi: 10.1029/2003GL017374. URL `http://dx.doi.org/10.1029/2003GL017374`.

F. Crameri, H. Schmeling, G. J. Golabek, T. Duretz, R. Orendt, S. J. H. Buiter, D. A. May, B. J. P. Kaus, T. V. Gerya, and P. J. Tackley. A comparison of numerical surface topography calculations in geodynamic modelling: an evaluation of the sticky air method. *Geophysical Journal International*, 189, 2012. doi: 10.1111/j.1365-246X.2012.05388.x.

M. Crouzeix and P.-A. Raviart. Conforming and nonconforming finite element methods for solving the stationary Stokes equations I. *Reveu française d'automatique, informatique, recherche opérationnelle. Mathématique*, 7(3):33–75, 1973.

M. Dabrowski, M. Krotkiewski, and D. W. Schmid. MILAMIN: MATLAB-based finite element method solver for large problems. *Geochemistry, Geophysics, Geosystems*, 9(4), 2008.

E. de Souza Neto, D. Peric, and D. Owen. *Computational Methods for Plasticity: Theory and Applications*. Wiley, 2008. ISBN 9781119964544.

N. G. Direen, H. M. J. Stagg, P. A. Symonds, and I. O. Norton. Variations in rift symmetry: cautionary examples from the Southern Rift System (Australia-Antarctica). *Geological Society, London, Special Publications*, 369(1):453–475, 2012. doi: 10.1144/SP369.4. URL `http://dx.doi.org/10.1144/SP369.4`.

J. Dunbar and D. Sawyer. Continental rifting at pre-existing lithospheric weaknesses. *Nature*, 1988. doi: 10.1038/333450a0. URL `http://dx.doi.org/10.1038/333450a0`.

J. A. Dunbar and D. S. Sawyer. How preexisting weaknesses control the style of continental breakup. *Journal of Geophysical Research: Solid Earth*, 94(B6):7278–7292, 1989. doi: 10.1029/JB094iB06p07278. URL `http://dx.doi.org/10.1029/JB094iB06p07278`.

S. Dyksterhuis, P. Rey, R. D. Muller, and L. Moresi. Effects of initial weakness on rift architecture. *Geological Society, London, Special Publications*, 282(1):443–455, 2007. doi: 10.1144/SP282.18. URL `http://dx.doi.org/10.1144/SP282.18`.

R. L. Evans, A. G. Jones, X. Garcia, M. Muller, M. Hamilton, S. Evans, C. J. S. Fourie, J. Spratt, S. Webb, H. Jelsma, and D. Hutchins. Electrical lithosphere beneath the Kaapvaal craton, southern Africa. *Journal of Geophysical Research: Solid Earth*, 116(B4), 2011. doi: 10.1029/2010JB007883. URL `http://dx.doi.org/10.1029/2010JB007883`.

J. Fairhead. The structure of the lithosphere beneath the Eastern Rift, East Africa, deduced from gravity studies. *Tectonophysics*, 30(3):269–298, 1976.

D. A. Falvey. The development of continental margins in plate tectonic theory. *APPEA Journal-Australian Petroleum Production and Exploration Association*, 14(1):95–106, 1974.

D. A. Falvey and J. C. Mutter. Regional plate tectonics and the evolution of Australia's passive continental margins. *BMR Journal of Australian Geology and Geophysics*, 6: 1–29, 1981.

L. Fleitout, C. Froidevaux, and D. Yuen. Active lithospheric thinning. *Tectonophysics*, 132, 1986. doi: 10.1016/0040-1951(86)90037-5.

Ø. Frey, S. Planke, and P. Symonds. Deep crustal structure and rheology of the Gascoyne volcanic margin, western Australia. *Marine Geophysical Researches*, 20:293312, 1998. doi: 10.1023/A:1004791330763.

T. Gerya. Introduction to numerical geodynamic modelling, 2010. ID: 646816277.

T. V. Gerya and D. A. Yuen. Rayleigh-Taylor instabilities from hydration and melting propel 'cold plumes' at subduction zones. *Earth and Planetary Science Letters*, 212(1): 47–62, 2003.

M. Gillard, J. Autin, G. Manatschal, D. Sauter, M. Munschy, and M. Schaming. Tectonomagmatic evolution of the final stages of rifting along the deep conjugate Australian-Antarctic magma-poor rifted margins: Constraints from seismic observations. *Tectonics*, 34(4):753–783, 2015. doi: 10.1002/2015TC003850. URL `http://dx.doi.org/10.1002/2015TC003850`.

G. C. Gleason and J. Tullis. A flow law for dislocation creep of quartz aggregates determined with the molten salt cell. *Tectonophysics*, 247(1):1–23, 1995. doi: 10.1016/0040-1951(95)00011-B. URL http://dx.doi.org/10.1016/0040-1951(95)00011-B.

R. L. Gresens. Composition-volume relationships of metasomatism. *Chemical geology*, 2: 47–65, 1967.

M. R. Handy and H. Stünitz. Strain localization by fracturing and reaction weakening – a mechanism for initiating exhumation of subcontinental mantle beneath rifted margins. *Geological Society, London, Special Publications*, 200(1):387–407, 2002. doi: 10.1144/GSL.SP.2001.200.01.22. URL http://dx.doi.org/10.1144/GSL.SP.2001.200.01.22.

L. N. Hansen, M. E. Zimmerman, and D. L. Kohlstedt. Laboratory measurements of the viscous anisotropy of olivine aggregates. *Nature*, 492(7429):415–418, 2012. doi: 10.1038/nature11671. URL http://dx.doi.org/10.1038/nature11671.

C. Heine, J. Zoethout, and R. D. Müller. Kinematics of the South Atlantic rift. *Solid Earth*, 4(2):215–253, 2013. doi: 10.5194/se-4-215-2013. URL http://dx.doi.org/10.5194/se-4-215-2013.

G. Hirth and D. Kohlstedt. Rheology of the upper mantle and the mantle wedge: A view from the experimentalists. In J. Eiler, editor, *Inside the subduction factory*, pages 83–105. AGU, 2003. ISBN 0-87590-997-3.

G. Hirth and D. L. Kohlstedt. Water in the oceanic upper mantle: implications for rheology, melt extraction and the evolution of the lithosphere. *Earth and Planetary Science Letters*, 144(1-2), 1996. doi: 10.1016/0012-821X(96)00154-9. URL http://dx.doi.org/10.1016/0012-821X(96)00154-9.

J. R. Hopper and W. R. Buck. The effect of lower crustal flow on continental extension and passive margin formation. *Journal of Geophysical Research: Solid Earth*, 101(B9): 20175–20194, 1996.

J. R. Hopper, T. Dahl-Jensen, W. S. Holbrook, H. C. Larsen, D. Lizarralde, J. Korenaga, G. M. Kent, and P. B. Kelemen. Structure of the SE Greenland margin from seismic reflection and refraction data: Implications for nascent spreading center subsidence and asymmetric crustal accretion during North Atlantic opening. *Journal of Geophysical Research: Solid Earth*, 108(B5), 2003.

T. J. R. Hughes. *The finite element method: linear static and dynamic finite element analysis*. Dover Publications, Mineola, NY, 2000. ISBN 0486411818 9780486411811. ID: 301049178.

R. Huismans and C. Beaumont. Symmetric and asymmetric lithospheric extension: Relative effects of frictional-plastic and viscous strain softening. *Journal of Geophysical Research: Solid Earth*, 108(B10), 2003.

R. Huismans and C. Beaumont. Depth-dependent extension, two-stage breakup and cratonic underplating at rifted margins. *Nature*, 473(7345):74–78, 2011. doi: 10.1038/nature09988. URL `http://dx.doi.org/10.1038/nature09988`.

R. S. Huismans and C. Beaumont. Asymmetric lithospheric extension: The role of frictional plastic strain softening inferred from numerical experiments. *Geology*, 30(3): 211–214, 2002.

R. S. Huismans and C. Beaumont. Roles of lithospheric strain softening and heterogeneity in determining the geometry of rifts and continental margins. *Geological Society, London, Special Publications*, 282(1):111–138, 2007. doi: 10.1144/SP282.6. URL `http://dx.doi.org/10.1144/SP282.6`.

R. S. Huismans, S. J. H. Buiter, and C. Beaumont. Effect of plastic-viscous layering and strain softening on mode selection during lithospheric extension. *Journal of Geophysical Research: Solid Earth*, 110(B2), 2005. doi: 10.1029/2004JB003114. URL `http://dx.doi.org/10.1029/2004JB003114`.

S. Ingebritsen and C. E. Manning. Geological implications of a permeability-depth curve for the continental crust. *Geology*, 27(12):1107–1110, 1999.

M. Kameyama, D. A. Yuen, and S.-I. Karato. Thermal-mechanical effects of low-temperature plasticity (the Peierls mechanism) on the deformation of a viscoelastic shear zone. *Earth and Planetary Science Letters*, 168(1):159–172, 1999.

S. I. Karato and P. Wu. Rheology of the upper mantle: A synthesis. *Science*, 260(5109): 771–778, 1993.

S.-I. Karato, M. S. Paterson, and J. D. FitzGerald. Rheology of synthetic olivine aggregates: Influence of grain size and water. *Journal of Geophysical Research: Solid Earth*, 91(B8):8151–8176, 1986. ISSN 2156-2202. doi: 10.1029/JB091iB08p08151.

B. J. Kaus, H. Mühlhaus, and D. A. May. A stabilization algorithm for geodynamic numerical simulations with a free surface. *Physics of the Earth and Planetary Interiors*, 181(1):12–20, 2010. doi: 10.1016/j.pepi.2010.04.007.

B. J. P. Kaus. Factors that control the angle of shear bands in geodynamic numerical models of brittle deformation. *Tectonophysics*, 484(1):36–47, 2010.

C. Keen and R. Boutilier. Interaction of rifting and hot horizontal plume sheets at volcanic margins. *Journal of Geophysical Research: Solid Earth*, 105(B6):13375–13387, 2000.

P. Kelemen and W. Holbrook. Origin of thick, high-velocity igneous crust along the US East Coast Margin. *Journal of Geophysical Research*, 100(B7):10077–10094, 1995. doi: 10.1029/95JB00924.

S. C. Kramer, C. R. Wilson, and D. R. Davies. An implicit free surface algorithm for geodynamical simulations. *Physics of the Earth and Planetary Interiors*, 194:25–37, 2012. ISSN 0031-9201. doi: http://dx.doi.org/10.1016/j.pepi.2012.01.001.

N. J. Kusznir and R. G. Park. The extensional strength of the continental lithosphere: its dependence on geothermal gradient, and crustal composition and thickness. *Geological Society, London, Special Publications*, 28(1):35–52, 1987. doi: 10.1144/GSL.SP.1987.028.01.04. URL `http://dx.doi.org/10.1144/GSL.SP.1987.028.01.04`.

L. L. Lavier and W. R. Buck. Half graben versus large-offset low-angle normal fault: Importance of keeping cool during normal faulting. *Journal of Geophysical Research: Solid Earth*, 107(B6), 2002. doi: 10.1029/2001JB000513. URL `http://dx.doi.org/10.1029/2001JB000513`.

X. Le Pichon. Sea-floor spreading and continental drift. *Journal of Geophysical Research*, 73(12):3661–3697, 1968.

R. Lebensohn and C. Tomé. A self-consistent anisotropic approach for the simulation of plastic deformation and texture development of polycrystals: application to zirconium alloys. *Acta metallurgica et materialia*, 41(9):2611–2624, 1993.

E. R. Lundin and A. G. Doré. Hyperextension, serpentinization, and weakening: A new paradigm for rifted margin compressional deformation. *Geology*, 39(4):347–350, 2011.

L. E. Malvern. *Introduction to the Mechanics of a Continuous Medium*. Prentice-Hall, 1969.

G. Manatschal and D. Bernoulli. Architecture and tectonic evolution of nonvolcanic margins: Present-day Galicia and ancient Adria. *Tectonics*, 18(6):1099–1119, 1999. ISSN 1944-9194. doi: 10.1029/1999TC900041. URL `http://dx.doi.org/10.1029/1999TC900041`.

R. McConnell. Geological development of the rift system of eastern Africa. *Geological Society of America Bulletin*, 83(9):2549–2572, 1972.

D. McKenzie. Surface deformation, gravity anomalies and convection. *Geophysical Journal of the Royal Astronomical Society*, 48(2):211–238, 1977.

D. McKenzie. Some remarks on the development of sedimentary basins. *Earth and Planetary Science Letters*, 1978. doi: 10.1016/0012-821X(78)90071-7. URL `http://dx.doi.org/10.1016/0012-821X(78)90071-7`.

D. P. McKenzie and R. L. Parker. The North Pacific: an example of tectonics on a sphere. *Nature*, 216:1276–1280, 1967.

M. Menzies, K. Gallagher, and A. Yelland. Volcanic and nonvolcanic rifted margins of the Red Sea and Gulf of Aden: crustal cooling and margin evolution in Yemen. *Geochimica et Cosmochimica Acta*, 61(12):2511–2527, 1997.

T. Minshull. Geophysical characterisation of the oceancontinent transition at magma-poor rifted margins. *Comptes Rendus Geoscience*, 341:382–393, 2009.

T. Minshull, S. Dean, R. White, and R. Whitmarsh. Anomalous melt production after continental break-up in the southern Iberia Abyssal Plain. *Geological Society, London, Special Publications*, 187(1):537–550, 2001.

L. Moresi and H. B. Mühlhaus. Anisotropic viscous models of large-deformation Mohr-Coulomb failure. *Philosophical Magazine*, 2006. doi: 10.1080/14786430500255419. URL `http://dx.doi.org/10.1080/14786430500255419`.

L. Moresi, F. Dufour, and H. B. Mühlhaus. A Lagrangian integration point finite element method for large deformation modeling of viscoelastic geomaterials. *Journal of Computational Physics*, 184(2):476–497, 2003. ISSN 0021-9991. doi: 10.1016/S0021-9991(02)00031-1. URL `http://www.sciencedirect.com/science/article/pii/S0021999102000311`.

L. Moresi, S. Quenette, V. Lemiale, C. Mériaux, B. Appelbe, and H. Mühlhaus. Computational approaches to studying non-linear dynamics of the crust and mantle. *Physics of the Earth and Planetary Interiors*, 163(1):69–82, 2007. ISSN 0031-9201. doi: http://dx.doi.org/10.1016/j.pepi.2007.06.009.

J. P. Morgan, J. W. Morgan, and E. Price. Hotspot melting generates both hotspot volcanism and a hotspot swell? *Journal of Geophysical Research: Solid Earth*, 100(B5): 8045–8062, 1995.

W. J. Morgan. Rises, trenches, great faults, and crustal blocks. *Journal of Geophysical Research*, 73(6), 1968. doi: 10.1029/JB073i006p01959. URL `http://dx.doi.org/10.1029/JB073i006p01959`.

O. Müntener and G. Manatschal. High degrees of melt extraction recorded by spinel harzburgite of the Newfoundland margin: The role of inheritance and consequences for

the evolution of the southern North Atlantic. *Earth and Planetary Science Letters*, 252 (3):437–452, 2006.

T. K. Nielsen and J. R. Hopper. From rift to drift: Mantle melting during continental breakup. *Geochemistry, Geophysics, Geosystems*, 5(7), 2004.

D. S. O'Hanley. Solution to the volume problem in serpentinization. *Geology*, 20(8): 705–708, 1992.

M. Pérez-Gussinyé. A tectonic model for hyperextension at magma-poor rifted margins: an example from the West Iberia–Newfoundland conjugate margins. *Geological Society, London, Special Publications*, 369(1):403–427, 2013.

M. Peréz-Gussinyé and T. J. Reston. Rheological evolution during extension at nonvolcanic. *Journal of Geophysical Research*, 106(B3):3961–3975, 2001.

M. Pérez-Gussinyé, D. Klaeschen, and J. Totterdell. Margin architecture and oceanization of the Australian Bay Bight. In preparation for *Tectonics*.

M. Pérez-Gussinyé, T. J. Reston, and J. P. Morgan. Serpentinization and magmatism during extension at non-volcanic margins: the effect of initial lithospheric structure. *Geological Society, London, Special Publications*, 187(1):551–576, January 01 2001.

M. Pérez-Gussinyé, T. J. Reston, and J. P. Morgan. Serpentinization and magmatism during extension at non-volcanic margins: the effect of initial lithospheric structure. *Geological Society, London, Special Publications*, 2001. doi: 10.1144/GSL.SP.2001.187.01.27. URL `http://dx.doi.org/10.1144/GSL.SP.2001.187.01.27`.

M. Pérez-Gussinyé, J. P. Morgan, T. J. Reston, and C. R. Ranero. The rift to drift transition at non-volcanic margins: Insights from numerical modelling. *Earth and Planetary Science Letters*, 244(12):458–473, 4/15 2006.

J. Poirier. Shear localization and shear instability in materials in the ductile field. *Journal of Structural Geology*, 2(12):135 – 142, 1980. ISSN 0191-8141. doi: http://dx.doi.org/10.1016/0191-8141(80)90043-7. ¡ce:title¿Shear zones in rocks ¡/ce:title¿.

G. Ranalli. *Rheology of the Earth*. Chapman & Hall, London, 2nd ed. edition, 1994. ISBN 9780412546709; 0412546701.

C. R. Ranero and M. Pérez-Gussinyé. Sequential faulting explains the asymmetry and extension discrepancy of conjugate margins. *Nature*, 468(7321):294–299, 2010.

T. F. Redfield and P. T. Osmundsen. The long-term topographic response of a continent adjacent to a hyperextended margin: A case study from Scandinavia. *Geological Society*

of America Bulletin, 125(1-2):184–200, 2012. doi: 10.1130/B30691.1. URL `http://dx.doi.org/10.1130/B30691.1`.

T. Reston, J. Pennell, A. Stubenrauch, I. Walker, and M. Perez-Gussinye. Detachment faulting, mantle serpentinization, and serpentinite-mud volcanism beneath the Porcupine Basin, southwest of Ireland. *Geology*, 29(7):587–590, 2001.

T. J. Reston and J. P. Morgan. Continental geotherm and the evolution of rifted margins. *Geology*, 32(2):133–136, 2004.

J. R. Rice. Fault stress states, pore pressure distributions, and the weakness of the San Andreas fault. *International Geophysics*, 51:475–503, 1992.

J. Ridley. The relations between mean rock stress and fluid flow in the crust: With reference to vein- and lode-style gold deposits. *Ore Geology Reviews*, 8(1-2):23–37, 1993. doi: 10.1016/0169-1368(93)90026-u. URL `http://dx.doi.org/10.1016/0169-1368(93)90026-u`.

J. Ritsema and H. van Heijst. New seismic model of the upper mantle beneath Africa. *Geology*, 28(1):63–66, Jan. 2000.

E. Rybacki and G. Dresen. Dislocation and diffusion creep of synthetic anorthite aggregates. *Journal of Geophysical Research: Solid Earth*, 105(B11), 2000. doi: 10.1029/2000JB900223. URL `http://dx.doi.org/10.1029/2000JB900223`.

V. Sacek and N. Ussami. Upper mantle viscosity and dynamic subsidence of curved continental margins. *Nature Communications*, 4, 2013. doi: 10.1038/ncomms3036. URL `http://dx.doi.org/10.1038/ncomms3036`.

J. R. Shewchuk. Triangle: Engineering a 2D Quality Mesh Generator and Delaunay Triangulator. In M. C. Lin and D. Manocha, editors, *Applied Computational Geometry: Towards Geometric Engineering*, volume 1148 of *Lecture Notes in Computer Science*, pages 203–222. Springer-Verlag, May 1996. From the First ACM Workshop on Applied Computational Geometry.

R. H. Sibson. Conditions for fault-valve behaviour. *Geological Society, London, Special Publications*, 54(1):15–28, 1990. doi: 10.1144/GSL.SP.1990.054.01.02.

J. Sibuet, S. Srivastava, and G. Manatschal. Exhumed mantle-forming transitional crust in the Newfoundland-Iberia rift and associated magnetic anomalies. *Journal of Geophysical Research*, 112(B6), 2007. ISSN 2156-2202. doi: 10.1029/2005JB003856.

J.-C. Sibuet. Formation of non-volcanic passive margins: A composite model applies to the conjugate Galicia and southeastern Flemish cap margins. *Geophysical Research*

Letters, 19(8):769–772, 1992. ISSN 1944-8007. doi: 10.1029/91GL02984. URL `http://dx.doi.org/10.1029/91GL02984`.

H. Stagg, J. Willcox, D. Needham, G. OBrien, C. Cockshell, A. Hill, B. Thomas, and L. Hough. Basins of the Great Australian Bight region-geology and petroleum potential: Continental margins program folio 5. *Bureau of Mineral Resources, Geology and Geophysics and Department of Mines and Energy, South Australia*, 1990.

J. E. Streit. Low frictional strength of upper crustal faults: a model. *Journal of Geophysical Research: Solid Earth*, 102(B11):24619–24626, 1997.

K. Subrahmanya. Arabian Sea-the prime witness to the drama of India-Madagascar-Seychelles separation. *Gondwana Research*, 4(4):792–793, 2001.

M. Talwani, J. Mutter, R. Houtz, and M. Konig. The crustal structure and evolution of the area underlying the magnetic quiet zone on the margin south of Australia: Rifted margins. In *Geological and Geophysical Investigations of Continental Margins*, pages 151–175. AAPG Special Volumes, 1979.

A. Tommasi, D. Mainprice, G. Canova, and Y. Chastel. Viscoplastic self-consistent and equilibrium-based modeling of olivine lattice preferred orientations: Implications for the upper mantle seismic anisotropy. *Journal of Geophysical Research: Solid Earth*, 105(B4):7893–7908, 2000. doi: 10.1029/1999JB900411. URL `http://dx.doi.org/10.1029/1999JB900411`.

A. Tommasi, M. Knoll, A. Vauchez, J. W. Signorelli, C. Thoraval, and R. Logé. Structural reactivation in plate tectonics controlled by olivine crystal anisotropy. *Nature Geoscience*, 2(6):423–427, 2009. doi: 10.1038/ngeo528. URL `http://dx.doi.org/10.1038/ngeo528`.

J. Totterdell, J. Blevin, H. Struckmeyer, B. Bradshaw, J. Colwell, and J. Kennard. A new sequence framework for the Great Australian Bight: Starting with a clean slate. *APPEA Journal-Australian Petroleum Production and Exploration Association*, 40(1): 95–120, 2000.

J. Tugend, G. Manatschal, N. Kusznir, E. Masini, G. Mohn, and I. Thinon. Formation and deformation of hyperextended rift systems: Insights from rift domain mapping in the Bay of Biscay-Pyrenees. 33(7):1239–1276, 2014. doi: 10.1002/2014TC003529.

D. Turcotte and G. Schubert. *Geodynamics*. John Wiley & Sons, 1982. ISBN 9780521666244.

D. Turcotte and G. Schubert. *Geodynamics*. Cambridge University Press, 2002. ISBN 9780521666244.

M. Voss, M. C. Schmidt-Aursch, and W. Jokat. Variations in magmatic processes along the East Greenland volcanic margin. *Geophysical Journal International*, 177(2):755–782, 2009.

J. K. Weissel and G. D. Karner. Flexural uplift of rift flanks due to mechanical unloading of the lithosphere during extension. *Journal of Geophysical Research: Solid Earth*, 94 (B10):13919–13950, 1989.

R. Whitmarsh, G. Manatschal, and T. Minshull. Evolution of magma-poor continental margins from rifting to seafloor spreading. *Nature*, 413(6852):150–154, 2001.

K. Wilks and N. Carter. Rheology of some continental lower crustal rocks. *Tectonophysics*, 182(1-2):57–77, October 1990.

J. T. Wilson. Hypothesis of Earth's behaviour. *Nature*, 198(4884):925 – 929, 1963.

J. T. Wilson. A new class of faults and their bearing on continental drift. *Nature*, 207 (4995):343–347, 1965.

J. T. Wilson. Did the atlantic close and then re-open? 211(5050):676–681, 1966.

J. Wimert and S. Hier-Majumder. A three-dimensional microgeodynamic model of melt geometry in the Earth's deep interior. *Journal of Geophysical Research: Solid Earth*, 117(B4), 2012.

S. Zaleski and P. Julien. Numerical simulation of salt diapir formation in small and extended geometries. *Report, Total-Compagnie Francaise des Petroles*, 1990.

S. Zhong, M. Gurnis, and G. Hulbert. Accurate determination of surface normal stress in viscous flow from a consistent boundary flux method. *Physics of the Earth and Planetary Interiors*, 78(12):1–8, 6 1993.

S. Zhong, M. Gurnis, and L. Moresi. Free-surface formulation of mantle convection-i, basic theory and application to plumes. *Geophysical Journal International*, 127(3):708–718, 1996.

O. Zienkiewicz, J. Vilotte, and S. Toyoshima. Iterative method for constrained and mixed approximation. an inexpensive improvement of FEM performance. *Computer Methods in Applied Mechanics and Engineering*, 51(13):329, September 1985.